UNIVERSITY OF
Southampton
School of Engineering Sciences

Adaptive Composite Blades for Horizontal Axis Tidal Turbines

Rachel F. Nicholls-Lee

Doctor of Philosophy

Faculty of Engineering and the Environment
School of Engineering Sciences
Fluid Structure Interactions Research Group

May 2011

Abstract

The oceans are a huge resource of untapped energy. There are many marine renewable energy sources however tidal energy has the advantage of being highly predictable. The range of devices for tidal energy extraction is extensive with power being generated either by extracting potential or kinetic energy. Due to environmental concerns regarding potential devices it is thought that a breakthrough will occur in the area of kinetic energy devices, most likely horizontal axis tidal turbines (HATTs). No HATT technology is yet commercial and further research into the field is required to advance the concepts, improve the feasibility of maintenance and make devices more efficient and economic.

The blades of a HATT are the source of energy extraction for the device and are required to operate in a harsh subsea environment for a long (20 year) life cycle with minimal need for maintenance. Choice of an appropriate foil section for the blade is integral. A novel bi-directional section has been developed for use on a HATT and compared to a variable pitch device. The concept of using adaptive composite blades in order to improve energy capture but also decrease design complexity has been considered. Preliminary analysis was undertaken and it suggested that a 2.5% increase in annual energy capture and a 10% decrease in thrust loading could be expected through the use of a bend-twist coupled adaptive HATT blade. An experimental method was developed for the assessment of bend and induced twist in a coupled spar, and the results compared well to numerical analysis with the conclusion that the numerical model is very sensitive to manufacturing accuracy. A design tool for the development of adaptive composite bend-twist coupled HATT blades has been developed. The tool couples finite element analysis, computational fluid dynamics and blade element theory to create optimal blades.

Coupling the passively adaptive bend-twist coupled spar with actively adaptive snap-through asymmetric laminates to create an efficient blade that works optimally in both directions of tidal flow has been considered. A comparison between four arrays of 4 turbines in a staggered grid, one each with standard fixed pitch, bi-directional, passively adaptive and actively adaptive blades illustrated that annual energy capture could be increased by up to 120% with the use of actively adaptive blades when compared to a base fixed bladed rotor.

This thesis is dedicated to the University Dolphin, may he rest in peace:

Dolphins Dolphins over there
Dolphins swim any where
Diving deep down in the sea
Wish they could be with you
And me

[Anon]

Acknowledgements

I could not have achieved this thesis without the support of my supervisors, Stephen Turnock and Steve Boyd, who have tolerated me through several years of tidal research. I would also like to thank Ajit Shenoi for funding many enlightening trips to conferences around the globe, Dominic Hudson for loitering in the office and providing a welcome distraction, Tony Molland for being the font of all knowledge, and Pompey <*ahem*> supporter Prof Price for informative football discussions.

I include my parents for their invaluable advice on the Chemistry Hotline and unfailing shame that I will never have a 'real' job – which, if nothing else, kept me going through sheer obstinacy. My siblings have helped with their unswerving confidence in both myself and my work, and proof-reading my thesis. SUWAKE for preventing me from becoming a hermit and getting me out on the water occasionally, despite the steady decline in brain cells that occurred after sessions failing to land the kicker.

I would like to thank all of my friends and fiends from FSI without whom I would have gone insane years ago. Specifically Rachel Blackburn for supplying me with quality write up snacks and keeping me on the straight and relatively narrow, Simon Lewis for extensive Skype counseling, Tom Coe for HHGTTG and Monty Python quotes, Richard Fruehman for simply being the eccentric yoghurt loving Austrian that he is, Rachael Waugh for tea breaks, Adam Sobey for reinstigating Friday Beers, George Dadd for keeping me on my toes with continual relocation of office supplies, Sally Denchfield for attending step and body conditioning with me and exchanging woeful write up stories, Matt Findlay for enlightening philosophical debates on the ethics of UK Sport, and Alex Phillips for his fantastic proof-reading, sarcastic comments and general cantankerous nature.

My thanks go to the staff at At One, Braunton, and The Puffin Café, Woolacombe, for feeding me mochas when I spent days in there writing up between surf sessions.

Last, and by no means least, I would like to accede to my true status of the crazy cat lady of FSI by thanking my mogs, Benjy and Molly. The aforementioned furballs have tag teamed on keeping me company, giving me warm furry hugs, getting me through those really, really bleak moments, and dragging me back from the brink when I really felt like I was up that proverbial foul smelling creek without means of propulsion.

Authors declaration and list of papers

I, Rachel Felicity Nicholls-Lee declare that the thesis entitled:

Adaptive Composite Blades for Horizontal Axis Tidal Turbines

and the work presented in the thesis are both my own, and have been generated by me as the result of my own original research. I confirm that:

- this work was done wholly or mainly while in candidature for a research degree at this University;
- where any part of this thesis has previously been submitted for a degree or any other qualification at this University or any other institution, this has been clearly stated;
- where I have consulted the published work of others, this is always clearly attributed;
- where I have quoted from the work of others, the source is always given. With the exception of such quotations, this thesis is entirely my own work;
- I have acknowledged all main sources of help;
- where the thesis is based on work done by myself jointly with others, I have made clear exactly what was done by others and what I have contributed myself;
- parts of this work have been published as:
  - LOG+1 Limited, ALSTOM Power Limited, WUMTIA (2007) **Economic Viability of a Simple Tidal Stream Energy Capture Device**. DTI Project No: TP/3/ERG/6/1/15527/REP, URN 07/575, February 2007.
  - Nicholls-Lee, Rachel and Turnock, Stephen R. (2007) **Enhancing performance of a horizontal axis tidal turbine using adaptive blades.** In, *OCEANS 2007, 18-21 June 2007, Aberdeen, Scotland, U.K.,* USA, Institute of Electrical and Electronics Engineers, 1-6.
  - Turnock, S.R., Nicholls-Lee, R.F., Allton, R., McKenzie, D., Sharpe, M. and Rigg, R. (2007) **Economic viability of alternative horizontal axis tidal turbine concepts: operation and maintenance simplicity is the key?** In, *Wave and Tidal Technology*

Symposium (WATTS 2007), Cowes, UK, 4 Sep 2007. UK, Renewable Energy Association, 19pp.

- Turnock, S.R., Muller, G., Nicholls-Lee, R.F., Denchfield, S., Hindley, S., Shelmerdine, R. and Stevens, S. (2007) **Development of a floating tidal energy system suitable for use in shallow water.** In, *7th European Wave and Tidal Energy Conference (EWTEC 2007), Porto, Portugal, 11-14 Sep 2007*. Portugal, European Wave and Tidal Energy Conference, 9pp.
- Nicholls-Lee, R.F. and Turnock, S.R. (2007) **The use of computational fluid dynamics in the optimisation of marine current turbines.** In, *10th Numerical Towing Tank Symposium (NuTTS'07), Hamburg, Germany, 23-25 Sep 2007*. Hamburg, Germany, 6pp.
- Nicholls-Lee, Rachel F., Turnock, Stephen R. and Boyd, Stephen W. (2008) **Simulation based optimisation of marine current turbine blades.** In, Betram, Volker and Rigo, Philippe (eds.) *7th International Conference on Computer and IT Applications in the Maritime Industries (COMPIT'08), Liège, 21-23 April 2008.* Liège, Belgium, Architecture Navale, Génie Maritime, Navigation Intérieure et Maritime, Analyse des Systèmes de Transport, 314-328.
- Nicholls-Lee, Rachel F., Turnock, Stephen R. and Boyd, Stephen W. (2008) **Performance prediction of a free stream tidal turbine with composite bend-twist coupled blades.** In, *2nd International Conference on Ocean Energy (ICOE 2008)*, *15th – 17th October, Brest France,* 9pp.
- Nicholls-Lee, Rachel F., Boyd, Stephen W. and Turnock, Stephen R. (To Be Published 2009) **Development of high performance composite bend-twist couple blades for a horizontal axis tidal turbine.** *In 17th International Conference on Composite Materials, 27th – 31st July 2009, Edinburgh, Scotland, U.K.*
- Nicholls-Lee, R.F and Turnock, S.R. (2008) **Tidal energy extraction: renewable, sustainable and predictable.** *Science Progress*, 91, (1), 81-111, (doi:10.3184/003685008X285582).
- Turnock, S.R., Keane, A.J., Bressloff, N.W., Nicholls-Lee, R.F. and Boyd, S.W. (2009) **Morphing of 'flying' shapes for autonomous underwater and aerial vehicles.** In, *NATO RTO Modelling & Simulation Conference 2009, Lisbon, Portugal*.

- Turnock, S.R., Phillips, A.B., Nicholls-Lee, R.F., Banks, J. (2009) **Modelling marine current turbine wakes using a coupled RANS-BEMT model as a tool for analysing optimum arrays of turbines**, submitted to Renewable Energy.
- Nicholls-Lee, Rachel F., Boyd, Stephen W. and Turnock, Stephen R. (2010) **Obtaining experimental data suitable for validation of a numerical design tool for an adaptive composite free stream tidal turbine.** *In The 11th International Symposium on Practical Design of Ships and Other Floating Structures, Rio de Janeiro, Brazil, 19th-24th September 2010.*
- Nicholls-Lee, R.F., Boyd, S.W., Turnock, S.R. (2011) **Comparison of Experimental and Numerical Analyses of a Composite Bend-Twist Coupled Double Box Beam**, submitted to Composites Part B.
- Nicholls-Lee, R.F., Turnock, S.R., Boyd, S.W. (2011) **Tidal Turbine Blade Selection for Optimal Performance in an Array**, accepted for publication in the *30th International Conference on Ocean, Offshore and Arctic Engineering, 19th-24th June 2011, Rotterdam, The Netherlands.*
- Nicholls-Lee, R.F., Turnock, S.R., Boyd, S.W. (2011) **A Method for Analysing Fluid Structure Interactions on a Horizontal Axis Tidal Turbine**, accepted for publication in the *9th European Wave and Tidal Energy Conference, 5th-9th September 2011, Southampton, U.K.*

Signed: ……..

Date:…….

Table of Contents

List of Figures

List of Tables

Nomenclature

a	-	First coefficient taking into account thermal effects
a'	-	Circumferential flow factor
a_i	-	Axial interference factor
a_r	(m)	Radius of Earth
b	-	Second coefficient taking into account thermal effects
c	-	Third coefficient taking into account thermal effects
c_h	(m)	Section chord
c_w	(ms^{-1})	Wave speed
d	-	Fourth coefficient taking into account thermal effects
d_c	(m)	Half chord length
g	(ms^{-2})	Acceleration due to gravity
h	(m)	Depth of laminate
h_c	(m)	Maximum height of segment
k	(m)	Height above seabed
l	(m)	Height of column of water
m	(kg)	Mass of fluid
n	(rps)	Number of revolutions per second
r	(m)	Radius
t	(m)	Thickness
t_i	(s)	Time
u^o	(m)	Midplane displacement in the x direction
v	(ms^{-1})	Velocity of fluid
v_f	(ms^{-1})	Free stream fluid velocity
v_{max}	(ms^{-1})	Maximum fluid velocity
v_{mean}	(ms^{-1})	Mean flow velocity
v^o	(m)	Midplane displacement in the y direction
v_p	(ms^{-1})	

v_r	(ms^{-1})	Velocity of the fluid of the rotor plane
v_t	(ms^{-1})	Fluid velocity at the tidal turbine
v_{tip}	(ms^{-1})	Blade tip speed
w^o	(m)	Midplane displacement in the z direction
z	(m)	Distance of layer from neutral axis
A	(m^2)	Area through which the flow passes
A_f	(m^2)	Area of the fibres in a layer of the laminate
A_{ij}	(Nm)	Laminate extensional stiffnesses
A_m	(m^2)	Area of the matrix in a layer of the laminate
B_{ij}	(N)	Laminate coupling stiffnesses
C_D	-	Drag coefficient
C_F	(N)	Centrifugal force
C_{ijkl}	-	Elastic constants
C_L	-	Lift coefficient
C_P	-	Pressure coefficient
C_{pow}	-	Power coefficient
C_{POWmax}	-	Theoretical maximum power coefficient
C_Q	-	Torque coefficient
C_T	-	Thrust coefficient
D	(m)	Diameter
D_r	(N)	Drag
D_{ij}	(Nm)	Laminate bending stiffnesses
E	(J)	Kinetic energy of a body of fluid
E_1	(GPa)	Transverse Young's Modulus
E_2	(GPa)	Longitudinal Young's Modulus
E_f	(GPa)	Young's Modulus of the fibres in a layer of the laminate
E_m	(GPa)	Young's Modulus of the matrix in a layer of the laminate
F_g	(N)	Gravitational force
F_{gG}	(N)	Gravitational attraction of the Moon at point G
G	(Nm^2kg^{-1})	Universal gravitational constant
G_{12}	(GPa)	Shear modulus of the laminate

G_f	(GPa)	Shear modulus of the fibres in a layer of the laminate
G_m	(GPa)	Shear modulus of the matrix in a layer of the laminate
H	(m)	Half of the depth of the seabed
K_0	-	Constant derived from the flow velocity over a tidal cycle
K_1	-	Constant derived from the flow velocity over a tidal cycle
L	(N)	Lift
L_x	(m)	Laminate side length in the *x* direction
L_y	(m)	Laminate side length in the *y* direction
M	(Nm)	Moment about the *z* axis
M_1	(kg)	Mass of body one
M_2	(kg)	Mass of body two
M_x^T	(Nm)	Effective moment resultant including thermal effects in the *x* direction
M_y^T	(Nm)	Effective moment resultant including thermal effects in the *y* direction
N	(rpm)	Number of revolutions per minute
N_x^T	(N)	Effective force resultant including thermal effects in the *x* direction
N_y^T	(N)	Effective force resultant including thermal effects in the *y* direction
P	(W)	Power
P_0	(Nm^{-2})	Dynamic head
P_{AT}	(Nm^{-2})	Atmospheric pressure
P_L	(Nm^{-2})	Local fluid pressure
P_{max}	(W)	Theoretical maximum power
P_V	(Nm^{-2})	Vapour pressure
Q	(Nm)	Torque
$\overline{Q}_{ij}$	(Nm^{-2})	Transformed reduced stiffnesses
R	(m)	Radius of curvature
R_b	(m)	Distance between the centre of body one and body two

Re	-	Reynolds Number
S	(m)	Span
T	(N)	Thrust
T_p	(s)	Period
T_T	(N)	Axial force
T_0	(hours)	The lunar month
T_1	(hours)	The period between two successive high tides
TPF_G	(N)	Tide producing force at point G
U_o	(ms^{-1})	Onset flow velocity
V_f	(m^3)	Volume of the fibres in a layer of the laminate
V_k	(ms^{-1})	Flow velocity at height above seabed, k
V_m	(m^3)	Volume of the matrix in a layer of the laminate
V_{neap}	(ms^{-1})	Maximum flow velocity at neap tide
V_{spring}	(ms^{-1})	Maximum flow velocity at spring tide
W	(J)	Total potential energy of a laminate
α	(^{o})	Effective angle of attack
α_1	($/^oC$)	Transverse coefficient of thermal expansion
α_2	($/^oC$)	Longitudinal coefficient of thermal expansion
α_{ij}	($/^oC$)	Linear coefficients of thermal expansion
α_x	($/^oC$)	Coefficient of thermal expansion in the x direction
α_{xy}	($/^oC$)	Coefficient of thermal expansion in the xy direction
α_y	($/^oC$)	Coefficient of thermal expansion in the y direction
β_{ij}	-	Constants related to the elastic and thermal expansion properties of the material
γ	(^{o})	Yaw angle
γ_{xy}	-	Strain in the xy direction in a layer of the laminate
$\gamma_{xy}^{\ o}$	-	Midplane strain in the xy direction
$\gamma_{xy}^{\ T}$	-	Strain caused by temperature change in the xy direction
ΔT	(^{o}C)	Temperature change from cure temperature
ε_{ij}	-	Strains in the material
ε_x	-	Strain in the x direction in a layer of the laminate

ε_x^o	-	Midplane strain in the *x* direction
ε_x^T	-	Strain caused by temperature change in the *x* direction
ε_y	-	Strain in the *y* direction in a layer of the laminate
ε_y^o	-	Midplane strain in the *y* direction
ε_y^T	-	Strain caused by temperature change in the *y* direction
η_1	-	Gearbox efficiency
η_2	-	Generator efficiency
θ	(^{o})	Fibre orientation angle
θ_t	(^{o})	Section twist at a given radius *r*
κ_x^o	(m^{-1})	Midplane curvature in the *x* direction
κ_{xy}^o	(m^{-1})	Midplane curvature in the *xy* direction
κ_y^o	(m^{-1})	Midplane curvature in the *y* direction
λ	-	Tip speed ratio
μ	($kgm^{-1}s^{-1}$)	Dynamic fluid viscosity
ρ	(kgm^{-3})	Density of fluid
σ	-	Cavitation number
σ_{ij}	(Nm^{-2})	Stresses in the material
σ_x	(Nm^{-2})	Stress in the *x* direction in a layer of the laminate
σ_x^T	(Nm^{-2})	Stress caused by temperature change in the *x* direction
σ_y	(Nm^{-2})	Stress in the *y* direction in a layer of the laminate
σ_y^T	(Nm^{-2})	Stress caused by temperature change in the *x* direction
τ_{xy}	(Nm^{-2})	Stress in the *xy* direction in a layer of the laminate
τ_{xy}^T	(Nm^{-2})	Stress caused by temperature change in the *x* direction
υ_{12}	-	Major Poisson's ratio of the laminate
υ_{21}	-	Minor Poisson's ratio of the laminate
υ_f	-	Poisson's ratio of the fibres in a layer of the laminate
υ_m	-	Poisson's ratio of the matrix in a layer of the laminate
Φ	(^{o})	Induced flow angle
Ψ	(^{o})	Undisturbed hydrodynamic pitch
ω	($rads^{-1}$)	Speed of rotation
Ω	($rads^{-1}$)	Rotation speed

1 Introduction

The oceans of the world are a largely untapped resource, capable of making a major contribution to our ever-increasing energy needs. They may have the potential to equal, or even exceed, wind energy in the make-up of our future electricity demands; with assessments showing that around 20% of the electrical energy requirement of the UK may be feasibly extracted at 51 sites around the British Isles [1-4].

In the search for a non-polluting renewable energy source, there is a push to find an economical way to harness energy from the oceans. Several different forms of ocean energy exist that are being investigated as potential sources for power generation; these types of energy include thermal, wave, offshore wind, tidal and ocean current energy [5]. The seas can offer one of the largest clean energy resources in the form of waves and currents, but these can only be applied if the technology can be successfully developed to exploit such resources reliably and cost-effectively.

The gravitational attraction and subsequent relative motion of the Earth, Moon and Sun induce tidal movements in the oceans and seas of the world. The energy related to the change in sea level (potential energy) and associated currents (kinetic energy), although extremely small compared to the motion of the planet, is still a significant resource. With research currently flooding the field of renewable energy, it is thought that the energy inherent in the tides could be feasibly converted into a resource that is both renewable, high tide occurring as it does cyclically, and sustainable - at least with respect to the timescale of the eventual collapse of the Sun. As yet the majority of this tidal energy resource is unexploited. If it can be efficiently and effectively captured using suitably engineered systems it has the potential to make a considerable impact on our future energy usage.

While marine energy is being developed in order to limit or avoid climate change, its reliance on the natural environment means that some sources may be vulnerable to the variations in climate that result from rising carbon emissions. Extreme weather alterations resulting in more erratic winds, sea level rises, and changes in ocean circulation are expected to have an adverse effect on wind and wave energy [6]. Tidal energy has the advantage of insusceptibility to climate change; whereas wind, solar, wave, and Hydro Electric Power (HEP) are all sensitive to the unpredictable changes in renewable fluxes brought about by

shifts of climate regimes. An advantage of the tidal current resource is that, being gravitation bound, it is predictable and quantifiable both spatially and temporally. Even with a likely rise in sea levels, few locations for energy extraction from tidal streams would be affected [7].

Devices designed for tidal energy extraction come in a plethora of shapes, sizes and forms. Principally they are all harnessing either kinetic energy or potential energy from the tide, and converting it into electricity. Devices can be classified into two types: tidal barrages and fences that typically generate power through discharge but can extract energy in either or both directions of tidal flow, and tidal current devices which are fixed or moored within a tidal stream [8]. It is this latter category that renewed interest has been focused on in the past few years, and it is expected to be in this realm that a breakthrough will be made in the near future.

There are many aspects of horizontal axis tidal turbine (HATT) design that could be optimised, not least the support structures, hub and nacelle; but the major components of the turbine that extracts energy from the tidal flow are the blades. The efficiency, and therefore annual energy capture, of a device could be increased by improving the blade design. With design for through-life performance and decommissioning becoming ever more prevalent, turbines are required to withstand the aggressive subsea environment for many years whilst being environmentally disposable come the end of their life. This has a large impact on fatigue loading with a horizontal axis device typically experiencing in the order of $1x10^8$ rotational cycles over a 20 year life span. While maximising annual energy capture is the most apparent aim for tidal turbine design, a major factor that should be considered is ease of maintenance. With devices typically operating in remote regions at sea, and in areas of high flow velocity, it is difficult to obtain the correct weather and tidal current window in which to send out maintenance vessels. Optimisation of the blade design could increase the amount of energy capture, reduce structural loading and also minimise the need for maintenance.

Many techniques are being applied in the field of design and development of tidal energy extraction devices; computational methods include Blade Element Momentum Theory (BEMT), Computational Fluid Dynamics (CFD), Finite Element Analysis (FEA), and coupling of these into Fluid Structure Interaction (FSI) analyses. In order to reduce the time and expense of long, complex computations for more advanced analyses, optimisation techniques can be utilised. Experimental testing in wind tunnels, towing tanks, circulating

water tunnels, cavitation tunnels and open water testing is vital for validation of numerical methods and 'real world' performance estimates.

The fundamental assumption is that the design methodology for a composite lifting surface, such as a turbine blade, should in general follow that for conventional isotropic materials that use sufficient stiffness to maintain a given optimum design shape [9]. A 'composite' is defined as two or more different materials combined together to create a superior and unique material; for example carbon fibre and epoxy. This conventional approach to lifting surface design relies on their being a fixed optimum shape and yet, as the flow regime experienced is rarely steady, every shape will deflect under a given load condition and will dynamically respond to the time varying fluid load fluctuations. Typically, this hydroelastic response is based on a modal frequency analysis. Access to significant computational resource now allows research into time accurate analysis of the coupled fluid-structure response [10]. Composite materials can ease the fatigue problem through their inherent fatigue tolerance. If the composite blades are appropriately designed they can also deliver the required stiffness. The material anisotropy can be exploited to control what is considered a negative aspect of fibre reinforced composites; coupled distortions. By either symmetrically or anti-symmetrically stacking individual lamina in a structure, an applied load will result in a coupled response. Typical coupled deformation behaviours in tailored composites are bend-twist, bend-extension and extension-shear. There is an increasing interest in the use of composite materials for potential improvements in hydrodynamic and structural performance of horizontal axis tidal turbines. In addition to the obvious advantages of high strength-to-weight ratio and high strength-to-stiffness ratio, anisotropy of the laminated fibre composites can be designed to allow three dimensional tailoring of the blade deformation. Although many advances have been made in the use of composites to improve aeroelastic performance [11-15], only limited work has been carried out in the marine industry [16-20].

Composite panels with an unsymmetric layup undergo warpage phenomena due to residual stresses caused in the manufacturing process. Depending on stacking sequence and geometry, these processing stresses cause the laminate to have two stable cylindrical configurations at room temperature. A snap-through from one stable deformation state to the second state is possible which can be initiated by forces and moments generated by adapted

actuators [21-24]. It is thought that this aspect of composite technology could be incorporated into an actively adaptive turbine blade.

In this work, a review of tidal energy has been completed, with the conclusion that blade design is an area in which considerable progress could be made towards more efficient and cost effective operation of HATTs. Different design tools have been analysed, and the manner in which a blade operates discussed. An innovative bi-directional blade foil section has been developed and assessed for increased energy capture in both directions of tidal current.

A combination of both passively and actively adaptive composite technology has been considered in the design of HATT blades. The use of composite, passively coupled blades for more efficient energy capture has been assessed and deemed to have considerable potential. A new method for the design of a passively adaptive, bend-twist coupled blade has been developed, and is discussed. Comparisons have been made with regards to the efficiency of an array of turbines with different blades.

1.1 Aims and Objectives

1.1.1 Aim

The principal aim of this research is *to increase the efficiency of horizontal axis tidal turbines through optimisation of the blade design utilising adaptive composites.* This aim is achieved through a series of objectives.

1.1.2 Objectives

- Understand where tidal energy originates, what makes an area good for energy extraction, and gain an idea of technology to date.
- Focus on one aspect of the turbine for optimisation – the blade. Understand how the blade performs in relation to the turbine and surrounding flow. Consider the key factors that govern blade performance. Gain an understanding of computational tools used in horizontal axis tidal turbine design.
- Consider the use of adaptive composite blades. Undertake a preliminary investigation to assess the viability of bend-twist coupled blades. If this is successful, to develop a method to predict the performance of devices utilising

adaptive blades. Use selected design tools to model a passively adaptive blade spar and compare these results with those determined through experimentation.

- Combine the methods developed to create a design tool for the development of passively adaptive composite horizontal axis tidal turbine blades.
- Compare the performance of an array of turbines using a variety of blades.

1.2 Structure of Thesis

The first section of this work reviews the physics of tidal flows, the methods by which tidal energy can be extracted, and considers available and proposed technologies for capturing it. With all such technologies, it is the through-life impact of the whole system that needs to be addressed. The exciting engineering challenge is therefore to devise systems that can be constructed, installed, operated, maintained and decommissioned without requiring more energy than they capture; or that have other detrimental environmental impacts.

The author then moves on to consider one integral aspect of free stream turbine design – the blade. The operation of the blade in varying currents is discussed, along with challenging aspects facing the designer. A wholly bi-directional foil section to enable a turbine to operate efficiently in both directions of tidal flow is considered. Different design tools that can be used in the development of horizontal axis tidal turbine blades are examined.

With HATT blade design having been identified as an area which could benefit from improvement, the concept of composite blades is addressed. The use of adaptive composites – those that change shape in response to varying loads – is considered for use in the tidal industry. Preliminary analysis indicates that passively adaptive blades could increase annual energy capture and alleviate loads on the turbine. The author then goes on to develop a tool for predicting the performance of HATTs with passively adaptive blades. A numerical model to assess the level of coupling in a composite bend-twist box beam is developed, and an innovative experimental method undertaken to provide data for comparison.

Several computational techniques are then coupled to create a design tool for the design of composite passively adaptive bend-twist coupled HATT blades. Operation of the tool is discussed, and an example analysis illustrated.

With performance increases indicated for HATTs using passively adaptive blades, the concept of a blade that not only utilises passive adaptation but also active adaptation is

presented. A performance analysis of turbines situated in an array using different types of blades is presented showing the merits of bi-directional, passively and actively adaptive blades when compared to standard fixed pitch devices.

2 Tides – Dynamics, Resources and Extraction

In the study of tidal energy, it is important to understand how tides work, what causes them, what makes a site desirable for energy extraction, and what the problems associated with extracting energy at such locations are. An overview of where the tidal energy industry is as a whole, and what techniques are currently available is essential in order to gain perspective as to where the problems are and how new techniques and research can overcome one or more of these issues. This section reviews tidal dynamics, energy resources, and energy extraction.

2.1 Tidal Dynamics

The longest oceanic waves are those associated with tides, and are characterised by the rhythmic rise and fall of sea level over a period of half a day or a day. The rise and fall result from horizontal movements of water (tidal currents) in the tidal wave. Figure 2-1 illustrates the relationships between wavelength, wave frequency and period, the nature of the forces that cause them, and the relative amounts of energy in each type of wave.

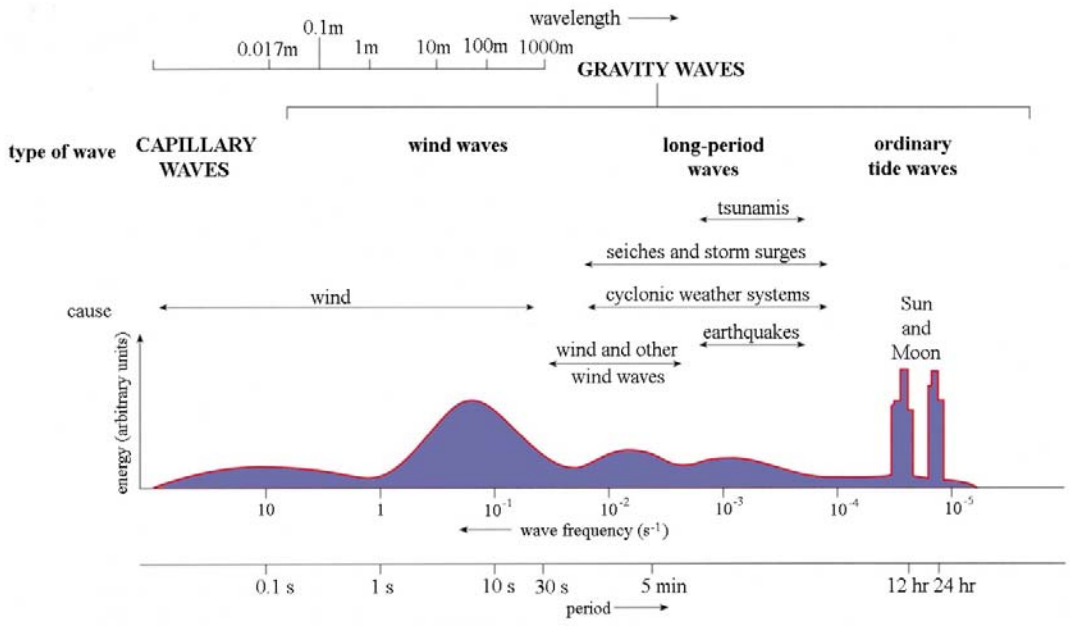

Figure 2-1: Types of surface wave

The rising tide is referred to as the flood, whereas the falling tide is called the ebb. The ebb and flood of the tide at the coast are manifestations of the general rise and fall in sea-level caused by a long wavelength that affects the oceans as well as shallow coastal waters. Nonetheless, because of their long period and wavelength, Figure 2-1, tidal waves behave as shallow water waves.

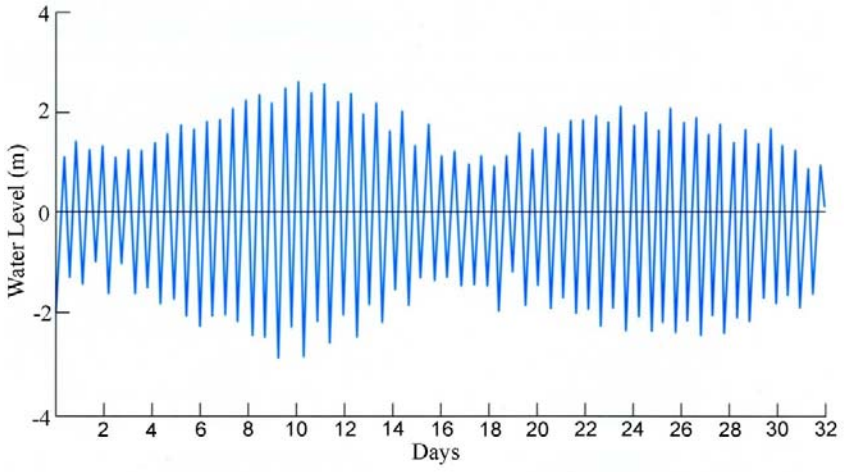

Figure 2-2: A typical 30 day tidal record at a station in the Tay Estuary, Scotland

Figure 2-2 is a typical tidal record, illustrating regular vertical movement of the water surface relative to a mean level, over the period of one month. There are two important differences between wave motions resulting from the tides and those associated with wind generated waves:

1) The period of oscillation of wind generated waves is in the order of seconds, and both period and amplitude of the oscillations can be quite irregular. In contrast to this, Figure 2-2 the period of the tides to be about 12.5 hours, and that both period and amplitude vary in a systematic way.
2) The heights of wind-generated waves can range from virtually zero, to in excess of thirty metres. By contrast, in the majority of places, the tidal range is typically of the order of a few metres; although tidal ranges of more than about ten metres are known in a few locations. Tidal range nearly always varies within the same limits at any particular location, Figure 2-2; and because the cause of the tidal wave motion is continuous and regular, tidal range can be very reliably predicted. Wind-generated

waves are much less predictable, because of the inherent variability of the winds, and are likely to be influenced by climate change.

Figure 2-2 also exhibits a 7 to 8 day recurrance, where an increase in tidal range is apparent. This alteration of high and low tidal range (spring and neap tides respectively) can also be predicted with accuracy and characterises tides all over the world.

Tides are a self-gravitating, near-resonant, sloshing of water in a rotating, elastic, ocean basin with ridges, mountains, and submarine basins. Strictly speaking, they are the vertical movement of the ocean and seas caused by the rotation of the Earth and the relative movements of the Earth, Moon, Sun, and to a much lesser extent other celestial bodies – although this appears as both vertical and horizontal movement of the Earth's seas. Thus, the primary forces responsible for the tides are gravitational and centripetal in nature (although the secondary agents, including inertia and frictional forces, also play an important role). If there were no land, the tidal current would be very small; therefore useable tide is heavily dependent upon the local bathymetry and coastal morphology, i.e. headlands and islands, to accelerate the flow and result in higher velocity currents, which produce feasibly extractable energy.

2.1.1 The Equilibrium Theory

The Sun and the Moon both produce tractive forces on the Earth, and therefore on the seas of the Earth. Tide-producing forces vary directly with respect to the mass of the attracting body, but are inversely proportional to the square of its distance from Earth. Therefore, although the Sun is significantly greater in mass than the Moon, it is 360 times further from the Earth such that the magnitude of the solar tide producing force is less than half that of the Moon. In a simplified case, assuming the Earth as a water covered ball with no land masses and the oceans being very deep, these forces result in the movement of water towards the two celestial bodies creating two bulges directed towards and away from the Moon (due to the greater attraction). An equilibrium state is thus reached – the equilibrium tide [25], Figure 2-3.

If the two bulges were to maintain their positions relative to the Moon, they would have to travel around the world at the same rate as the Earth rotates about its axis. Any point on the surface of the Earth would therefore encounter two high and low tides during each

complete rotation of the Earth. This assumption means the tidal bulges remain stationary during a complete rotation of the Earth, which cannot be the case as the Moon continues to travel in its orbit as the Earth rotates.

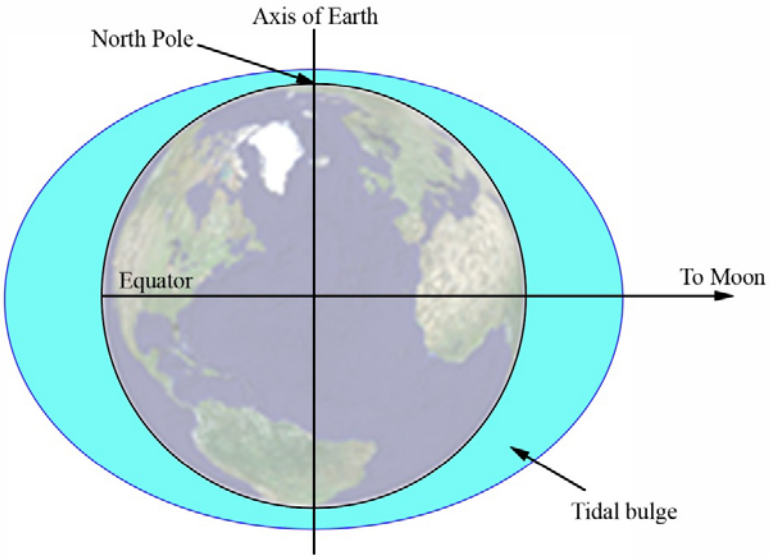

Figure 2-3: The equilibrium tidal ellipsoid

The Moon revolves around the Earth-Moon centre of mass once every 27.3 days, in the same direction the Earth rotates upon its own axis (once every 24 hours); the period of the Earth's rotation with respect to the Moon is 24 hours and 50 minutes – the lunar day. This makes the interval between successive high (and low) tides approximately 12 hours 25 minutes.

The relative positions and orientations of the Earth and Moon are not constant, but vary due to a number of interacting cycles. The elliptical orbits of the Moon and the Sun, the declination of the Sun and the Moon and the tilt of the Earth's axis of rotation all have an effect on the distribution of the Earth's seas and cause the tidal bulges to vary from the basic equatorial position.

Many harmonic components manifest in tides, with the most important being spring and neap tides (each having a 14 day periodicity); where spring tides typically have twice the tidal range of neap tides, Figure 2-4.

In Figure 2-4(a), the tide generating forces of the sun and moon are acting in the same directions, and the solar and lunar equilibrium tides coincide; i.e. they are in phase and thus reinforce each other. The tidal range produced is larger than average, which gives rise to the term spring tides. When spring tides occur, the sun and moon are either in conjunction (new moon) or in opposition (full moon). In Figure 2-4(b), the sun and moon act at right angles to each other, the solar and lunar tides are out of phase, and these features do not reinforce each other. The tidal range produced is smaller than average; these are neap tides, where the moon is in quadrature.

The complete cycle of events in Figure 2-4 takes 29.5 days. In the 27.3 days taken by the moon to make a complete orbit of the earth, the earth-moon system has also been orbiting the sun. For the moon to return to the same position relative to both the earth and sun it must move further round in its orbit, taking roughly an extra 2.2 days.

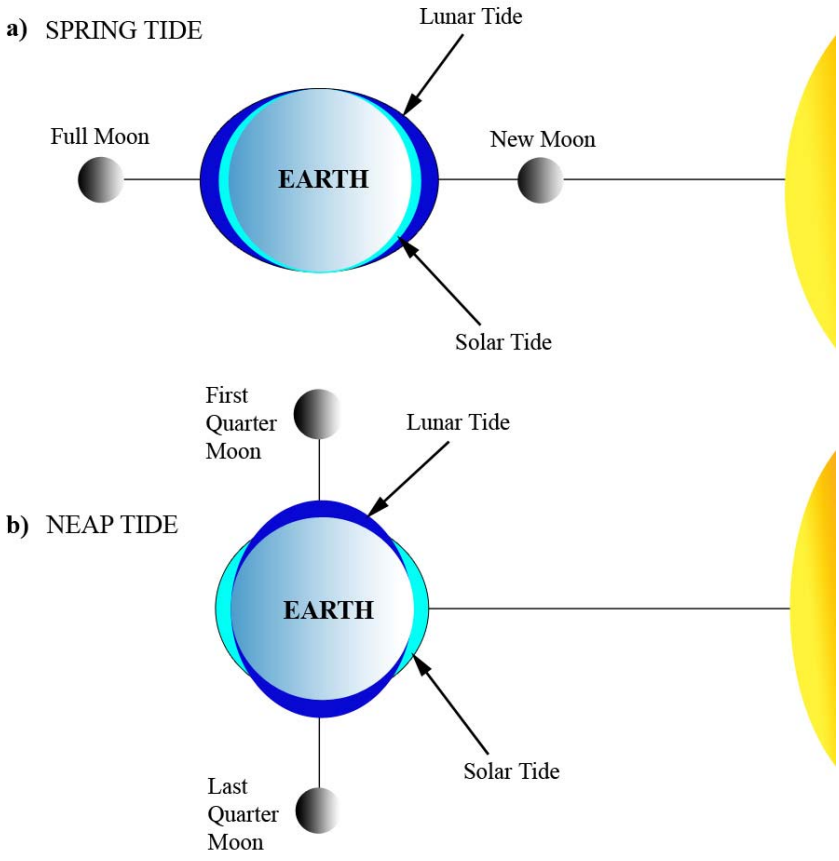

Figure 2-4: Schematic of spring and neap tides

The overall effects of the gravitational attractions and relative movements are cyclic tides of varying magnitude and periodicity. At most locations, the dominant harmonic is semidiurnal, featuring two highs and two lows in each lunar day, and these are more likely to occur when the moon is over the Earth's equator. Diurnal tides, exhibiting a single high and low in a tidal day, occur in areas where the moon is furthest from the equator. Tidal currents may be semi-diurnal, diurnal, or of mixed type, corresponding largely to the type of tide at the site, but often with a stronger semi-diurnal trend. The most common type is a mixed one although this varies around the globe. Figure 2-5 illustrates the difference in tidal spectra at several sites around the world.

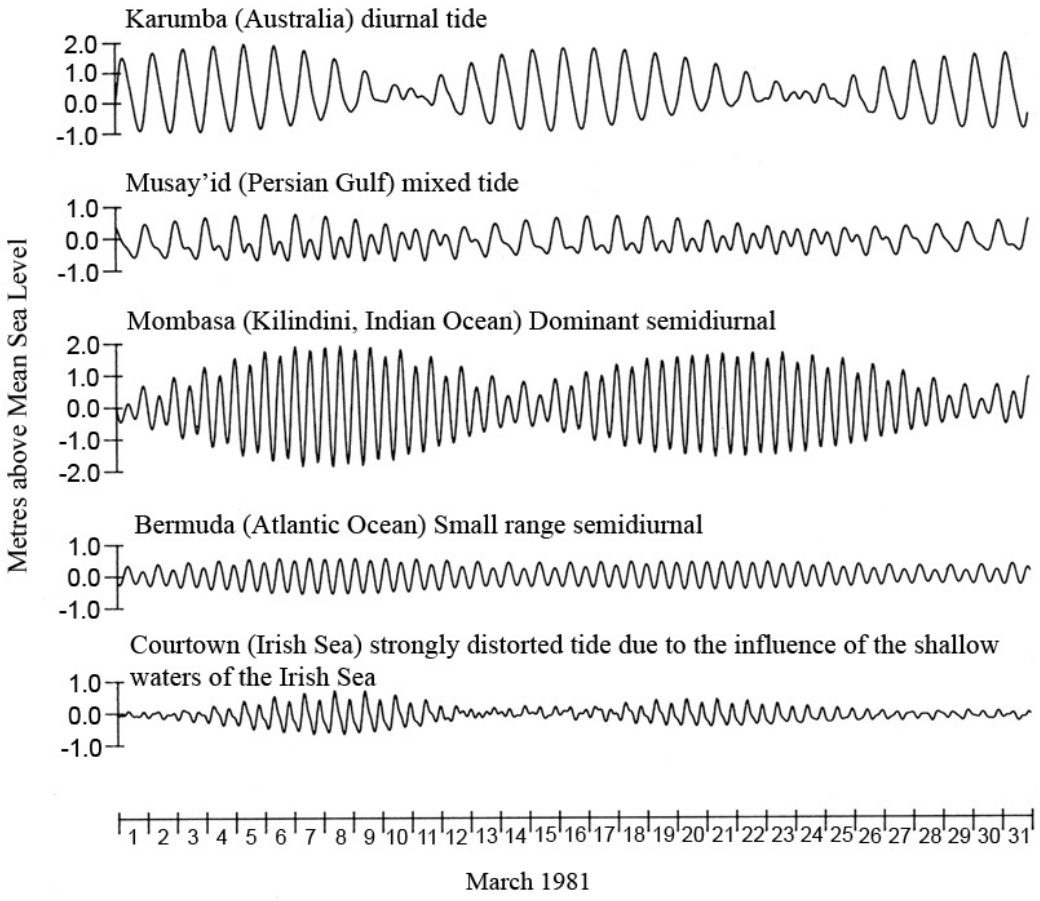

Figure 2-5: Tidal spectrum at specific sites globally, March 1981[25]

For example, Mombasa has a relatively simple tidal system with semi-diurnal tides and a relatively small tidal range, as does Mombasa in the Indian Ocean (Figure 2-5). Australia

is, however, very complex from a tidal point of view: it has a full spectrum of tidal regimes, and a tidal range varying from 1m to over 10m. This is due to coastal topography, and the bathymetry, which play a major role in determining the tidal patterns around the country. Modelling studies indicate that, through the phasing of different tidal current energy extraction installations, it may be possible to achieve baseload supply [7].

2.1.2 The Dynamic Theory

In contrast to the "static" equilibrium theory, the dynamic theory recognises the fact that water covers only three-quarters of the globe that is confined to seas and ocean basins which are fixed on a rotating earth. The basic principles of the equilibrium theory still hold where ocean waters respond with a wave like motion characterised by definite periods; however, when the fluid encounters a solid boundary reflection of the waveform occurs. When a reflected wave meets one advancing towards the boundary, the combination can lead to a standing wave – depending on wave period, and size and shape of the basin.

Another consequence of being on a rotating earth is that objects in motion experience an apparent force per unit mass, the Coriolis acceleration, which encourages objects away from a straight line path – this is known as the Coriolis effect. The Earth is constantly rotating towards the east, and the speed of rotation varies greatly at different latitudes; faster on the equator and slower towards the poles. As a result of this, the Coriolis effect forces moving objects to follow curved paths on the Earth. In the northern hemisphere flows tend to the right, whilst in the southern hemisphere they tend to the left. The Coriolis effect acts on all objects moving freely over the surface of the Earth and has a dramatic effect on ocean circulation, currents and tides. Most ocean basins in the northern hemisphere will exhibit a circular current-flow rotating clockwise and vice versa in the southern hemisphere [25].

As previously mentioned, tides are an extreme example of a shallow water wave, although friction with the ocean floor slows tidal waves to a speed of about 700 km/h. Continents restrict tidal movement to an even greater extent. The tidal waves cannot keep up with the rotation speed of the earth and this, coupled with lateral boundaries, counters the flow and produces rotary waves – Kelvin waves. There are about twelve such Kelvin waves worldwide, with five in the Pacific Ocean. In the middle of each rotary wave is an amphidromic node – a no-tide point located near the centre of an ocean basin, around which

the tidal crests, and troughs, rotate through each tidal cycle. Owing to the shape and location of the land masses surrounding the ocean basins, the tidal crests and troughs cancel each other out at these points. The tidal wave sweeps around each amphidromic point, and because it is such a large volume of water it is strongly influenced by the Coriolis effect.

Generally the tidal waves move anticlockwise around amphidromic points in the northern hemisphere, and clockwise in the southern hemisphere. The farther from the amphidromic point, the higher the tide level becomes. Figure 2-6 shows a cotidal map of the Atlantic, exhibiting cotidal lines (solid) which connect all points experiencing the same phase of the tide (e.g. maximum or minimum), radiating from the central amphidromic point; cotidal range lines (dotted) which connect all points with equal tidal range; and the amphidromic points and direction of rotation of the waters about such points.

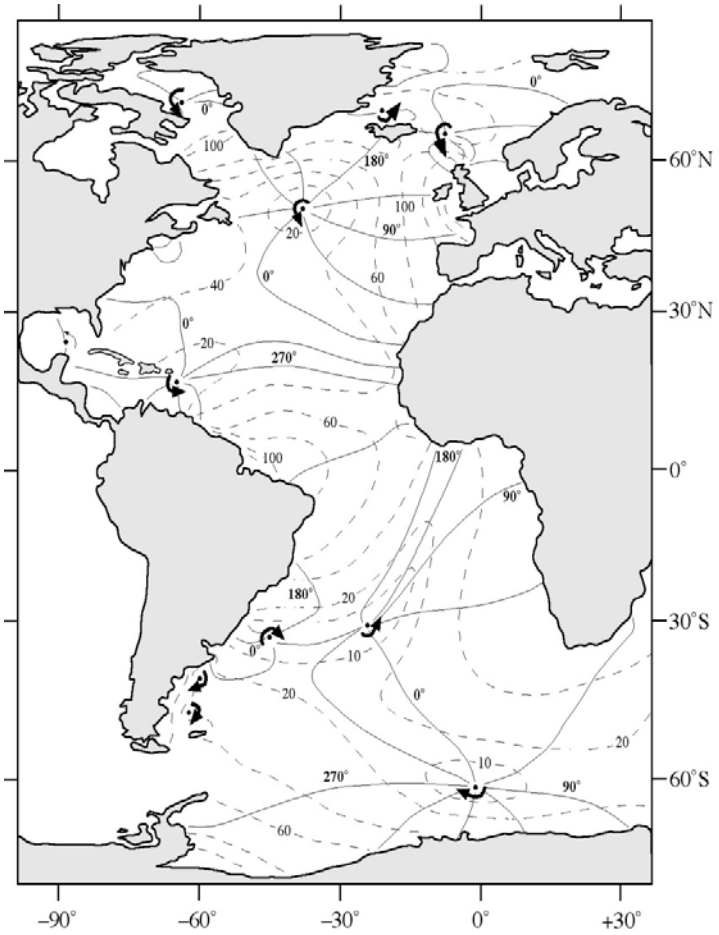

Figure 2-6: Co-tidal map of the North Atlantic

There are some exceptions to the general pattern of rotation of tidal waves around amphidromic points, and these are those systems less obviously constrained by land masses; e.g. in the South Atlantic centred on 30^{o}S 25^{o}W, Figure 2-6.

2.1.3 Prediction of Tides

As tides are driven by the regular motion of the planets, they are inherently predictable. Tidal prediction can be separated into two parts; prediction of tides in shallow waters and ports where it may be easily measured, and the prediction of tides in the deep ocean. Two methods are used to predict tides at a tide gauge station using past observations of sea level measurement in shallower waters; the traditional Harmonic Method and the Response method. The Harmonic Method uses decades of tidal observations from which the amplitude and phase of each tidal constituent in the tide gauge record are calculated (Fourier series decomposition). The Response method calculates the relationship between the observed tide at some point and the tidal potential. A functional (admittance) relationship is found between this difference and the tidal constituents. Future tides are then calculated by multiplying the tidal potential by the admittance function [26].

Prediction of deep water tides relies on the sea surface altimeter data from the Topex/Poseidon satellite which was launched into orbit in 1992 and was designed especially for measuring the Earth's oceans. The altimetric system is sufficiently accurate to identify the many constituent tidal harmonics, and data from the satellite has now been used to determine deep-ocean tides to within an accuracy of ±5cm. Figure 2-7 illustrates a map of the sea levels over the Pacific acquired from Topex. The black areas are land masses, the white areas are those of an increase in sea level from the mean, and the purple areas show a decrease in sea level when compared to the mean. Using several years' worth of data collected by Topex it is possible to predict accurately the heights of tides in years to come.

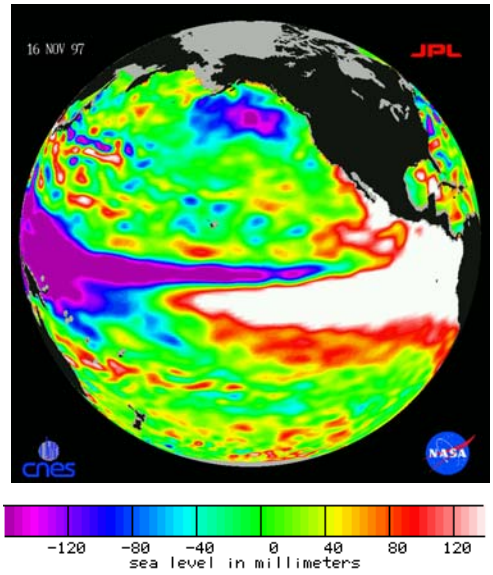

Figure 2-7: Sea level heights measured by Topex

2.2 Tidal Energy Resources

Tidal currents are formed by the energy dissipated by the tides. They typically exhibit a dominant diurnal or semi-diurnal periodicity in accordance with their associated tides. While in general the energy flux associated with ocean tidal flows is diffuse, and a common criticism is that renewable resources suffer from energy diffuseness, numerous locations offer high energy concentrations. Current velocities are strongly affected by ocean depth, bathymetry, and coastal morphology meaning that in locations of constrained topologies, such as narrows, shallows, headlands and estuaries - flow velocities may be markedly pronounced. Phasing of proximate tides also influences tidal currents, for example through the passages connecting the Georgia and Johnstone straits along the east coast of Vancouver Island in Canada, where the tidal range is a moderate 5m but peak current velocities can exceed 7m/s [7].

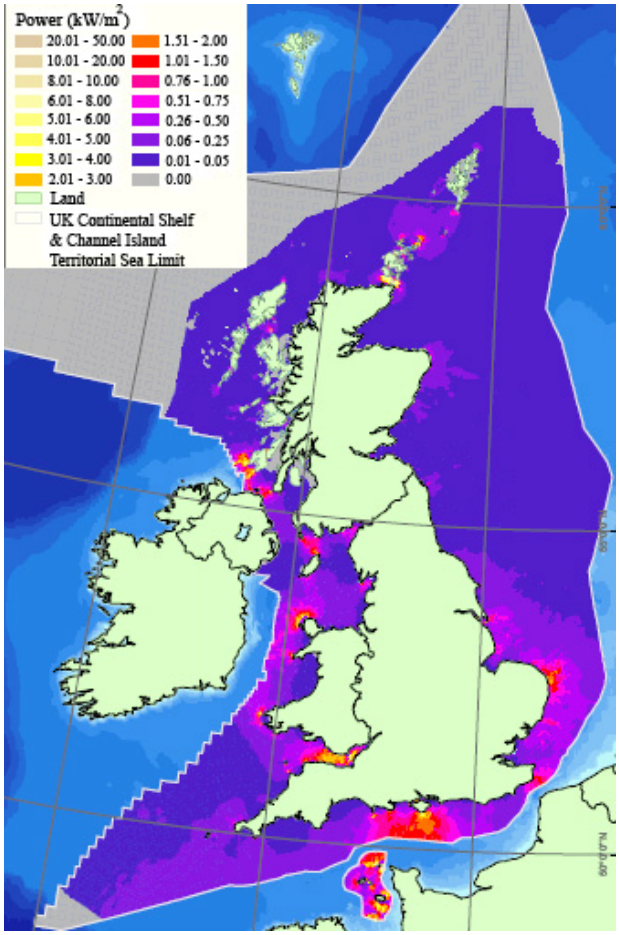

Figure 2-8: Annual mean power tidal density [27]

Figure 2-8 illustrates the annual mean tidal power density around the UK; it can be observed that the greatest density is indeed in areas of constrained topography, for example south of the Isle of Wight, the Channel Islands, the Bristol Channel and the Pentland Firth.

Many tidal sites are relatively bi-directional. However, some sites can have flow reversal of 20^{o} or more away from $180^{o,}$ such as the flow around islands [28] and headlands [29] e.g.: Portland Bill, UK, where a swing upon flow reversal of around 35^{o} from rectilinearity is apparent. It has been shown by experimentation and calculation that an increase in turbine yaw angle, to the flow, causes a consistent power decrease and thus a fully rectilinear flow is more desirable [30]. Assessment of the available energy present in the tidal stream at a particular site forms an important first step towards successful device deployment. Numerous reports have been published concerning estimates of exploitable resources [28, 29, 31-36].

Several criteria need to be considered when selecting an area in which to site a tidal energy extraction device. For a free stream turbine, a strong maximum spring peak current is deemed necessary for economic electricity generation, typically in excess of 2m/s; it is also required that the flow velocity be relatively uniform for long periods to maximise the power capture. The device and installation procedure need to be considered in conjunction with the depth of water at the site, and accessibility for maintenance. Conflict with other sea users needs to be minimised, as does impact on marine flora and fauna. Ideally the site should not be too exposed to open seas, waves and winds in order to reduce the risk of weather-induced delays and for ease of installation and servicing.

It is thought that there are 106 potential locations in European territorial waters for extracting tidal energy which, if put into service, would provide an exploitable 48TWh/year [34]. Studies in Canada have indicated around 50,000MW of installed capacity being achievable along the coasts of British Columbia alone. It is also thought that Russia has great potential for tidal energy extraction with a possible 90,000MW of available power off the northwest coast and a further 20,000MW at the point where the Mezen River flows into the White Sea. Small areas of Western India also show promise with a possible 8000MW from the Kutch area alone. As mentioned previously, it is estimated that the UK could obtain circa 20% of its electricity from tides with new findings suggesting that the technical UK tidal stream resource is 18TWh/year, which is currently 10-15% of the known worldwide tidal stream resource [1-3]. Possible locations for siting tidal devices globally include the Arctic Ocean, the English Channel, The Gulf of Mexico, The Amazon, The Straits of Magellan and Taiwan to name but a few; Figure 2-9 shows areas of tidal energy potential throughout the world. Current studies suggest that the maximum recoverable tidal energy globally is around 1800 TWh/year.

Figure 2-9: World tidal energy potential

2.3 Tidal Energy Extraction

Tidal energy has been used for many centuries, however the power requirements of the industrialised world are greatly in excess of the output of the early devices, and it was not until 1967 that the first commercial scale modern-era tidal barrage was constructed at La Rance, France. Initial hydromechanical devices, such as the paddlewheel and overshot waterwheel, have given way to highly efficient bulb type hydroelectric turbine generator sets. The French barrage uses twenty four, 10MW, low head, bulb type turbine generator sets and has now been functioning for 40 years producing around 600GWh/year [37].

A river current bulb turbine project based on the Nile at Juba, Sudan was the first modern free stream energy extraction source used from 1976-1984. The turbine was suspended under a floating platform in the slow (1m/s), but consistent, river current adjacent to the bank and was used for irrigation pumping – 200l/hr of water was pumped through a head of 5m which demonstrated the considerable potential of kinetic energy water turbines, or 'zero head hydro'.

The first tidal current turbine was introduced in the 1990s as a "proof of concept" prototype. Suspended beneath a floating raft moored in the Corran Narrows, Loch Linnhe, Scotland the 3.5m diameter turbine was designed to achieve a maximum shaft power of 10kW but the maximum consistent power recorded was over 15kW [38]. Subsequently a more

advanced model of this turbine was installed off the coast of Norway near Kvalsund, in September 2003, in the 2.5m/s current with a capacity of 3MW, it was the first grid-connected free stream tidal turbine in the world [39].

The diversity of marine environments from which we may begin to tap tidal energy has ensured that no single technical development is likely to emerge that can solve all our tidal energy extraction problems. At present, the industry is following up a range of experimental devices, as none have demonstrated themselves the clear technological leader. Shallow tidal estuaries can play host to extreme tidal ranges. It is the high tidal range that potential energy devices such as barrages and their concept offspring, artificial lagoons and impoundment basins, use. All other tidal devices fall into the category of harnessing kinetic energy from tidal currents, what is being talked of as "tidal stream" or "zero head hydro".

Most tidal energy extraction devices are based on rotors, either horizontal or vertical axis. Each year sees the proposed development of more original, and often eccentric, methods of extracting energy from the tides. Devices based on the concept of the tide as a progressive wave are emerging [40, 41] as well as those related to water wheels – the tidal mill [42]. Devices can be azimuthing, fixed pitch, variable pitch, tethered, zero head, barrage, lagoon, water column, ducted, hydrofoil, vertical axis, horizontal axis, surface piercing, submerged, bi-directional… The following sections give an overview of tidal energy extraction methods to date.

2.3.1 Potential Energy Devices

Potential energy devices exploit the natural rise and fall of tidal waters. In the open ocean tidal ranges are small, typically having amplitude of 1m or less. These ranges increase towards coasts, and particularly in estuaries, because of the shelving of the seabed, the funnelling of water and resonance effects.

Most tidal barrage schemes have been built in – or considered for – estuary locations. They involve constructing a barrage across an estuary, allowing tidal waters to fill the estuary through sluice gates and then emptying the water back into the sea via turbines, Figure 2-10.

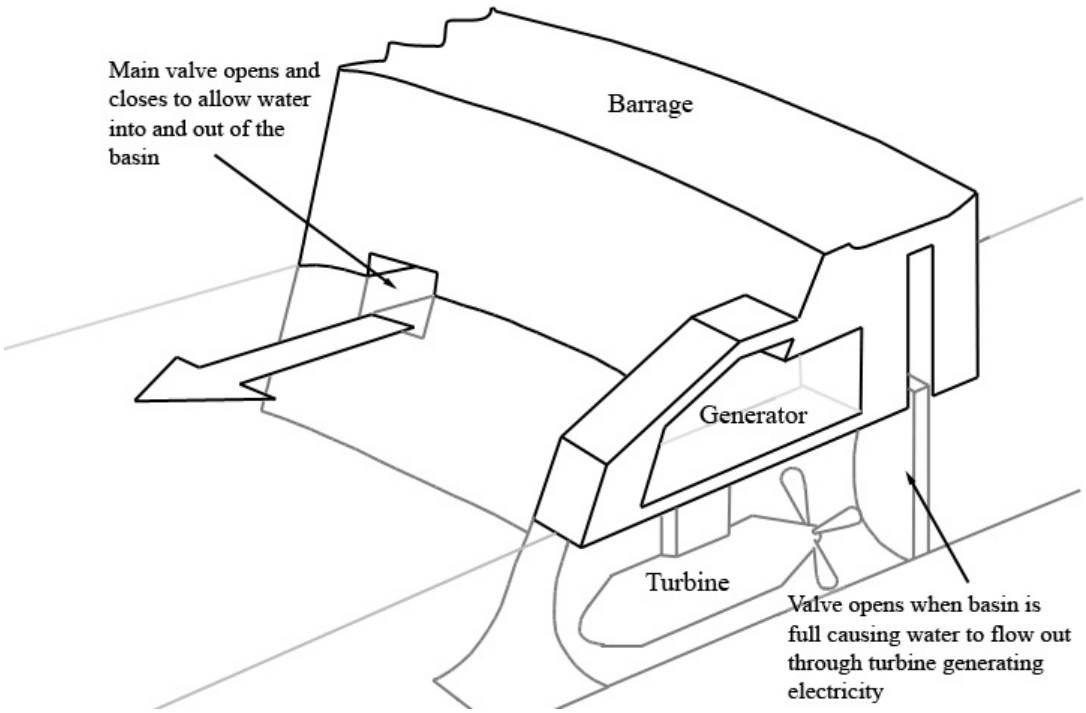

Figure 2-10: Tidal barrage schematic

Ebb generation is the simplest mode of operation for a barrage scheme. The cycle consists of four steps:

1) Letting water in through the sluice gates during the flood tide, filling the basin.
2) Holding the impounded water until the ebb tide creates a suitable head.
3) Letting the water empty from the basin to the sea through a turbine. This takes place during the ebb tide and continues until the tide turns and the rising water reduces the head to the minimum operating point.
4) Holding the water again until the tide rises sufficiently to repeat stage 1).

Ebb generation with flood pumping is a modification of this mode that is favoured by potential UK developers because of the ability to alter the timing of the energy output. By using the turbines in reverse (as pumps) the level of water in the basin, and hence the generating head, can be raised allowing the barrage to be used as a slow-release pumped storage scheme.

Electricity is generated using large axial flow turbines with diameters of up to 9m. Because of the continuously varying head of water that drives them, variable control of both distributor blades and turbine runner (i.e. double regulation) may be necessary for maximum

efficiency. Double regulation is also required if the turbine is to be used in both directions for generation, or in reverse for pumping.

The installation of the early estuarine tidal barrages has demonstrated the ecological problems associated with large scale estuarine constriction. Recent events have seen opposition to tidal barrage schemes from a broad array of environmental groups and local inhabitants. This can be attributed to four main problems:

1) Barrages cause problems for shipping. Locks may be installed; however, they are a slow and costly alternative.
2) Anadromous fish spawn in fresh water and outmigrate to salt water, then return after three or four years to spawn and die. They are therefore instinctively obliged to pass through the turbines multiple times and are therefore at risk of their lives.
3) The size and location of the intertidal zone (the area that is alternatively wet and dry during tidal cycles) is affected. The habitat in this area is unique and much rare flora and fauna is present which would be obliged to adapt, move or die as a result of a change in the zone. For example, it is thought that if the Severn Barrage scheme were to go ahead it is predicted that a total of six species of bird might become extinct [43].
4) The tidal regime downstream is affected. Both the Bay of Fundy in Canada and The Severn Estuary in the UK have had opposition on this front due to a significant increase in the high tide levels up to as much as 800 miles upstream in Canada and the lack of flushing action to remove waste in the Severn river. This also simulates silting in some areas and causes coastal erosion in others that may not have been present previously.

It has been mentioned that with the knowledge and experience gained from the La Rance barrage over the years, a similar construction would never gain the required permission to be built in France, despite working well and efficiently for over 40 years.

The exploration of the tidal barrage concept and environmental difficulties has encouraged the concept of impounding water for both electricity generation and energy storage to move beyond the strict geological walls of tidal estuaries. Artificial tidal lagoons

are now being seriously considered as a cheaper more environmentally friendly method of developing potential energy from tides.

Offshore tidal power generation (OTP) is a new approach to tidal power conversion that resolves the environmental and economic problems of the familiar tidal barrage technology. OTP uses a rubble-mound impoundment structure and low head hydroelectric generating equipment situated offshore in a high tidal range area. Shallow tidal flats present the most economical sites. Multi-cell impoundment structures, Figure 2-11, make the lagoon completely self-contained and independent of the shoreline, thereby eliminating the environmental problems associated with blocking off and changing the coastline [44].

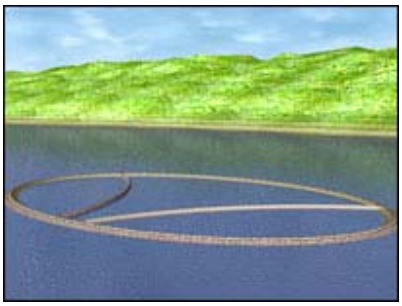

Figure 2-11: Tidal lagoon concept

Despite the possible environmental issues, barrages are a proven form of tidal energy with several devices around the world now grid-connected and in service [45]. Barrages may also offer additional communication links and provide a flood defence against storm surges on high spring tides, and also the rising sea levels resulting from global warming due to the ability to control the water levels behind the barrage. The edifice may also be used as an alternative way to cross the estuary.

2.3.2 Kinetic Energy Devices

To date, most of the kinetic energy extraction device designs under trial are based on marinised horizontal axis wind turbine concepts, although work has also focused on extracting energy via oscillating hydraulic hydrofoils. Broadly speaking, kinetic energy extraction devices can be categorised into: horizontal axis turbines (axial flow turbines), vertical axis turbines (cross-flow turbines), and alternative devices.

2.3.2.1 Horizontal Axis Devices

Most horizontal axis tidal turbines (HATTs) operate similarly to their wind turbine counterparts, and in fact their relatively advanced state of development, in relation to the other techniques, is largely attributed to the technological achievement and maturity of the wind industry. In principle, the relative fluid flows over the airfoil shaped rotating blades creating a pressure differential, and hence lift and drag forces. The lift force is far greater than the

drag force and the result is a net movement of the turbine around the rotational axis. Essentially, the greater the velocity of the fluid, the greater the amount of electricity produced. In general, the larger the device diameter the higher the power coefficient, C_{pow}, providing the geometric pitch and resultant blade twist are matched for current and revolutions per minute (RPM).

In order to determine the feasibility of a tidal current site, and the amount of available energy, it is important to understand and calculate the extractable power from a free stream of velocity, v. From the basic equation for kinetic energy, $E = \frac{1}{2}mv^2$, the instantaneous power, P, of a fluid stream, with mass flux ρAv, is found to be:

$$P = \frac{1}{2}\rho Av^3 \tag{2.1}$$

where A is the stream area through which the flow passes. As the density of sea water, ρ, is approximately 1025kg/m^3, and current velocities upwards of 2m/s are commonly encountered in optimal sites for tidal energy extraction, considerable power densities are present (4.1kW/m^2 for the cited values). Also, owing to the cubic dependency on the free stream velocity, higher power densities are often observed in areas of constricted flow and ideal bathymetry. Discovery Passage, located along the inside passage of Vancouver Island, Canada, has a peak tidal current velocity, v_p, of 3.6m/s resulting in a power density of 24kW/m^2. Whereas at Sechett Rapids, in a similar location, v_p = 7.7m/s which results in a power density of 235kW/m^2.

Extractable power is much less than the inherent power in a fluid stream, by a factor of the power coefficient, C_{pow}, which is the portion of the power of the flow that can be converted to mechanical power. Thus extractable mechanical power is given by:

$$P = \frac{1}{2}C_{pow}\rho Av^3 \tag{2.2}$$

For flow through an idealised free stream turbine the power coefficient is given by:

$$C_{pow} = 4a_i(1-a_i)^2 \tag{2.3}$$

Where a_i is an axial interference factor, defined as the fractional decrease in fluid velocity between the free-stream and the velocity at the plane of the turbine, i.e.:

$$a_i = \frac{\left(v_f - v_r\right)}{v_f} \tag{2.4}$$

where v_f is the free stream velocity of the fluid, v_r is the velocity of the fluid of the rotor plane. It can be shown that the maximum power occurs when a_i =1/3 or C_{pow} =16/27 (0.593).

In practise the power output will be lower than the theoretical maximum power given by:

$$P_{\max} = \frac{1}{2} C_{pow\max} \rho A v^3 \tag{2.5}$$

The actual C_{POW} values and associated power outputs are affected by the following:

- The operational Tip Speed Ratio (TSR) – ratio of the rotational speed at the rotor tip (πnD) divided by the flow speed at the turbine, v.
- The performance of the foil section used – how much lift force it generates compared to its hydrodynamic drag.
- The number of rotor blades.
- The distribution of blade chord length and twist from the root to tip of the blade.

In the process of converting the energy of the rotating turbine axis to electrical output, mechanical losses by way of the gearbox and electrical losses in the generator are incurred. Typically, gearbox and generator losses, η_1 and η_2 respectively, are relatively low - in the order of a few percent each, however for completeness:

$$P = \frac{1}{2} \eta_1 \eta_2 C_{pow} \rho A v^3 \tag{2.6}$$

Since tidal current flow is not constant the power may be expressed as a time-dependent function:

$$P(t) = \frac{1}{2} \eta_1 \eta_2 C_{pow} A v^3(t_i) \tag{2.7}$$

Tidal current velocities can be approximated using a time-dependent sinusoidal function. Thus for a tidal current which varies as a single harmonic of period, T_p:

$$v(t) = v_{\max} \sin\left(\frac{2\pi t_i}{T_p}\right) \tag{2.8}$$

Substituting this into equation (2.7) power output at time, t is:

$$P(t) = \frac{1}{2}\eta_1\eta_2 C_{pow}\rho A v_{\max}^3 \sin^3\left(\frac{2\pi t_i}{T_p}\right) \quad (2.9)$$

The efficiency of the generator and gearbox essentially vary as a function of the turbine speed of revolution, thus for a constant speed turbine these efficiencies can be assumed to be constant, i.e. not varying as a function of time. The speed at which the turbine actually rotates is determined by the load applied by the generator; for a fixed flow speed, the operating point of a turbine when the torque developed by the turbine matches the torque required by the generator for a given RPM.

Open turbines extract energy from the fluid by reducing the flow velocity with little or no pressure reduction as the fluid passes through the turbine rotor. The fluid streamlines must therefore expand to maintain continuity of mass, although they cannot expand indefinitely; hence there is a theoretical limit to the percentage of kinetic energy that can be extracted from the fluid. Setting $\frac{dC_{pow}}{da_i} = 0$, C_{pow} is found to have a maximum value of 59.3% for a single actuator disk. This theoretical maximum value, C_{powmax}, is referred to as the Betz limit [46].

Horizontal axis turbines generally require three blades in order to produce enough torque to rotate the gearing and thus be 'self-starting', although one design has been successfully implemented with a two bladed device [9]. In order to deal with the bi-directional nature of the current they have to either only operate for half the tidal cycle, be capable of operating in both directions, ideally with similar efficiencies, or be able to yaw to face into the oncoming flow.

Some horizontal axis machines have flow enhancers, in the form of ducts, that take the flow from a larger area and funnel it into a smaller rotor. The flow boundaries of the tidal current are defined, and streamline expansion is limited, by the duct geometry. Energy is extracted primarily by a pressure drop, and in this way the turbine behaves more like an ultra-low head hydro turbine. The maximum power available is the product of the flow and available pressure drop. Designs such as these are thought to improve the safety of the device by placing a screen on the upstream opening thus decreasing the risk of swimmers and marine life interacting with the turbine [47]. It is also thought that the duct would protect the turbine blades from weed growth, but primarily that such an attachment would eliminate tip losses from the blades, thus increasing power output and reducing turbine and gearbox size. Despite

the cost increases associated with additional design and build complexity, it is proposed that ducts could be constructed from an economical, and/or heavy, material which would also act as part of the weight, anchoring the system to the seabed. The duct may also lessen the efficiency drop experienced by a bi-directional turbine when the currents do not reverse by exactly 180^{o} [1, 48, 49].

2.3.2.2 Vertical Axis Devices

Vertical axis turbines are those in which the axis of rotation is perpendicular to the fluid flow. There are two main types of vertical axis turbines, lift based and drag based designs. Drag based designs work in a similar manner to water wheels. The fluid hits the blade and, in effect, pushes it causing the turbine to rotate. Such designs have a tip speed ratio of less than 1, i.e. the blades will not travel faster than the fluid velocity in which they are being propelled, and thus drag based designs will always have limited efficiency. The Savonius rotor is an example of a drag based design, Figure 2-12(a).

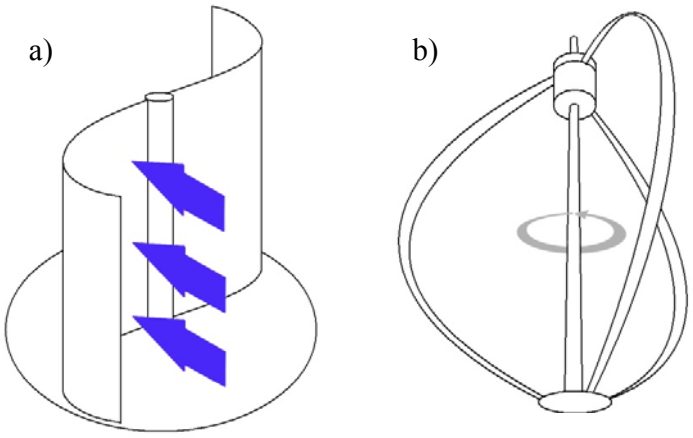

Figure 2-12: a) Savonius turbine, b) Darrieus turbine

Lift based rotors operate in much the same manner as the horizontal axis turbines – as the tidal currents pass over the airfoil shaped blades lift is generated perpendicular to the flow direction which creates rotational motion. The blades follow a circular path and the lift force provides driving torque for the system. The lift and drag forces are dependent upon several variables including angle of attack, relative flow velocity and blade geometry. Such turbines are capable of achieving high TSRs, meaning the speed of rotation is in excess of the velocity

at which the fluid is flowing. These devices are much more efficient than the drag-based devices, and tend to produce significantly more power for a given fluid velocity. The Darrieus turbine is the original lift-based vertical axis turbine, with two C shaped blades, connected at the top and bottom of the shaft causing its "egg beater" appearance. More modern types of Darrieus rotor exhibit multiple blades, straight blades, or twisted ones in the case of a helical turbine, Figure 2-12(b). Ideally, the blade should continually vary its geometric angle of attack as the device rotates in order to maximise the contribution to torque, otherwise the blade will require supplementary power to rotate.

The cycloidal vertical axis tidal turbine is a relatively new concept comprising of a number of blades orientated parallel to the axis of rotation and perpendicular to the plane of rotation. The blades are evenly spaced on a rotating disc along a fixed orbit diameter. The turbine operates in much the same way as a conventional lift-based Darrieus vertical axis turbine with the addition that the blades have a controllable angle of attack, each being able to rotate upon their own axis in order to optimise the process [50]. Vertical axis turbines of this type have the advantage that they do not require a support tower, thus making maintenance and installation simpler and less expensive. They may also be mounted with the generator set located above the waterline. The main advantage, however, is that they are self-starting – a quality lift-based vertical axis turbines without controllable pitch blades cannot achieve. They also have no need for a yawing mechanism and operate efficiently in flows of varying levels of bi-directionality [51]. They are, however, likely to have lower efficiencies when compared to horizontal devices with the same capture area [52].

2.3.2.3 Alternative Devices

As kinetic energy devices are still in their relative infancy, much thought has been given to alternative devices, and there are a few turbines that work on a fundamentally different principle to those detailed above. Notably, oscillating hydrofoil turbines differ from other proposed devices in that they utilise an oscillating motion rather than rotation to capture the energy from the tidal flow. Hydraulically powered cylinders are used to alter the angle of the oscillating hydrofoil such that the apparent angle of attack, relative to the oncoming current, is maintained at the optimum angle. As the current lifts the hydroplane, this causes the arm to lift, actuating hydraulic cylinders at the arm/frame junction. The high-pressure oil

developed by the cylinders turns a hydraulic motor that, in turn, drives an electric generator. When the hydroplane (and arm) reach their upper limit, the hydroplane angle is reversed such that the arm is driven down, and the cycle repeated [53]. For devices such as this, the capture area is the height of the stroke of the foil multiplied by the span. At any one instance it will only be using a small fraction of the available energy and is therefore unlikely to have a high efficiency when compared to the two main classes of device; i.e. horizontal and vertical axis turbines [52].

Another unconventional principle relates to those devices which run a standard turbine on the pressure drop generated by a constriction of the flow. The concept involves a wing/funnel which is placed underwater to channel tidal flows. As the water passes through the choke it decreases in pressure and accelerates, sucking more water into pipes and driving an on-shore turbine to generate electricity. The advantage of this design is that it has no submerged moving parts and can generate constant power; however, the relative energy extraction efficiency of pure venturi effect devices is not as high as that of less complex turbines.

The property of the tide of being a progressive wave is thought to be exploitable to create a head over a specifically designed artificial structure – a floating dam 30km long and 25m deep, attached perpendicular to the coastline. The idea being that the tidal dynamics create an energy head over the dam. The water is then released to the lower side via turbines in the dam, thus transforming the pressure difference over the turbine into electrical power [40, 54]. There are concerns, however, that such a system may cause environmental problems by changing the sedimentation and coastal erosion processes, such as long shore drift, thereby affecting the local wildlife of the area.

Other designs involve the use of HATTs to power hydraulic energy converters based onshore [55]; some incorporate the turbine into a kite which is ‘flown’ in the tidal stream [56], another a helical screw arrangement [57], and others use sails to convert current to electricity [58].

2.3.3 Device Overview

Table 2-1: Tidal energy extraction device overview

Device	Description	Power Rating	Picture
Seagen, Marine Current Turbines Ltd. U.K. [51]	Twin two bladed rotor, sheath mounted, HATT	1.2MW	
The Blue Concept, Hammerfest Strom, Norway [53]	Three bladed pile mounted HATT	1MW	
THG, Tidal Hydraulic Generator, U.K.	Array of four bladed HATTs attached to a gravity mounted frame	3MW	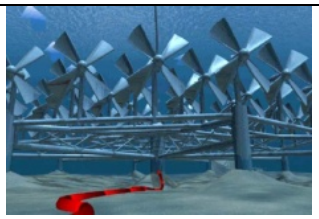
TidEL, SMD Hydrovision, U.K. [59]	Twin two bladed tethered rotor, able to yaw into the current	1MW	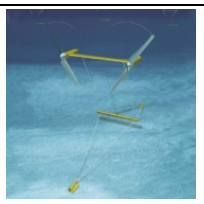
Stingray, Engineering Business Ltd. U.K. [60]	Oscillating hydroplane	500kW	
Blue Energy, Blue Energy Inc. Canada [61]	Four bladed, moored, surface piercing, vertical axis turbine	500kW	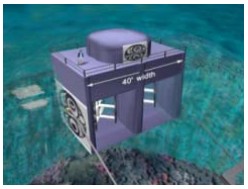
KHPS, Verdant Power, U.S.A.[62]	Three bladed, HATT, pylon mounted	25-250kW	

OTP, Tidal Electric, U.K.[63]	Tidal Lagoon	30-500MW	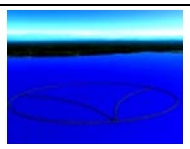
Tidal Stream, Tidal Stream, U.K. [22]	Quad two bladed horizontal axis, tethered, yawing turbines	4MW	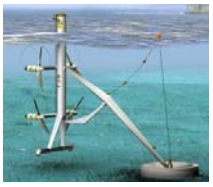
La Rance Barrage, France [64]	Tidal Barrage 24 x 10MW Turbines	240MW	
Lunar Energy, Lunar Energy Ltd, U.K. [47]	Gravity base mounted ducted horizontal axis turbine	2MW	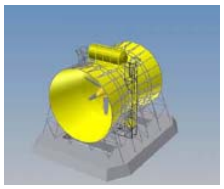
Flumill Power Tower, Flumill, U.K.[57]	Buoyant, solid helical twin screw turbine, four point base mount	4MW	
Deep Green Technology, Minesto, U.K. [56]	HATT imbedded in a kite 'flying' in the tidal stream tethered to the seabed	0.5MW	
Kepler Energy, U.K. [65]	Transverse horizontal axis water turbine	5.3MW	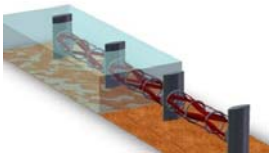
Atlantis Technologies, Atlantis Resources Corporation, U.K. [66]	Twin rotor, HATT, bi-directional operation	3.5MW	

2.3.4 Support Structures

Difficulties and challenges are faced when deploying and recovering equipment within a fast flowing tidal stream. The thrust on a marine turbine of a given rated power is significantly greater than that experienced by a wind turbine of the same rated power, even though the marine turbine will be considerably smaller, so there is a major structural problem inherent in holding the rotor securely and reliably in place in the harsh and corrosive subsea environment [1, 67].

Several different concepts for the fixing of tidal energy extraction devices are under consideration with carrying opinions on each. These range from pile-mounted devices to moored devices, those weighted to the sea bed and semi-submersible designs [68].

Support Structure Concept	Description	Advantages	Disadvantages
Pile Mounted 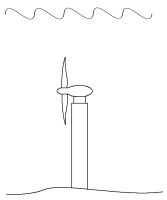	A tower is built on the seabed which supports the rotor at a predetermined depth.	• Stiff structure able to withstand complex loadings • Not subject to wave action • No visual impact • Low collision risk	• Minor maintenance requires complete removal of nacelle. • Additional navigation marks required as no surface component present. • Unable to rotate turbine into flow • Difficult and costly to install
Moored 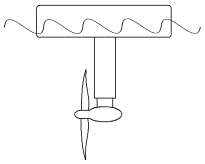	The turbine is mounted underneath a moored, floating platform on the surface.	• Low cost installation and construction • No need for additional navigational markers • Minor maintenance possible at the site • Can be used in waters of any depth	• Subject to weather and wave effects • Structure flexible and susceptible to fatigue in complex loading situation • Cannot yaw into flow • Surface piercing hence an eyesore and increased collision risk
Tethered 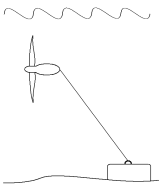	A buoyant system anchored to the seabed via a cable or rigid arm.	• Low cost installation and construction • Can be used in deep water • Self aligning to flow • Not subject to wave or visual impact • Low collision risk	• Maintenance is difficult and costly • Structure flexible and susceptible to fatigue loads • Additional navigational markers required • Fewer devices can be installed in one area

Sheath System 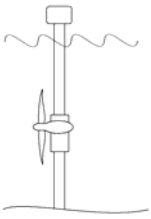	Surface piercing tower installed on the seabed. The rotor and generator are mounted on a sheath and moved up and down mechanically.	• Electrical components above water • Minor maintenance possible at the site • Stiff structure can withstand complex loadings • No additional navigational markers required	• Surface piercing hence an eyesore • Increased shipping collision risk • Subject to weather and wave action • Structure installation costs increase with depth of water • Hoist mechanism exposed to marine corrosion and growth • Unable to rotate turbine into flow
Guyed Tower 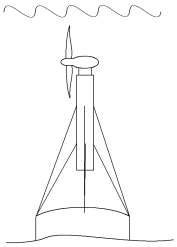	The buoyancy of the nacelle is used to tension multiple chain anchors.	• Low cost structure • Easily adapted for deeper waters • Not subject to wave and weather actions • No visual impact • Low collision risk	• Minor maintenance not possible on site • Flexible structure vulnerable to fatigue loads • Additional navigational markers required • Unable to rotate turbine into flow • Installation difficult and thus costly
Telescopic 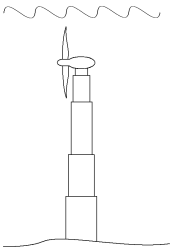	A system of telescopic towers is used to maintain the turbine at the required depth for operation.	• Minor maintenance possible at site • Stiff structure can withstand complex loading situation • Not subject to weather and wave actions • No visual impact • Low collision risk	• High design and construction costs • Additional navigational markers required • Unable to rotate turbine into flow • Construction costs increase markedly with increase in water depth.
Shroud Concept 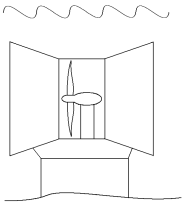	A cylindrical shroud or duct surrounds the rotor, the middle section of which can be separated for removal and maintenance. The device weight and use of anchor chains fixes it to the seabed.	• No yawing mechanism required • Stiff structure able to withstand complex loading • Can be positioned in deep waters • Not subject to weather and wave action • No visual impact • Low collision risk	• Minor maintenance not possible on site • High cost of materials and construction • Additional navigation markers required • Vulnerable to marine fouling as shroud remains in place for life of turbine • Greater exposure to ocean bottom boundary layer decreasing flow speeds

2.3.5 Economics

All of the financial cost projections of tidal energy extraction developments are necessarily speculative by their very nature since a utility-scale commercial tidal farm is yet to be developed.

Continual improvements to wind turbines since 1980 have reduced the cost of grid connectivity fivefold and it is now economically competitive with fossil fuels in some areas [1]. Currently tidal power is expected to retail at around 12p/kWh [69] with wind energy costing only 3p/kWh [70]. The target for commercial competitors in the long term is to generate electricity for around 2p/kWh, which is the same as the current 'fossil fuel' generated price.

Unit prices of ~5.5p/kWh (comprising of the basic energy price of ~2p/kWh plus 3.1p/kWh from the Renewables Obligation and up to 0.43p/kWh from the local electricity companies) might, potentially, be available for project developers. The high level of predictability from barrage schemes over a period of several years could attract favourable prices [71-73].

These costs are much higher than other forms of conventional and renewable generation. This is unsurprising, however, given that wave and tidal stream energy technologies are at early stages and initial farms have limited economies of scale [3]. Variations in predicted economic performance reflect site-specific conditions and as such, these figures given are only an overview of what may be possible.

2.4 Summary

The oceans are a huge resource of untapped energy. Unlike many other marine renewable energy sources, tidal energy is highly predictable and the range of devices for tidal energy extraction is extensive and growing all the time. Potential energy devices have been proven to be effective, however have considerable impact on the local environment. Kinetic energy devices are thought to have great potential, especially HATTs, and it is in this area significant improvement is expected. The technology is already available and some devices proven to be effective, though further research into the field is required to advance the concepts, improve the feasibility of maintenance and make the devices more efficient at capturing energy economically.

3 Blade Design

With HATT design still in its relative infancy, there are many design aspects that have potential for improvement; not least the hub, support structure, nacelle and housing, but also the fundamental components of the energy conversion process – the blades. The work in this chapter demonstrates how efficiency, and therefore annual energy capture, of a device could be increased by improving the blade design without a significant increase in overall cost.

HATT design has to confront problems that do not occur when operating such a system in air; as a result, the blade section, plan form and twist differ from those used on a Horizontal Axis Wind Turbine (HAWT). Due to differences in fluid density, for instance, the thrust on a HATT is significantly greater than that experienced by a HAWT of a given rated power, despite the HATT having a significantly smaller swept area. Several other loads are present on a HATT that are not experienced by a HAWT. Examples include increased cyclic loads, cavitation, and wave loading. The variations in static pressure and velocity across the vertical water column also impose cyclic dynamic effects on the rotor blades; the tip of a blade of a typical 15m diameter rotor experiences a 1.5 bar cyclic pressure variation as it moves from the top to the bottom of the circular path, in addition to potentially large velocity fluctuations.

The design of a tidal energy extraction device is a balance between cost and energy yield. There are many points to consider when designing a tidal turbine including [1, 48];

- the presence of excessive downstream drag forces due to strong tidal currents promotes the need for strong anchorages,
- the device should be moored in a manner that allows periodic repair and maintenance of the equipment, although this is costly in the harsh subsea environment and should be minimised,
- marine growth on the blades decreases efficiency,
- corrosion/reliability of components in subsea environment,
- storm damage to the turbine and superstructure,
- the effect the device has on other marine traffic and wild life in the chosen area,
- extracting energy efficiently from reversing current flows that may not be totally rectilinear, and

- design for lifetime performance and reliability, including decommissioning – a HATT will experience around $1x10^8$ rotational cycles over a 20 year device life.

A further consideration is associated with the matching of the system to the generator, namely as to whether the generator needs to operate at a near constant rate of revolution or whether a range of operational RPM is permissible. The first case requires a mechanism for controlling the pitch of the blade to regulate power output, whereas the second can use a simpler fixed pitch arrangement. Bi-directional operation of the turbine requires that the blade pitch be rotated by at least 180^o. Other mechanisms for solving the bi-directional problem could involve the rotation of the entire support structure – this is awkward for monopole supports - or by tethered support systems that allow the whole system to reverse as the tide changes [52].

3.1 Blade Performance

There are three characteristic dependent measures required for assessing turbine performance, these are:

- **Power coefficient**

$$C_{pow} = \frac{16nQ}{\pi\rho v^3 D^2} \tag{3.1}$$

Where the power generated arises from a rotational speed of n revs/sec and Q is the torque acting on the generator. For a geometrically similar turbine, and excluding the effects of the Reynolds Number, the actual power captured is proportional to the cube of the free stream speed and the square of the diameter, as illustrated in Section 2.3.2.1.

- **Thrust Coefficient**

$$C_T = \frac{8T}{\pi\rho v^2 D^2} \tag{3.2}$$

Where T is the thrust loading that has to be resisted by the supporting structure.

- **Torque Coefficient**

$$C_Q = \frac{16Q}{\pi^2\rho v^2 D^3} \tag{3.3}$$

$$C_Q = \frac{C_{pow}}{\lambda} \tag{3.4}$$

A crucial element is to ensure that the performance of the generator system matches that of the turbine system. That is, there should be a balance between the mechanical strength of the low speed shaft, the performance of any necessary gearbox and finally the electrical generator's performance.

Values of C_{pow} cited in literature vary considerably from 0.3-0.4 [51, 72]. Based on wind power experience, higher values of C_{pow} should be achievable by varying the pitch angle of the turbine blades, so that a higher average C_{pow} value may be obtained across a range of flow velocities. Recent estimates of the power coefficient speculate that values as great as 0.5 may be reached by optimising the whole turbine design [74].

C_{pow} is enhanced through pitch control of the blades. This may be explained by considering the tip speed ratio, λ, which is the ratio of blade tip velocity, v_{tip}, to tidal current velocity, v_f. With respect to performance, C_{pow} may be optimised for a particular value of λ. Since the tidal current velocity is not constant, v_{tip} must be varied in order to maintain a constant λ. This may be achieved through pitch control of the turbine blades, as is done routinely in the wind industry. Modelling studies suggest that for low velocity sites the difference in energy extraction between fixed pitch and variable pitch devices may be substantial – around a 23% increase in annual energy capture [7, 69, 75].

The effective onset speed a local section experiences will depend on the relative contribution of the undisturbed free-stream fluid velocity, v_f, and that, due to the speed of rotation,

$$\omega = 2\pi n = \frac{\pi N}{30} \tag{3.1}$$

where N is revolutions per minute. For a turbine of diameter, D, the tip speed effectively controls the relative speed, and is defined as:

$$\lambda = \frac{\pi n D}{v_f} \tag{3.2}$$

The overall performance of the turbine is thus controlled by this ratio.

3.1.1 Two Dimensional Foil Performance

Two dimensional foil performance is analysed in terms of the local lift, drag and moment coefficients i.e. performance per unit span.

$$C_l = \frac{L}{\frac{1}{2}\rho v^2 c_h} \tag{3.3}$$

$$C_d = \frac{D_r}{\frac{1}{2}\rho v^2 c_h} \tag{3.4}$$

$$C_m = \frac{M}{\frac{1}{2}\rho v^2 c_h^2} \tag{3.5}$$

Where L and D_r are the forces in the directions perpendicular and parallel to v, and M is a moment about the z axis, Figure 3-1.

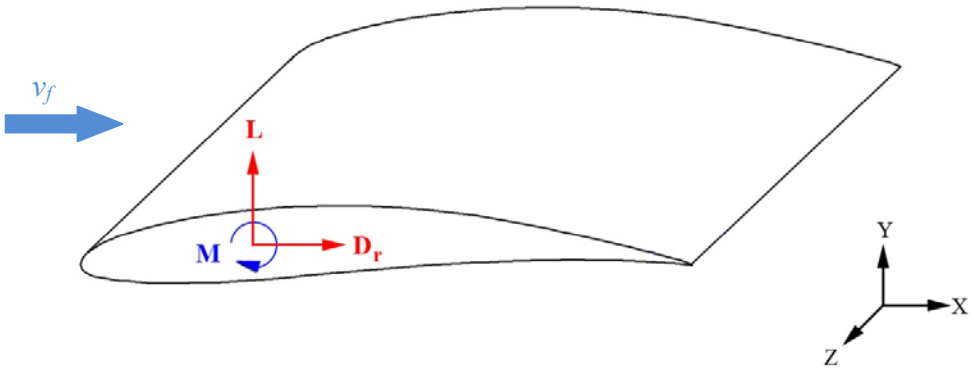

Figure 3-1: Foil orientation

Typical methods of presenting two-dimensional performance data are in terms of variation against angle of attack, or drag, as a function of lift. Lift tends to vary almost linearly with angle of attack, until stall (where significant areas of flow separation occur). Flow separation changes the drag regime from one dominated by viscous shear (caused by the shearing of a viscous fluid over the surface of a body due friction), to one where pressure drag (the form drag created as a body is moved/moves through a viscous fluid) predominates [76]. When considering the flow regime around a lifting foil operating at a turbulent (high) Reynolds number, $\mathrm{Re} = \frac{\rho v_f D}{\mu}$, points of interest include:

- Behaviour near the stagnation point at the leading edge.

- A region of laminar flow as the flow exchanges static pressure for velocity and accelerates. If curvature changes are too rapid then laminar separation may occur. It is in this region that foil performance is most sensitive to the presence of surface disturbances. Such disturbances, as well as being a local source of pressure drag (proportional to their cross-sectional area), also provide unsteady perturbations that eventually trigger transition to turbulent flow. This transition is also strongly influenced by the background turbulence levels in the onset flow.
- Post transition, turbulent flow develops a thicker boundary layer within which surface roughness has a proportionally less significant effect. At higher angles of attack, the adverse pressure gradient towards the trailing edge is sufficient that trailing edge separation initiates – the stall condition. This causes a significant drop in lift, a movement in the centre of effort of the developed force, and a rapid increase in drag. The speed with which this process develops is the controlling factor in the stall process. One method of speed control on turbines employs stall regulation – as sections stall, the drop in lift and rise in drag regulates the achievable driving torque. In this case, 3D effects are crucial to the effectiveness with which stall regulation can be used.

Certain levels of stall, however, may improve the energy capture of a device. Increased peak power production for HAWT rotors has been attributed to the phenomenon of stall delay [77]. Radial flow along rotating blades results in delayed flow separation, and thus the lift produced at high angles of attack is greater than those given by two dimensional measurements and conventional theory. This causes the stall angle of attack to be greater than predicted and peak power being underestimated.

Experimental evidence suggests that measured power output is far in excess of predicted values for high blade inflow angles when approximately half of the blade is operating above the stall angle of attack; which represents 25% of the rotor disk area producing power under heavy stall. Values of overpower up to 140% were recorded which is comparable to previous studies [77-79].

The desired operating condition for a foil is one where the ratio of lift to drag is maximised, whilst avoiding cavitation. As a turbine rotates and the tip speed ratio alters the effective angle of attack experienced by the section is influenced, therefore the section behaviour away from the optimum is of considerable importance.

One systematic approach for defining section shape uses a camber line describing the height of the mid-thickness position, around which a thickness variation is prescribed as a function of thickness/chord ratio. A foil with zero camber is symmetric and will generate zero lift at zero angle of attack. A cambered foil will generate positive lift at zero angle of attack with the magnitude dependent on the amount of camber.

The performance of a three-dimensional lifting surface, such as an aircraft wing, ship rudder or turbine blade, is influenced by the local flow regime at the free tip and at the blade connection to the hub. The effective angle of attack experienced by a section at a certain spanwise location will be reduced by the flow action of the other sections. In addition, there may also be significant spanwise flow, especially near the tip or within a three-dimensional separation bubble (cavitation) resulting from centripetal action on the rotating flow.

3.1.2 Blade Element Momentum Theory (BEMT)

The basis of turbine performance can be considered in terms of the performance of an infinitely thin disk that acts to convert the kinetic energy of an onset current into rotational motion. The disk can be analysed in terms of the work done to convert axial momentum into rotational momentum. This momentum conversion is controlled by the shape and orientation of the blade sections. The blade is divided into strips at a fixed radius. The effective onset flow, containing the axial free stream and rotational flow, determines the effective angle of attack. The blade element analysis, which uses the 2D section performance, including the influence of stall and/or cavitation, requires knowledge of the deceleration of the free-stream and reverse spin (circumferential/tangential component of velocity) [80].

Coupling together the momentum analysis and the blade element analysis using an iterative approach allows the performance at a given tip speed ratio, and a given radius, to be calculated. A spanwise integration produces the generated torque, axial thrust and power. BEMT provides a rapid technique for analysis and is therefore suitable for blade geometry optimisation.

3.1.2.1 Momentum Theory

The initial analysis of a rotor is based on the concept of an infinitely thin actuator disk. The actuator disk represents the influence of an infinite number of rotating blades which

function, for an energy extractor, by causing a step change in static pressure and hence total pressure along a streamline, whilst maintaining continuity of flow speed.

Figure 3-2 is a sketch of the outer stream tube showing the upstream area (less than the disk area) which expands after passage through the disk.

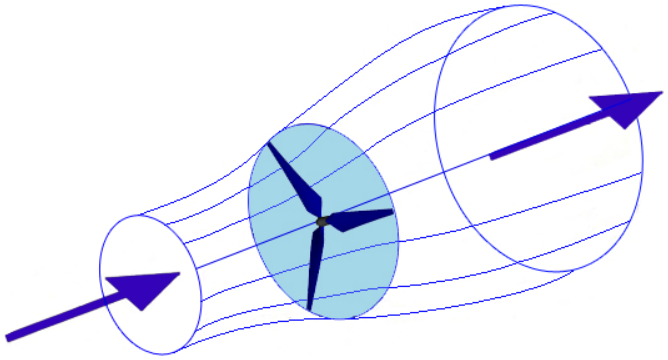

Figure 3-2: Stream tubes around a turbine

Initially, for this expansion region or wake, the static pressure is below atmospheric and the flow speed less than free stream. Further expansion occurs as the static pressure across the wake equalises to that of the atmospheric pressure and further slows the flow. Figure 3-3 indicates four stations along a single stream tube: 1 – some way upstream of the turbine, 2 – directly in front of the rotor, 3 – directly behind the rotor and 4 – some way downstream of the device.

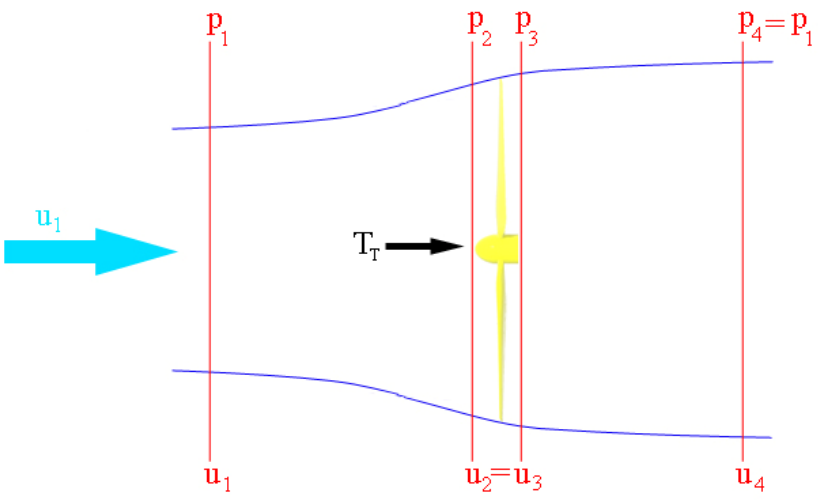

Figure 3-3: Single stream tube analysis

Applying Bernoulli's equation:

$$p_1 + \frac{1}{2}\rho u_1^2 = p_2 + \frac{1}{2}\rho u_2^2 \text{ and } p_3 + \frac{1}{2}\rho u_3^2 = p_4 + \frac{1}{2}\rho u_4^2 \tag{3.6}$$

Hence
$$p_2 - p_3 = \frac{1}{2}\rho\left(u_1^2 - u_4^2\right) \tag{3.7}$$

For flow down an annulus at position *r* and thickness *dr*, and as force equals pressure divided by area:

$$dT_T = \left(p_2 - p_3\right)dA \tag{3.8}$$

Then

$$dT_T = \frac{1}{2}\rho\left(u_1^2 - u_4^2\right)dA \tag{3.9}$$

Considering the decrease in axial flow velocity through the turbine, the axial induction factor, a_i, is:

$$a_i = \frac{u_1 - u_2}{u_1} \tag{3.10}$$

Thus

$$u_2 = u_1\left(1 - a_i\right) \text{ and } u_4 = u_1\left(1 - 2a_i\right) \tag{3.11}$$

Substituting yields:

$$dT_T = \frac{1}{2}\rho u_1^2\left(4a_i\left(1 - a_i\right)\right)2\pi r dr \tag{3.12}$$

Now considering the rotating annular stream tube, Figure 3-4, with the same four stations as previously defined; as the water passes between stations 2 and 3 the rotation of the turbine causes the blade wake to rotate also.

Applying the conservation of angular momentum to this annular stream tube, where the wake rotates with an angular velocity, ω, and the blades rotate with an angular velocity of, Ω, the torque for a rotating annular element of fluid can be defined as:

$$dQ = 4a'\left(1 - a_i\right)\rho v_f \Omega r^3 \pi dr \tag{3.13}$$

Where the tangential induction factor, *a'*, is:

$$a' = \frac{\omega}{2\Omega} \tag{3.14}$$

Therefore there are two equations from momentum theory which represent the axial and tangential force on a fluid element, equations (3.12) and (3.13) respectively.

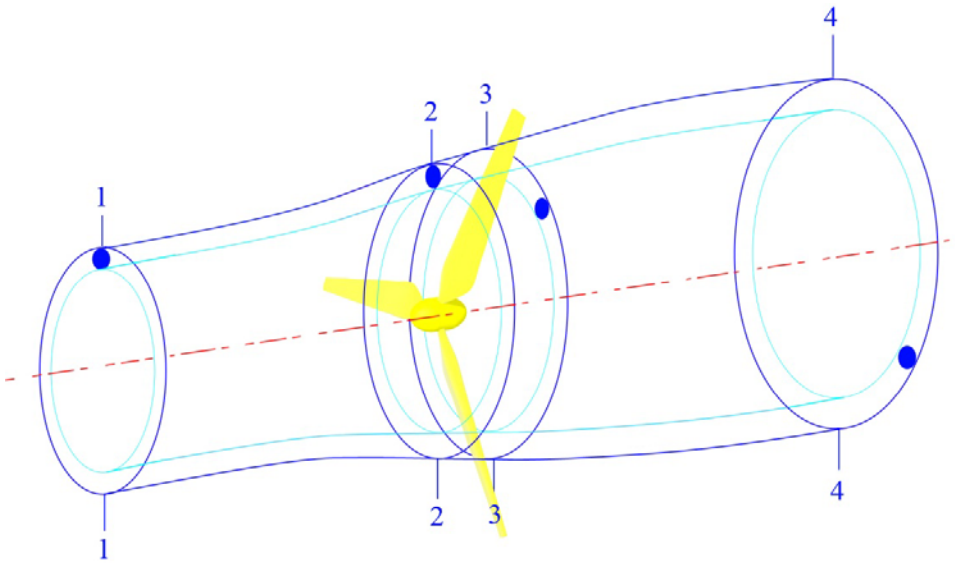

Figure 3-4: Rotating annular stream tube

3.1.2.2 Blade Element Theory

The forces on a turbine blade can be calculated by means of a two dimensional (2D) foil characteristics using blade element theory. The blade is spilt up into a series of 2D sections, these are the blade elements. Blade element theory relies on two key assumptions:

1. There are no aerodynamic interactions between different blade elements.
2. The forces on the blade elements are solely determined by the lift and drag coefficients.

The blade is broken down into several small parts, and then the forces on each of these elements are determined. These forces can then be integrated along the entire blade, and over one rotor revolution if there is a non-uniform inflow, in order to obtain the forces and moments produced by the entire rotor. Figure 3-5 illustrates the blade element velocities and forces.

Each of the blade elements will experience a slightly different flow, as they have a different rotational speed, a different chord length and a different twist angle. The angle of attack is determined by the velocity components at a radial position, r, expressed in terms of the current velocity, v_f, flow factors, a_i and a', the rotational speed of the rotor, $r\Omega$.

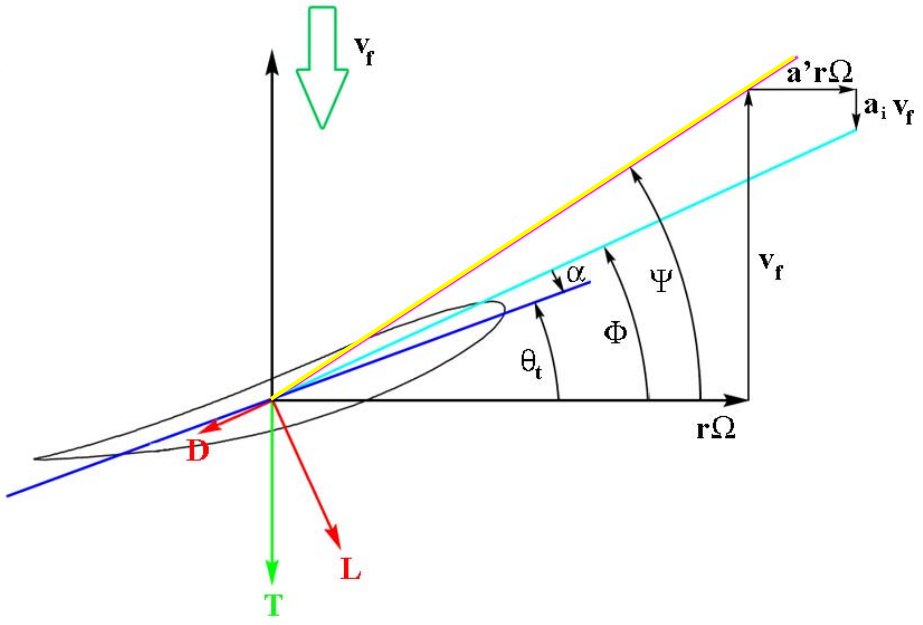

Figure 3-5: Blade element momentum theory velocities and forces

The Reynolds number and 2D lift and drag coefficients vary for each foil design. Foil performance information can be obtained from two dimensional CFD or experimental data; these tests are performed on stationary, non-rotating aerofoils; therefore a flow relationship between a rotating aerofoil and a stationary test needs to be defined. Since the blades rotate with a speed, Ω, and the flow exiting the blade with a speed, ω, the average tangential velocity that the blade experiences is:

$$\Omega r + \frac{\omega r}{2} = \Omega r\left(1 + a'\right) \qquad (3.15)$$

Recalling equation (3.11) and the fact that the local tip speed ratio is $\lambda_r = \frac{\Omega r}{v_f}$ the inflow angle, □, between the incoming flow velocity and the average tangential velocity becomes:

$$\tan\phi = \frac{v_f\left(1 - a_i\right)}{r\Omega\left(1 + a'\right)} \qquad (3.16)$$

This is dependent on the radial position of the element under consideration and hence varies for each blade element.

It can be seen in Figure 3-5 that the lift, L, and drag, D, forces are perpendicular and parallel to the oncoming flow. dL and dD_r can be obtained using experimental definitions of the lift and drag coefficients for an aerofoil, and assuming the local blade solidity, σ', is:

$$\sigma' = \frac{Bc}{2\pi r} \tag{3.17}$$

(where B is the number of blades) and that the torque on a blade element is equal to the product of the tangential force, and radius, r. Resolving the lift and drag forces for each blade element gives the spanwise elemental contributions to thrust and torque:

$$\begin{aligned} \frac{dT_T}{dR} &= \frac{1}{2}\rho v_f Bc\left(C_l\cos\phi + C_d\sin\phi\right) \\ \frac{dQ}{dR} &= \frac{1}{2}\rho v_f rBc\left(C_l\sin\phi + C_d\cos\phi\right) \end{aligned} \tag{3.18}$$

3.1.2.3 Blade Element Momentum Equations

There are therefore four equations for axial thrust and torque: Two from momentum theory which express these values in terms of flow parameters, and two from blade element theory that express them in terms of the lift and drag coefficients of the foil. The blade element and angular momentum equations are then set in terms of the non-dimensional performance parameters; C_T, C_{pow}, σ' and $x = \frac{r}{R}$, leading to the primary blade element equations:

$$\begin{aligned} \frac{dC_T}{dx} &= \frac{2x^2\lambda^2\sigma'\left(1+a'\right)^2\left(C_l\cos\phi + C_d\sin\phi\right)}{\pi\cos^2\phi} \\ \frac{dC_{pow}}{dx} &= \frac{2x^3\lambda^3\sigma'\left(1+a'\right)^2\left(C_l\sin\phi + C_d\cos\phi\right)}{\pi\cos^2\phi} \end{aligned} \tag{3.19}$$

And the momentum equation

$$\frac{dC_{pow}}{dx} = 8x^4\lambda^3 Ka'\left(1+a'\right)\tan\phi \tag{3.20}$$

where K is the Goldstein momentum averaging factor.

Equating the two expressions for $\frac{dC_{pow}}{dx}$ gives

$$a' = \frac{1}{\left[1 - \frac{\sigma'}{4\pi xK}\frac{\left(C_l\sin\phi - C_d\cos\phi\right)}{\cos\phi\sin\phi}\right]} - 1 \tag{3.21}$$

And from the definition of $tan\phi$, it follows that

$$a_i = 1 - x\lambda\left(1 + a'\right)\tan\phi \tag{3.22}$$

The induction factors can be determined from these equations by iterating along the span of the blade. By integrating the contribution to the power output by each rotating annulus along the blade span, the total power output of the rotor becomes:

$$P = \int_{r_h}^{R} dP dr = \int_{r_h}^{R} \Omega dT_T dr \tag{3.23}$$

where r_h is the hub radius. The power coefficient is then calculated using:

$$C_{pow} = \frac{P}{P_0} = \frac{\int_{r_h}^{R} \Omega dT_T dr}{1/2\, \rho\pi R^2 v_f^3} \tag{3.24}$$

The basis BEMT code used in this work was Cwind [79]. The code is based on the theory described above in which equality of local forces derived from consideration of angular and axial momentum is established, with those forces described in terms of local lift and drag coefficients. The program then uses the Goldstein tip loss correction method, and the Prandtl-Glauert correction for sub critical compressibility effects, based on local approximations of Mach number. The output provides power, thrust and torque data for a turbine of constant radius, at a single flow velocity and tip speed ratio (TSR). The spanwise distribution of section bending moments about the chordal, and normal to chord axes are also calculated.

3.1.3 Computational Fluid Dynamics

Computational fluid dynamics (CFD) is one of the branches of fluid mechanics that uses numerical methods and algorithms to solve and analyse problems involving fluid flows. CFD is a powerful tool which, when used either singly or in conjunction with other tools, can provide vital information as to the performance of a tidal turbine in varying flow conditions. Turbine performance data can be obtained; lift and drag readings can be converted into thrust, torque and power estimates, and also pressure distribution on the device enabling computation of likely cavitation. CFD can also give a detailed picture of the flow around the turbine enabling a more advanced outlook on possible environmental problems, such as scour,

erosion and the change in tidal magnitude, to be understood and in addition provides vital data regarding the positioning of tidal device arrays.

The fundamental basis of any CFD code are the Navier-Stokes momentum equations, which define single-phase fluid flow. Simplification of these equations by removing terms describing viscosity, yields the Euler equations. If the terms describing vorticity are also discarded the full potential equations are produced; these equations can then be linearised to yield the linearised potential equations.

3.1.3.1 Two Dimensional Analysis

In the two-dimensional realm, panel codes have been developed for airfoil analysis and design. These codes typically have a boundary layer model included, so that viscous effects can be modelled. Some incorporate coupled boundary layer codes for airfoil analysis work. Codes such as XFOIL use a conformal transformation and an inverse panel method for airfoil design. XFOIL is a linear vorticity stream function panel method, with a viscous boundary layer and wake model; and has been found to be suitable for producing section performance data and cavitation criteria for a tidal turbine at the preliminary design stage [75], although care should be taken to consider the apparent underestimation of drag and the overestimation of leading edge pressure coefficient [69]. Two dimensional analyses can be achieved using most CFD programs, although some are more suited to the technique. Section performance data at this stage includes the lift and drag coefficients of differing sections from which estimates of the power, thrust and torque on the turbine rotor and structure can be attained.

Figure 3-6 illustrates a typical plot of data acquired from XFOIL. The foil under examination is a NACA 63815 at an angle of attack of 6^{o} and a Reynolds number of 2.101×10^{6}. The blue line represents the C_P distribution over the upper surface of the foil, and the red line that over the lower surface. Evaluation of ventilation and cavitation of tidal turbine blades is required in the design process, this is discussed in further detail in Section 3.2, with specific reference to C_P plots of the form illustrated in Figure 3-6.

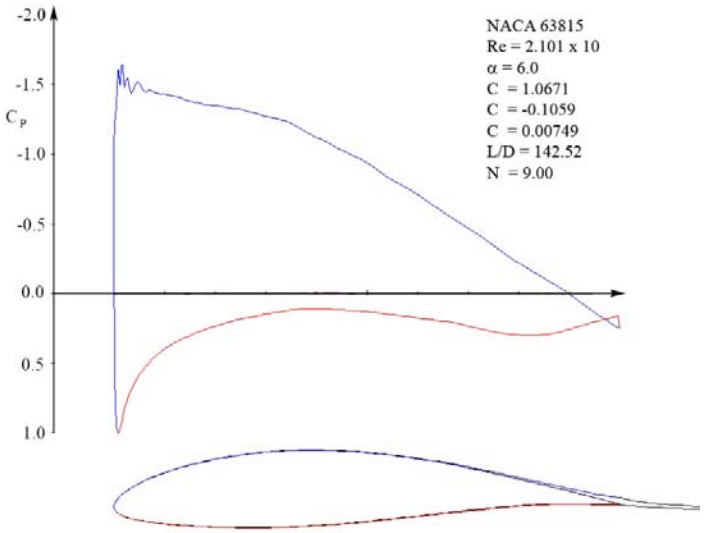

Figure 3-6: Pressure distribution over the NACA 63-815 section

Some two-dimensional analysis codes also provide fundamental section structural characteristics, such as second moment of area, for minor modifications to the base section made within the program. This data can be used for basic structural analysis of the turbine blade, which is important at this stage in the design process. Computational times are very short – in the order of seconds.

The process is very easy to parameterise and optimise due to its simplicity. Two dimensional analyses prove a powerful tool at the preliminary design stage for a tidal turbine and should not be underestimated; it is apparent, however, that for more detailed design information a more complex code able to model the more complex three-dimensional situations is required.

3.1.3.2 Three Dimensional Analysis

Surface panel codes allow a more thorough analysis of the performance of the turbine to be attained. Such codes calculate the characteristics of each panel over the surface of the body under analysis to produce lift and drag data for the panel and a pressure distribution, and ultimately the body as a whole. The calculated local pressure distribution can be used as a more detailed prediction of cavitation inception on the turbine blades and also as a source of detailed blade loading data for further structural calculations. Since the panels are geometric shapes and are flat, increasing the panel density models a three-dimensional, complex curved

shape such as a tidal turbine more effectively. Surface panel codes are more computationally intensive than two dimensional analysis methods; overall a reasonable compromise between computational effort and physical accuracy in modelling the flow interaction may be achieved [81, 82].

The surface panel code used in this work is PALISUPAN (PArallel LIfting SUrface PANel) [83] and was initially developed to investigate ship rudder-propeller interaction. By describing a set of quadrilateral panels on the surface of a body, and distributing a set of surface sources and dipoles on the surface of the model, the code generates a numerical solution of the flow over the individual components. For a lifting body, a wake is described downstream of the body to solve for the Kutta Condition. This condition is imposed by iteration until the solution has converged to a defined maximum value.

The basic potential flow mathematical model was refined by the addition of an empirical skin friction calculation which enabled viscosity effects to be considered. It does not, however, model the boundary layer, separation or stall in any form. An additional module allows boundary layer interaction to be studied. For rotating devices, such as propellers or turbines, operating at high Reynolds numbers the boundary layer is thin in comparison to the geometry of the body and therefore this viscous component forms only a small part of the total resistive torque; the majority of load arising from lift based processes. This code has been used to model the behaviour of a representative tidal turbine and good comparisons were obtained with published data, although significant problems were experienced in getting low twist sections to work [69].

The panel distribution over the turbine model becomes very important with relation to the accuracy of the results and the time taken for each calculation. During previous studies [69] it has been found that an optimum panel distribution can be achieved that maintains the accuracy of the result obtained with a finer distribution, but reduces the calculation time to around twenty minutes. Parameterisation and optimisation of surface panel codes is relatively simple, due to the low process times when implementing multiple runs – over 30 at a time – being highly feasible. Using a frozen wake model it is possible to reproduce the helical wake characteristic of tidal turbines. The number and distribution of panels in the wake is also very important for accurate modelling of device performance. Codes have been

developed that generate optimal panel distributions over complex shapes, such as a propeller or tidal turbine, and the associated wake panel arrangement [84].

These simple three-dimensional analyses provide a much more detailed picture of the pressure distribution over the turbine blades and body, therefore giving a more comprehensive picture of areas of the blade at which cavitation will occur. Figure 3-7 illustrates the pressure distribution of a three bladed tidal turbine obtained from a surface panel code.

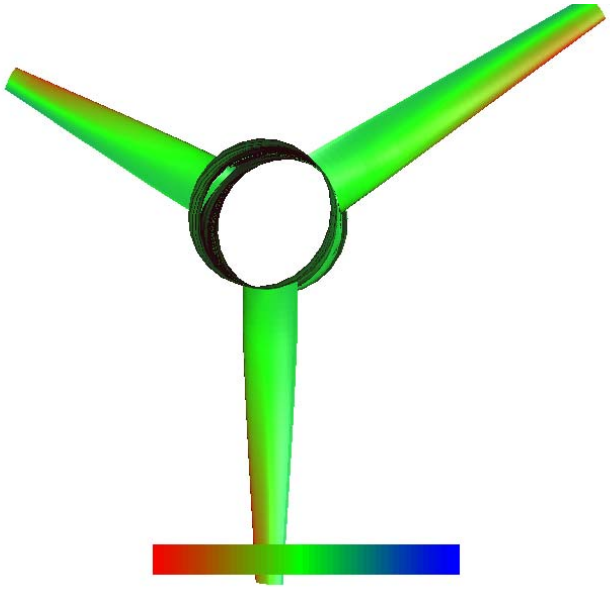

Figure 3-7: Representation of the pressure distribution over a three bladed turbine obtained using a surface panel code

The areas of red illustrate those parts of the blade where low pressure occurs, i.e. where the pressure coefficient is a minimum, and onset of cavitation is most likely. Areas of green are those with a more even pressure, and those nearing blue are areas tending towards stagnation.

Due to their simplicity, surface panel codes cannot capture severe changes in the flow regime, i.e. separation and stall. For a full design scenario, more advanced numerical simulation of the area around the turbine may be necessary in order to incorporate these effects.

3.1.3.3 Reynolds Averaged Navier Stokes Models

The Reynolds-averaged Navier-Stokes (RANS) equations result from time-averaging the Navier Stokes equations, and represent the mean flow. They are primarily used while dealing with turbulent flows. These equations can be used, with approximations based on knowledge of the properties of flow turbulence, to give approximate averaged solutions to the Navier-Stokes equations. The nature of RANS equations brings about the need for complex domain discretisation schemes as well as complex modelling with large numbers of elements. This leads to complex mesh structures on which the equations must be solved, and building such meshes is time consuming.

Turbulent flows contain many unsteady eddies covering a range of sizes and time scales. The RANS equations are averaged in such a manner that turbulent fluctuations in space and time are eliminated, and become expressed by their mean effects on the flow through the Reynolds, or turbulent, stresses. These stresses need to be interpreted in terms of calculated mean flow variables in order to close the system of equations, thereby rendering them solvable. This requires the construction of a mathematical model known as a turbulence model, involving additional correlations for the unknown quantities [85].

The RANS solver ANSYS CFX 11.0 was used to model a 20m diameter, three bladed, free stream, tidal turbine. The analysis did manage to converge, Figure 3-8, however the numerical results were poor when compared to validated BEMT data. Subsequent research into the field of RANS solvers for large scale tidal turbines has shown that commercial packages are too generic in their approach. While acceptable results can be achieved for small scale turbine modelling [86], the mesh complexity, coupled with cavitation analysis and streamline contraction, proves too complex and many groups are in the process of developing multifaceted in-house software aimed specifically at solving the tidal turbine problem accurately [87].

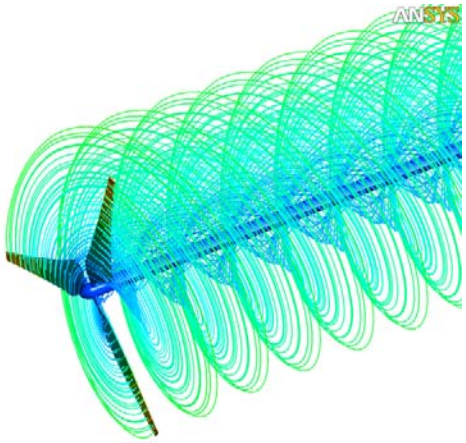

Figure 3-8: Velocity streamlines around a 20m, three bladed, free stream tidal turbine in CFX

3.2 Cavitation

In the course of one revolution, the tidal turbine blade will encounter a non-uniform inflow velocity, with implications for the design of the blade. Such a blade has the potential to suffer cavitation, depending on local inflow speed, forces (pressure reductions) and depth of immersion [75]. Cavitation occurs where the local pressure on the blade falls below that of the vapour pressure of the fluid and bubbles of gas form on the surface of the blade. The cavitation phenomenon was first observed and reported scientifically on a marine propeller over one hundred years ago [88, 89].

It can be assumed that cavitation will develop at any point on a blade where the pressure level is reduced to the level of the saturated vapour pressure of the ambient fluid. Different types of cavitation may occur – tip, vortex, sheet, bubble, cloud – depending on the effects of operating conditions, blade geometry, and water quality. Some undesirable effects may be allied with the type of cavitation incurred including;

- erosion of the blade due to imploding cavities near to the blade surfaces,
- associated noise as well as structural vibration,
- performance degradation depending on the extent, volume and fluctuating nature of the developed cavitation.

Cavitation tends to occur towards the ends of the blades on the face and near the tip, reducing the efficiency the turbine as a whole. Experimental evidence suggests that tidal

turbines may experience strong and unstable sheet and cloud cavitation, and tip vortices at a shallow depth of shaft submergence [75, 90]. Figure 3-9 illustrates a model turbine in a cavitation tunnel exhibiting both sheet and cloud cavitation, and tip vortices.

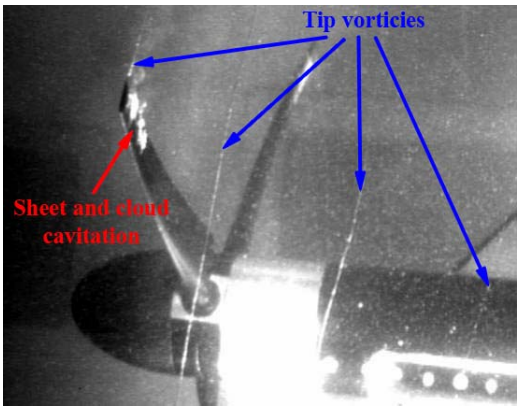

Figure 3-9: Cavitation experienced by a model turbine in a cavitation tunnel [75].

For cavitation analyses a cavitation number, σ, is defined as:

$$\sigma = \frac{P_o - P_v}{0.5\rho v^2} = \frac{P_{AT} + \rho g l - P_v}{0.5\rho v^2} \qquad (3.25)$$

Where P_o is the reference static pressure, P_{AT} is the atmospheric pressure, and P_v is the vapour pressure of the fluid. Cavitation inception may be predicted from the pressure distribution, since cavitation will occur when $P_L = P_v$ (where P_L is the local pressure), or the minimum negative pressure coefficient, $-C_p$, is equal to σ, Figure 3-10.

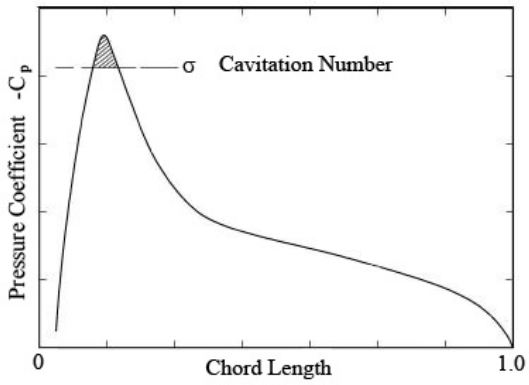

Figure 3-10: The relationship between pressure coefficient and chord length, illustrating cavitation inception [75]

The cavitation characteristics for a particular section can be described by a minimum pressure envelope, or cavitation-free bucket, as a function of the section cavitation number. Since the lift coefficient of the section is a function of the pressure distribution then, for a particular section, the cavitation-free bucket can be represented as a limiting C_L envelope to a base of σ. A schematic outline of a cavitation bucket, together with some likely types of cavitation, may be seen in Figure 3-11.

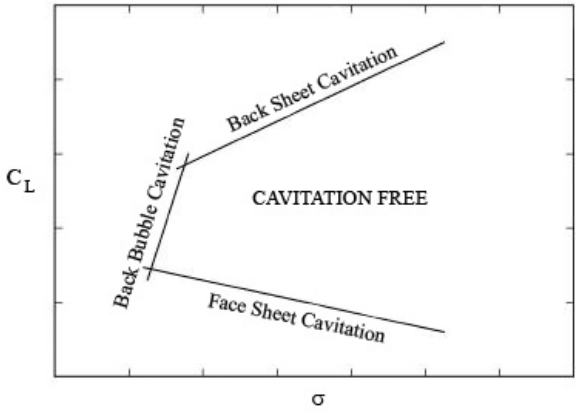

Figure 3-11: The cavitation bucket [75]

The width of the bucket, represented vertically in Figure 3-11, is a measure of the tolerance of the section to cavitation-free operation, i.e. if a section has a wider bucket it will be able to tolerate a much greater variation in angle of attack without cavitating. The width and shape of the bucket are dependent on the section characteristics such as thickness, camber, overall shape and nose shape. For example, an increase in section thickness tends to widen the bucket, while an increase in section camber tends to move the same bucket width and shape vertically to higher values of C_L.

Accepted levels of cavitation on tidal turbines are not yet clear. Marine propellers are capable of withstanding a reasonably high amount of cavitation (up to 20% of the blade surface) without significant loss in performance; it is not known whether tidal turbines may cope with a similar level of cavitation. Another factor to consider is the erosion of the blade surface due to cavitation; how do different blade materials respond to cavitation erosion? The phenomenon of cavitation erosion can be defined as a loss of material from a solid surface due to damaging effects from nearby collapsing cavitation bubbles. Bhagat [91] states that in

ductile matrix/brittle fibre composites, fibres do not contribute toward increasing the cavitation erosion resistance of the composites. The brittle fibres break and accelerate the erosion of composites. Cracks develop easily causing removal of large chunks of matrix material. Therefore, the energy absorption capability of these composites is drastically reduced and the materials have poor resistance to cavitation erosion. Hammond et al [92] examined the response of several different polymer matrix composite systems subject to vibratory cavitation. It was concluded that the mechanical response of the matrix material dominated erosion resistance. Saturation was found to decrease the damage resistance of composite materials by disrupting the interface, degrading the fibres, and swelling the matrix. Carbon fibre/epoxy composites were found to be least affected by saturation, whilst woven E-glass/epoxy and carbon fibre/thermoplastic matrix composites were most affected. They also noted that observation of the damaged surfaces over time indicated that the topography of the eroded surface significantly influenced the erosion behaviour. Due to the evident lack of performance of GRP with respect to cavitation erosion, protection alternatives were evaluated by Light [93]. Results showed that a GRP composite system could be designed to increase the cavitation erosion resistance of the material; however, the performance still remained below that of common metallic materials. Mention is also made of the low resistance of composite materials to cavitation erosion by the Specialist Committee on Cavitation Erosion on Propellers and Appendages on High Powered/High Speed Ships [94]. Whilst the majority of literature suggests that the cavitation erosion performance of composites is lower than that of metals, there are conflicting opinions [95]. Recent published research on the subject is limited and this could be an area of potential further work. The noise associated with cavitation is also a point for discussion; some theories suggest that it is beneficial for the device to create some noise in order to provide a sort of warning signal to marine mammals. It is undesirable, however, for such noise to be heard above the water surface.

3.3 Structural Analysis

The hydrodynamic loading present on the tidal turbine causes both shear forces and bending moments to increase from tip to root. In addition, depending on the magnitude of the blade buoyancy, the blade experiences a periodic variation in vertical force and associated moment. Centrifugal loading is also present; although, as rotational speeds are small, this

does not play a significant role. If the turbine axis is yawed relative to the onset flow, the blade experiences a periodically varying, axial, circumferential and radial load. Blade fatigue is an important design consideration as typically a blade experiences $1x10^8$ cycles over a 20 year device life[1]. Figure 3-12 illustrates the distribution of shear force and bending moment over the length of a single free stream tidal turbine blade.

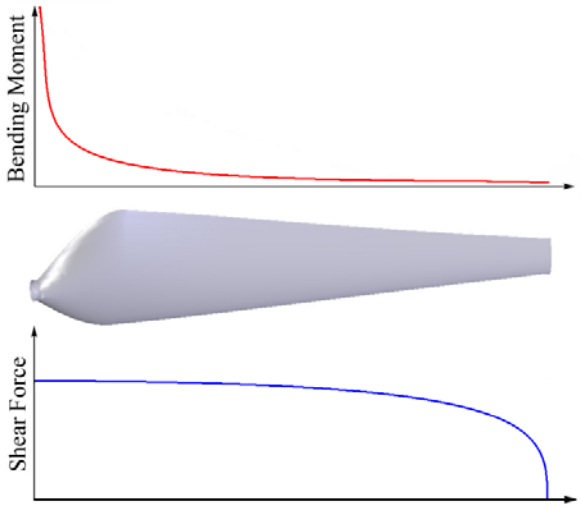

Figure 3-12: Shear force and bending moment over the length of a turbine blade

The largest moments are in the vicinity of the hub, and the magnitude of the local stresses depends critically on whether a controllable pitch or fixed pitch system is implemented. As a controllable pitch device is required to rotate, a blended zone is necessary between the outboard hydrodynamic section and a circular cross-section, and associated pitch mechanism and support bearings. Experience from wind turbines suggests that the sizing of the pitching mechanism and bearing design should be driven by imposed axial loading, i.e. thrust, rather than the hydrodynamic moment about the blade generator. The cross-section of the blade is not equally thick in all directions and thus the direction of the loading is important; this, relative to the cross-section, depends on the direction of the net force and on the angle of the section, both of which vary along the span of a turbine blade. The direction in which the blade bends is dependent upon the direction of the net loading, the second moment of area of the blade section, and the magnitude and direction of the applied load.

[1] For a typical 3 bladed turbine, rotating at 14 RPM

With a fixed pitch blade the loading scenario is much less complex, due to the lack of machinery required in the hub which is present in the variable pitch blades. A simple structural analysis is sufficient to give a basic understanding of the loads encountered at this point [96]. If the blades were to be made out of composites as opposed to metal, the stresses in the hub are likely to be less as the fibres and matrix work together to absorb some of the stresses.

The subject of Finite Element Analysis (FEA) has been used in the field of engineering for over half a century and has been continuously developed throughout this time. It has only been in the last few decades, with improvements in computational efficiency and power, that use of FEA has become more commonplace. Various different types of code exist, although these tend to differ with respect to the discipline under examination (i.e. structural, thermal, electromagnetic and so forth), and with additions to the equations, rather than variation in the mathematical formulations on which the code is based. The main advantage of this type of analysis is that complex design forms can be studied when an analytical solution is either not possible or not feasible. It is possible to undertake dynamic analyses, in order to simulate complex problems such as unsteady loading and time varying excitations.

FEA is based on subdividing the structure under investigation into elements, each element being of simpler geometry, and thus easier to analyse than the whole structure. In essence, the complex solution is approximated by a model consisting of piecewise-continuous simple solutions [97].

Basic structural analysis can be carried out by obtaining the pressures at each two-dimensional section and then integrating along the span of the blade. For more accurate modelling, the pressure distribution over the blade due to the fluid flowing over it can be computed through the use of Computational Fluid Dynamics and this input into the FEA code.

3.4 Yaw Characteristics

In Chapter 2, mention was made of the bi-directionality of tidal sites, and those that do not have completely rectilinear flow. If a yawing turbine, rather than a fixed turbine, were to be used at sites such as Portland Bill, an extra 10% of the energy may potentially be harnessed [30]; the additional complexity of the yawing mechanism, however, and the increased forces

experienced by the structure (when compared to a HAWT) mean that such mechanisms will be costly to produce and maintain for hydrodynamic devices.

Experiments have been carried out to measure power and thrust on a model tidal turbine under yawed flow conditions [30, 98]. Such experiments show that there is a consistent decrease in power and thrust with an increase in yaw angle, where optimal orientation for any turbine is based on the design flow speed. Momentum theory suggests that the power is proportional to the square of the cosine of yaw angle, γ, and the thrust as a cosine of the yaw angle :

$$C_{POW} = 4a_i\left(\cos\gamma - a_i\right)^2 \tag{3.26}$$

$$C_T = 4a_i\left(\cos\gamma - a_i\right) \tag{3.27}$$

Batten et al [30] demonstrated that the data attained from experiments is directly comparable to the momentum equations and the cosine square rule. Thus, the curve fits obtained may be confidently used to compare the effect of fixed and yawing turbines at different locations. Consequently, literature suggests that a yawing mechanism, albeit complex and costly, would benefit the energy capture of a device considerably. If, however, the blade design could be tailored in order to enable the turbine to operate more efficiently in a yawed flow, this could decrease the complexity and expense of the system whilst maintaining a high level of energy extraction.

Figure 3-13 illustrates a turbine in a yawed inflow. At A, the effect of the yaw flow is to increase the apparent angle of attack on the rotor blade towards stall, therefore reducing the efficiency of the blade. At point D, a reduction in blade angle of attack is experienced, again reducing the efficiency of the blade. At points B and C, however, the angle of attack on the blade sections remains consistent and the yawed flow affects the efficiency of the device by affecting the amount of radial flow along the blades.

In order to operate over a wide range of conditions, a blade section with a broad array of lift coefficients is desirable, with delayed separation and stall. In the case of a tidal turbine, it also desirable that the section shape is such that cavitation inception is delayed; and from an efficiency point of view, a low drag coefficient is also required. Structural requirements, however, tend to lead to relatively thick sections (particularly near the blade root) with an ensuing higher drag coefficient. Section shapes likely to meet all these requirements can be

developed using experimental and numerical methods. Suitable section data, including cavitation characteristics are required for any detailed design of a tidal turbine blade [75, 78, 98].

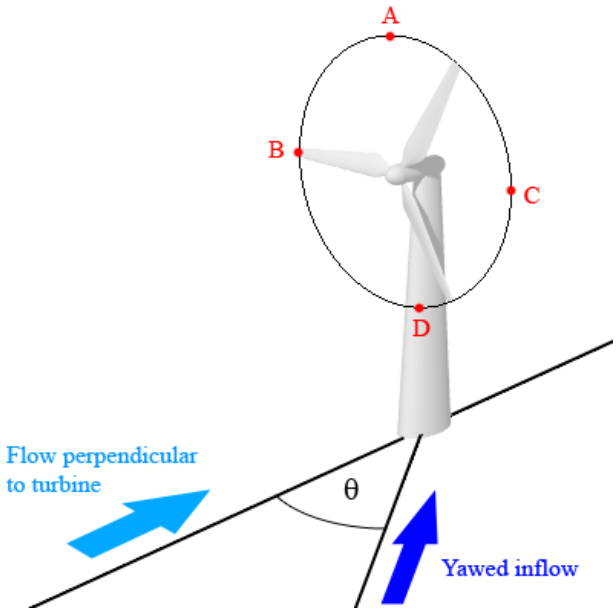

Figure 3-13: A turbine in a yawed inflow

It may be desirable to have a turbine that operates bi-directionally, thus enabling the energy from the whole tidal cycle to be captured. This negates the requirement of a yawing device, thus creating a less complex turbine, which is less costly to construct and maintain. One method of achieving this would be to use variable pitch blades, which can optimise their angle of attack to the inflow direction and also rotate 180^{o} when the tide changes. Another method would be the use of a fixed pitch bi-directional blade using a rotationally symmetric section shape, or lastly, the creation of an actively adaptive blade which is able to reverse the section shape upon the change in tidal direction.

3.5 Variable Pitch Blades

Analytical reports suggest that a considerable performance advantage can be gained from using variable pitch (VP) blades [99]. Such blades use a variable pitch mechanism placed at the root to rotate the entire blade in response to a changing inflow, thereby maximising the absorbed power at any moment in time. Radial flow along rotating blades

results in delayed flow separation, hence the lift produced at high angles of attack is greater than those given by two dimensional measurements and conventional theory; this is increased by a yawed flow. In addition, increased peak power production for horizontal axis rotors has been attributed to the phenomenon of stall delay [9]; the stall angle of attack tends to be greater than predicted, and peak power subsequently underestimated. A VP blade could encourage such situations to be attained, thus producing a greater power yield.

3.5.1 Unidirectional Section

Batten et al [78] demonstrated how blade pitch angle and changes in camber alter stall performance and delay cavitation inception. Previous section studies have shown the NACA 5 digit 63-xxx series to have a higher lift coefficient and lower drag coefficient than several NACA 4 digit sections [75]. Good cavitation performance is noted, with a large cavitation bucket for the 5 digit sections when compared to the 4 digit sections. The NACA 63-8xx series has improved cavitation performance at high values of lift coefficient when compared to the NACA 63-2xx series; this is illustrated in Figure 3-14. It is also shown that the NACA 63-2xx section blade at 0^o pitch is likely to suffer some cavitation on the outer parts of the blade whereas the NACA 63-8xx section is cavitation free [78].

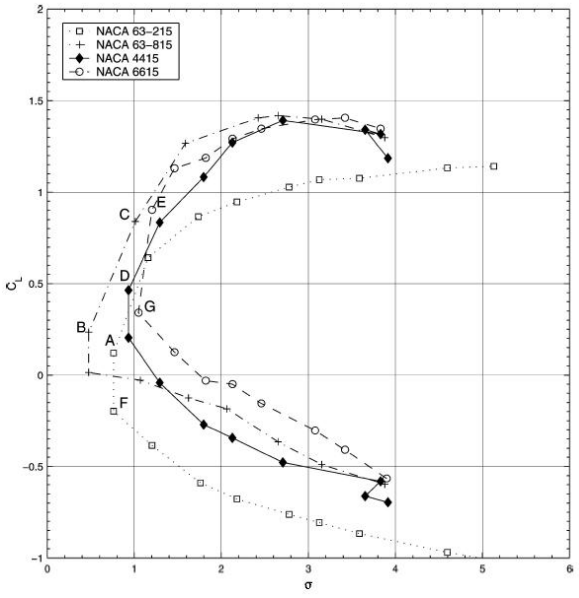

Figure 3-14: Cavitation bucket section comparison [75]

The NACA 63815 was found to be a suitable section for use in the design of HATT blades [75]. Performance curves for the NACA 63815 airfoil were developed using XFOIL; the C_l and C_d curves are illustrated in Figure 3-15 and Figure 3-16.

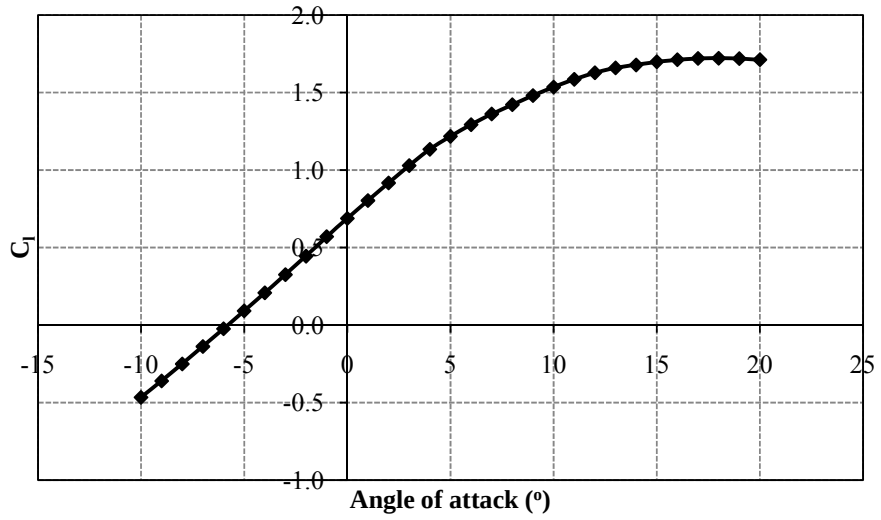

Figure 3-15: Lift curve for a NACA 63815

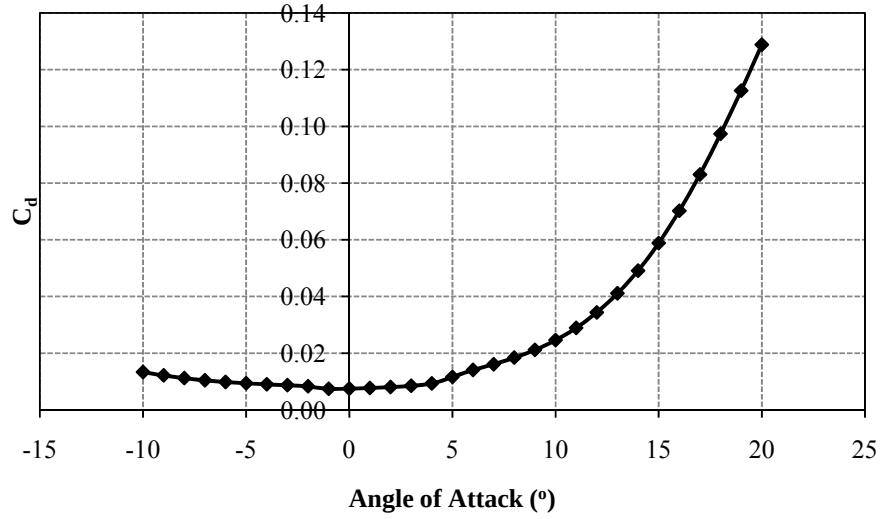

Figure 3-16: Drag curve for a NACA 63815

3.5.2 Blade Optimisation

Once the section has been chosen, the planform of the turbine blade must be optimised. For this case it was assumed that the hub/diameter ratio was held at 0.2. The

turbine in question was a three bladed, horizontal axis, 20m diameter device in a flow with a spring peak current of 2.5m/s. The BEMT code Cwind, discussed in Section 3.1.2, was used for a basic rapid optimisation analysis. Minor modifications were integrated in order to take into account the increased density of sea water when compared to air, and to also remove the compressible flow checks which are unnecessary for subsea devices. The default blade planform is detailed in Table 3-1.

Table 3-1: Default blade planform

Radius *(m)*	Chord *(m)*	Twist *(°)*
2.00	1.92	16
2.89	1.76	10.93
3.78	1.62	7.57
4.67	1.48	5.32
5.56	1.34	3.75
6.44	1.20	2.80
7.33	1.06	2.16
8.22	0.92	1.63
9.11	0.78	1.20
10.00	0.64	0

Several input variables relating to the blade planform were altered – area, twist, taper, pitch – and the code run in excess of 30,000 times with the goal to determine the optimal planform for maximum power extraction. The best performing blade in this respect had a resulting turbine power coefficient of 0.4946 and operated at a TSR of 12.15. Further optimisation, incorporating very small changes in the variables, resulted in little change from these values and thus the initial search was deemed suitably accurate.

Figure 3-17a) and b) show C_{pow} and C_T as a function of TSR respectively. It can be observed that while this blade has a maximum C_{pow} of all those considered, C_T is also high especially at higher values of λ.

The blade optimisation analysis in this case simply considered maximum C_{pow} as the goal to optimise towards. Multiple objective optimisation with variable weighting would be beneficial, however, as the designer could then consider key outcomes such as C_T, torque and cost.

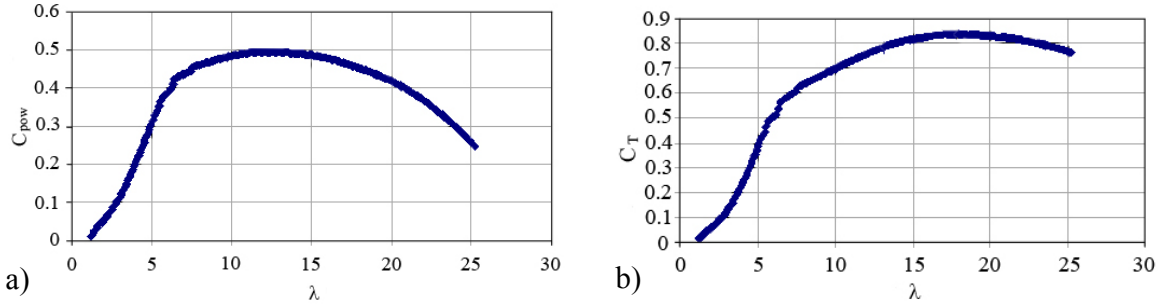

Figure 3-17: a) C_{pow} and b) C_T as a function of tip speed ratio

Figure 3-18 illustrates the optimum blade pitch settings for each TSR. It can be seen that increased blade control is highly beneficial at lower TSRs, equating to higher flow velocities, but less so at the lower current velocities. This has implications for the lifespan of the tidal device, with higher flow velocities putting increased loads onto the turbine and associated structure. VP mechanisms are complex and thus require more maintenance than a simple fixed pitch blade, which considerably increases the in service cost, and could also reduce the life span of the device.

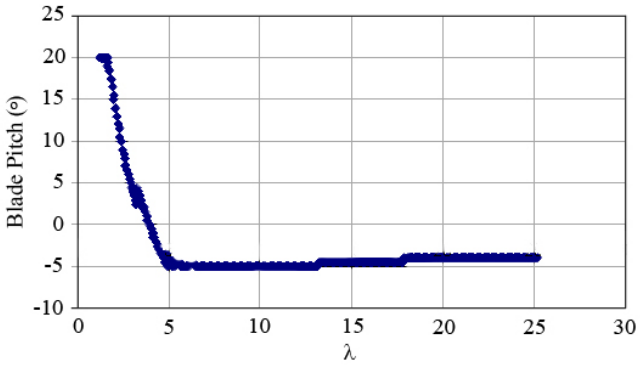

Figure 3-18: Optimium blade pitch setting

Therefore, it could be beneficial to consider a fixed pitch device that can perform in both directions of the tidal current, without the need for a VP mechanism. One method of doing so would be to use a blade that has a wholly bi-directional foil section.

3.6 Bi-directional Blades

In order for the turbine to produce thrust in both directions of tidal flow – thus optimising the power output – the turbine must either rotate to face the oncoming flow, have VP blades that can be reversed 180°, or the blade sections must be rotationally symmetric. Rotational sections would mean that when the flow is reversed the turbine generates thrust in the opposite direction, creating an induced flow velocity in that orientation, albeit with the current approaching and flowing over an identical surface. This is illustrated in Figure 3-19, where reversing the flow causes the apparent velocity of the fluid over the blade, due to the turbines rotation, $r\Omega$, to change direction. In turn this causes the thrust, T, to reverse. Eventually, the axial inflow velocity is also reversed, as the turbine begins moving in the opposite direction. Operation in the opposite direction is equivalent to that illustrated, although all velocities and forces also act in the opposite direction. The foil presents exactly the same shape to the flow in both situations as it is rotationally symmetric.

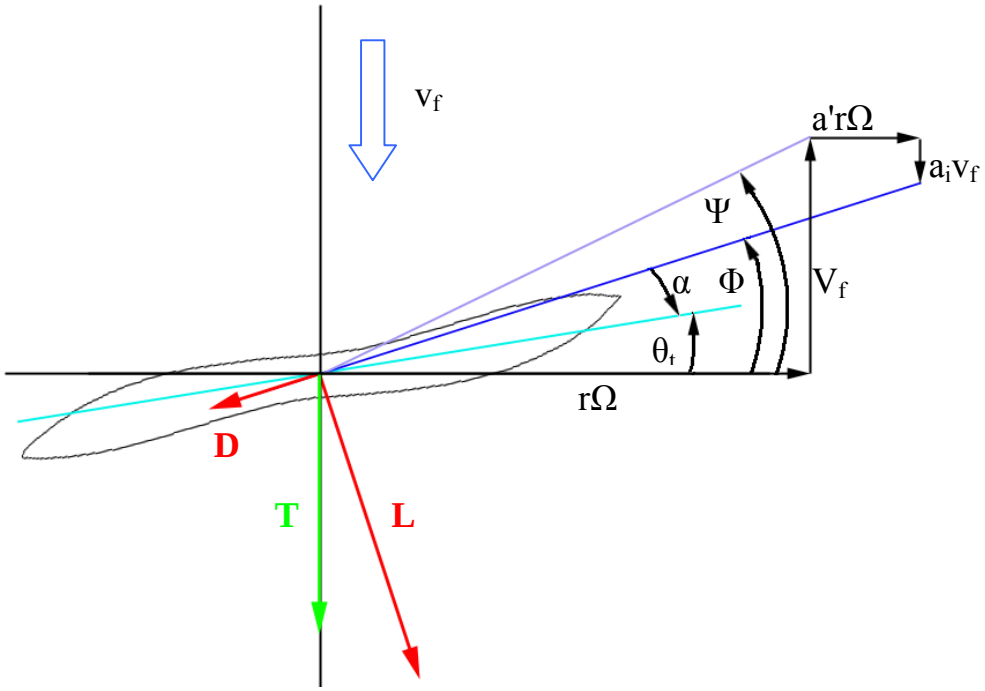

Figure 3-19: Blade element velocity and forces on a bi-directional section

3.6.1 Bi-directional Section

A program was developed, and subsequently modified, to create rotationally symmetric foil sections [77]; initially, by creating a thickness distribution, and adding and subtracting it from a camber line to define the top and bottom surfaces. This was found to be limited as, in order for the foil to be rotationally symmetric, the camber line must also be rotationally symmetric. Flexibility of the program was increased by altering the polynomial camber line whilst maintaining rotational symmetry.

The developed method uses circle quadrants at the ends of the foil, joined by two cubic splines, with the continuity of gradient and curvature enforced. Parameters were included to specify the transition between the cubic splines, and the leading and trailing edge circles. This prescription of the arc/spline matching, however, only results in optimum behaviour at the design thickness/chord ratio. The result of the development is a program that can create smooth, complete foils of any thickness, or leading edge sharpness, with seven input parameters. These parameters are:

- Leading, and therefore also the trailing, edge radius;
- Point of transition to the first spline, as an angle around the circle of the leading edge;
- Thickness at the point of transition to the second spline and its chord-wise location;
- Point of transition from second spline to trailing edge circle, again as an angle;
- Coefficients of x^3 and of x^5 in the camber line equation.

Problems were experienced with the 2D panel code, Xfoil, used to assess section performance. The amount of separation at the trailing edge, due to the end radius, was causing difficulties as the program is unable to calculate information for sections that have significant trailing edge separation – which is inherent with a rounded end. Modifications were made to the program to replace the surface distribution towards the trailing edge with a straight line, in order to generate foils with a sharp trailing edge. For this an extra parameter was added, to control the chord-wise location of the start of this replacement.

Several sections were developed using this and subsequent programs. Through preliminary investigations: using Xfoil [100] the choice was reduced to two, with superior performance in lift, drag and minimal pressure spikes, Section A and Section B. Sections A and B can be seen overlaid with a NACA 0012 section in Figure 3-20.

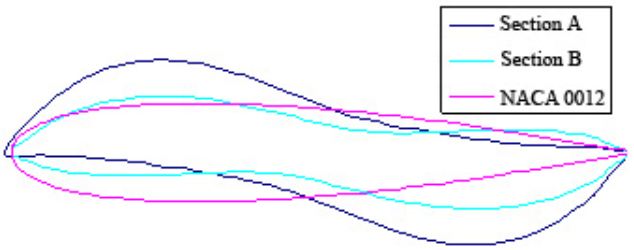

Figure 3-20: Sections A, B and NACA 0012

Further analysis was carried out to better understand the performance differences of the three sections. Figure 3-21 and Figure 3-22 show the variation of C_l and C_d with angle of attack, α, for each section respectively. The performance of the NACA 0012 outweighs the bi-directional sections when the section is facing the flow in the conventional manner, however, the performance of such a section in reverse is inadequate.

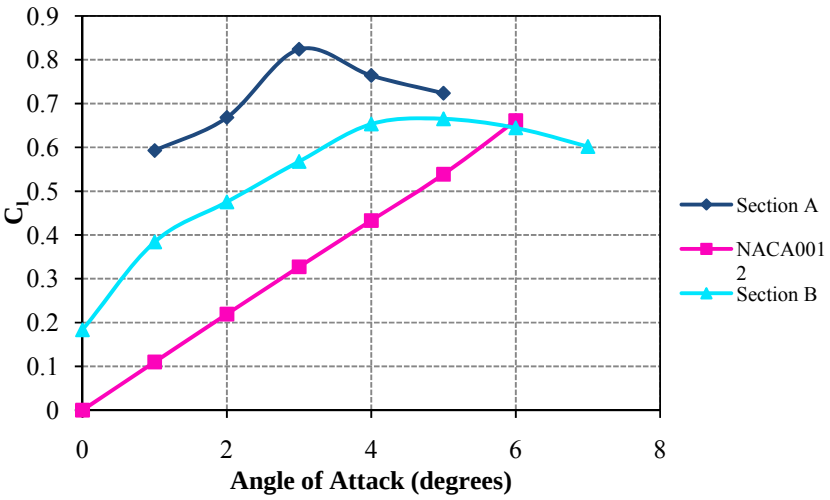

Figure 3-21: Variation of C_l with angle of attack on a section with t/c=0.096

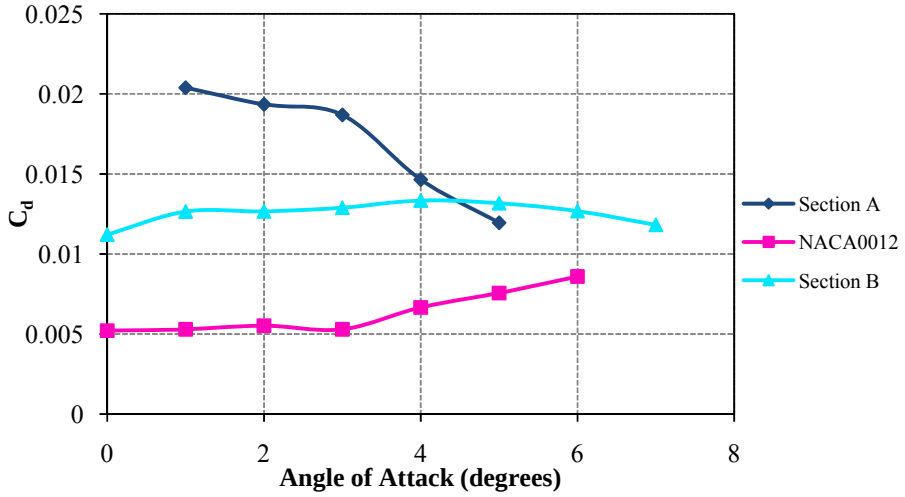

Figure 3-22: Variation of C_d with angle of attack on a section with t/c=0.096

Of the two rotationally symmetric sections, Section A causes program failure at angles of attack greater than 5° and less than 1°, due to separation occurring as the stall condition is reached. Therefore, the more constant and reliable curve of Section B is preferable, which indicates delayed separation in similar flow conditions. In the case of a tidal flow, a constant angle of attack is unlikely to be achieved and thus, where any section may be optimised for one angle, Section B would also perform well over a range of angles hence increasing the captured energy. Due to the more extreme shape, and relatively small operating envelope, it is likely that Section A would incur increased levels of cavitation in off-design operation. Cavitation is undesirable for a number of reasons (Section 3.2) and hence Section B was chosen for its more steady performance characteristics and reduced cavitation inception.

3.6.1.1 Section Characteristics

The pressure distribution over a range of angles of attack of the chosen section at a flow speed of 2.5m/s is illustrated in Figure 3-23. The upper set of lines represents the pressure distribution over the upper side of the foil, and the lower set that over the lower side of the foil. In general the pressure coefficient, C_P, becomes more negative and cavitation is more likely to occur with an increase in angle of attack.

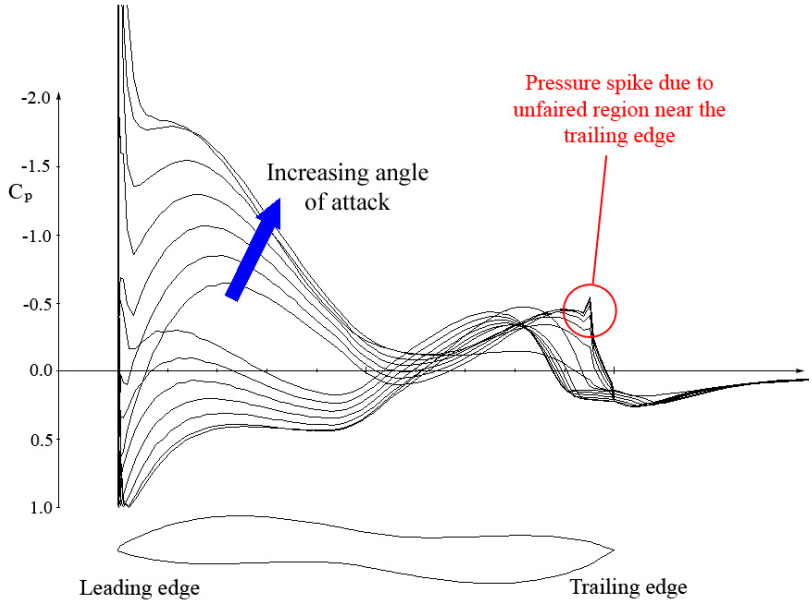

Figure 3-23: Pressure distribution of section B over a range of angles of attack

Recalling theories that there is a tendency for XFOIL to over-predict leading edge pressure [75], the extreme peak present at the leading edge of the foil may be taken as a secondary consideration, provided that it is not markedly greater than the primary upper surface pressure peak – and this was deemed to be the case. The smaller pressure spike towards the trailing edge of the foil was caused due to unrefined fairing of the section in this region. The discrepancies in the C_P plot from that of a standard unidirectional section are best discussed with reference to Figure 3-24 and Figure 3-25.

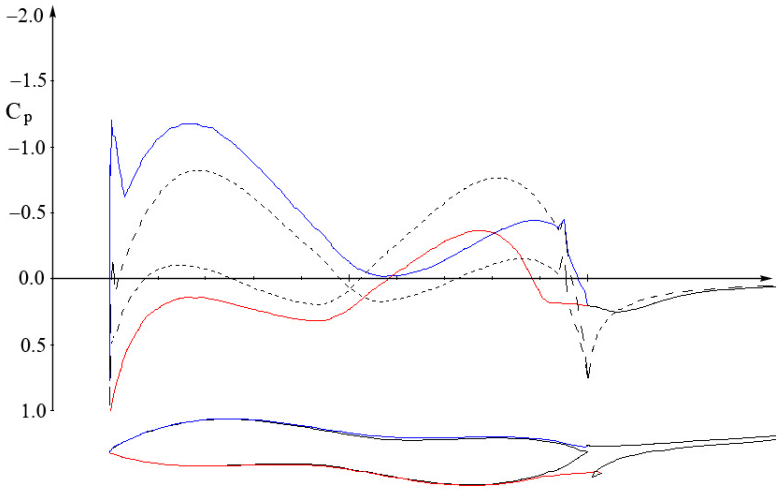

Figure 3-24: Pressure distribution over section B at 2.5m/s and 3°

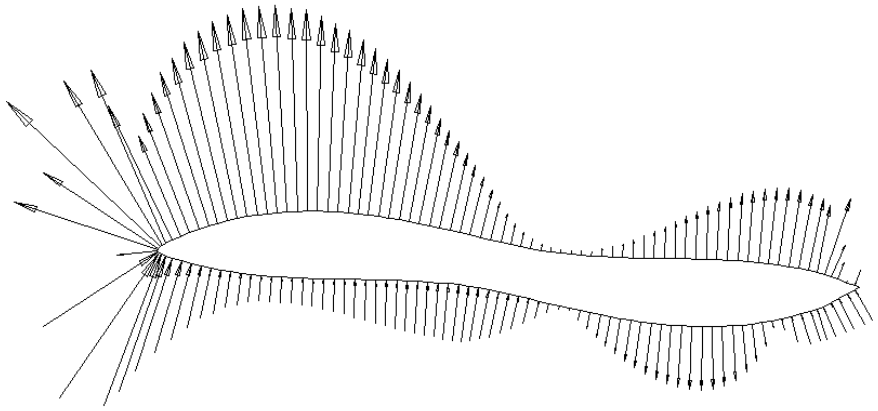

Figure 3-25: Pressure vectors around section B at 2.5m/s and 3°

The majority of the lift is generated from the first half of the foil, whereas a region of negative lift is present over the second half of the foil due to the rotational symmetry of the section. There is a large zone of separation apparent at the trailing edge of the foil, Figure 3-24, which is because of the increased thickness of the section – required for operation in the reverse direction. Cavitation is likely to occur at the front of the blade due to the region of high curvature here which causes a more prominent pressure drop. There is also a second low pressure peak apparent on the pressure face of the foil towards the trailing edge which is not exhibited with conventional foil sections, although not as large as that exhibited by the suction face at the leading edge, and cavitation may also occur here but only if it has already occurred at the front of the foil. The pressure peak close to the trailing edge is unlikely to be present in operation and is due to the need to create a sharp trailing edge in order to model the section in XFOIL, and as such may be discounted.

The difference between the true viscous C_P distribution (solid line) and the inviscid C_P distribution (dashed line) in Figure 3-24 is due to the modification of the effective airfoil shape by the boundary layers. This effective airfoil shape is shown superimposed on the current airfoil shape. The gap between these effective and actual shapes is equal to the local displacement thickness, which is approximately half as large as the overall boundary thickness. The boundary layer velocity profile may be observed in Figure 3-26.

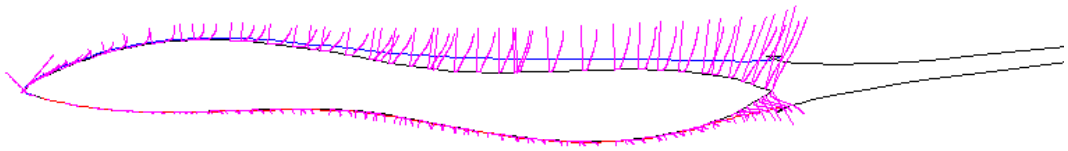

Figure 3-26: Boundary layer velocity profile for section B at 2.5m/s and 3°

3.6.1.2 Thickness/Chord Ratio Alteration

The thickness/chord, t/c, ratio of Section B was increased and decreased and the resulting sections run through XFOIL to obtain the relevant performance data. Figure 3-27 shows the variation of C_l/C_d over a range of t/c ratios. The intermediate t/c ratio of 0.096 is the optimum for the section as it exhibits good performance over the range of angles of attack. Generally, the trend is a loss in performance for a greater or lesser t/c ratio than this intermediary. It can be observed that a section with marginally greater t/c actually outperforms the intermediate section at higher angles of attack, but underperforms at lower angles. Conversely, the marginally thinner section performs nearly as well at lower angle of attack, but less so at greater ones. Considering the blade as a whole, with thicker sections nearer the root and thinner nearer the tip, this information may be utilised to obtain the best pitch angle along the blade for optimum performance of each section as the t/c ratio decreases with blade length.

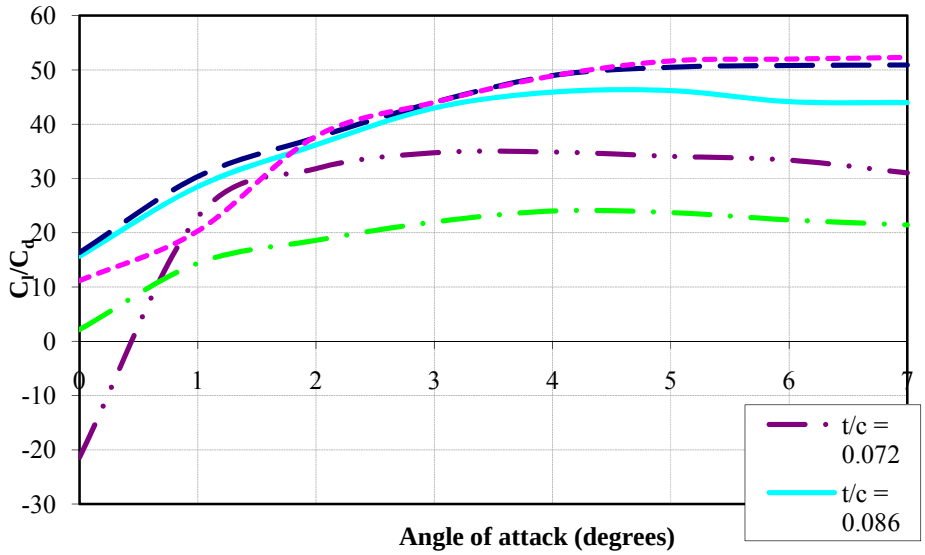

Figure 3-27: Variation of C_l/C_d with t/c ratio

As a further check on the section, a low geometric aspect ratio (3.0) rectangular plan form wing was analysed in Palisupan using the boundary layer routines. This gave similar section performance to XFOIL and predicted stall at a similar angle; and thus gave confidence that the results could be applied for the subsequent optimisation. It also allowed a simple evaluation of the cavitation criterion to be applied. Figure 3-28 and Figure 3-29 show the derived lift and drag curves for the section respectively, the values beyond negative and positive stall were extrapolated based on similar behaviour to that seen by Barnsley & Wellicome [79].

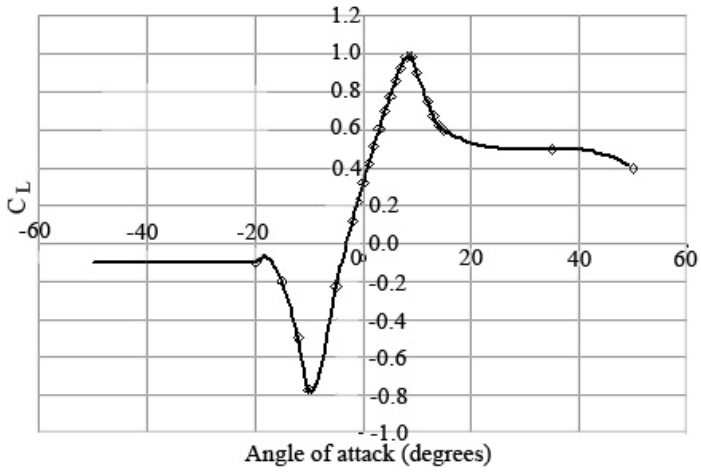

Figure 3-28: 2D section lift curve

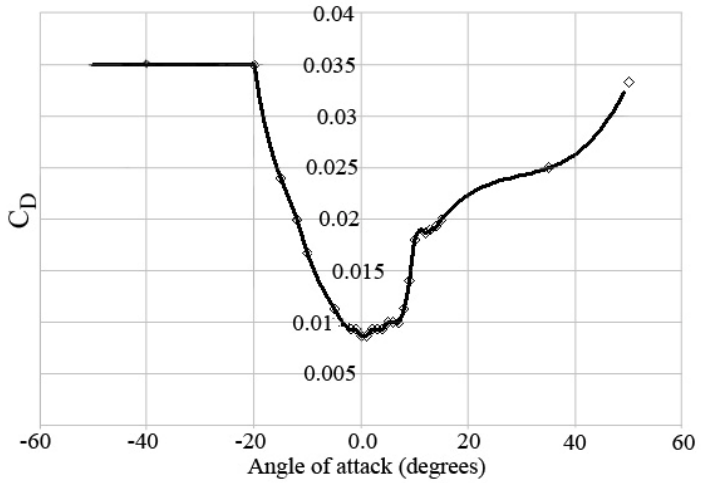

Figure 3-29: 2D section drag curve

It is noted that there appear to be some curvature discontinuities in the section shape. This would need to be resolved prior to production; the pressure spikes, however, are unlikely to change the section performance or cavitation significantly as they are extremely localised.

It is worth considering that, with these bi-directional sections especially, the phenomenon of stall delay could be utilised to benefit the turbine energy capture. As these sections are designed for simplicity of manufacture and maintenance of the turbine blades, i.e. avoiding the complex machinery relating to yawing mechanisms and pitch control devices, they are likely to stall at a lesser angle of attack than conventional sections.

3.6.2 Blade Optimisation

The blade planform optimisation procedure for the bi-directional blade is the same as that used for the VP blade, detailed in Section 3.5.2. The base blade planform is the same as that for the VP blade, Table 3-1. Again the BEMT code was run for in excess of 30,000 simulations and the overall turbine was optimised for maximum power absorption. The best performing blade in this respect had a resulting turbine power coefficient of 0.4489 and operated at a TSR of 7.12. Figure 3-30a) and b) illustrate C_{pow} and C_T as a function of TSR respectively.

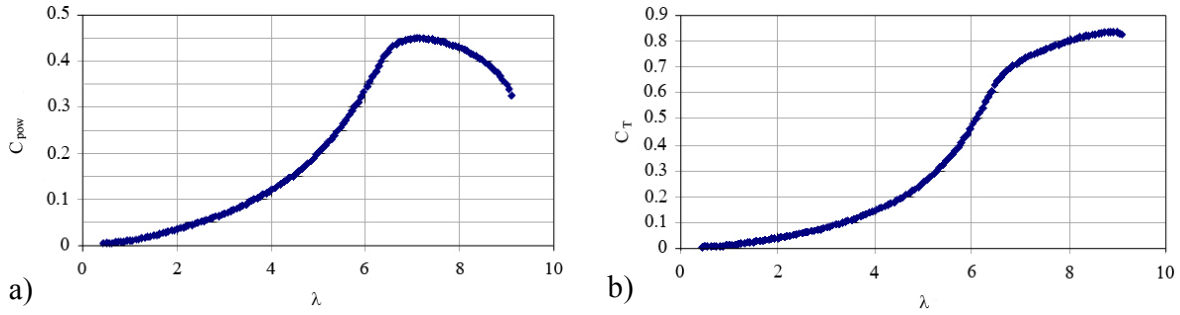

Figure 3-30: a) C_{pow} and b) C_T as a function of tip speed ratio

An additional variable to be considered is that of the hub diameter. The VP blade requires the root to be faired so as to present a circular cross section suitable for the pitch mechanism. In the case of the fixed pitch bidirectional design there is no need to vary the shape of the blade root in this manner, although there is a need to have significant absolute

thickness near the root in order to resist the axial blade load. The blade, so far, has been optimised using a hub/diameter ratio, x_{hub}, of 0.2. The effect of altering x_{hub} on the maximum power of the bi-directional blade is shown in Table 3-2.

Table 3-2: Effect of Hub/Diameter ratio on maximum power

x_{hub}	*AFac*	*PFac*	*TFac*	*Pitch*	*Power at 2.5m/s*
0.1	0.7	1.9	0.6	11	1152 kW
0.15	0.7	1.7	0.6	8	1145 kW
0.2	0.6	1.3	0.7	2	1129 kW

Where *AFac, PFac* and *Tfac* are factors governing area, pitch and taper respectively:

- AFac - Area – this linearly scales all the section chords. Values less than one give a proportionate reduction in blade area;
- *PFac* - Pitch – this changes the increment in blade twist between each section. Values greater than one cause a larger twist change between two sections than in the original design;
- *TFac* - Taper – values less than one result in a smaller tip chord/root chord than in the original design.

It can be observed that an extra 1m in blade length, changing x_{hub} from 0.2 to 0.1, results in a gain of 2% in power, however also causes a 10% increase in root bending moment which has implications for the structural design of the blade and through-life fatigue properties.

3.6.3 Blade Comparison

Figure 3-31 displays the power curves of standard fixed pitch, variable pitch, and bi-directional bladed turbines. It should be noted that the bi-directional blade has an 8% increase in blade surface area. This reflects the poorer section performance and causes a reduction in power capture over a lunar cycle. This drop in performance is not as significant as is initially apparent, due to the large decrease in area beneath the curve of the bi-directional device when compared to the other two.

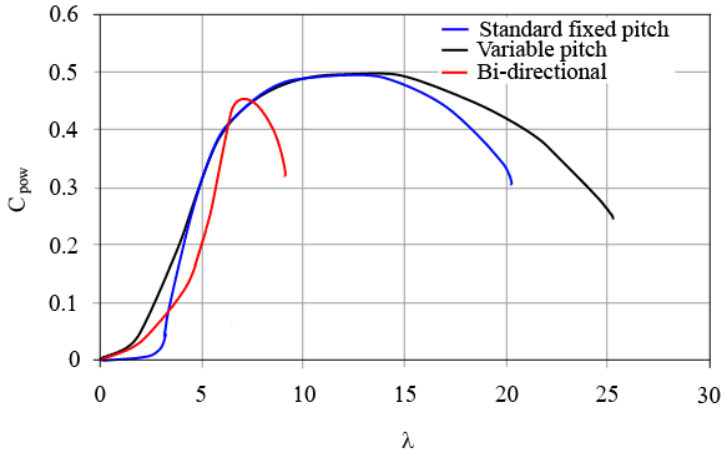

Figure 3-31: C_{pow} curves for a standard fixed pitch, variable pitch and bi-directional bladed turbine

It is apparent that the bi-directional blade, despite having a significantly narrower power curve, could be economic in certain locations – ones where a higher tidal velocity is sustained. For example the Solent, near Yarmouth, where the ebb tide lasts longer and maintains a higher velocity for a longer period of time and the flood tide is a shorter part of the cycle.

The power curve indicates over how much of the tidal cycle a device operates at a particular TSR. If a suitable generator control can be implemented, the bi-directional device could operate at or near its optimum TSR; however, the range of effective operational TSRs is significantly lower than for the more robust hydrodynamics of the other devices, but is not necessarily so for the power captured. This is illustrated in Table 3-3 for the VP turbine operating at constant design RPM where the turbine is inefficient at higher TSR despite the broad power curve.

Table 3-3: Operational data for the VP turbine at constant design RPM

TSR	***Current Velocity (m/s)***	***Turbine Performance***	
		Operational (%)	***Power absorbed (%)***
≥30	Slow <0.55	*stationary*	0
≥20	Modest <0.9	13.5	1.2
≥10	Reasonable <1.78	44.2	36
<10	High <2.5	20.9	62.8

The ability to control pitch to change the working RPM such that the turbine is operating at, or near, the design TSR, would result in increased power absorption in the modest and reasonable current regimes.

If x_{hub} were altered for the bi-directional device, as discussed in Section 3.6.2, a 1m increase in blade diameter would enable the bi-directional device to capture the same amount of energy as the 20m variable pitch device with optimal operating conditions.

One of the effects of a less efficient blade is an increase in thrust - more energy is transferred into thrust rather than blade rotation. The maximum thrust coefficient, C_T, for the bi-directional bladed turbine is 0.83 but with the ability of the VP blade to alter pitch and thus operate at the design TSR a value of less than 0.8 is achieved. If both blades are assumed to operate at maximum C_{pow} for a mean spring peak current of 2.5m/s the thrust is 3.75% greater for the bi-directional device; coupling this with a proposed reduction in x_{hub}, a 1m increase in diameter results in an overall increase in thrust of 14.4%. This increase in thrust is detrimental not only to the turbine blades but also the support structure and foundations, and would need to be properly addressed during the design cycle.

3.6.3.1 Cavitation

For the purposes of the preceding analyses it has been assumed that cavitation only has a limited effect on the relative power capture of the designs. Cavitation is most likely to occur when the blade is located at top dead centre, blade tip closest to sea surface, and when the local tip velocity is highest. When operating within the optimal current and TSR range the variable pitch and bi-directional devices have maximum blade tips speeds of 26m/s and 19.3m/s respectively.

As the non-dimensional distance along blade span from the axis $\left(\frac{r}{R}\right)$ reduces, the pressure increases. Cavitation initiates when the pressure drops below the local vapour pressure of the fluid (1020 N/m^2 at 15^{o}C). The local flow speed over the blade surface is higher than the blade speed by a factor proportional to the local surface pressure coefficient (based on local blade speed), which further reduces the local static pressure.

The BEMT program was modified to include a fractional cavitation check based on a series of rules taken from the typical cavitation bucket curves, Figure 3-14:

- $\sigma \geq 4.0$ - local section not cavitating
- $\sigma \leq 1.0$ - section cavitating
- $C_l > 1.0$ - section cavitating
- $C_l < (-0.3\sigma + 0.7)$ - section cavitating

This basic representation indicated that the bidirectional turbine should not cavitate to any great extent. In the event that it does, it only occurs near to top dead centre. Significant cavitation only occurs for a mean spring peak current of 2.5 m/s and at RPM values far exceeding the design RPM. The VP turbine operates at a higher design RPM and hence increased cavitation was found to occur. The tip section (outermost 10% of the blade) was estimated to cavitate at top dead centre, and maximum design current between 21-24 rpm. Progressively more cavitation occurs beyond 24rpm.

3.7 Summary

Of the different types of tidal energy extraction it is expected that HATTs will ultimately be the favoured method. The blades of a HATT are the main source of energy extraction for the device and are required to operate in a harsh subsea environment for a long (20 year) life cycle, with minimal need for maintenance. As such, optimisation of the design of the HATT blades is important. BEMT is a key tool in the design of tidal devices and the theory behind the technique is presented. Choice of an appropriate foil section for the blade is integral. While most tidal devices have an asymmetric blade for increased efficiency, this requires the turbine, or the blade, to be rotated for use in both directions of tidal flow. This, in turn, introduces complex mechanisms into the turbine structure, which complicate design and maintenance. A blade utilising a fully bi-directional section would not need any vaning or variable pitch mechanism to operate throughout the entire tidal cycle. A novel bi-directional section has been developed and examined for use on a HATT and the performance compared to that of a variable pitch blade. The bi-directional blade is site specific due to the narrow power curve, and may be more economic in certain locations where a higher tidal velocity is sustained thus taking advantage of the area of increased performance at lower TSR.

4 Composite Blades

Initial tidal turbine blade design considered, and indeed produced, the required stiff and unyielding marine rotors in steel. Achieving the necessary compound-curved profile in steel was expensive. In addition steel is heavy, prone to fatigue and susceptible to corrosion induced by salt water therefore prompting the decision to adopt composites instead. Composite materials ease the fatigue problem, both through their inherent fatigue tolerance and by reduced blade weight. If the composite blades are appropriately designed they can deliver the required stiffness. Where some HAWT blades rely solely on the form stiffness of a sandwich envelope structure, however, a robust internal 'skeleton' was considered essential for efficient HATT operation.

The increased loading that water puts on a turbine makes blade strength and stiffness more critical than they are in wind turbine blades. Neither wind-turbine designs nor standard hydroelectric dam turbines can simply be submerged into an ocean current. Tidal turbines are likely to be placed in more remote locations - for instance, fifteen metres or more underwater and several kilometres offshore – therefore turbine weight, methods of construction and installation, and maintenance/repair strategies become critical considerations. The benefits of better structural designs and improved fabricating techniques also cascade throughout the cost structure of the turbine. A lighter and/or more efficient blade decreases the demands on the hub components and tower structure, decreasing capital and operating expenses for the entire turbine.

As they have in wind turbines, composites are playing a key role in tidal turbine design. The high loading on the blades makes composites an ideal material choice with the increased rigidity preventing bending away from the design condition, minimising hydrodynamic losses. With the reduction in weight of a composite blade, maintenance may become more feasible as the blades are easier to manhandle and replace. Sub-marine structures also have to withstand the notoriously aggressive marine environment with its corrosive salt water, fouling growth and abrasive suspended particles.

The blistering and osmosis that can attack marine composites are a major issue on small boats because they operate at the air/water interface where sunlight can penetrate. Turbines, in contrast, are located well below the surface where there is little sunlight. Nevertheless, keeping blistering at bay for decades might be difficult and a combination of

material quality control and surface protection is required to deal with it. A high quality laminate with low void content and incorporating hydrophobic (water repelling) epoxy resin is a good starting point, while innovative surface finishes that also resist marine growth may also reduce the problem. As mentioned in Chapter 3, cavitation performance of composites is also a concern requiring further investigation.

4.1 Adaptive Composites

An adaptive textile composite is a structure tailored to exhibit desirable elastic deformation behaviour not necessarily proportional to the imposed load. An example of such a structure would be a box beam so tailored that an imposed cantilever load results in twisting as well as bending, although no torsional load was imposed. Reversible behaviour would be exhibited if, in addition, an imposed torsional load results in bending as well as twisting, although no cantilever load was imposed. Such a structure is said to exhibit bend-twist coupling.

In the process of improving HAWT performance, new methods are continually being sought for capturing additional amounts of energy and alleviating loads. Composites offer several advantages over metals such as superior fatigue characteristics, high stiffness to weight ratio, construction of complex geometries, and a potential for aeroelastic tailoring [101]. Composite blade elastic coupling can not only be tightly controlled but varied over the span by appropriate selection of ply angles, thicknesses and spanwise layup. Resulting anisotropy provides direct bending-axial torsion elastic coupling not possible with metallic blades. There are added benefits of such as a dramatic reduction in manufacturing costs when compared to steel. A 60-70% reduction in production costs was seen in the marine propeller industry upon embarkation of research into coupled composite propeller blades, along with smoother power take up, reduced blade vibration, reduced noise, and better fatigue performance [17].

The primary advantage of the use of flexible composites in the production of turbine blades is the ability to tailor the structure to deflect in response to load changes. This allows the shape of the blade to adjust automatically to a changing inflow. This can be exploited to reduce the changes in thrust and cavitation that occur when the inflow changes locally/globally. In the case of a circumferentially varying inflow, changes in velocity cause

changes in thrust which are transmitted to the shaft. The change in loading may also result in blade surface and tip vortex cavitation. It is proposed that a flexible composite turbine blade could be so designed such that the fluctuation in loading causes an alteration in blade shape that reduces the magnitude of the change in thrust and delays the inception of cavitation.

4.1.1 Application to Tidal Turbines

Eisler [102] suggests that for wind turbines, the turbine can never be operated exactly at the target tip speed ratio because of the transient nature of the wind. This is not such a severe problem for tidal turbines as, despite load fluctuations due to boundary layers, waves, free surface proximity etc., tides are inherently predictable and a simplified version of the load on a turbine at a particular site may be calculated from predicted tidal data.

In the wind industry average power is increased by operating at speeds that maintain the efficiency below the rated power and are arbitrarily adjusted to regulate power above rating. Eisler [102] believes that this aggressive, variable pitch, speed control approach represents an upper bound on performance, although it many not be realisable due to the extreme changes in rotor speed required as a function of the wind speed. It is suggested that this aggressive approach may not be improved substantially by adaptive blade structures. As load fluctuations on tidal turbines are less sudden and extreme than those experienced by wind turbines, this may not be the case and further investigation is required into this field.

As presented in Section 2.3.2, the power of a kinetic energy device is proportional to the cube of the current velocity. The vertical, and to some extent lateral variation, of v_f, however, can be large as most devices will have a capture area that is a significant fraction of the local water depth. These variations are important both in predicting performance but also in assessing the likely magnitude of cyclic loads acting on the rotor blades. Representations of the likely variation in current profile vary in complexity. At its simplest for unconfined water a power law for the vertical variation associated with a fully developed turbulent boundary layer profile from a zero slip condition at the seabed and maximum current at the sea surface can be used [52]. If the boundary layer thickness is less than the local water depth then a zone of almost constant flow is assumed up to the sea surface. This will need to be modified if there is significant wind shear and/or wave action. Both of these can have strong influences for those parts of the device operating near to the free surface. Unless the devices

are operating in an area of the ocean with a reasonably constant depth, however, the local velocity profiles will also be strongly influenced by the local bathymetry [52].

The current will also vary as a function of the depth of the flow. The velocity at a height above the seabed, *k*, approximately follows a seventh power law as a function of depth in the lower half of the flow:

$$V_k = \left(\frac{k}{0.32l}\right)^{\frac{1}{7}} v_{mean} \qquad \text{for } 0<k<0.5\text{H} \qquad (4.1)$$

And in the upper half:

$$V_k = 1.07 v_{mean} \qquad \text{for } 0.5\text{H}<k<\text{H} \qquad (4.2)$$

It can be shown from this that approximately 75% of the energy is to be found in the upper 50% of the flow. In practice, areas with high flow velocities will generally be relatively turbulent and flow modelling is not as simple as this and many variations can occur depending on both location as well as on the state of the tide (flow patterns and velocity shear change throughout the tidal cycle) [103].

One of the basic requirements of wind turbine control is to ensure that the rotor does not produce more power than the rest of the system (drive train, generator set etc) can withstand. The simplest approach is passive stall regulation that uses the characteristics of the airfoils to stall in high winds and regulate power production or the rotor with no moving parts. More advanced controllers use changes to rotor configuration to maximise system efficiency while wind speed is fluctuating. Examples are variable speed, variable pitch (full span/tip actuation), ailerons, passive pitch actuators and the like. There is a balance to be struck between the complexity of the system, and the ability of the controller to limit loads and/or deliver more energy.

The composite fabrication technique required to produce such a complex response to loading as adaptive blades exhibit can be either, intrinsically-smart (passive) where the symmetry and balance of the composite filament plies controls the elastic deformation response to loading of the composite structure, or extrinsically-smart (active) where the sequence of actuation of actuators embedded between composite plies controls the elastic deformation response to loading to the composite structure.

4.2 Passively Adaptive Blades

Passive control of a turbine blade can be achieved by integrating advanced composite materials into the blade structure and taking advantage of the directionality of anisotropic composite material. Anisotropic structures show different levels of elastic coupling, depending on the ply angle in the layers that comprise such a material.

Much research has been undertaken in this field in the wind industry. Wind turbines carry loads primarily by twisting and bending, much like tidal turbines. Coupling between bending and twisting can be used to reduce loads and improve fatigue performance. Incremental loads are reduced because when the blade deforms in bending the bend-twist coupling produces a decrease in the blade twist and angle of attack. The level of load reduction depends on the twist distributed along the blade length, which is controlled by the amount of bend-twist coupling. This, in turn, depends on the blade cross sectional geometry, the level of anisotropy in the structural material, and the material distribution [104].

Karaolis et al [11] introduced the concept of using biased layup blade skins to achieve different types of twist coupling for wind turbine applications. By changing the blade skin from an orthotropic to a biased fibre layup the blade can be aerodynamically tailored with minimal disturbance to the beam stiffness properties or manufacturing costs.

Kooijman [105] evaluated building the elastic coupling into the skin of the turbine blade and concluded that the use of such technology would give the potential for an increase in energy yield. For stall controlled rotors, both constant and variable speed, large annual energy gains (~25%) may be made by enhancing the stall regulation whilst increasing rotor diameter. On pitch controlled mechanisms there are smaller gains (1-3%) to be had by optimising the aeroelastic blade design over the operating range. On variable speed, pitch controlled mechanisms, the best opportunity is to replace the pitch mechanism with a passive twist coupling that replaces some of the lost energy production whilst improving reliability and lowering installation cost [14].

Lobitz [106] showed how a substantial improvement in system performance can be realised by enhancing the stall regulation of a constant speed system via adaptive blade twist. The adaptive blade twists elastically in response to loads, creating a change in the angle of attack and thus influencing loads and power production. The approach described assumes the blade twists towards stall in response to loads that are proportional to wind speed or power.

A blade design may employ coupling between bending and/or extension, and twisting so that as it bends and extends due to the action of the aerodynamic and inertial loads, it also twists, modifying the aerodynamic performance in someway. These performance modifications also have associated aeroelastic effects including effects on aeroelastic instability [12].

There are issues related to the use of aeroelastic tailoring as a cost-effective, passive means to shape the power curve and reduce loads. Results show that twist-coupling of wind turbine blades towards stall produces significant decreases in fatigue damage. These damage reductions seem to be relatively independent of the material exponent, b_m [107]. The parameter b_m is often used to define the fatigue behaviour of a material that follows the trend $N \propto S^{-b_m}$, where S is the stress amplitude and N is the number of cycles to failure. Concurrent with lower fatigue damage estimates for positive twist-coupling, maximum loads decreased modestly and average power increased due to elevations in the power curve in the stall region.

Other considerations include the fact that the performance of the turbine is also critically dependent on the accuracy and reliability of the manufacturing techniques for layered composites [20]. Flexible blades introduce additional complexity into the turbine design, including load dependent blade deformations, complex material failure modes, potential blade vibrations, and fatigue problems associated with increased flexibility; all of which must be properly accounted for by using fluid-structure interaction methods. It is, however, hypothesised that the advantages of coupled blade designs outweigh the possible problems and thus this area is of considerable interest in the field of renewable energy at this time.

A blade of unbalanced composite laminates under axial or bending moments experiences a torsional deformation known as induced twist. The magnitude and direction of the hydrodynamic force applied on the blade, and consequently the blade and turbine performance, strongly depends on the angle of attack of the blade. Angle of attack depends upon the inflow angle and twist angle of the blade. Blade twist angle may be expressed as a combination of three elements: pretwist, pitch angle and induced twist due to elastic coupling [108]. In turbines with adaptive blades, the induced twist due to elastic coupling is a variable parameter which depends on the turbine running condition as well as material and structural

characteristics of the blade. An adaptive blade has a dynamic topology that varies with the flow speed and rotor angular velocity.

Using a relatively simple bend-twist coupled blade could enable the turbine to deal with the severe complex loads induced upon it whilst also maintaining a more consistent power output of the turbine, thus reducing the cost of the generator but maximising the energy capture of the device. It may also negate the need for a variable pitch blade therefore improving maintenance feasibility and costs. Furthermore it decreases the chance of overpowering the generator or gearbox, or rather enables a more predictable peak level of power to be reached thus reducing the need for an overrated, and much more costly, generator. By delaying the onset of stall and making the turbine more efficient over a greater range of tip speed ratios, the turbine can capture more energy from an increased range of flow velocities therefore bringing the turbine efficiency closer to the Betz limit.

4.2.1 Composite Layup

For conventional laminated composites constructed of orthotropic layers, the level of anisotropy is determined by the fibre orientation with respect to the primary loading direction. Fibres orientated at an angle, θ, can be used to produce either bend-twist coupling or extension-twist coupling. Kooijman [105] found that the mirror layup, Figure 4-1a), is required for bend-twist coupling, and the helical layup, Figure 4-1b), is required for extension-twist coupling to be exhibited.

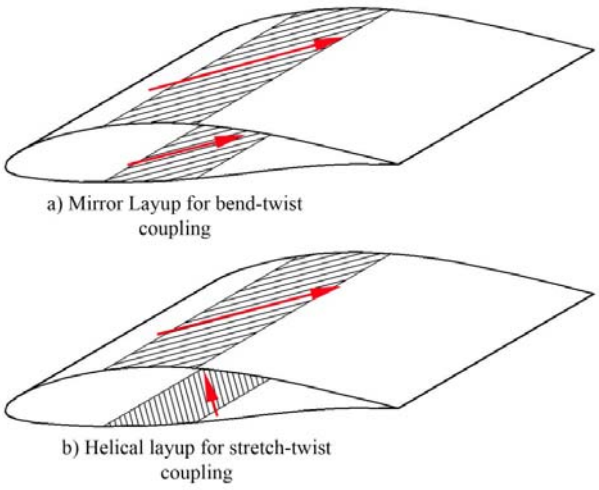

Figure 4-1: Layup for a) bend-twist coupling and b) extension-twist coupling

In the case of coupled spars, it is considered beneficial to use braided planforms rather than a more conventional lamination method. A key advantage in using braided planforms is the relative ease of manufacturing compared to conventional laminated composites. Moreover, the structural box is continuous, and fatigue/damage tolerance performance is better than conventional laminated composites [104]. The use of a single braided preform would produce the helical layup (Figure 4-2a)). If, however, a single preform is cut and used in two halves to create a double box beam, the mirror layup can be achieved (Figure 4-2b)). This is thought to be significantly more robust than the patch layup technique for creating bend-twist coupling, which has joint strain incompatibilities and is prone to delamination when exposed to cyclic loads (Figure 4-2c)) [109].

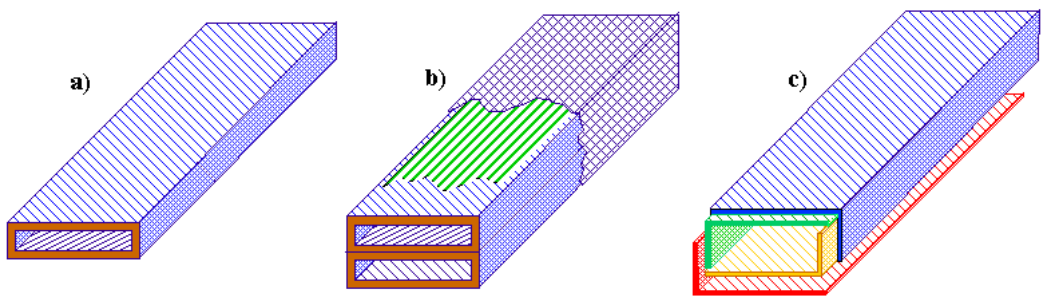

Figure 4-2: a)Single box layup, b) double box layup and c) patch layup

According to Ong et al [110] a range of braid angles between 15° and 30° is the most favourable for bend-twist coupling, with the maximum coupling observed at a braid angle of 20°. The leading and trailing edges are near the flapwise elastic axis so curtailing the biased fibres in the region should have minimal effect on the coupling achieved. This could be particularly important as research in the wind industry has indicated that there is some difficulty in achieving good bend-twist coupling while maintaining blade stiffness and strength [111].

4.3 Preliminary Blade Analysis

A basic section analysis for a tidal turbine blade section forced to exhibit deflection in the latter third of the foil has been carried out in XFOIL and preliminary results suggest that

even a simple, coupled turbine blade could increase energy capture and operate more efficiently. Figure 4-3 and Figure 4-4 illustrate the pressure distributions over the surfaces of a foil with a deflecting tail section at an angle of attack of 0^o and 6^o respectively.

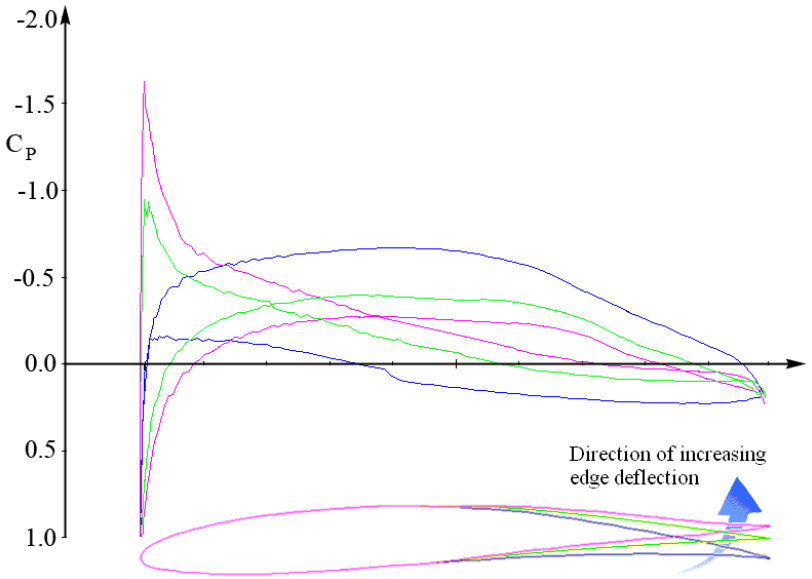

Figure 4-3: C_p distribution over a deflecting section at an angle of attack of 0^o

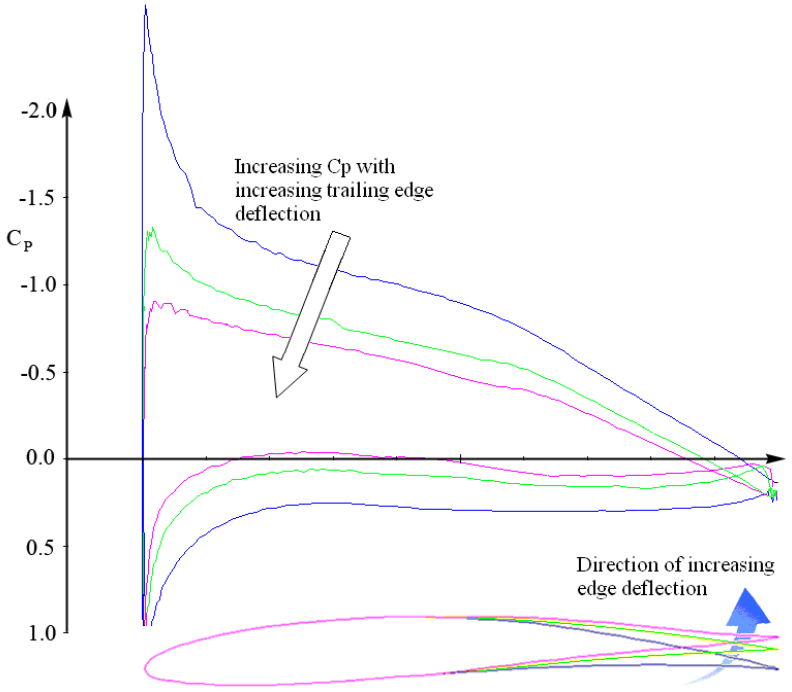

Figure 4-4: C_p distribution over a deflecting section at an angle of attack of 6^o

It is clear that operation at the lower angle of attack, α, with the section in its undeformed state (blue lines), is the most efficient with a maximum negative pressure coefficient of -0.65. The deflected tail foils at this α exhibit large negative pressure on the underside of the foil – it is the underside pressure streamline that is creating the negative pressure peak – thus suggesting that they are not effective and efficient at this α. At the increased α, the most deflected section is clearly the more efficient of the three (pink line) with a minimum negative pressure coefficient. This demonstrates that without changing the pitch of the blade, and hence having a simple fixed pitch bend-twist coupled blade, energy capture could be increased and minimum pressure on the blade decreased thus improving performance and minimising cavitation.

Under normal circumstances, the blade geometry is fixed for blade element momentum calculations; in this case, however, as a surrogate for a passive deflection based on loading the blade, twist is prescribed as various functions of tidal velocity and spanwise location on the blade. The aim is to simulate blade motion that may be achieved with an adaptive blade without requiring a full composite blade design process and associated computation of the coupled fluid-structural response of the device to the hydrodynamic loads. It is important to realise that the blade twist prescription as a function of tidal velocity is, at this stage, based on initial judgment as to what may be possible with a composite structure. The expectation was that there would be an increase in annual energy extraction, similar to that found with a variable pitch blade, and a decrease in the fatigue loads experienced by the turbine blade. The modification to the structure should not significantly increase blade cost but would remove the need for a complex and expensive pitch varying mechanism. This preliminary analysis is to establish a proof of concept.

Two configurations were analysed for twist as a function of blade position - constant with span and linear with span. A blade exhibiting constant twist with span effectively models a blade with a variable pitch device (e.g. fixed angle rotation about the blade axis) the blade with the linear twist variation along the span, where the twist at each individual section is altered independently, models the passively adaptive blade. Two different twisting distributions were imposed on both of these twist configurations – the first involved a linear variation with tidal velocity and the second a square root variation with tidal velocity. These are exhibited in Table 4-1.

Table 4-1: Blade configurations and twist distributions

Blade Configuration	*Twist Distribution*	*Plot of twist vs v_f*
Variable Pitch 1 (VP1)	v_f	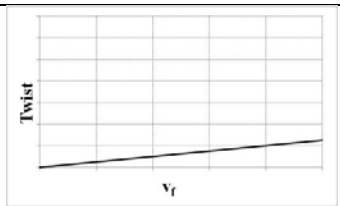
Variable Pitch 2 (VP2)	$2v_f^{1/2}$	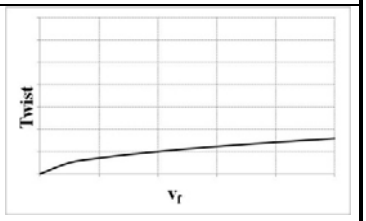
Adaptive Blade 1 (AB1)	Sv_f	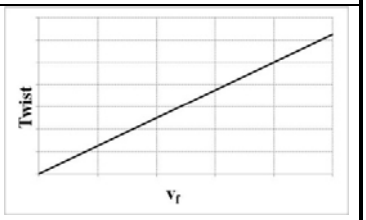
Adaptive Blade 2 (AB2)	$2Sv_f^{1/2}$	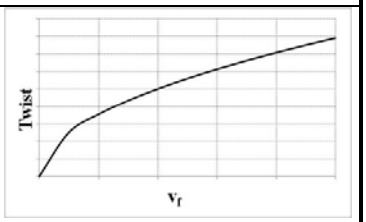

The turbine under analysis was a three bladed, horizontal axis, free stream device with a diameter of 20m, a hub/diameter ratio of 0.2 and was analysed for a maximum free stream tidal velocity of 2.5m/s. Initially a reference power curve was established for the rigid "base" rotor, illustrated in Figure 4-5.

The power data attained was then analysed in MATLAB to obtain an annual energy estimate for the device as detailed in Appendix A. The twist distributions were applied to the two twist configurations and a similar process repeated for each.

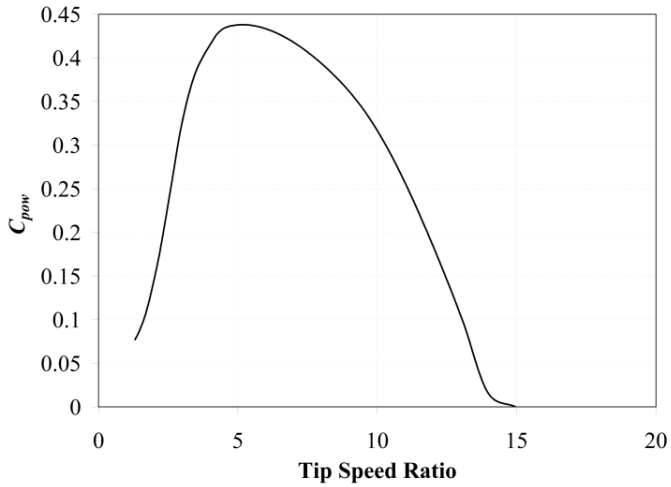

Figure 4-5: C_{pow} as a function of tip speed ratio for the fixed blade constant RPM device - the base reference power curve

Figure 4-6 shows the change in C_{pow} with λ attained for the different twist distributions and configurations. It can be observed that all of the twist distributions cause the C_{pow}-λ curve to broaden, and higher values of C_{pow} are maintained at the lower flow velocities, corresponding to higher λ. At higher flow velocities, lower λ, the C_{pow} distribution is relatively unaltered implying that the blades which have had a twist distribution imposed upon them are more efficient. Both configurations also show an increase in the maximum C_{pow} from that of the base fixed turbine. Between the two twist configurations a slight variation is observed, with the passively adaptive blades showing a marginally lower and less extensive C_{pow}, hence poorer performance than the variable pitch blades.

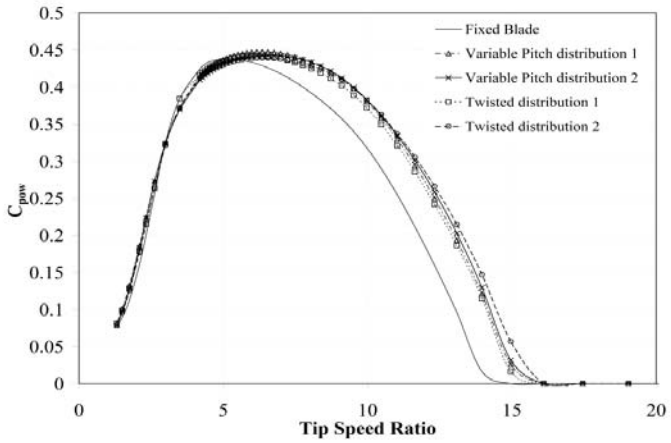

Figure 4-6: C_{pow} as a function of tip speed ratio for the various twist distributions and configurations overlaid on the reference power curve

The thrust force on the rotor is directly applied to the blades and hub, but also the support structure of the device, and thus considerably influences the design. Figure 4-7 illustrates the change in thrust coefficient, C_T, as a function of tip speed ratio over the various twist distributions and configurations.

$$C_T = \frac{8T}{\rho \pi v^2 D^2} \tag{4.3}$$

It may be observed that at moderate to high values of λ, equating to flow velocities under 3m/s, values of C_T tend to lessen indicating less thrust produced by the turbine. The twist configuration with the optimum thrust profile is that of the variable pitch blade with the second twist distribution imposed on it.

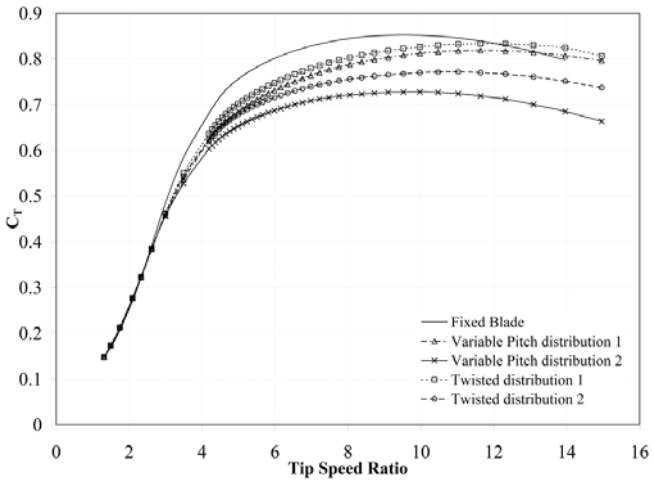

Figure 4-7: Thrust coefficient as a function of tip speed ratio for the various twist distributions and configurations

Table 4-2 shows the percentage increase of both C_{pow} and annual energy capture and percentage decrease of C_T from the base fixed blade configuration. Each blade configuration has increased the annual energy capture and decreased the unfavourable thrust loading. Little is evident between the increase in C_{pow} and both the increase in annual energy capture and decrease in C_T indicating that it is not the maximum value of C_{pow} that is significant, rather the longevity of a higher C_{pow}, illustrated by a broader C_{pow}-λ curve. The variable pitch blade and linear twist variation with tidal velocity shows the greatest improvement in annual energy

capture, increasing the value of the base turbine by over 2.5%. This equates to an extra 60.5 MWh per year and a £4840 increase in energy sales (taking the price of energy to be 8 p/kWh [71]).

Table 4-2: Percentage change of C_{POW}, annual energy capture, and C_T from the baseload configuration

Blade Configuration	C_{pow}	Annual Energy Capture	C_T
	%	%	%
Fixed	0	0	0
VP distribution 1	2.20	2.65	-3.93
VP distribution 2	1.17	1.56	-14.62
Twisted distribution 1	0.90	1.80	-2.19
Twisted distribution 2	0.29	1.35	-9.45

It is important to consider that all of the financial cost projections of HATT developments are necessarily speculative, as a utility-scale commercial tidal farm is yet to be implemented. The same blade, however, also has one of the lesser decreases in C_T which, when coupled with the design and maintenance cost and feasibility of a variable pitch blade device, is not as desirable as a smaller increase in annual energy capture with a large decrease in loading. The greatest decrease in C_T was experienced by the second variable pitch blade, which reduced C_T by over 14.5%. This design, however, had one of the lower annual energy capture increases and, again, utilizes the expensive and complex variable pitch mechanism. It is clear that a compromise between an increase in annual energy capture and a decrease in loading on the device needs to be reached in order to produce an effective design.

Although a series of simplifying assumptions are inherent in these calculations, not least that the basis blade is evidently not optimal for the applied tidal current regime, the performance of the passively twisted blades shows only a small decrease in energy capture, when compared to that of the best performing blade, which it could be expected would be compensated for by the removal of the variable pitch mechanism.

4.3.1 Surface Panel Code Analysis

In this section the performance of the alternative turbine blades was analysed by observing the variation of the minimum surface pressure coefficient at each blade span as a measure of likely cavitation inception.

The surface panel code Palisupan [83] was used to model the performance of different blade twist arrangements at a single tip speed ratio close to maximum (λ=5, v_f=2.1 m/s). In these calculations a frozen wake model was used with in excess of 2800 panels distributed over the blade and the hub. The advantage of a surface panel analysis is that a detailed knowledge of the actual blade surface loading is generated. Checks are required, however, as the onset of local stall is not captured by a potential flow analysis. A validation study for the use of Palisupan to estimate the loads present on a HATT is detailed in Appendix B.

Figure 4-8 shows the pressure coefficient, C_P, as a function of turbine radius for the various twist distributions and configurations. All of the turbines are 20m in diameter and assumed to be operating in water of at least 40m depth such that the both the surface and seabed boundary have limited effect. At this flow velocity, the cavitation number is approximately 2; indicating that cavitation inception will occur on areas of the blade where the pressure coefficient is less than -2. Both of the fixed blades exhibit a maximum negative C_P of less than -2, and thus these blades will cavitate at this flow velocity. Imposing a twist configuration on the blade causes the C_P over the outer two thirds of the blade to decrease significantly.

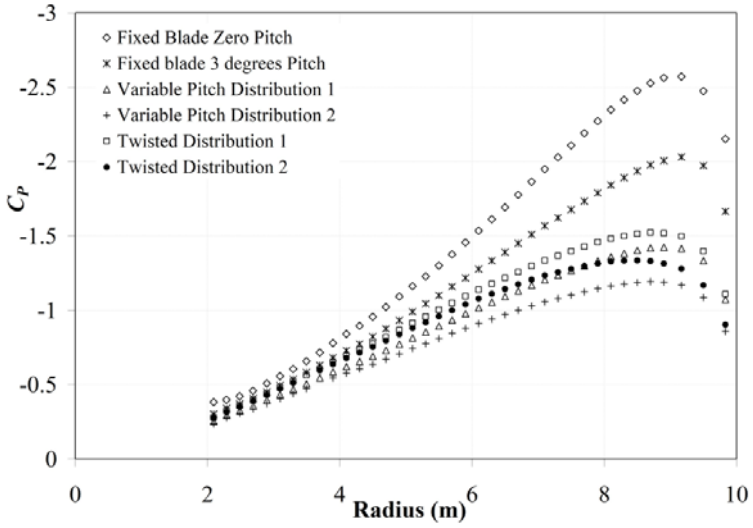

Figure 4-8: C_p as a function of turbine radius for the various twist distributions and configurations

Table 4-3 provides the maximum negative C_P for each of the twist distributions and configurations. In this case the most favourable blade configuration is that of the variable pitch blade with the second pitch distribution imposed on it as this produces the least negative value for maximum C_P and most even spanwise pressure distribution. All of the blades that have been altered from the base design, however, perform well in this aspect and the likelihood of cavitation occurring has been significantly reduced.

Table 4-3: Maximum negative C_P for the various blade twist configurations

Blade Configuration	Maximum Negative C_P
Fixed Blade, no pitch	-2.57
Fixed Blade, 3^o pitch	-2.03
Variable Pitch Distribution 1	-1.42
Variable Pitch Distribution 2	-1.19
Twisted Distribution 1	-1.52
Twisted Distribution 2	-1.33

It has been shown that the combination of a fixed pitch and passively twisting blade is likely to increase the profitability of a free stream tidal turbine in comparison with a rigid fixed pitch or variable pitch mechanism turbine. Increases in annual energy capture of over 2.5% and a reduction in thrust coefficient of greater than 14.5% were observed when compared to the original design for the different twist distributions and configurations. A twisting blade is felt to be the most optimum solution when a compromise between annual energy capture and negative loadings on the turbine is required.

4.4 Coupled Blade Performance Prediction

A computationally efficient, yet realistic, model has been developed in order to estimate the amount of induced twist present on a bend-twist coupled blade in a tidal stream. This model takes into account the effect on the induced twist of fibre orientation, blade loading and cross section, material mechanical properties, and shell thickness – and as such is more detailed than the preliminary analysis, 4.3. The method has been incorporated into a Blade Element Momentum code, and modified to predict the performance of free stream tidal devices; such that the performance of a HATT with composite bend-twist coupled blades could be estimated in greater depth.

The previous preliminary analysis (Section 4.3) showed that, when compared to a free stream tidal turbine with fixed blades of a similar configuration, a HATT that utilises composite bend-twist couple blades can reduce fatigue loading, bring the turbine efficiency closer to the Betz limit and increase the annual energy capture.

4.4.1 BEMT Code

The basis BEMT code used in this analysis was Cwind [79] as discussed in Section 3.1.2. During the course of the research the BEMT code has been modified in several different ways in order to achieve more optimal performance analysis of tidal energy extraction devices. Modifications include optimisation parameters which can be useful at the initial design stage of a tidal turbine in that a few optimal designs may be achieved in a short period of time giving the engineer a sound base-point from which to further optimise the device. Previous variations of the code are detailed in Table 4-4.

Table 4-4: BEMT code variations

Code variation	***Description***	***Output***
1	Determines the power curve for a user specified shape	Summary and detailed performance for each *TSR*
2	Finds the best *Pitch* for a specified shape. User specifies *AFac*, *PFac*, *TFac*	As above but specifies best pitch for each *TSR*
3	Global Search – uses baseline shape and aerodynamic performance and applies variations	For each design finds *TSR* for which C_{pow} is maximum
4	Local Search – uses defined starting point (*AFac*, *Pfac*,*TFac*, *Pitch*) and searches using user define increment	For each design find *TSR* for which C_{pow} is maximum
5	Detailed performance, users specifies operating point *TSR* as well as the geometry	Gives much more detail as to performance of numerical convergence for each section.
7	Global Search for Fixed RPM	Lists C_{pow} and parameters
8	Local Search for Fixed RPM	List C_{pow} and parameters
9	Sensitivity of overall performance to section performance (C_l,C_d vs α) for a fixed geometry	Outputs a list of C_{pow} vs *TSR* and extrapolates a maximum *TSR* for which $C_{pow} = 0$

For the evaluation of the performance of a turbine with bend-twist coupled blades, the main body of the code is run as a program based in Fortran 77; with a separate piece of code written in MATLAB which incorporates the algorithm to determine the induced twist, and hence the overall final twist, of the blade. The MATLAB code calls the main BEMT program at various points in order to gain data required to complete calculations. There is then a separate algorithm based in MATLAB which calculates the annual energy capture of each tidal device under examination.

4.4.2 The Induced Twist Model

As previously discussed a blade of unbalanced composite laminates under axial or bending moments experiences a torsional deformation known as induced twist. The magnitude and direction of the hydrodynamic force applied to the blade, and consequently the blade and turbine performance, strongly depends on the angle of attack of the blade. Angle of attack depends upon the inflow angle and twist angle of the blade. Blade twist angle may be expressed as a combination of three elements: pretwist, pitch angle and induced twist due to elastic coupling [108].

The induced twist due to elastic coupling of a tidal turbine blade changes the effective angle of attack of the flow, Equation (4.4). This therefore affects the hydrodynamic characteristics of the turbine blade and hence the performance of the device as a whole.

$$\alpha = \varphi + \beta - \beta_0 - \gamma \tag{4.4}$$

Where α is the angle of attack, φ is the inflow angle, β is the induced twist, β_o is the blade pre-twist and γ is the pitch angle of the blade – all in degrees.

The algorithm used in this study is one that has been developed for the performance prediction of wind turbines [112]. The design algorithm is based on analysis rather than synthesis and requires the use of a performance prediction program for the tidal turbine. With any device that uses adaptive blades – specifically bend-twist coupled blades – the induced twist is the parameter that affects the device performance. The induced twist depends both on the hydrodynamic loading experienced by the turbine blade and the structural and material properties of the blade. Therefore it is apparent that some form of structural analysis must be undertaken in order to predict the induced twist with any degree of accuracy.

The model estimates the induced twist principally as a function of the blade topology and the turbine run condition. Induced twist, $\beta(r)$, can be expressed as:

$$\beta(r) = \beta^*(r)\beta_T \tag{4.5}$$

Where $\beta^*(r)$ is the normalised induced twist and β_T is the maximum value of induced twist at the blade tip. It is assumed that the material of the blade is uniform, such that the mechanical properties of the blade, fibre orientation and shell thickness do not vary in the spanwise direction. Maheri et al [112] have shown that the effect of fibre orientation on the normalised induced twist is minimal and therefore it is not considered in the algorithm.

Considering the blade as a box beam with bend-twist coupling, then β^* can be derived as:

$$\beta^* = \frac{\int_0^{y^*} (1-y^*)\,dy^*}{\int_0^1 (1-y^*)\,dy^*} = (2-y^*)\,y^* \tag{4.6}$$

Where y^* is the normalised radius of the turbine and is defined by Equation (4.7).

$$y^* = \frac{r - R_{hub}}{R - R_{hub}} \tag{4.7}$$

Where R is the radius of the turbine, r is the instantaneous radius under analysis and R_{hub} is the hub radius, all in metres.

It should be noted that Equation (4.6) estimates β^* without any information regarding blade material except the fact that the material properties are constant spanwise along the blade. In a bend-twist coupled beam, the bending moment is mostly due to lateral loading and partly due to the torsional loading of the beam acting through the coupling effect. Each blade only experiences a small pitching moment when compared to the lateral loading, and therefore the induced bending moment due to the elastic coupling can be neglected, thus enabling the flapwise bending moment to be considered independent of the material properties.

As such β_T can be split into two parts; one part relating to the hydrodynamics of the blade – the moment about the hub, M_{hub}, and one part relating to the material properties (shell thickness, fibre orientation, and mechanical properties) of the blade, f.

$$\beta_T = fM_{hub} \tag{4.8}$$

M_{hub} is calculated directly for various tidal stream velocities and turbine radii using the BEMT program. β_T needs to be estimated at a reference point in order for further calculation to be undertaken. This reference point can be taken as the design flow velocity, V_d. The reference induced twist at the blade tip at this flow velocity is an independent variable – or rather a design variable – and as such must be chosen to suit the turbine. Using M_{hub} at V_d and the chosen induced tip twist the material factor, f, can be calculated. This material factor does not vary with the tidal current velocity and therefore can be used to calculate β_T at other flow velocities. More detailed methodology for the induced twist model is covered by Maheri et al [112].

4.4.3 MATLAB Algorithm

The MATLAB code runs the modified version of Cwind remotely in order to determine the necessary turbine performance parameters. Initially the normalised induced twist and the material factor at the design flow velocity are calculated and then these values are used to determine the induced twist at other flow velocities. The pre-twist of the turbine blade will be modified in order to cancel the effect of the induced twist at V_d, such that the ordinary blade and the adaptive blade are identical in exterior geometry at this flow velocity.

The program obtains initial data assisting the designer in the most optimum choice for the initial induced twist angle at the tip. Once this is settled, the material factor, f, is calculated and the performance of the turbine assessed over a range of tidal flow velocities at a constant RPM. The outputs of the code include turbine performance data such as mechanical power, thrust loading, torque and blade twist data.

The algorithm is run as illustrated in Figure 4-9. Once the results of the BEM simulation are complete the predicted performance can be used to obtain an estimate of the annual energy capture of the device.

The expected annual energy capture was calculated in a manner similar to that detailed in Appendix A. K_0 and K_1 were determined, the frequency of occurrence of each flow velocity, and the power generated at each flow velocity, determined and annual energy capture calculated.

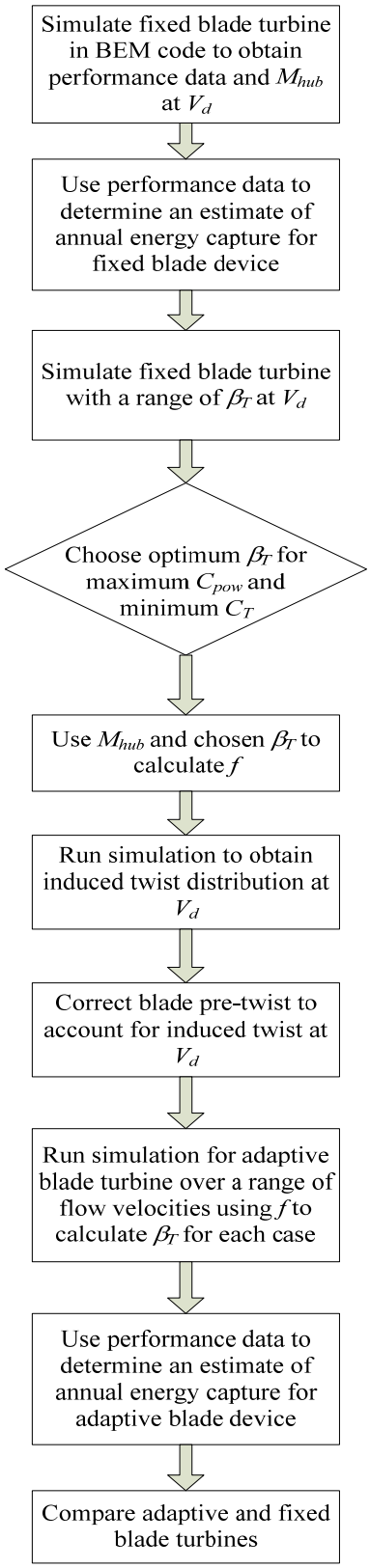

Figure 4-9: Flow chart of the bend-twist calculation procedure

4.4.4 Results

The principle particulars for the free stream, horizontal axis turbine under analysis are shown in Table 4-5.

Table 4-5: Turbine principle particulars

Rotor radius	20 m
Hub radius	2 m
Number of blades	3
Pitch angle	4^o
Rated power	1.3 MW
RPM	14 rpm
Design flow velocity	2.5 m/s

The power curve for the fixed blade, base rotor is the same as that illustrated in Figure 4-5. Thus M_{hub} at the design flow velocity was calculated and β^* could be found. The next stage was to choose an initial value for the tip twist at the design flow velocity. The BEM code and associated algorithm was run for a series of β_T and a power and thrust curve, this time plotted against initial induced tip twist, was developed and is shown as Figure 4-10.

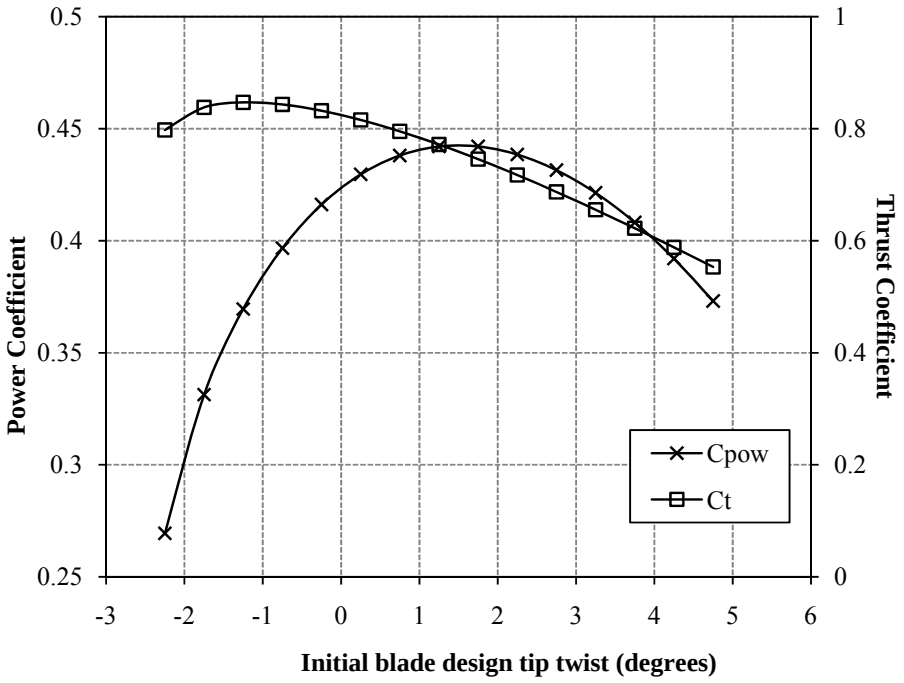

Figure 4-10: Power and thrust coefficient plotted as a function of initial blade tip twist

In order to achieve the optimum performance from the turbine, a high value of C_{pow} and a low value of C_T are required coupled with a broad C_{pow}-λ curve. C_T tends to decrease as β_T increases, whilst C_{pow} is maximum for $\beta_T = 1.5^o$. The value of $\beta_T = 1.5^o$ was considered to be optimum for this turbine as C_T was approximately half of the maximum value and C_{pow} was maximum with a value of 0.446. For this value of β_T the material factor, f, was calculated to be 0.000462.

Using this value of f, the twist distribution of the turbine was adjusted such that the device maintained the optimal shape at the design flow velocity. The performance of the turbine with bend-twist coupled blades, but no other alterations, was then calculated.

It is interesting to observe the relationship between overall blade tip twist and TSR. This is illustrated in Figure 4-11. With increasing flow velocity, decreasing TSR, the twist at the tip of the blade increases more rapidly with the blade twisting towards stall. Overall, the blade tip twist decreases inversely with increase in TSR.

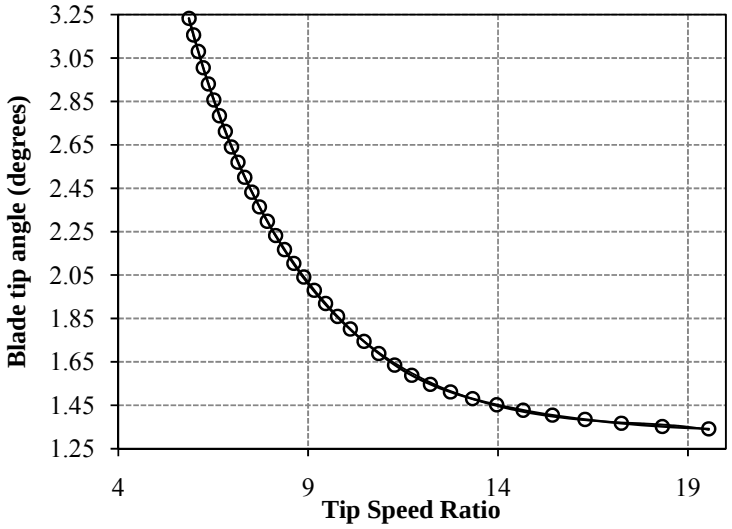

Figure 4-11: The relationship between overall blade tip twist and TSR

Figure 4-12 compares the power curves for the fixed and adaptive blade turbines over the operating range of TSR, and hence flow velocities.

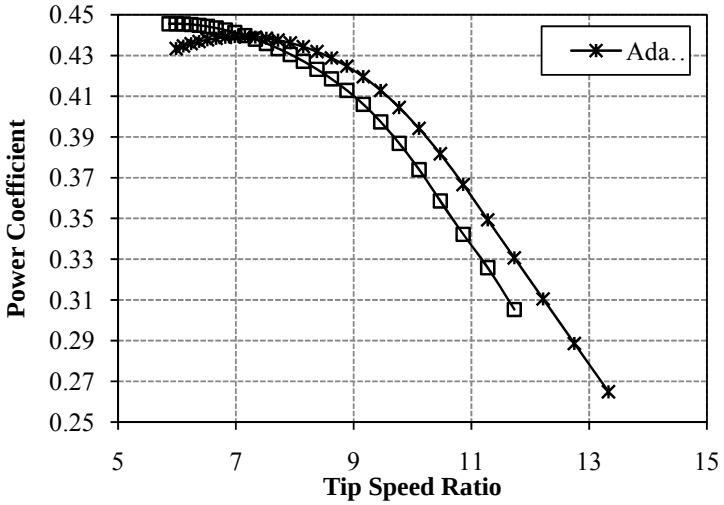

Figure 4-12: Comparison of the fixed blade turbine and adaptive blade turbine power curves

It can be observed that whilst the fixed blade has a higher maximum value of C_{pow} the adaptive blade exhibits increased values of C_{pow} over the range of TSR from 7.5 – 13.3. Since the peak flow velocity in a tidal stream occurs infrequently, it is likely that the turbine with better performance over the lower flow velocities (higher TSR) will exhibit improved annual energy capture.

The thrust force on the rotor is directly applied to the blades and hub, but also the support structure of the device, and thus considerably influences the design. Figure 4-13 illustrates the change in thrust coefficient, C_T, as a function of tip speed ratio for the fixed blade and adaptive blade turbines.

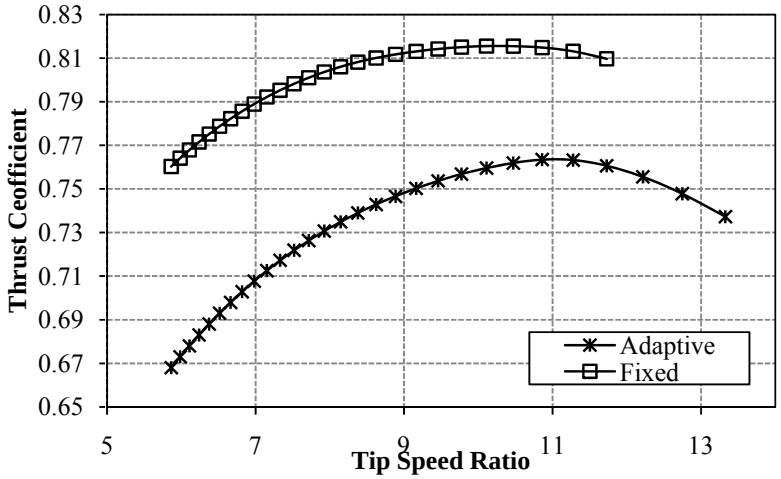

Figure 4-13: Comparison of the fixed blade turbine and adaptive blade turbine thrust curves

It can be seen that the use of adaptive blades significantly reduces the thrust coefficient over the full range of TSR, thus reducing the harmful loads on the turbine structure. This has positive connotations for the design and maintenance of the device, in that the amount of material used and the level of maintenance required may both be reduced, thereby reducing the overall cost of the HATT.

The performance data was then used in the annual energy capture program and the energy capture of both the fixed blade and adaptive blade turbine was calculated over the period of one year. The adaptive blades improved the energy capture of the device by 2.5% over that of the fixed bladed device. It is thought that this is due to the more optimal performance over the higher TSR (lower tidal flow velocities) which occur more frequently over both the spring and neap tidal cycles. This increase in energy capture, coupled with the reduction in thrust force on the device, makes the concept of adaptive blades an attractive proposition for future turbine designs.

4.5 Finite Element Analysis

With both the preliminary analysis and more in depth performance prediction of a HATT with passively adaptive bend-twist coupled blades producing positive results, a proof of concept has been achieved. The purpose of this section of work is to continue the development of a tool to be used as part of the design process of an adaptive composite HATT blade. This section discusses the numerical analysis of a bend-twist coupled double box beam using Finite Element Analysis (FEA). Such a beam is intended for use as the central spar of the blade of a HATT. Carbon fibre reinforcements were chosen as they were found to produce a higher level of bend-twist coupling when compared to glass fibre reinforcements [12, 111]. Experimental testing of a carbon double box beam is then considered (Section 4.6) and comparisons made with regards to the accuracy of the numerical model (Section 4.7). If the numerical and experimental results show good correlation then the numerical method can be used as a design tool to form beams with more complex taper and twist arrangements and applied load distributions.

A 1.25m bend-twist coupled double box beam was modelled in ANSYS 12.1 [113] using SE84LV HEC 300/400 UD carbon prepreg, the mechanical properties of which are shown in Table 4-6. This length of beam was chosen as it was the maximum that could be processed in the autoclave at the University of Southampton. The SE84LV resin system was chosen as it is a toughened system, and offers good mechanical properties on a variety of reinforcing fabrics and fibres. It has a high compressive strength and is widely used in large heavily loaded components, such as yacht hulls, and spars. It has been selected for use by various America's Cup syndicates and boats racing in the Volvo Ocean Race and is, as such, suitable for a range of marine structures [114].

Table 4-6: Mechanical properties of SE84LV HEC 300/400

Property	Value
Fibre weight	300 g/m^2
Cured ply thickness	0.281 mm
E_X	129.2 GPa
E_Y	8.76 GPa
E_z	8.76 GPa
ν_{XY}	0.335
ν_{YZ}	0.0172
ν_{XZ}	0.0172
G_{XY}	5.76 GPa
G_{YZ}	5.76 GPa
G_{XZ}	5.76 GPa

A rectangular beam with a conventional cross section and without any taper in any dimension was used as it is more straightforward to construct such a beam. Each individual box beam was effectively laid up, and then the two placed together before the final outer wrap was laid over the assembly. As such the resulting beam has the mirror layup necessary for bend-twist coupling, Figure 4-2b). Each box had the lay-up $[45,20_4]$, and the outer roving $[60_2]$. The plies that are responsible for the majority of the bend-twist coupling are those at 20^o, this was found to be the fibre angle that produced the maximum level of coupling [12]. Figure 4-14 illustrates the layup of the beam, and indicates the different layers.

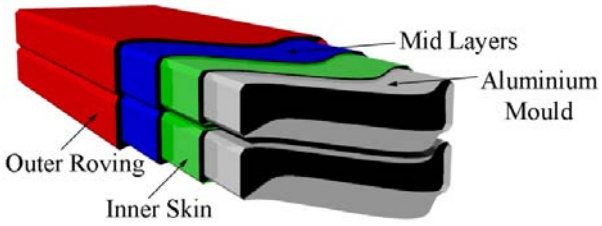

Figure 4-14: Layup of the double box beam

The models were meshed using the SHELL 281 8 node finite strain shell element and solved using a large displacement static non-linear analysis. The SHELL 281 element is suitable for analyzing thin to moderately-thick shell structures. It is well-suited for linear, large rotation, and/or large strain nonlinear applications. It is suited to layered applications for modelling laminated composite shells or sandwich construction. The accuracy in modelling composite shells is governed by the first order shear deformation theory. Each layer of the laminate is defined by the material properties and thickness – they were modelled from the inner skin out to the outer roving. Each model consisted of 11340 quadrilateral elements. This was a very fine mesh and was such that discretisation issues were not significant. One end of the beam was fixed in all degrees of freedom and a static load applied to the free end. Figure 4-15 shows the meshed and loaded beam.

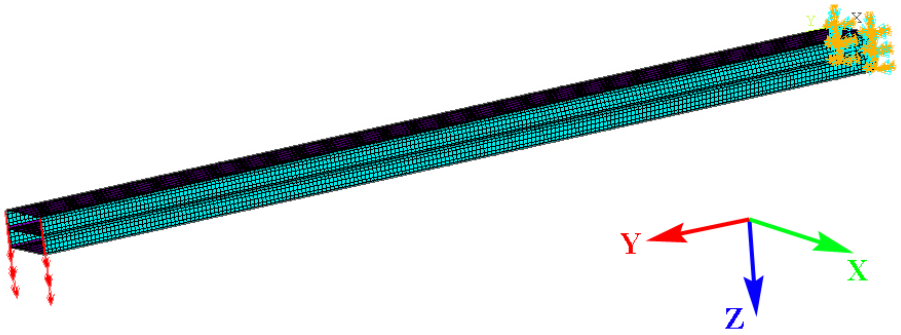

Figure 4-15: The meshed and loaded beam in ANSYS 12.1

The displacements in the global coordinate system of several key points along the beam were analysed and the bend and twist occurring over both the top and bottom surfaces of the beam were calculated.

The nodal deflection in three degrees of freedom due to a 308.3 N load is illustrated in Figure 4-16. It is clear that there is greater deflection towards the tip of the beam as was expected. While the level of induced twist in the beam is small it is still possible to determine visually that twist has indeed occurred by observing the diagonal interfaces between the coloured regions of displacement. These indicate one side of the beam has deflected to a greater degree than the other, thus illustrating the induced twist.

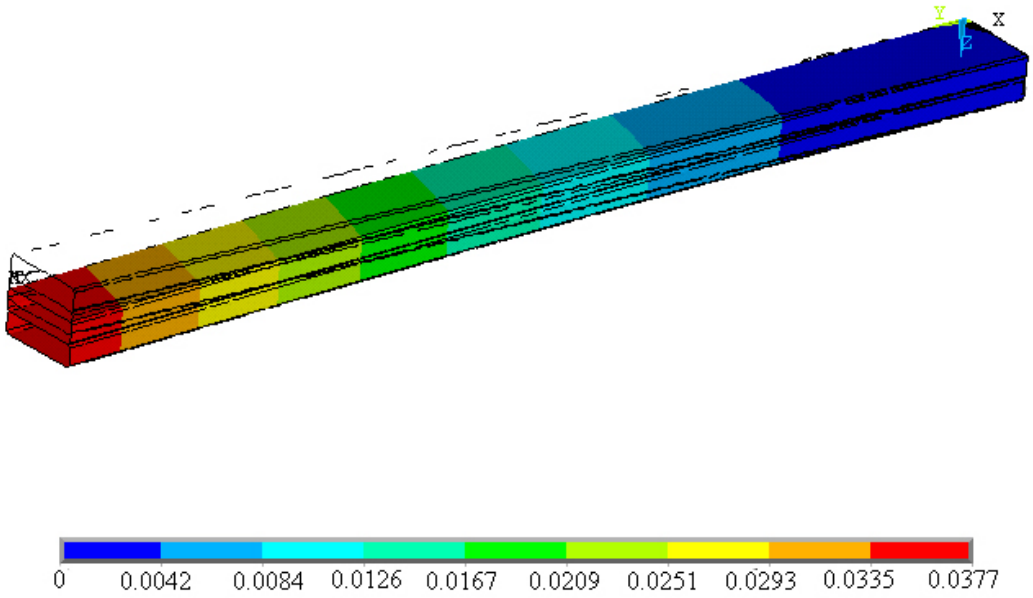

Figure 4-16: Nodal deflection in three degrees of freedom due to a 308.3N load

The amount the beam bent and twisted for each weight applied to the end of the beam was calculated by applying trigonometry to the initial and displaced positions of nodes located at predefined sections along the beam. Figure 4-17 illustrates the relationship between bend and twist, and tip load. It can be seen that the relationship between both bend and tip load, and induced twist and tip load is linear. This is to be expected in a numerical analysis where fibre inconsistencies and individual fibre failures are not considered. The data exhibited in this graph were not tip displacements, rather those measured at a distance along the beam equivalent to Station 2 (1069mm from the beam root) in the experimental procedure.

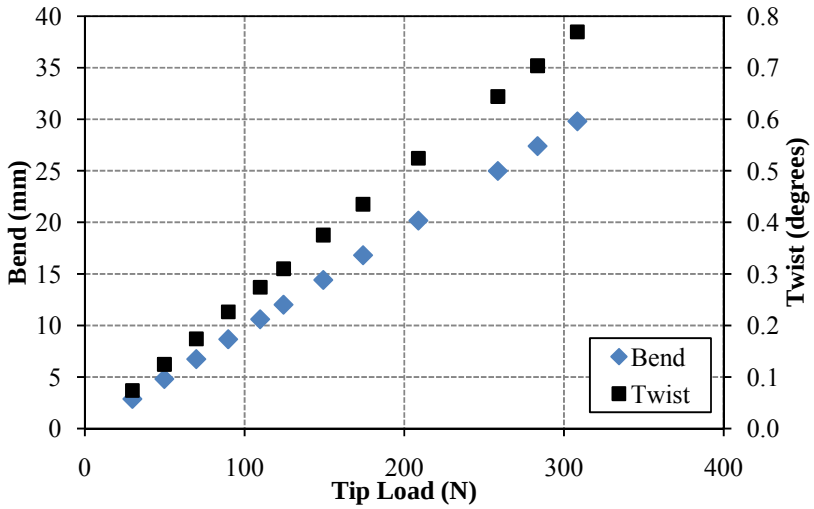

Figure 4-17: Theoretical relationship between bend and induced twist and applied tip load.

Figure 4-18 shows the variation of bend along the length of the beam for each tip load. Basic beam theory states that a beam with a standard orthotropic layup bends following a cubic relationship with regards to length [115]. It can be seen that the relationship between bend and beam length is non-linear for the bend-twist coupled beam and follows a square law, indicating the biased layup has altered the beam response. Increasing tip load increases the bend in the beam and makes this relationship more pronounced. The maximum bend occurs under a tip load of 308.3N (31.431kg) and has a value of 37.61mm.

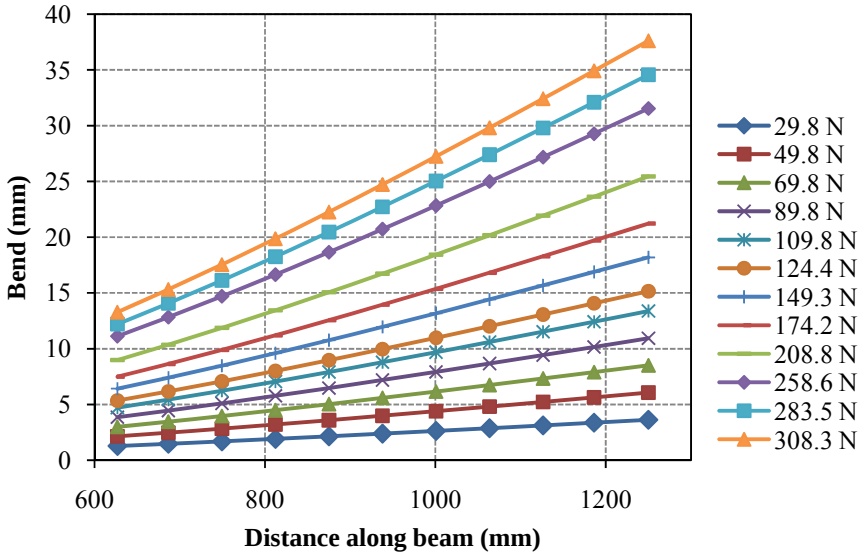

Figure 4-18: Relationship between bend and beam length for each tip load.

The relationship between induced twist and beam length can be observed in Figure 4-19. It is apparent that as tip load is increased, so the induced twist increases. It can be observed that the relationship is non-linear.

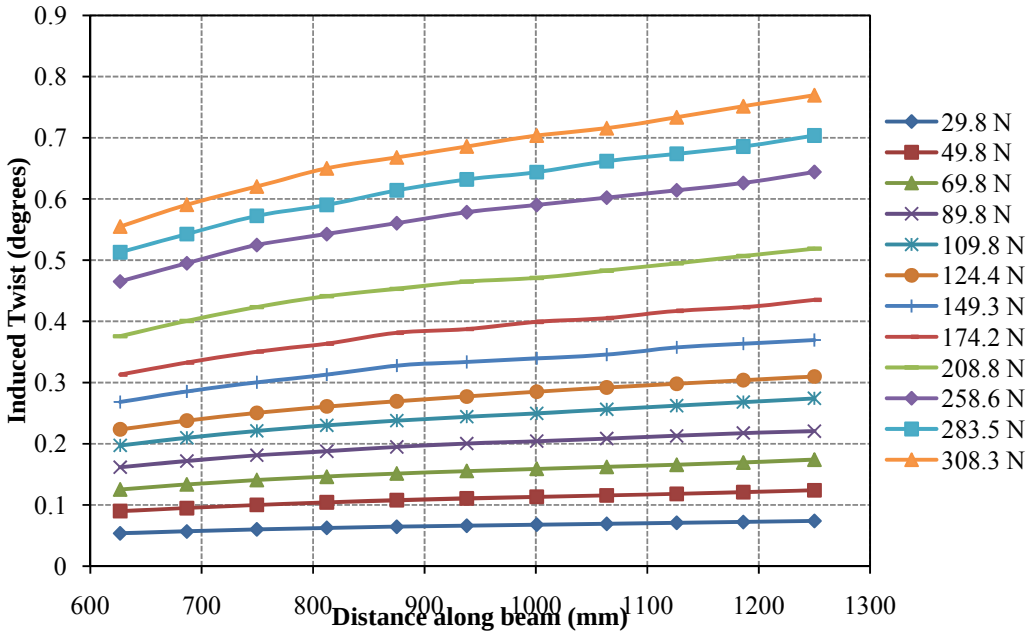

Figure 4-19: The relationship between induced twist and beam length for each tip load

The trends for the lower tip loads seem to have a more uniform distribution, whereas those at the higher tip loads exhibit minor fluctuations. The maximum induced twist occurs under a tip load of 308.3N (31.431kg) and has a value of 0.77^{o}.

4.6 Experimental Testing

Experimental analysis has been carried out in order to provide a comparison with the results attained from the numerical model. The basis of the experimental assessment is a carbon, bend-twist coupled, uniform planform, double box beam of the same lay-up and planform as that in the FE model. In order to construct this specimen unidirectional carbon fibre strips in prepreg form (SE84LV/HEC300) were cut from a 400mm wide roll and manually wound around a polished aluminium mould to make a box beam with orientation $[45,20_4]$. Two similar sized wound composite mould systems were then placed on top of one

another to achieve the required mirror layup, Figure 4-2b), and a final outer roving wound around the complete assembly of orientation $[60_2]$. The complete beam was then cured in an autoclave at 120°C for 45 minutes at a pressure of 3 bar. The aluminium moulds were then removed and the resulting composite beam tested.

The experimental setup is illustrated in Figure 4-20. The beam was fixed at one end, A, and a point load suspended from the free end on a rope affixed to the centre of the end of the beam through a hole, B, whilst leaving the beam free to bend and twist. Nine pairs of laser pointers were affixed to the upper surface of the beam at 100mm intervals starting from the tip of the beam, C, such that the beams of light intersected the two grids which were at a known distance either side of the test specimen, D. The initial positions of the beams at each station were marked.

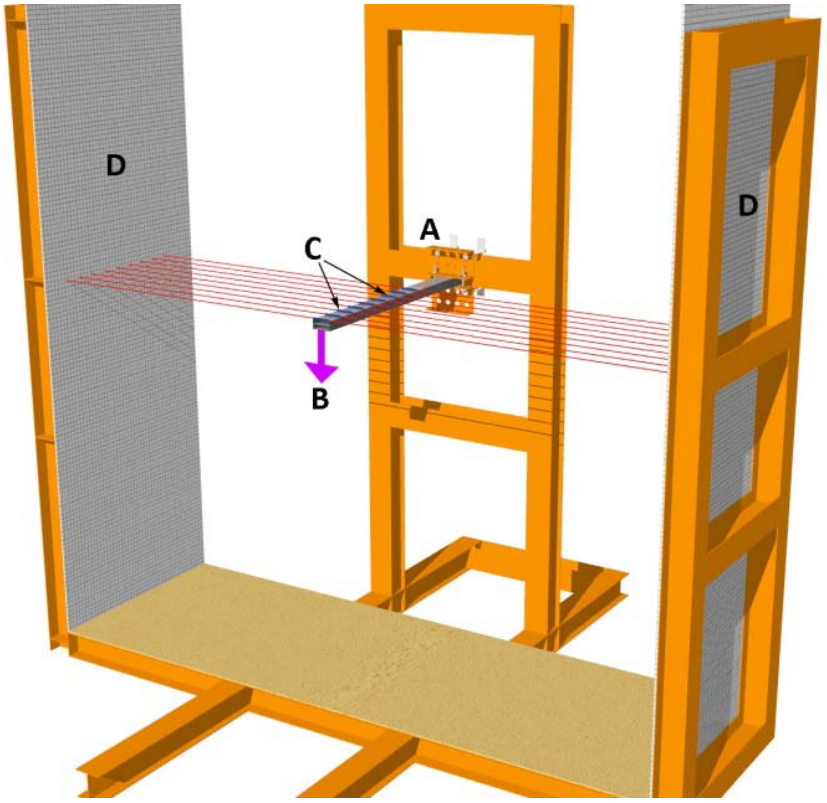

Figure 4-20: Experimental setup

As the beam was loaded, and subsequently bent and twisted, the laser beams moved over the grid and the loaded position was marked, Figure 4-21. As the distances from the

pointers to the surfaces, and the difference between the initial positions (red) and loaded positions (green) were known, the angle of induced twist and bending displacement were calculated at each station. Digital image correlation (DIC) was used on the cross-section at the free end of the beam to obtain the angle of induced twist and degree of bend at this point.

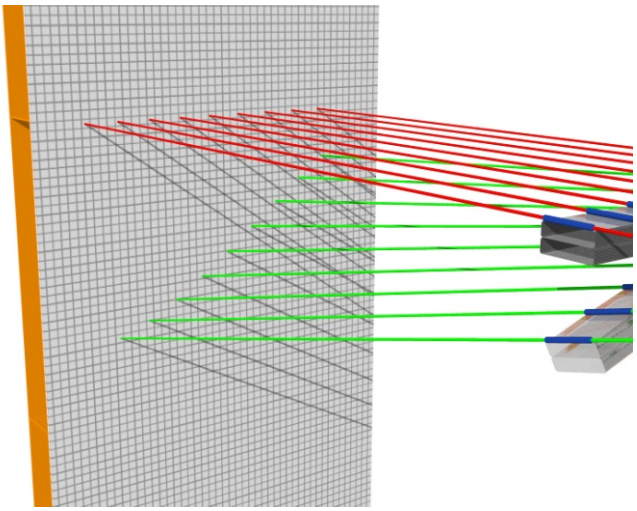

Figure 4-21: Initial beam/laser position (red) and displaced beam/laser position (green)

A series of masses was suspended from the free end of the beam; these are detailed in Table 4-7. To begin with, the lowest mass was applied and the initial and end positions of the laser beams were marked on the screens. The masses were then removed and the resulting position of the laser markers checked against the initial un-weighted position. This process was repeated three times. The mass on the free end of the beam was then increased and the process repeated.

Table 4-7: Masses used for tip loading of the beam

Mass (kg)	3.038	5.077	7.115	9.154	11.193	12.685	15.221	17.757	21.287	26.359	28.895	31.431
Load (N)	29.8	49.8	69.8	89.8	109.8	124.4	149.3	174.2	208.8	258.6	283.5	308.3

The amount the beam bent and twisted for each weight applied to the end of the beam was calculated using the following method. Figure 4-22 illustrates the tip of the beam before load application, position A, and after load application, position B. D is the distance between the screens in mm, H and h are the vertical displacements of the laser beams across the

screens in mm, θ is the induced twist angle in degrees and z is the vertical bend experienced by the beam in mm.

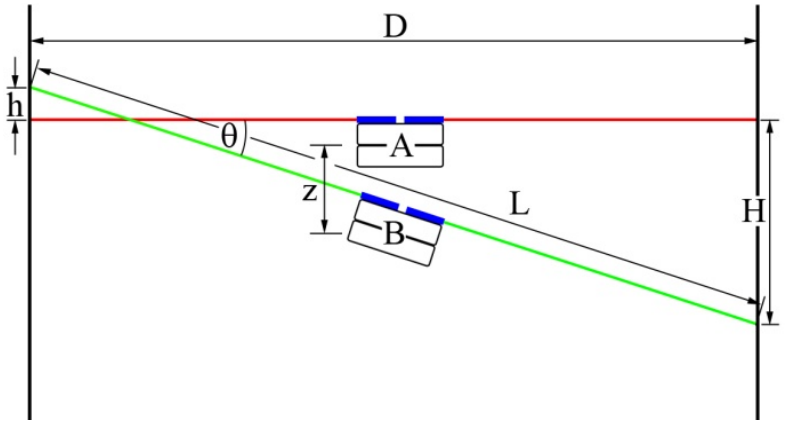

Figure 4-22: Schematic of the initial (A) and final (B) positions of the beam tip

Since D, H and h are known the induced twist angle can be found to be:

$$\theta = \tan^{-1}\frac{(H+h)}{D} \tag{4.9}$$

and L can be found to be:

$$L = \sqrt{(H+h)^2 + D^2} \tag{4.10}$$

Therefore z is:

$$z = (H+h) - \left(\frac{L}{2}\right)\sin\theta \tag{4.11}$$

Figure 4-23 shows the level of deformation from the initial flat surface with the maximum applied tip load of 308.3 N. The load is hung from a rope that runs through a series of holes in the upper, middle and lower skins of the tip of the beam. A penny washer was bonded to the upper skin of the beam in order to minimize failure due to the point load application.

Whilst failure was avoided, deformation due to the point load resulted in the upper skin becoming concave with a radius of curvature of 423mm. This caused the beams from the pair of lasers at station 1 to be deflected away from the expected path of a bend-twist coupled beam and thus not being an accurate representation of bend and induced twist. Therefore the

DIC results were used to calculate the vertical displacement and induced twist at the tip of the beam.

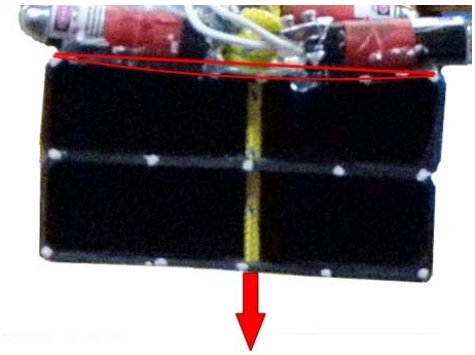

Figure 4-23: Deformation of the upper surface of the beam

Figure 4-24 shows a sample of four of the images obtained over an increasing range of tip load. The maximum bend and induced twist experienced at the tip of the beam was 60.7 mm and 1.89^{o} under a load of 308.3 N.

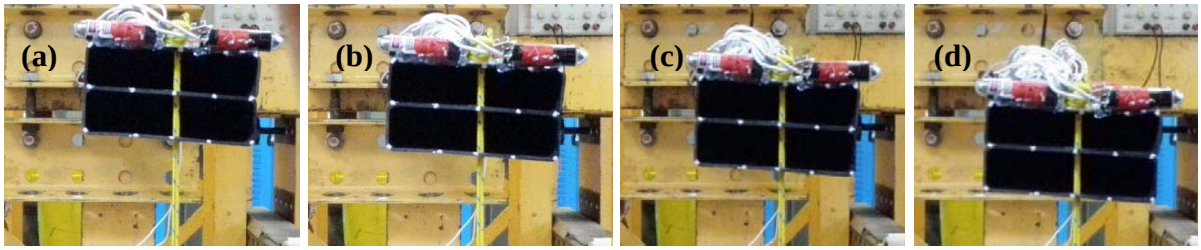

Figure 4-24: DIC images for (a) 29.8 N, (b) 109.8 N, (c) 174.2 N and (d) 258.6 N

It is apparent that the beam has some initial twist inherent in the construction. This occurred during the curing process where the beam was heated to 120^{o}C and then left to cool. There is an obvious progression of beam bending with the increase in tip load.

Figure 4-25 illustrates the relationship of both bend and induced twist to an increase in load. The bend and induced twist data has been compiled from that measured at station 2 on the beam – 1069mm from the clamped end, as opposed to station one due to deformation of the upper surface of the beam at the point through which the load was applied. It can be seen that neither relationship is linear. Both exhibit a cubic relationship to an increase in bending moment with a value of R^2 of 0.9992.

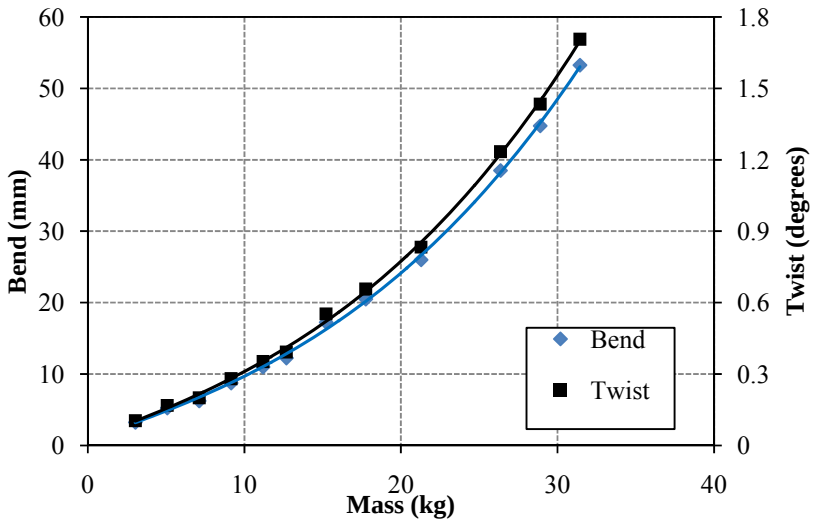

Figure 4-25: Experimentally determined relationship of bend and induced twist to mass

Figure 4-26 illustrates the vertical displacement due to the bending moment at each station along the beam for three different tip loads (29.8 N, 89.8 N and 124.4 N). Only the three results have been shown as it is felt that they display the trends exhibited by the results well, and these would not have been clear if all the results were plotted. There is a trend for increased bend with an increase in tip load. The relationship between bend and tip load is nonlinear.

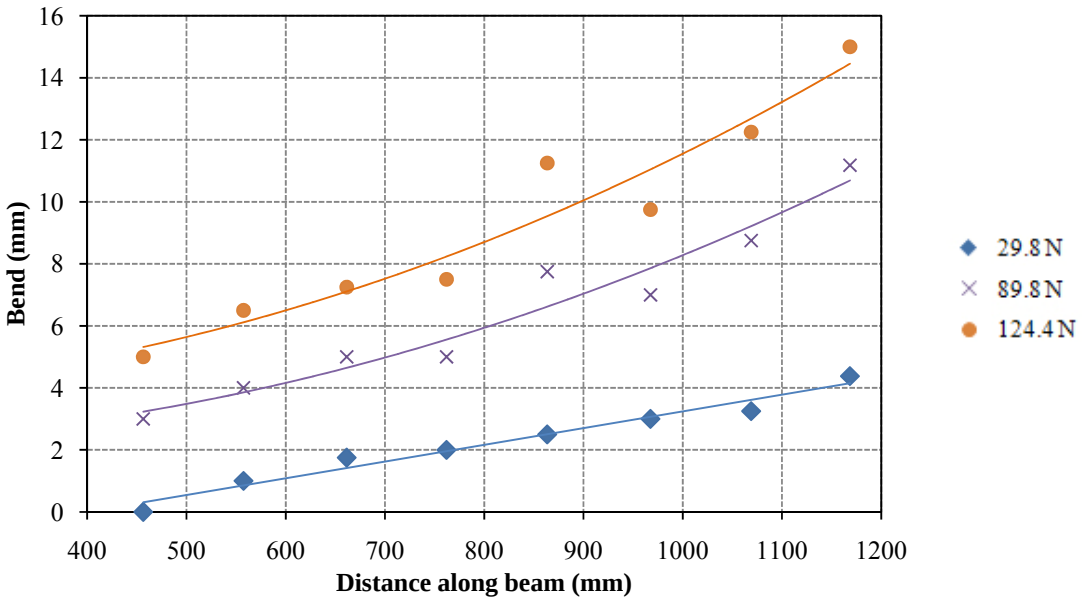

Figure 4-26: Bend resulting from the full range of tip loads

It can be seen in Figure 4-26 that there is some discrepancy in the data at some points along the lines, especially as the tip load is increased. The measurements acquired at station 3 (864mm from the clamp) and station 5 (762mm from the clamp) are noticeably erratic. This was due to a poor connection in the switch of the laser pen on one side each of station 3 and 5. In order to obtain a beam projection onto the screen it required manual manipulation thus skewing the results at this point.

The induced twist at each station resulting from the range of tip loads is illustrated in Figure 4-27 for the same three tip loads. It can be observed that induced twist increases with an increase in tip load. The maximum induced twist occurred at the free end of the beam under a tip load of 308.3 N and had a value of 1.89°. The relationship between induced twist and distance along the beam is non-linear.

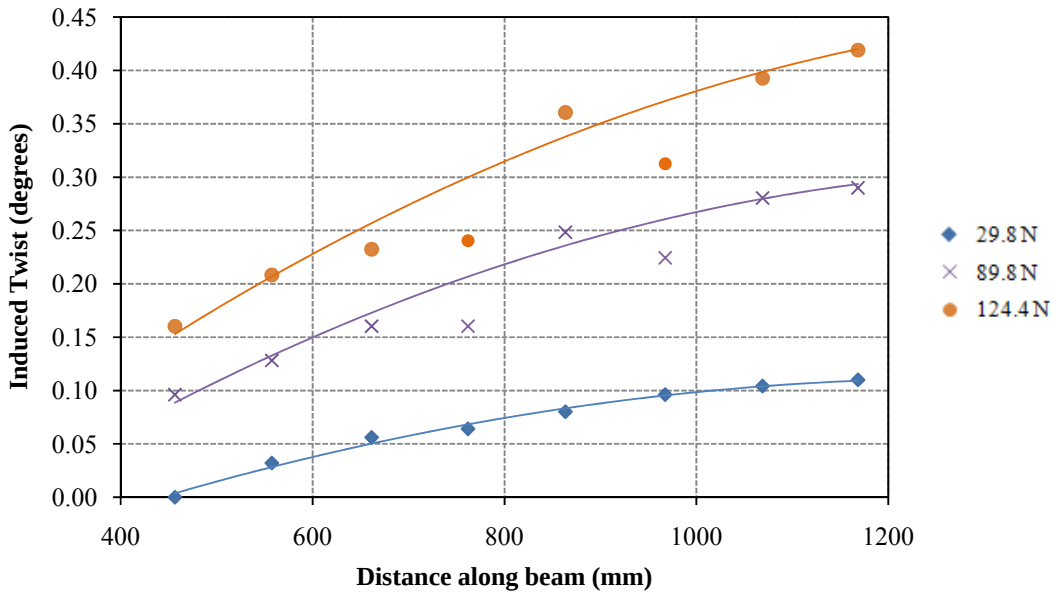

Figure 4-27: Induced twist due to tip load

Again both the points at station 3 (864mm from the clamp) and station 5 (762mm from the clamp) do not correspond to the general trend. The manual interference required to obtain data from these points during the tests had a greater effect on the more sensitive measurement of induced twist.

The tests at the lower tip loads (29.8 N – 174.2 N) were very repeatable. The laser beams returned to the initial starting point each time the load was removed during the repeated tests. Upon the introduction of a load of 208.8 N, fibre breakage was heard to occur towards the middle of the beam. Once the larger load was removed the beam did not return to its initial starting position. This was more apparent as the load was increased to a maximum of 308.3 N, and an increasing amount of fibre breakage was heard.

Figure 4-28 shows the extent of the damage in terms of residual bend and induced twist when compared to the initial beam shape. At the tip of the unloaded beam (1160mm) the residual bend and induced twist due to damage from the initial unloaded condition was 7mm and 0.21^{o} respectively. It is clear that despite the process being completely elastic at the lower tip loads, as soon as damage is sustained the shape and response of the beam changes. This is important to note for future design purposes as it will have an effect on the tidal turbine blade performance, the turbine should be so designed that failure does not occur and hence the blade does not change shape through its operative life.

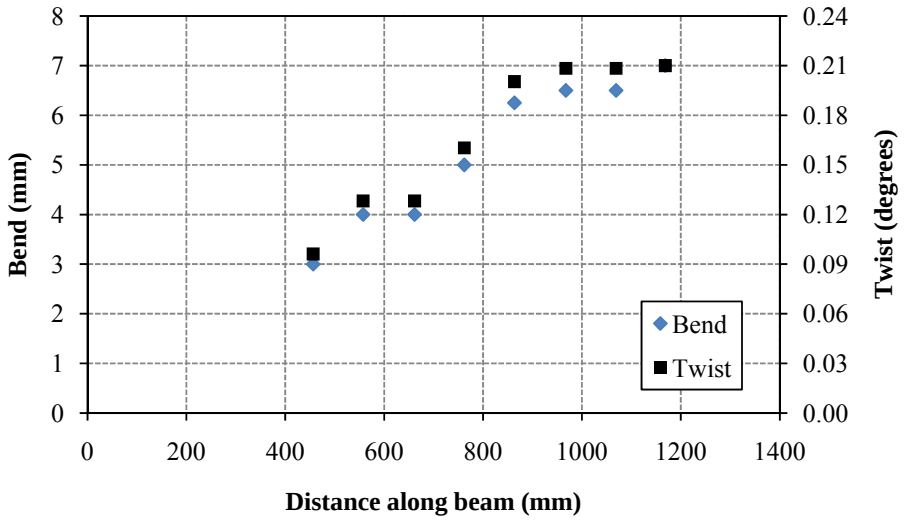

Figure 4-28: Extent of damage resulting from large tip loads

As with any experimental analysis errors occurred. Alongside the poor connection in a couple of the laser pens, the laser beam of all of the pens was relatively poorly focused such that when marking the points on the screens the centre of the beam needed to be estimated. The error associated with the displacements measured using the laser beams on the grid has a

maximum value of ±1mm as a result of the diffuse lasers beams having a diameter of approximately 1mm at the screen. The cumulative error associated in the calculation of the induced twist has a maximum value of ±0.036^o over the full spectrum of tip loads.

It was difficult to bond the laser pens precisely perpendicular to the beam thus introducing a small error due to misalignment. One of the lasers pens at station 9, that closest to the clamp, was poorly connected and shorted and therefore could not be used resulting in a lack of data at this station. Fortunately this station saw minimal bend and induced twist due to the proximity to the clamped end and hence the inoperative laser was deemed unimportant.

4.7 Comparison

The experiments were carried out in order to compare 'real life' results with those determined through the numerical finite element method of analysing a bend twist coupled composite beam. This was to enable the FE analysis to be used as part of a design tool for bend-twist coupled tidal turbine blades. In order to consider whether the numerical model is accurate the results of both analyses have been compared.

Comparison of the theoretical and experimental bend achieved along the length of the beam for a representative range of masses is illustrated in Figure 4-29. The suffixes T and E denote the theoretical and experimental results respectively. At the lower tip loads it is apparent that there is good correlation between the numerical and experimental results. With tip loads in excess of 149.3 N there is considerable divergence is evident which increases with increasing tip load. It is generally accepted that the perfect nature of numerical modelling can lead to an overestimation of stiffness, however the level of divergence shown in Figure 4-29 is too significant to be explained through numerical perfection. The numerical analysis used material properties supplied by the pre-preg manufacturer. A sensitivity analysis was conducted to investigate the influence of material properties on the beam response. It was found that a 10% change in the values of E_Y and E_Z (the transverse and through thickness properties of the UD laminate respectively) result in an increase of beam bending of 3% for an applied tip load of 208.82N. The theoretical analysis also assumed that the geometry of the beam and orientation of each layer were perfect; i.e. the mid-layers at 60^o are assumed to be at exactly 60^o in the model. A further sensitivity analysis revealed that a 10% reduction in

the mid-layer ply angle, from 60° to 54°, resulted in a 14% increase in bending deflection for a tip load of 208.82N. These analyses indicated that the level of bend the beam experiences for a given load is heavily influenced by accuracy in the manufacturing process, and is the most likely reason for the divergence of the experimental and numerical results. At the highest tip load this discrepancy is greater; however, observations in the experiments indicated the occurrence of internal ply failure which is not modelled in the numerical analysis.

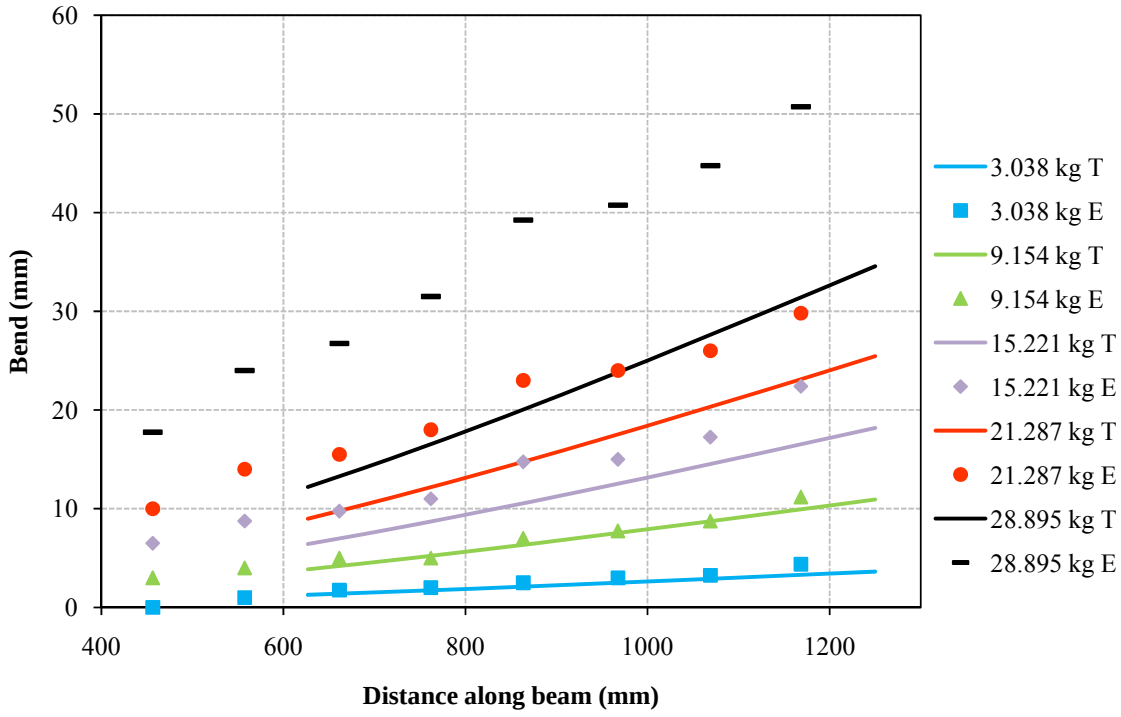

Figure 4-29: Comparison of theoretical and experimental results for bend along the length of the beam for a range of tip loads.

The comparison of the relationship between induced twist and beam length over a representative range of tip loads for the numerical and experimental results is shown in Figure 4-30. Again the divergence of the numerical and experimental results is apparent with increasing tip load. The results seem to correspond more closely at the shorter beam lengths and diverge towards the tip of the beam for each tip load. The sensitivity analysis on ply angle again showed that the response is highly sensitive to the accuracy of the manufacture.

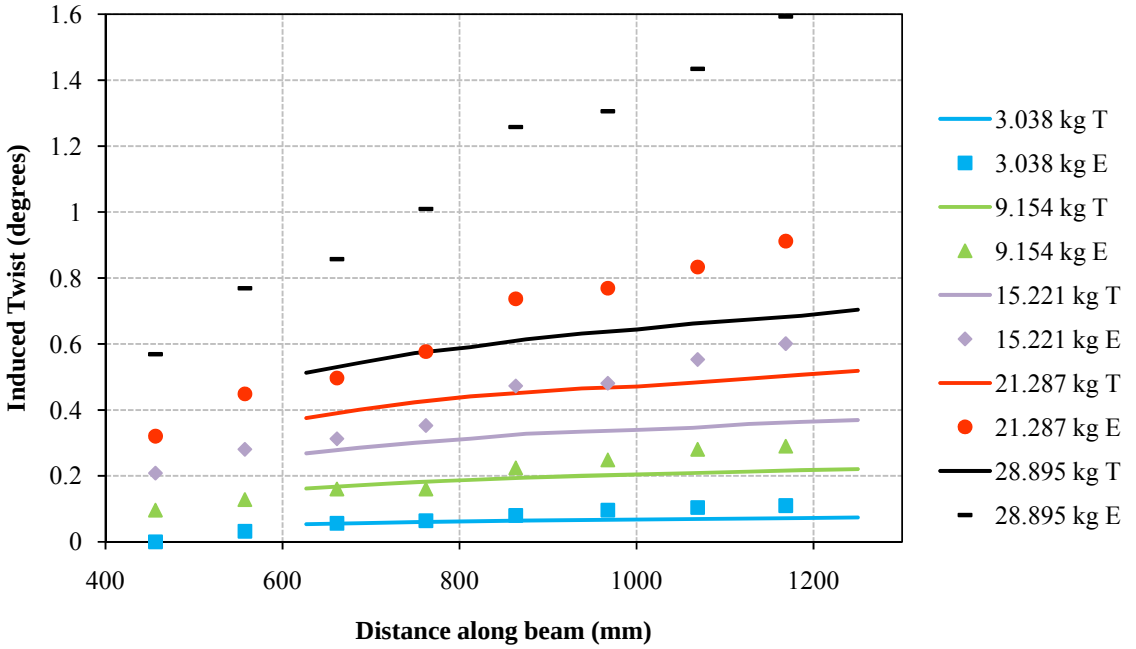

Figure 4-30: Comparison of theoretical and experimental results for induced twist against beam length over a representative range of masses

Figure 4-31 illustrates the relationship between theoretical and experimental bend and induced twist at station 2 on the beam for each tip load. While the results are relatively consistent for the lower tip loads (up to 124 N) there is marked divergence after this point. The number of load steps in the non-linear analysis was increased to 20; however the theoretical results still maintained a linear profile and did not capture the non-linear trends apparent in the experiments. The same sensitivity analyses, regarding material properties and accuracy of manufacture, showed that induced twist was similarly affected as with the beam bend and a considerable amount of this divergence is attributed to this. However, the discrepancy is also considered to have been caused by fibre breakage occurring in the beam when the heavier masses were hung from the free end. While the sounds of fibres breaking were only heard to start under a tip load of 208.8 N, after divergence of the theoretical and experimental results occurs, it is possible that failure may have started at lower loads but been less audible with the cumulative effects of ply failure and imperfections in manufacturing causing the difference in experimental and theoretical results.

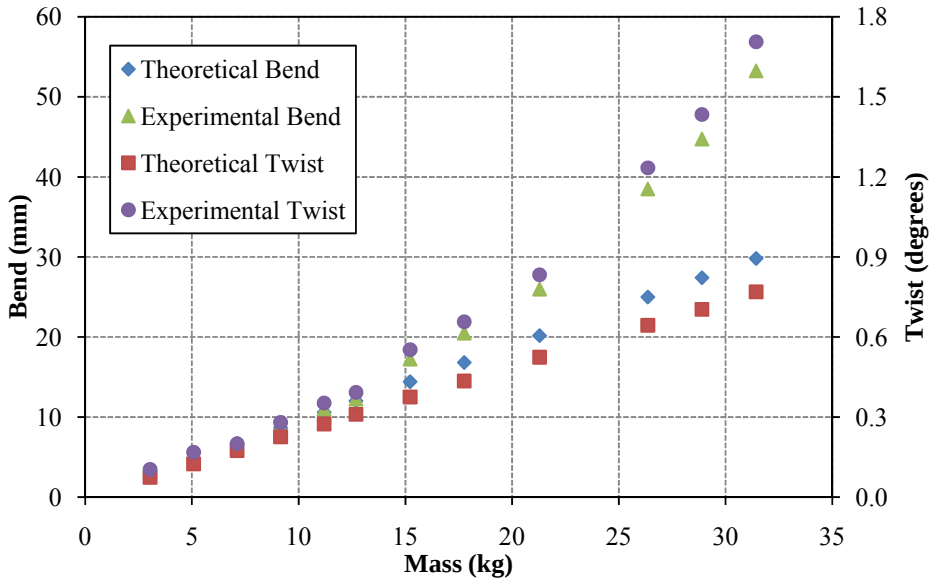

Figure 4-31: Comparison of theoretical and experimental bend and induced twist for each tip load at station 2

Judging by the fact that the numerical and experimental results, presented in Figure 4-31 diverge so markedly, and not all of this can be attributed to inaccurate manufacturing, the theoretical analysis may not account for fibre breakage and first layer (first ply) failure. Figure 4-32 illustrates the behaviour of a laminate upon first layer failure.

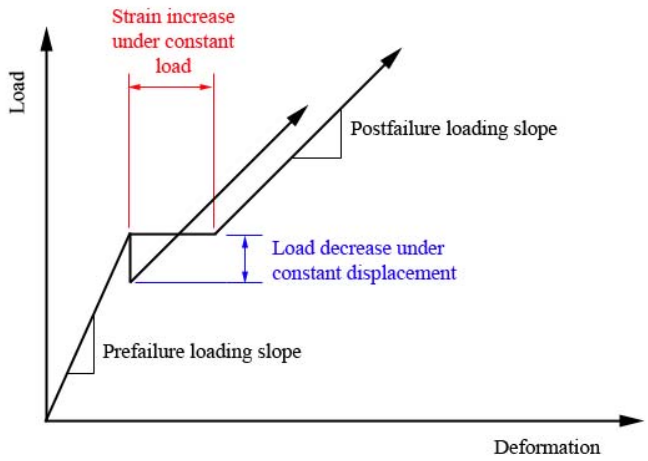

Figure 4-32: Behaviour upon first layer failure [116]

First layer failure can be defined as the layer or ply group that fails in a multidirectional laminate; the load corresponding to this failure is the design limit load. In Figure 4-32 the postfailure loading slopes are identical, but the curves are offset from one another. In reality, failures between fibres do not occur at precisely the same load and therefore the actual load-deformation curve is a series of small events as illustrated in Figure 4-33. This shows the progressive failure typical of a laminated composite.

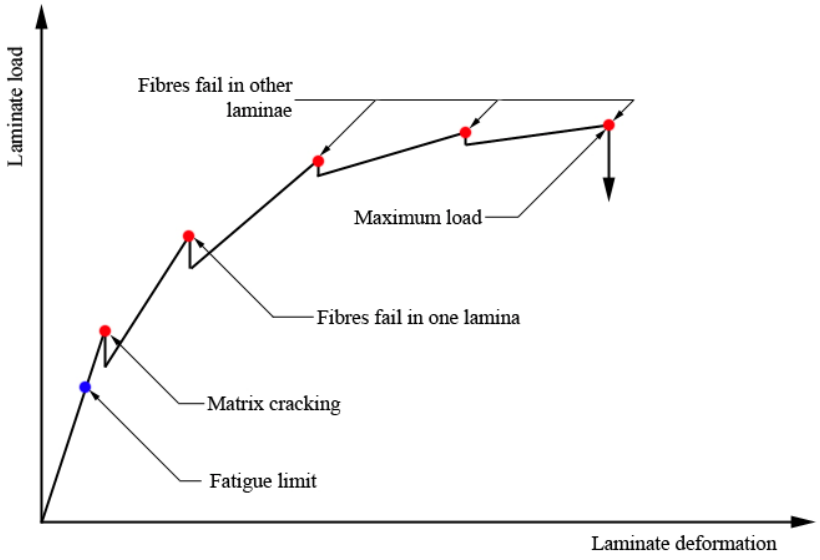

Figure 4-33: Typical laminate load-deformation curve [116]

The load-deformation (mass-bend data) presented in Figure 4-31 is plotted in a similar format to the classic load-deformation curve, Figure 4-34. It can be observed that it takes a similar form to that of the load-deformation curve in Figure 4-33, thus leading to the assumption that the reason for the divergence of results between the theoretical and numerical results in Figures 4-30 to 4-32 is partly due to laminate failure. It is apparent that that a progressive damage modelling approach may be required to model the material degradation due to excessive load application.

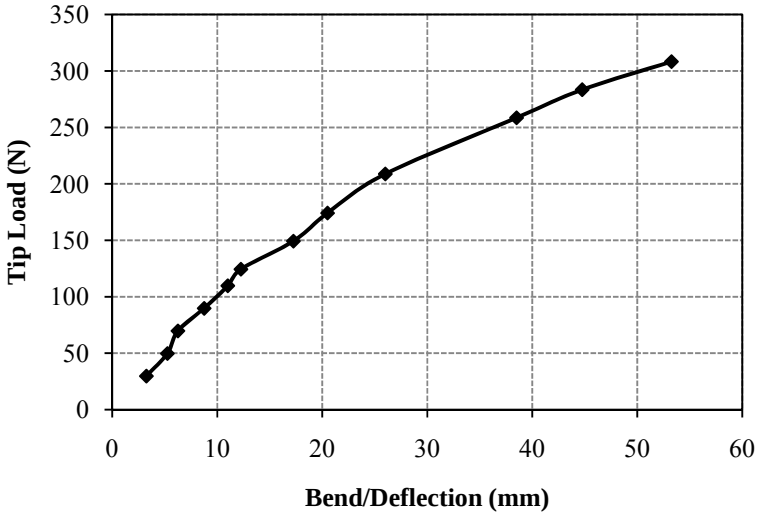

Figure 4-34: Load-deflection curve for the composite bend-twist coupled beam

Analysis of the Von Mises stresses experienced by the theoretical model of the beam indicated that the maximum stresses are at the root, where the beam is clamped. The maximum Von Mises stress in the beam when a load of 150N (15.22kg) was applied was 1.38GPa, whereas the maximum tensile stress of the SE84LV/HEC is 2.844GPa – over twice the value seen in the theoretical analysis. It is apparent, however, that failure of layers in the physical specimen occurred at a tip load just less than 150N. This could be due to the presence of voids and wrinkles in the laminate. Judd and Wright [117] state that the interlaminar shear strength of a composite decreases by about 7 percent for each 1 percent of voids up to a total void content of about 4 percent. Other mechanical properties are also affected [118]. Strong [119] suggests that a good quality laminate should have a maximum void content of 0.5%. Many large voids, visible to the naked eye, can be observed in the cut face of a section of the manufactured beam suggesting that the void content is considerably higher than 0.5% despite the beam having been cured at elevated temperatures and pressures in an autoclave. The presence of such defects may have contributed to the discrepancies between the theoretical and experimental results.

Initial studies (Sections 4.3 and 4.4) have indicated that the combination of a fixed pitch and passively twisting blade is likely to increase the profitability of a free stream tidal turbine in comparison with a rigid fixed pitch or variable pitch turbine blade [120]. Increases in annual energy capture of around 2.5% and a reduction in thrust coefficient of around 10%

were observed for a blade which was able to produce a tip twist in the region of a few degrees. These studies were undertaken assuming a distribution of twist of the form $0.5Sv_f^{½}$, where S is the blade span and V is the tidal flow velocity. This twist distribution is very similar to those produced as a result of both the FE analysis and experiments suggesting that performance improvements comparable to those mentioned previously may be expected.

Considering the carbon bend-twist coupled spar under experimentation, it may be assumed that a turbine of diameter 2.6m may have a similar length blade, with a similar thickness/chord ratio at the stock. Knowing that the thrust coefficient for a HATT, C_T, is:

$$C_T = \frac{T}{\frac{1}{2}\rho A v^2} \tag{4.12}$$

Assuming a reasonable value of C_T of 0.8, the flow velocity, v, can be calculated to be 2.3m/s. This is an acceptable value for the mean spring peak velocity for a tidal stream energy extraction site.

The experimental method used is considered to be a viable method for determining the induced twist of a bend-twist coupled beam. It will be used in future tests; however, methods to reduce the void content, optimise the repeatability of the fibre angle during layup, attachment of laser pens of higher quality will be included.

It is evident that there are limitations to the numerical model, and more care and consideration should be given to both theoretical modelling (ply wise failure) and manufacturing perfection in order to bring the results closer together. This work, however, clearly identifies a route to modelling passive adaptation for the design of HATT blades.

4.8 Summary

Adaptive composite technology has been assessed for integration into HATT blade design to improve the overall efficiency of the tidal device and hence annual energy capture. Preliminary analysis showed that a blade with forced bend-twist coupling has the potential to increase annual energy capture by around 2.5%, whilst decreasing thrust loading on the turbine by up to 10%, thereby increasing the fatigue life of the turbine and associated structure. A coupled blade performance prediction program has been developed to assess the performance of a range of devices, whilst also considering material properties in a simplified

manner. Finite element analysis of the central spar of a turbine – a bend-twist coupled, carbon, double box beam – has been undertaken, and the results compared to those gained from an experimental method for determining levels of induced twist in a composite spar. FEA was found to be an effective tool for this analysis, however care should be taken as it was found that it did not capture occurrences of ply wise failure in the composite beam leading to under prediction of bending and therefore induced twist at higher loads. Manufacturing accuracy was also a key factor in the discrepancy between the experimental and numerical results. Small changes in the material properties and ply layup angle in the numerical model resulted in increases in beam bending of 3% and 14% respectively.

5 The Design Tool

5.1 Fluid Structure Interactions

Fluid-structure interactions (FSI) occur when a fluid interacts with a solid structure, exerting pressure that causes deformation in the structure subsequently altering the flow of the fluid itself. If a situation involving structure flexure is to be analysed it is highly beneficial to couple both the fluid dynamics and the structural analysis programs to produce iterative solutions for complex problems.

There are three methods of joint fluid structural modelling in the time domain which involve solving the governing equations in a coupled, uncoupled or integrated manner. Uncoupled simulations are computationally inexpensive but are limited to small perturbations and minimal non-linearites. Integrated methods solve the fluid and structural equations simultaneously, while coupled methods solve the equations separately but in an iterative manner [121].

Coupled methods are subdivided into strongly or fully coupled and loosely coupled approaches; where the loosely coupled methodologies can be either integrated or modular. The integrated scheme modifies the source code of either the CFD or the FEA programs to include the coupling schemes; whilst the modular approach leaves both the FEA and CFD codes untouched, effectively making use of a “black box” which can manipulate the output of the CFD and/or the FEA and feed it into the other program respectively, thus allowing for a variety of software to be used. The key difficulty is ensuring the conservation of energy between frames of reference; from the kinetic energy of the fluid flow to the potential energy contained within the stress field of the deformed turbine.

In a loosely coupled approach the two domains are discretised to better suit the problem; as the CFD mesh will tend to require greater refinement in different areas of the structure than the FEA mesh, and vice versa. This ultimately leads to the main problem with loosely coupled analyses, the need to find a method to accurately pass boundary information from one simulation to the other.

In operation a HATT is subjected to hydrostatic pressure. In addition to this it is a lifting body with rotational motion; hence it is subjected to further hydrodynamic forces. Due to the complex loading scenario experienced by a tidal turbine, knowledge of the hydroelastic behaviour of the blades, hub, nacelle, and also the support structure under this regime could lead to a more thorough understanding of structural constraints and how performance of the turbine could be improved in order to bring the efficiency of the device closer to the Betz limit (Section 2.3.2).

In order to gain an insight into the hydroelastic behaviour of a HATT, practical experimentation may be used to quantify and visualise the response of the device to a multitude of environments. Experimental investigations, however, are costly, time consuming and difficult to design in order to gain credible and useful information from the test device. As can be observed from the coupled beam analysis detailed in Section 4, manufacturing accuracy is influential on the end results of practical experiments. Computational investigations are much less expensive, regarding both time and money – although both of these variables tend to increase with an increase in accuracy of results.

Whilst being a highly informative technique for the design analysis of a standard fixed blade device, FSI is essential when considering adaptive composite blades as the pressure loading alters the shape more significantly when compared to standard blades. A fixed blade can be analysed to maximise the stiffness of the structure. In the case of a passively adaptive blade, variables such as fibre orientation and number of plies in the laminate have a significant effect on the design as the blade shape alters in response to the incoming flow.

In this work, a loosely coupled, modular approach is used; the flow problem and structural problem are solved successively until the change is smaller than the convergence criterion. The CFD analysis is carried out using Palisupan [83] which has been shown to be adequate for predicting the pressure distribution across a HATT blade [69]. The FEA is performed in ANSYS 12.1, but unlike the analysis discussed in Chapter 4 this includes the blade skin encompassing the bend-twist coupled central spar. The “black box” coupling the results of the fluid analysis to the structural analysis is a program based in Matlab 2009b. This program alternately manipulates both the surface pressure distribution yielded from the fluid dynamics program and the displacement data output from the structural analysis, and

feeds them back into the next relevant stage of the process. This is illustrated schematically by the flow chart in Figure 5-1.

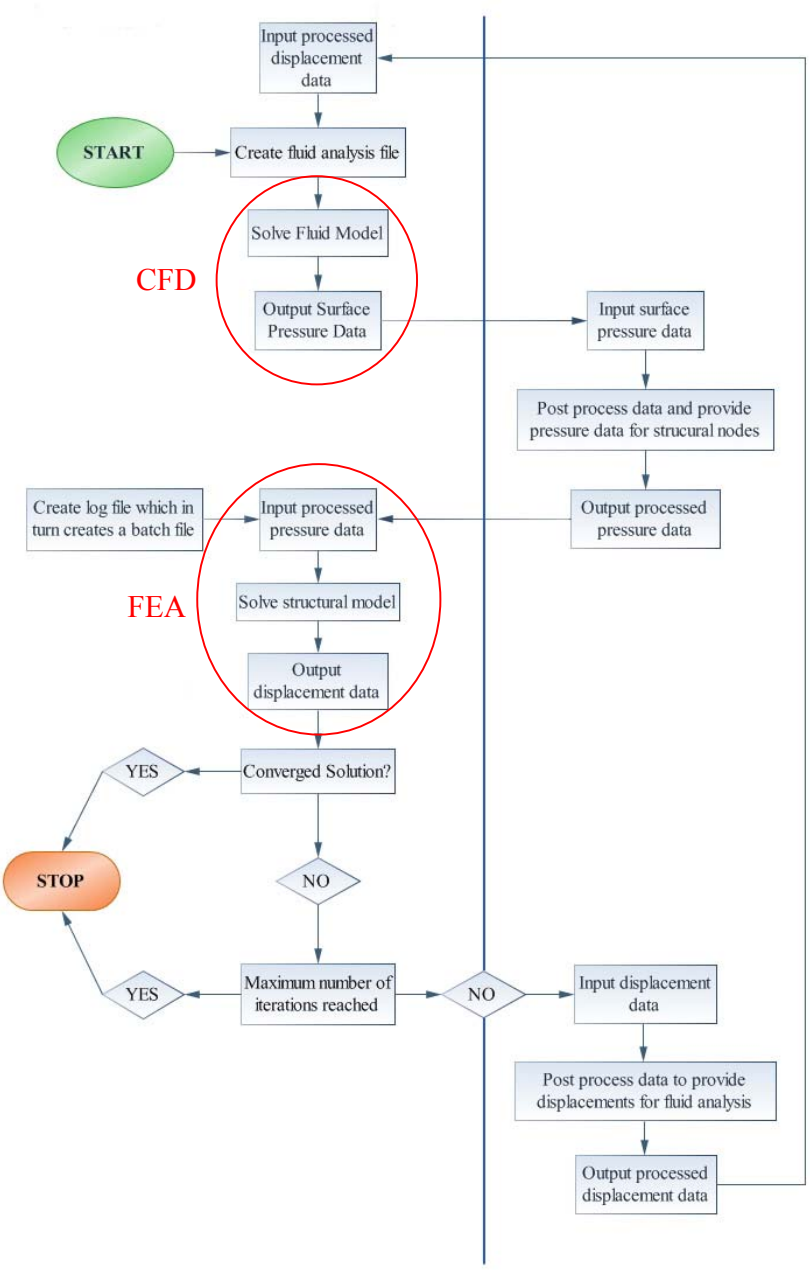

Figure 5-1: Flow diagram of the Fluid Structure Interaction simulation process

The left side of the vertical blue line is indicative of the actions carried out by the CFD and FEA software, the right hand side shows the actions carried out by the "black box". The

points in the flow chart illustrate an overview of the process. Similar methods to this have been shown to be successful by both Turnock and Wright [121] and Casagrande [122], and as such the concept of the use of a loosely coupled modular approach for marine structure analysis does not need to be proven, rather modified in order to operate effectively for a tidal turbine. This method differs from the previous analyses, detailed in Chapter 4, as it considers the whole blade – spar and skin – and resulting pressure loading and deflection.

5.1.1 Computational Fluid Dynamics

In order to run the CFD analysis, the input blade geometry must be developed. Propgen [84] requires the input of blade section data and section offsets, alongside the number of panels and distribution of panels over the body and wake of the geometry under analysis. The geometry is constructed from a set of section curves. These sections are generated for any given radius by defining the chord, thickness, skew, rake, pitch and 2-D section shape. The 2-D section is then mapped onto a cylindrical surface according to the specified variables using a transformation matrix. The program is constructed such that when the geometry is intended for use with surface panel codes including a frozen wake model an automatic helical wake sheet is generated. The final geometric output is illustrated in Figure 5-2. This assembly shows the options for having a duct, hub and cap alongside the blade geometry.

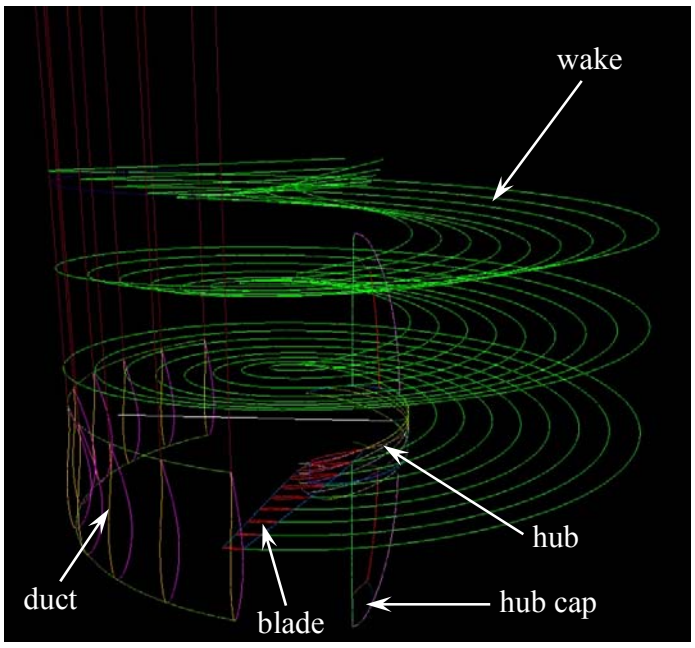

Figure 5-2: Propgen geometry output

Once the blade geometry was generated it was then exported to Adaptflexi [123] in which a surface is lofted through the sections to generate the blade and the turbine is rotated such that the flow is in the positive x-direction. In Adaptflexi other variables are defined for the HATT scenario such as flow velocity, RPM, number of blades, water density, and panel discretisation; and subsequently a surface mesh created consisting of quadrilateral panels. In the case of a turbine blade, it is necessary to concentrate the mesh around the leading and trailing edges of the control surface in order to most accurately capture the geometry of the body around which the fluid is flowing. The number and distribution of panels in the wake is also important for accurate modelling of device performance [76]. Figure 5-3 illustrates a single blade (colour) and wake panel distribution for analysis in the CFD code of a 20m diameter, three bladed HATT; there are in excess of 2800 panels in the blade of the turbine alone. A panel sensitivity analysis has been carried out for a 20m diameter, 3 bladed HATT and can be viewed in Appendix B. In the immediate wake a finer panel distribution can be observed when compared to the far wake downstream. This captures the flow more precisely leading to a more accurate CFD solution. The turbine is rotationally symmetric and therefore the body coefficients are rotated and copied twice more to simulate the whole entity. The output from Adaptflexi is in the form of a *.uns* file which contains the flow data for the simulation along with a list of panels throughout the turbine and wake model and the corresponding corner points.

The problem is then solved using Palisupan [83] where the turbine blade generator is in the positive y direction, with the onset current travelling in the positive x direction. The blade is rotating in the negative direction (anti-clockwise about the x-axis). In effect the moment about the y-axis is a measure of the torque required to rotate the blade about an axis passing through the origin. The resulting pressure loading across the surface of the blade was then calculated for input to the FEA model.

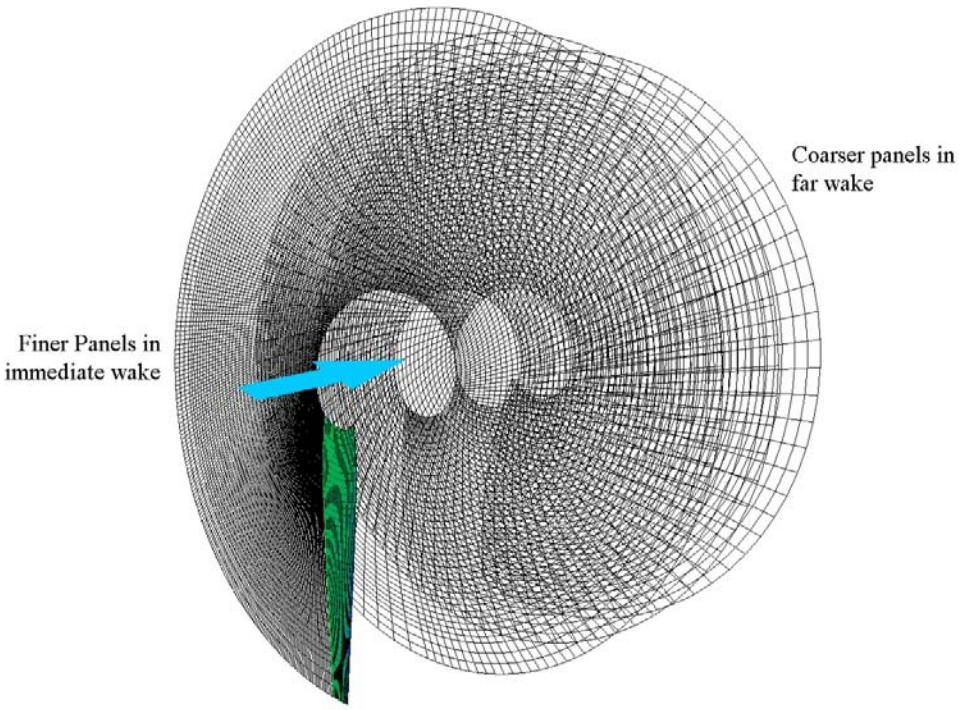

Figure 5-3: Panel distribution over blade and wake

5.1.2 Finite Element Analysis

Chapter 4 discussed the use of FEA as an analysis tool specifically in the case of composite bend-twist coupled beams. At lower tip loads there was good correlation between the theoretical and experimental results. With an increase in tip load, however, the two sets of results diverged. This was mostly attributed to the sensitivity of the numerical model to manufacturing accuracy, but also partly to progressive damage occurring in the beam during the experiments which was not captured. In this section the FEA will be used to determine the structural displacement of the passively adaptive HATT blade, but it is appreciated that there are limits to this numerical model and therefore improvements will be required for future use.

The geometry created for the CFD analysis is imported into ANSYS 12.1, and a central spar fitted through the blade, Figure 5-4. This ensured that nodes existed at the corner points of each panel of the CFD mesh. The spar was fitted such that it supported the blade at

one third of the local chord distance from the leading edge; this is where the centre of effort of the blade typically acts.

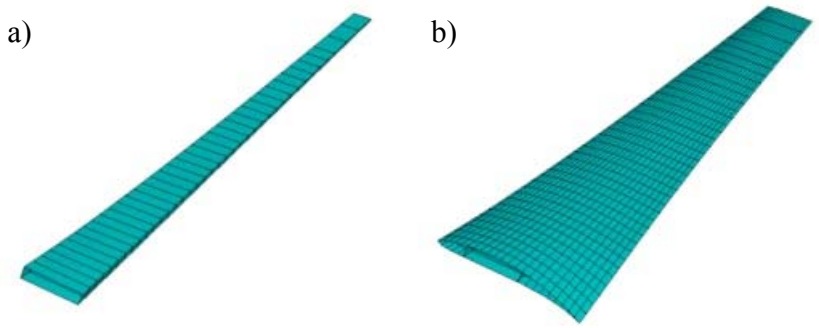

Figure 5-4: Geometry of blade showing the central spar (a) and the blade skin (b)

The resulting geometry was then meshed and the pressure loads from the CFD analysis applied. This was achieved directly, without requiring interpolation, by virtue of the FEA geometry having the same areas mapped out as the surface panel CFD model; the pressure at the centre point of each panel is output from Palisupan and applied to the corresponding panel in the FEA model. The bespoke FE blade mesh was created in the smallest areas first to ensure that it was adequately dense in these regions, resulting in a higher quality of mesh overall.

The geometry was solved using a static non-linear analysis such that large deflection effects were taken into account. The maximum stress seen in the blade is monitored with the criteria that it must not exceed a third of the yield stress of the beam material; thereby incorporating a safety factor of three in to the design. While wind turbine aerodynamic loads are subjected to a safety factor of 1.35 [124], they tend to be designed using the method of partial safety factors, i.e. the overall safety factor consists of several partial factors multiplied together. Each of the partial factors accounts for one effect, e.g. uncertainty of loading, ageing of the material, manufacturing variations or material type. By using partial factors, the differences between one manufacturing method or another can be taken into account more accurately than with a simple global factor. A further factor may be added for the "consequence of failure"; thus if the integrity of a particular part is essential for the turbine's survival, that part's factor will be higher to reduce the probability of failure of the whole machine. In this work the partial safety factor method has not yet been integrated and

therefore a safety factor of three was chosen in an effort to account for the through-life stresses present on the turbine and the inaccessibility for maintenance.

If this value is exceeded the number of plies in the mid-layer of the bend-twist coupled beam is altered, and the FEA rerun for the same pressure loading until a reasonable stress level is reached. The deflections are output at the nodes corresponding to the panel corner points in the CFD geometry. The deflection of the blade is then remapped into a new *.uns* input file for the CFD analysis and the problem rerun. This simulation is continued in an iterative manner until the deflection of the blade between successive runs is less than 10mm, which is small in comparison to the blade length (circa 20m).

5.1.3 Coupling Design Tools

Coupling of both the FEA and CFD analyses has been carried out in Matlab. Figure 5-5 shows a flow chart of the process. Excerpts of the code behind this procedure are presented in Appendix D. These have been limited to those aspects of the code that pertain to the coupling procedure and geometry manipulation, rather than to the creation of text files, in order to limit the length of the document.

Initially tables of data for the range of variables under investigation are generated; these variables can include RPM, diameter, flow velocity, section shape and number of blades. The relevant data for the first run is then extracted from these tables and the *Propoptions* and *Propeller* input files for Propgen created; example files are illustrated in Appendix D. Propgen is then run to create the blade, hub, and wake geometry ready for CFD analysis.

A script is then generated to pass the geometry through Adaptflexi, a sample script is presented in Appendix D. The output required from the CFD analysis is governed through this script; pressure information, panel configuration data, and overall turbine loadings. Adaptflexi is then used to generate the *.uns* file and *.cmd* file and the case passed through the CFD analysis. Each run through the CFD analysis takes in the order of 20 minutes.

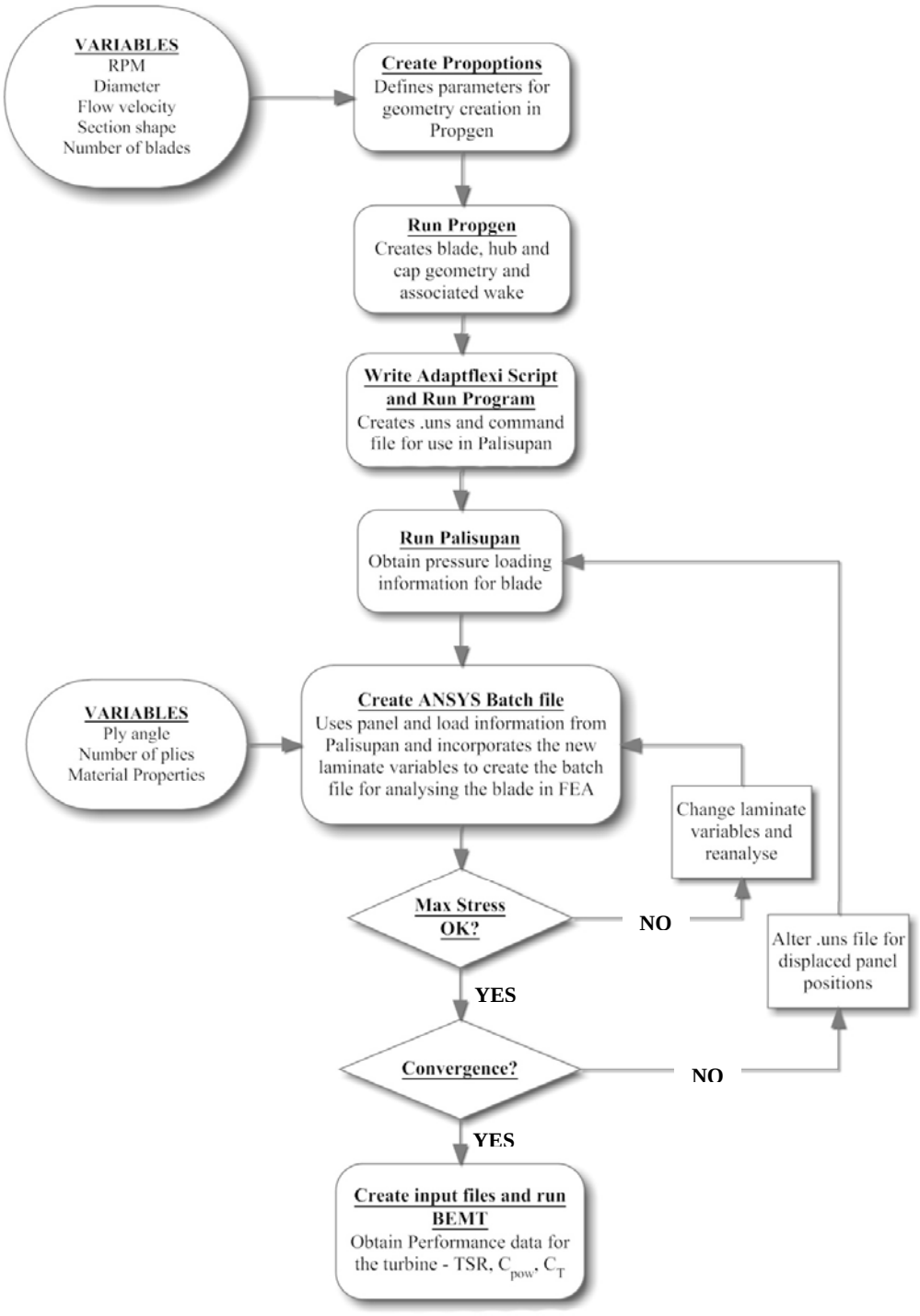

Figure 5-5: Flow chart detailing the coupling process

Structural variables are now introduced in the form of ply angle, number of plies and material data. The information from the CFD analysis is manipulated in order to create an

ANSYS batch file. This file takes the geometry data and generates a blade within ANSYS that has a coupled box beam as the main central spar and applies the required lay-up information to the correct areas; the pressure loading is then applied and the problem solved through a non-linear static analysis to take into account large displacements. The problem takes around 30 minutes to solve. Once a solution is achieved a check is performed to make sure the maximum stress at any point in the structure does not exceed a third of the yield stress of the material of that section. If this check fails the FEA is rerun with different laminate properties until a positive result is achieved. The deformed positions of the loaded blade are then calculated through knowledge of the displacements of each node; and bend and induced twist determined.

The nodal displacements are then transferred to the *.uns* file for the relevant panel corner points. The panel list in the *.uns* file is divided into trailing edge body panels, main body panels, wake panels attached to the trailing edge, mid wake panels and far wake panels. Each panel has four corners, and the points that represent these are listed in order; top left, top right, bottom right, bottom left. The displacements of each panel on the trailing edge of the main body are known from the FEA and are evaluated as axial, radial and angular displacements in cylindrical co-ordinates and then applied to the body keypoints in the *.uns* file. These displacements are then translated back through the wake panels to give a deformed wake to match the deformed blade. The 'black box' utilises the knowledge of the *.uns* file format to search for the panels associated with the trailing edge of the main body and apply the relevant displacement to each. In turn the subsequent panels in the wake are displaced in a similar manner until the whole wake reflects the deformation of the geometry.

The problem is then run through the CFD program again to determine a new surface pressure loading for the deflected blade. This loading is applied to the deflected blade in ANSYS and the structural analysis carried out. These stages are repeated until corresponding structural analyses converge – i.e. the maximum bend in the blade is less than 10mm different from the previous run.

In order to perform a final check on the data obtained, once convergence has occurred the input files for the BEMT code are created from the main blade parameters and performance characteristics calculated for the device. This data is compared to that gained through the final iteration of the CFD analysis to ensure that the thrust and torque estimates

are similar. In this manner a composite, bend-twist coupled blade can be designed for use on a HATT.

5.2 Example Case

In order to illustrate the FSI blade design method, an example design problem has been considered. The turbine in question is to be situated in the strong tidal race in the Bristol Channel, U.K. The maximum spring peak current here is around 2.5m/s, with both the ebb and flood stages of the tide having similar velocity profiles [125]. The turbine has a diameter of 20m, a hub-diameter ratio of 0.2 and three bend-twist coupled blades. The section shape to be used for the blade is the NACA 63815 which was shown previously to perform well (Chapter 3). The blade is of the form detailed in Table 5-1. A three-dimensional representation of the example turbine is illustrated in Figure 5-6.

Table 5-1: Example case blade design data

r/R	*Chord (m)*	*P/D*	*t/c*
0.2	2.304	0.3365	0.0858
0.3	2.033	0.2263	0.0753
0.4	1.798	0.1593	0.0653
0.5	1.576	0.1166	0.0616
0.6	1.367	0.0866	0.0581
0.7	1.170	0.0678	0.0546
0.8	0.986	0.0556	0.0511
0.9	0.814	0.0458	0.0476
1	0.655	0.0358	0.0441

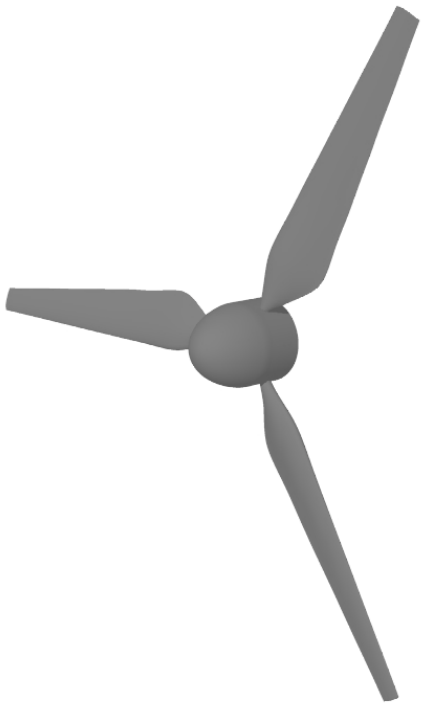

Figure 5-6: 3D representation of the example HATT

The bend-twist coupled spar is constructed of SE84LV UD carbon pre-preg (Table 4-6) and initially has 20 plies in the mid-layer at 20^o, 30 plies in the inner skin at 45^o and 5 plies in the outer roving at 90^o – each ply has a thickness of 2.81×10^{-4}m. The number of plies in the mid-layer are then increased in steps of five plies until the maximum stress criteria is achieved ($\sigma_y/3$).

Figure 5-7 illustrates a contour plot of the deformed blade indicating the undeformed edge, with displacement measured in metres. As expected the maximum displacement is at the tip of the blade, with a value of 1.48m. The changing contours can be observed to form diagonal stripes across the blade surface, indicating that the blade is twisting and the direction that twist is taking – clockwise around the axis down the centre of the blade (y-axis). The blade already has an inherent level of pre-twist, and therefore it is important to model the fibre orientation in the correct manner so that the induced twist accentuates this pre-twist rather than negating it.

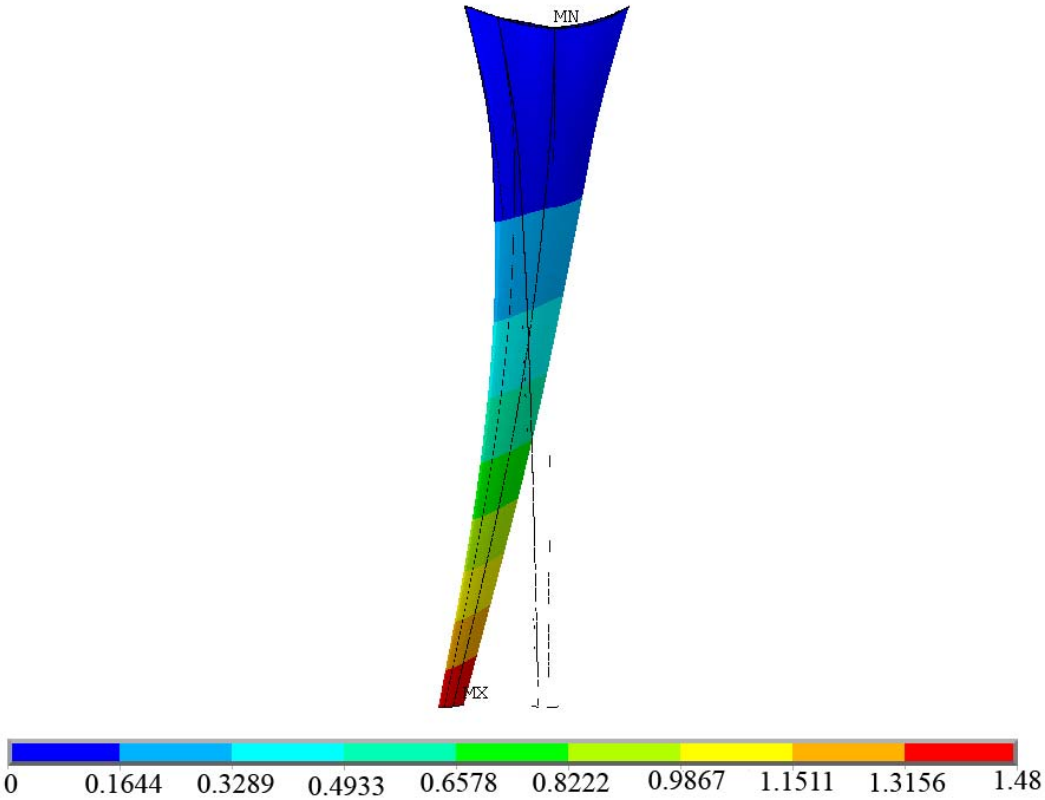

Figure 5-7: Contour plot of blade displacement in metres

Figure 5-8 illustrates the decrease in maximum stress in the beam with an increase in the number of plies. The maximum stress is located at the root of the blade. In this instance, each change increased the number of mid-layer plies by five. It can be observed that, for the turbine in question, increasing the number of plies in the mid-layer over 35 ensures the structure of the beam is adequate. An increase value of five was chosen to illustrate the procedure as each run is time consuming; however, in the case of a real life design scenario, the number of plies would be optimised to bring the maximum stress in close to the limiting criterion. This would prevent the structure being overdesigned and also minimise the amount of material (in this case carbon prepreg) that is required and hence structural weight, reducing costs and improving through-life performance. This is a relatively simple structural optimisation problem for obtaining the best layup, and it is thought that further work could be

carried out in order to optimise the structure fully in each layer of the beam and also the blade skin.

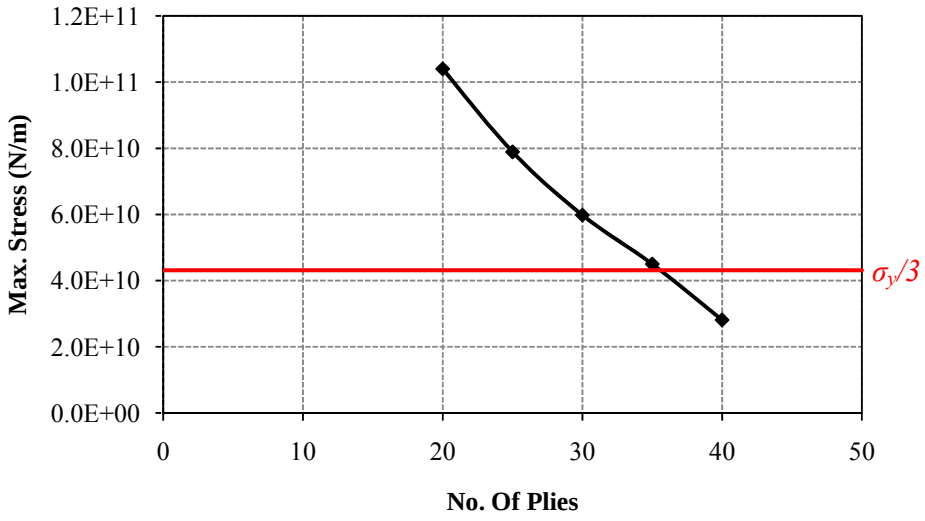

Figure 5-8: Decrease in maximum stress in the blade with increase in number of mid-plies

Once the maximum stress criterion has been satisfied, the problem is then looped back through the CFD code and iterations continued until the maximum bend in the blade is less than 0.01m (10mm) greater than the previous loop. In this case this occurred after 16 iterations, Figure 5-9.

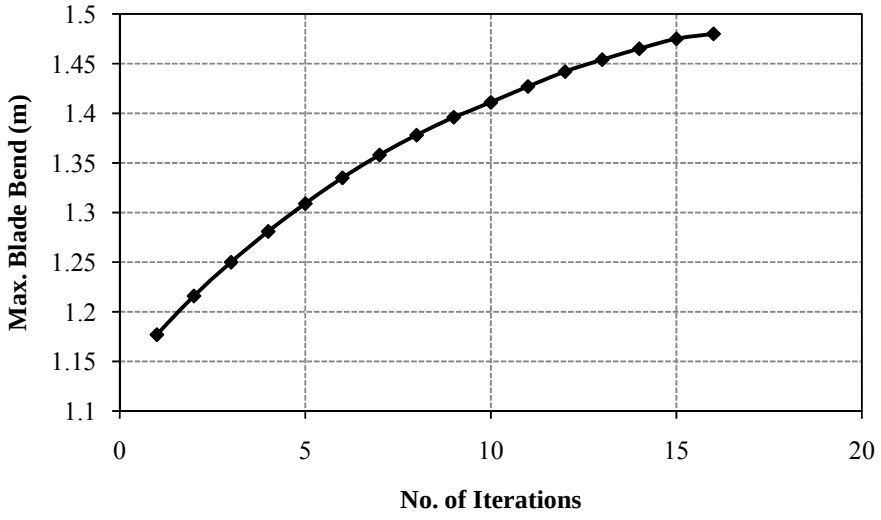

Figure 5-9: Number of iterations to convergence of maximum blade bend

There is good correlation between the results from the final iteration of the CFD study and the BEMT analysis, with less than 1% difference in thrust coefficient and 2% difference in power coefficient. The main properties of the turbine, and performance results, are detailed in Table 5-2.

Table 5-2: Case study turbine principal particulars and performance data

Current Velocity	2.5	(m/s)
Diameter	20	(m)
Number of blades	3	(blades)
Revolutionary speed	12	(RPM)
Mid-layer ply angle	20	(^{o})
Number of mid-layer plies	40	(plies)
Thrust	232.4	(kN)
Torque	792.3	(kNm)
Bend	1.48	(m)
Induced twist	8.6	(^{o})
Maximum stress	28.1	(GN/m^2)
Thrust coefficient	0.72	-
Power coefficient	0.40	-
Absorbed power	1248.9	(kW)

Figure 5-10 presents the bend and induced twist variation along the span of the example blade. Considering this in conjunction with Figure 4-18 and Figure 4-19, (which show similar data for the uniformly loaded, uniform section, bend-twist coupled double box beam) it can be seen that the pressure loading over the surface of the blade increases the non-linearity of the resulting bend in the blade. The relationship between induced twist and blade span is more linear than for the base double box beam; however, this will be dependent upon blade pitch, pre-twist distribution and turbine loading.

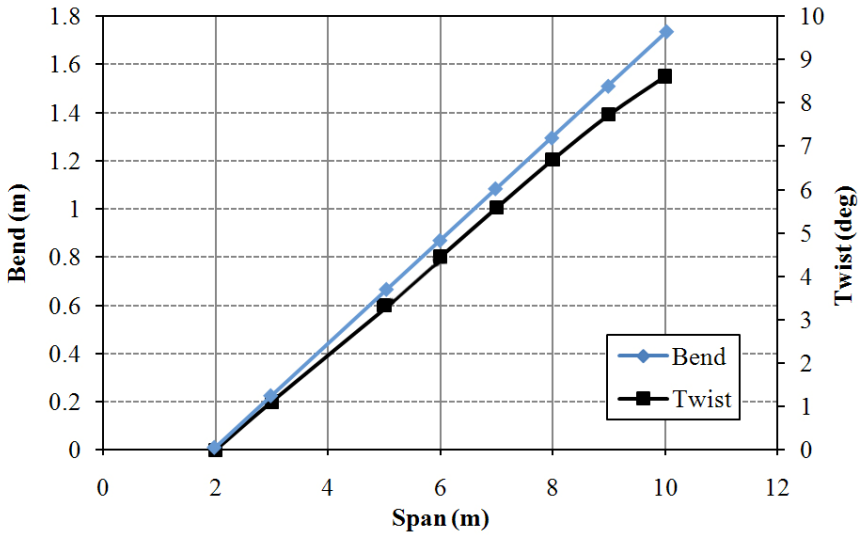

Figure 5-10: Bend and induced twist variation with span along the example blade

5.3 Discussion of Results

The design tool was used to analyse a range of turbines with bend-twist coupled blades in which the number of blades, flow velocity and diameter were varied whilst rotational speed was kept constant at 12RPM. The blade design for each turbine – section, chord, P/D etc. – is the same as detailed in Section 5.2. Table 5-3 details the results of this study indicating bend, induced twist, and C_T and C_{pow} from both the CFD and BEMT analyses.

It is apparent that the main limitation of BEMT, the assumed relation between disc and far wake induction, has a strong effect at high induction factors and thrust coefficients; indicated in Table 5-3 by the lower prediction of C_T from the BEMT. The CFD analysis predicted slightly higher values of C_{pow} than the BEMT. At this stage in the development of the design tool the iterative boundary layer prediction method was not included in the Palisupan calculations, thus explaining this increase. In practice a performance loss would be present due to the onset of stall; however, the cases at lower flow velocities in which stall was not occurring show better correlation between the BEMT and CFD results.

Case No.	No. of Blades	V_f (m/s)	D (m)	TSR	Bend (m)	Ind Twist (°)	Fixed				Adaptive				Change in C_T (%)	Change in C_{pow} (%)
							C_T CFD	C_{pow} CFD	C_T BEMT	C_{pow} BEMT	C_T CFD	C_{pow} CFD	C_T BEMT	C_{pow} BEMT		
1	2	1.5	10	4.189	0.08	0.94	0.194	0.046	0.161	0.023	0.172	0.047	0.147	0.024	-12.23	2.15
2	2	1.5	15	6.283	0.639	4.98	0.286	0.107	0.200	0.057	0.256	0.110	0.178	0.058	-11.86	2.82
3	2	1.5	20	8.378	2.513	14.41	0.777	0.154	0.543	0.140	0.693	0.160	0.495	0.146	-12.11	3.66
4	2	1.5	25	10.472	4.823	21.53	1.132	0.379	0.821	0.355	1.018	0.398	0.738	0.372	-11.23	4.58
5	2	2	10	3.142	0.061	0.72	0.217	0.077	0.179	0.043	0.196	0.078	0.162	0.044	-10.62	1.48
6	2	2	15	4.712	0.487	3.81	0.971	0.314	0.809	0.283	0.877	0.322	0.728	0.291	-10.74	2.44
7	2	2	20	6.283	1.912	11.06	1.073	0.438	0.751	0.402	0.973	0.451	0.678	0.418	-10.25	2.92
8	2	2	25	7.854	3.589	16.36	0.860	0.404	0.602	0.381	0.779	0.418	0.544	0.400	-10.50	3.29
9	2	2.5	10	2.513	0.05	0.59	0.453	0.139	0.374	0.088	0.413	0.142	0.338	0.090	-9.65	1.86
10	2	2.5	15	3.770	0.396	3.09	0.766	0.378	0.638	0.375	0.697	0.385	0.570	0.386	-9.77	1.62
11	2	2.5	20	5.027	1.548	9.00	0.670	0.336	0.468	0.320	0.614	0.346	0.420	0.333	-9.05	2.94
12	2	2.5	25	6.283	2.902	13.36	0.535	0.279	0.374	0.274	0.490	0.293	0.339	0.287	-9.17	4.85
13	3	1.5	10	4.189	0.071	0.84	0.140	0.033	0.116	0.017	0.125	0.034	0.106	0.017	-11.98	2.18
14	3	1.5	15	6.283	0.571	4.46	0.231	0.044	0.161	0.023	0.207	0.045	0.144	0.024	-11.61	2.87
15	3	1.5	20	8.378	2.25	12.95	0.269	0.052	0.188	0.048	0.240	0.054	0.172	0.050	-12.23	3.73
16	3	1.5	25	10.472	4.234	19.10	0.302	0.051	0.219	0.048	0.270	0.054	0.196	0.050	-11.48	4.66
17	3	2	10	3.142	0.054	0.64	0.135	0.041	0.111	0.023	0.122	0.041	0.100	0.023	-10.25	1.54
18	3	2	15	4.712	0.435	3.40	0.378	0.112	0.315	0.101	0.344	0.115	0.284	0.104	-10.01	2.49
19	3	2	20	6.283	1.709	9.91	1.041	0.221	0.728	0.203	0.942	0.228	0.657	0.211	-10.50	2.97
20	3	2	25	7.854	3.212	14.72	1.186	0.399	0.829	0.377	1.074	0.413	0.750	0.395	-10.38	3.35
21	3	2.5	10	2.513	0.044	0.52	0.172	0.038	0.142	0.024	0.158	0.039	0.128	0.024	-9.29	1.93
22	3	2.5	15	3.770	0.353	2.76	0.834	0.197	0.695	0.195	0.765	0.200	0.622	0.201	-9.05	1.66
23	3	2.5	20	5.027	1.382	8.05	1.030	0.424	0.720	0.404	0.944	0.437	0.645	0.420	-9.17	2.98
24	3	2.5	25	6.283	2.594	11.98	0.805	0.375	0.563	0.367	0.739	0.394	0.510	0.386	-8.81	4.91
25	4	1.5	10	4.189	0.064	0.75	0.091	0.003	0.075	0.002	0.081	0.003	0.069	0.002	-11.23	2.24
26	4	1.5	15	6.283	0.515	4.02	0.170	0.040	0.119	0.021	0.153	0.041	0.106	0.022	-11.36	2.88
27	4	1.5	20	8.378	2.033	11.74	0.231	0.026	0.161	0.023	0.208	0.027	0.147	0.024	-11.11	3.74
28	4	1.5	25	10.472	3.832	17.39	0.251	0.044	0.182	0.041	0.225	0.046	0.163	0.043	-11.36	4.67
29	4	2	10	3.142	0.049	0.57	0.124	0.025	0.102	0.014	0.113	0.025	0.092	0.014	-9.53	1.55
30	4	2	15	4.712	0.392	3.06	0.174	0.024	0.145	0.022	0.158	0.025	0.130	0.023	-9.77	2.51
31	4	2	20	6.283	1.541	8.95	0.256	0.047	0.179	0.043	0.233	0.049	0.162	0.045	-10.01	3.00
32	4	2	25	7.854	2.901	13.35	0.670	0.133	0.468	0.125	0.609	0.137	0.424	0.132	-9.89	3.36
33	4	2.5	10	2.513	0.04	0.47	0.119	0.026	0.098	0.016	0.109	0.026	0.088	0.017	-9.17	1.94
34	4	2.5	15	3.770	0.317	2.48	0.191	0.032	0.159	0.032	0.175	0.033	0.142	0.033	-8.81	1.67
35	4	2.5	20	5.027	1.245	7.26	0.973	0.226	0.680	0.215	0.885	0.233	0.610	0.224	-9.89	2.99
36	4	2.5	25	6.283	2.34	10.84	1.102	0.420	0.770	0.412	1.015	0.442	0.699	0.433	-8.58	4.92

Table 5-3: Design tool sample results

The solidity of a blade is defined as total blade area divided by the swept area – this can be altered by changing the number of blades or altering the blade chord. In this case it is the

number of blades that has been altered. It can be seen from Table 5-3 that C_{pow} changes less over a wide tip speed ratio for the two blade turbines (low solidity), cases 1-12. The higher solidity turbines tend to perform better at lower tip speed ratios, but are more sensitive to TSR changes. As was previously discussed in Section 2.3.2, in general turbines require a minimum of three blades to be self starting at low flow velocities, with two bladed devices requiring a greater flow velocity to start up thus negating the broader capture area under the C_{pow} curve that the low solidity creates. C_T can be observed to increase with an increase in solidity, although this is also dependent on the turbine diameter and resulting TSR. At higher tip speed ratios the lower solidity turbines experience greater thrust force.

Changing the diameter of the turbine alters the swept area of the device; an increase in diameter increases the amount of power available for extraction due to the increased rotor area. C_T and C_{pow} generally increase with an increase in diameter, but effectively it is the absorbed power of the device that is increasing which is reflected in the non-dimensional coefficients. The four bladed devices follow this trend, however the two and three bladed devices can be observed to have a reduction in C_T and C_{pow}, and hence absorbed power, at the highest flow velocities. The peak performance of the two bladed devices analysed occurred at a flow velocity of 2m/s with a diameter of 20m (case 7). The 25m diameter rotor then underperformed at this, and greater flow velocities for the lower solidity devices.

The final two columns of Table 5-3 show the percentage change of both C_T and C_{pow} between the initial fixed blade and the adaptive blades after the final run of the design tool. There is a general trend for a decrease in C_T, and an increase in C_{pow} with the use of the adaptive blades. This is in the same order as the preliminary analysis in Chapter 4 (10% decrease in thrust and 2.5% increase in power absorption); however, there are some interesting trends appearing in the more holistic analysis using the design tool. The reduction in C_T is, in general, greater at lower flow velocities (cases 1-4, 13-16 and 25-28) and also for lower solidity turbines. Conversely the improvement in C_{pow} increases slightly with increasing flow velocity. Previous work showed that while the adaptive blades did not increase the maximum C_{pow} of the turbine greatly, they caused the performance curve to broaden indicating the device was more efficient at higher tip speed ratios, and thereby capturing more energy over the whole tidal cycle. This trend has been confirmed by this more detailed analysis with a greater increase in C_{pow} at higher tip speed ratios. The larger

diameter devices tend to exhibit a greater improvement in C_{pow}; in the region of 4%. This can be attributed to the increased amount of coupling present in the blades due to the additional length. Comparing the bend and induced twist of the 10m and 25m diameter three bladed turbines at a flow velocity of 2.5m/s (cases 21 and 24 respectively) it can be seen that the bend increases from 0.044m to 2.594m and the induced twist increases from 0.172° to 11.98°. This is expected as the majority of torque, and hence thrust, to turn the turbine is developed from the outer third of the rotor diameter – the tip of the blade. The larger diameter turbine will therefore not only experience a greater thrust force due to the size increase, but also a significantly bigger bending moment thereby increasing the result of the bend-twist coupling present in the blade. Due to the manner in which the analysis has been carried out the number of plies in the mid-layer of each of these blades does differ in order to meet the maximum stress criterion, the 10m device had 35 plies and the 25m device 45 plies, this also contributes to the change in level of coupling. In this analysis the number of mid-layer plies were optimised for each individual condition (v_f, D, number of blades), whereas in reality for a specific number of blades and turbine diameter the composite layup will be the same as the tidal velocity changes.

Figure 5-11 illustrates three sets of power data for the three bladed device with zero degrees pitch at 12RPM: the initial fixed bladed device, the preliminary adaptively coupled device, and the coupled device analysed through the design tool. Each device has the same blade chord, section and pre-twist distribution.

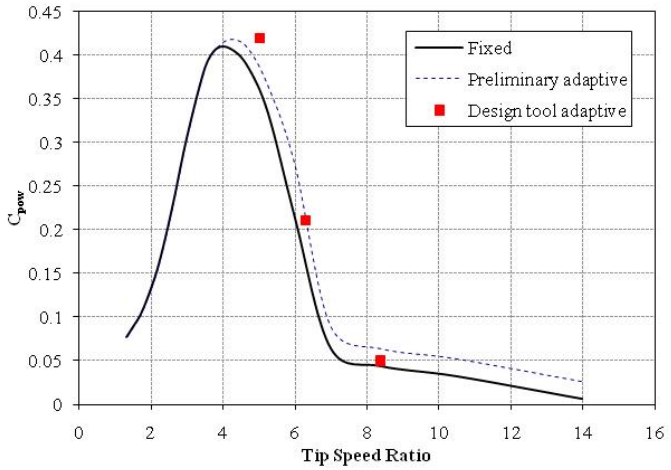

Figure 5-11: Relationship between TSR and C_{pow} for the fixed blade turbine, the preliminary analysis coupled turbine and the coupled turbine analysed using the design tool

The results gained through the design tool generally show good agreement with those of the preliminary analysis for the bend-twist coupled turbine. The maximum C_{pow} from the device analysed through the design tool is higher and occurs at a lower TSR than that for the preliminary device. Figure 5-12 illustrates the relationship between C_T and *TSR* for the same three cases, again for devices with blades at zero degrees pitch and rotating at 12RPM.

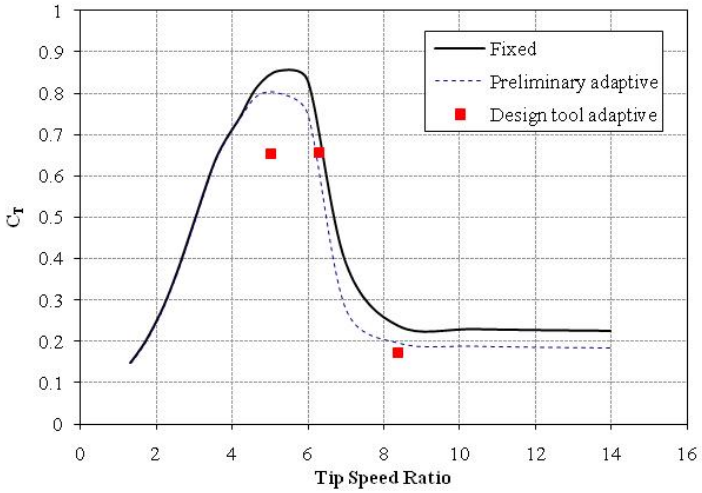

Figure 5-12: Relationship between TSR and C_T for the fixed blade turbine, the preliminary analysis coupled turbine and the coupled turbine analysed using the design tool

The results attained through the use of the design tool agree with the preliminary adaptive blade results for higher TSRs, but at lower TSR the more in depth analysis indicates an increased drop in thrust coefficient. This decrease in thrust loading causes a lessening in structural fatigue, and potentially increases turbine life-span, whilst reducing the frequency of maintenance required. This has positive implications for the through-life cost of the device, with maintenance being costly in the aggressive subsea environment; a reduction in the level of maintenance required should correspond to a reduction in through-life cost of the turbine.

It is understood that the flow regime into a tidal device at any one time is not constant, with variations in the vertical water column apparent alongside effects from turbines in arrays, and thus the blades experience changing inflow depending upon where they positioned in the area of the rotor disk. This transience should be reflected in both the CFD and FEA analyses in the design tool and is thought to be an area of further work.

The primary advantage of the use of flexible composite blades in the production of HATTs is the ability to tailor the structure to deflect in response to load changes, allowing the shape of the blade to adjust automatically to a changing inflow velocity therefore not compromising the performance over a range of conditions. There are many parameters that require optimisation in HATT blade design; not least the ones considered in this section but also blade rake, skew, pitch, section shape, and material choice and layup of both the blade skin and other regions of the bend-twist coupled central spar. Ultimately the blade analysis becomes complex and involves numerous time-consuming iterations of the design tool to produce an optimal design. In order to enable many iterations to be carried out multiple variable optimisation may be carried out through the use of an optimisation algorithm. The use of evolutionary optimisation techniques, such as Genetic Algorithms, allows a wide search space to be considered to find the global solution to a problem without solving for one of the many local optima within this search space. It is thought that a GA should be combined with the design tool in order to optimise the design problem whilst decreasing computational effort.

5.4 Blade Comparison

The physical constraints of most sites with sufficient energy density to allow cost-effective tidal power generation result in the need to install spatially distributed arrays of devices. This is not the case for wind turbines where there is more energy available at greater heights and it is structural constraints that limit the power of the machine [126]. As tidal current sites have predominantly bi-directional flow, the obvious approach is to place devices close together in a line perpendicular to the flow. Physical constraints, such as the width of channels, shipping lanes or insufficient water depth will often make it impossible to site enough turbines in a single line. Consequently multiple lines across the flow are likely to be required, in the form of an array similar to those used for multi-directional wind farms. By placing multiple turbines behind one another the inflow conditions into the downstream turbines will be dependent on the wake and blockage effects of the upstream row of turbines. The ability to propose a viable tidal energy scheme relies on an accurate assessment of the tidal resource at a specific location [127]. Detailed knowledge of how the local flow regime varies with depth and over short time scales comparable to the blade rate of rotation is

required for the specification of the blade strength and fatigue characteristics as well as the loading imposed on the support structure [128]. The interaction of an upstream turbine wake with a downstream turbine will make an important contribution to the unsteady fluctuations in velocity as well as to the overall kinetic energy available to a downstream tidal turbine.

Turnock et al [129] developed a method of replicating the wake downstream of a marine current turbine using a coupled RANS-BEMT approach. This method allows calculation of the power prediction from an array of turbines placed in close longitudinal and lateral proximity to each other. Extracting energy from the flow creates a turbulent region with reduced velocity behind the turbine. Turbulent mixing over the velocity gradient between the free stream and wake region starts to mix the two flows transferring momentum back into the wake. The turbulent mixing propagates both outwards and towards the wake's centreline, broadening the wake whilst reducing the velocity deficit. This continues far downstream where the velocity deficit becomes zero.

Figure 5-13 shows the broadening wake of a turbine, with locations of average radial velocity extraction taken at intervals of two diameters downstream.

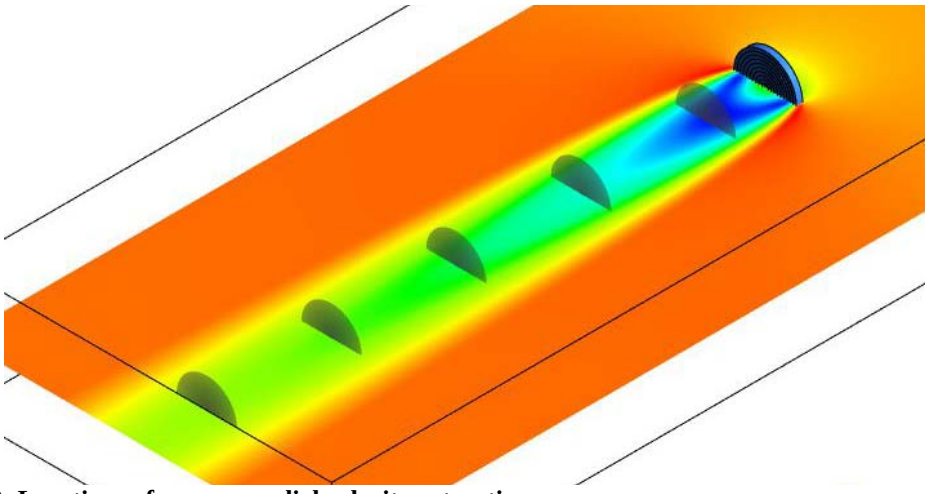

Figure 5-13: Locations of average radial velocity extraction

Blockage due to the presence of the turbine leads to acceleration of the flow either side of the turbine to maintain a constant mass flow rate, the smaller the turbine separation the more pronounced this effect becomes. This increased velocity results in larger velocity gradients which leads to more rapid mixing of the wake. The wake mixes more quickly with a reduced

turbine separation downstream. Figure 5-14 illustrates the wake structure with a two diameter lateral separation.

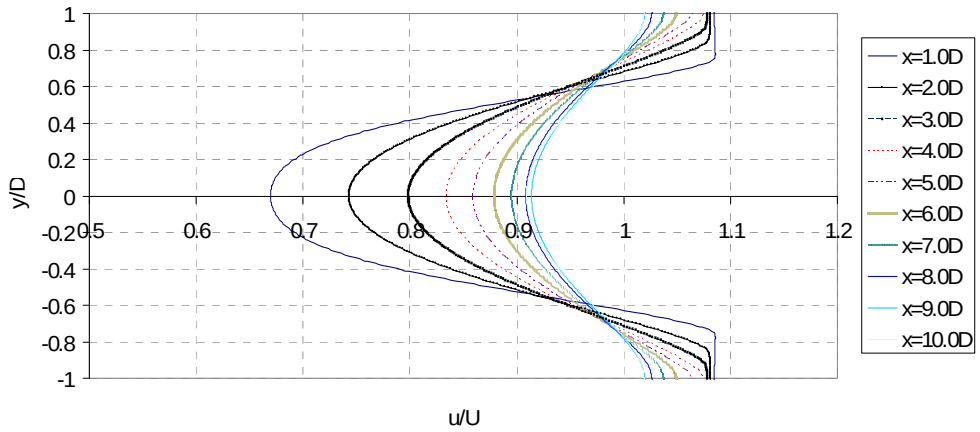

Figure 5-14: The turbine wake structure with a lateral separation of two diameters

Due to the blockage effect it was found to be beneficial to place the turbines in a staggered grid, Figure 5-15b), as opposed to a rectilinear grid, Figure 5-15a), in order to minimise detrimental wake influence on turbine performance and increase energy extraction from a tidal stream site. The subsequent analysis considers four HATTs in a staggered grid with a lateral spacing of 2D and a downstream spacing of 2D.

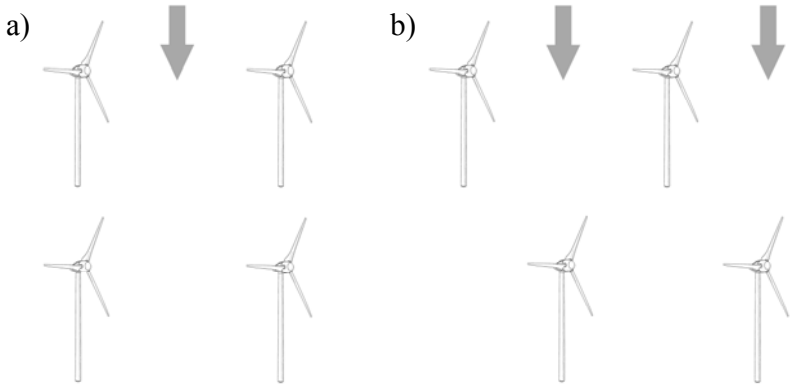

Figure 5-15: Turbines in a) a rectilinear array and b) a staggered array with two diameter lateral and longitudinal spacing

The turbines in this work are all 20m diameter, three bladed, HATTs. The only change being made to the devices is the type of blade in use. It was found using the RANS-BEMT analysis that for a 2D lateral and longitudinal spacing in a staggered grid the power absorption (P/P_o) of the downstream turbines was increased to 1.13 due to the accelerated flow resulting from blockage. For a single turbine situated in a tidal stream with a maximum spring peak current velocity of 2.0m/s, the P_o is 677.1kW and the annual energy capture of the device is 2.12MWh. For four individual turbines in a single row the annual energy capture is 8.48MWh, whereas for the four turbines situated in a staggered grid in the same flow regime, the total annual energy extracted is 8.99MWh. These turbines do not have any vaning or variable pitch mechanisms and therefore only operate throughout half the tidal cycle.

The second situation is one of four turbines in a staggered grid, but in this instance with bi-directional blades. The bi-directional turbine has the benefit of operating on both directions of the tidal flow and, as such, whilst the peak energy capture is less than that of a fixed blade rotor the overall annual energy capture will be higher. The annual energy capture of a single HATT with bi-directional blades in the same tidal stream as the fixed blade device is 3.59MWh; for four devices in a row this is 14.36MWh; and for four turbines in a staggered grid it is 15.29MWh. This is 70% greater than a standard, unidirectional, fixed blade turbine.

The third situation is one where the four turbines in the staggered grid have passively adaptive composite blades. The annual energy capture of a single turbine with passively adaptive, bend-twist coupled blades is 2.32MWh; that of four turbines in a row 9.28MWh; and that of four turbines in a staggered grid 9.88MWh. This a 10% improvement on the fixed blade turbines, however not as good as the bi-directional blade turbines due to the fact that it only operates in one direction of the tidal flow. It is apparent that turbines utilizing passively adaptive blades are more efficient than those with standard fixed blades (Chapter 4), and much more efficient than those with a bidirectional blade. The bi-directional devices are considerably more efficient when considering the whole tidal cycle. As mentioned previously variable pitch blades that can rotate 180^o would be one method of achieve bi-directionality, alternatively a mechanism allowing the turbine to yaw into the flow could also be employed. Both of these methods increase design complexity, however, and are difficult to maintain in the extreme subsea environment in which HATTs operate. The cost of getting boats and

divers out to the devices in the narrow operational windows of slack tide is large and hence maintenance is a key variable in the through life assessment of tidal turbine design.

Combining the concepts of both the passively adaptive, bend-twist coupled central spar and asymmetric snap-though laminates it may be possible to create a tidal turbine blade which is a sealed unit and that operates very efficiently in both directions of the tidal flow. The blade presents an asymmetric foil section to the flow in one direction, which adapts to local inflow conditions as a result of the couple spar; when the tide reverses, the asymmetric laminate skins are activated and the blade "snapped through" to create the same asymmetric foil section, but in the reverse direction. This enables the turbine to have optimal energy capture throughout the tidal cycle, whilst removing the need for variable pitch or vaning mechanism and therefore facilitating maintenance. This concept is covered in detail in Appendix E. The actively adaptive bladed turbine will have the same power curve as the passively adaptive bladed turbine but as the device can operate effectively in both directions of tidal flow it will have twice the annual energy capture. Hence the annual energy capture of a single device using actively adaptive blades would be 4.64MWh; that of a single row of four devices would be 18.56MWh; and that of a staggered grip of four turbines would be 19.77MWh. This is an improvement of almost 120% when compared to the base fixed pitch bladed turbine and around 25% more efficient than the bi-directional bladed turbine.

5.5 Summary

A tool for the design of passively adaptive, composite HATT blades has been developed. Initially both a CFD and an FE analysis are coupled together to create a holistic FSI interpretation of the flow over the blade and subsequent deformation. The CFD and FE analysis are iterated until a suitable level of convergence of blade deformation is reached. Several example problems have been analysed with the design tool and the results indicate that a significant improvement in turbine performance could be attained through the use of properly designed bend-twist coupled blades; with a decrease of up to 12% in C_T and an increase of up to 5% in C_{pow} apparent.

An array of four turbines in a staggered grid with different blades – fixed, bi-directional, passively adaptive and actively adaptive – has been considered and the annual energy capture for each situation calculated. While passively active turbine blades could

increase annual energy capture by around 10%, and bi-directional blades by 70%, actively adaptive blades could increase the annual energy capture of a fixed blade turbine by up to 120%. It is thought that the development of actively adaptive blades is an area of considerable scope for future consideration.

6 Conclusions

The use of adaptive composite blades has been shown to have the potential to increase power capture and decrease structural loading, and thereby increase the efficiency of horizontal axis tidal turbines.

6.1 Original Contributions and Summary

With a growing demand for renewable and sustainable sources of energy interest has turned towards our oceans and seas which are a huge resource of untapped energy. There are many marine renewable energy sources, but most are highly weather dependent. Tidal energy is, however, highly predictable and relatively unaffected by fluctuations in the climate. Tidal energy extraction devices have been in operation for a number of years with barrages a proven and effective method. With growing concerns for the environmental impact of potential energy devices, more attention has been drawn to free stream energy extraction projects. HATT technology is similar to that of wind turbines and therefore is already available to a certain degree. Some devices have been proven to be effective but few are grid connected and no commercial instalments exist as yet. Further research into advancing concepts, increasing the efficiency, and improving maintenance is required to enable the devices more efficient at capturing energy economically.

With the concerns surrounding potential energy devices it is expected that HATTs will ultimately be the favoured method. HATTs are required to operate in a harsh subsea environment for a long (20 year) life cycle with minimal need for maintenance and as such all of the components need to be designed as efficiently and effectively as possible. As such optimisation of the design of the HATT blades is important. Design tools for blade optimisation have been assessed. With tides being inherently bi-directional in nature, tidal devices either need to sacrifice half the tidal cycle or operate in both directions of the tidal flow. Most devices have an asymmetric foil section on the blade which is very efficient in one direction of tidal current, but significantly less so in reverse. Possibilities exist to vane the whole turbine to face the current, in the manner of wind turbines, or use a variable pitch mechanism to rotate the blade 180^{o} upon current reversal. Both of these methods, however, increase design complexity and are unlikely to last long before requiring maintaining. A blade utilising a fully bi-directional section does not require such mechanisms to operate

throughout the entire tidal cycle. A novel bi-directional section has been developed and examined for use on a HATT. The bi-directional blade is site specific but may be more economic in certain locations where a higher tidal velocity is sustained. Turbine performance and energy extraction for a device using VP blades and one using bi-directional blades have been compared and discussed.

Adaptive composite technology has been in use in the aerospace industry for some time, and is now also being integrated into blades for wind turbines; however there are limited applications in the marine field. Adaptive composite technology has been assessed for integration into HATT blade design in order to improve the overall efficiency of the tidal device and hence annual energy capture. Preliminary analysis of a new conceptual blade with an integrated bend-twist coupled composite spar showed that such a blade has the potential to increase annual energy capture by around 2.5%. A decrease in thrust loading of up to 10% was also observed, thereby increasing the fatigue life of the turbine and associated structure. The base BEMT code has been modified to create a coupled blade performance prediction program in order to assess the performance of a range of devices. An experimental method for measuring the level of bend and induced twist in a composite beam has been developed. The results from these experiments have been compared to those attained through the use of FEA of an identical coupled composite spar. It was found that the FEA was very sensitive to manufacturing accuracy. Alterations in material properties and ply layup angle resulted in an increase in beam bend estimates of 3% and 14% respectively. It was also observed that the FEA did not capture occurrences of ply wise failure in the composite beam leading to further under prediction of bending and therefore induced twist at higher loads. Overall the FEA was considered to be a powerful tool for the analysis of coupled composite spars, as long as care is taken when manufacturing the final beam so that the results are consistent.

A new tool for the design of passively adaptive, composite HATT blades has been developed. A surface panel code is used to predict the pressure loading on an initial HATT blade. This data is then used in FEA to assess the structural response of a composite beam. The deformed shape is then fed back into the CFD code and a new pressure distribution calculated. Likewise these forces are imported back into the FEA and so forth in an iterative manner until a suitable level of convergence of blade deformation is reached. The performance data is then checked using the BEMT code and the design of an adaptive blade

realised. Several example problems were analysed using the design tool. The results compare well to the preliminary studies and indicate that a decrease of up to 12% in C_T and an increase of up to 5% in C_{pow} could be achieved through the use of properly designed bend-twist coupled blades.

Passively adaptive blades have been shown to offer potential improvements in HATT efficiency and design. Introducing active adaptation to the passively adaptive blades in the manner of snap-through blade skins and telescopic blades edges has been suggested. Such a blade would proffer an efficient asymmetric section to the flow in one direction but upon current reversal is able to adapt and present the same asymmetric section to the flow in the other direction. The blade negates the need for complex variable pitch or vaning mechanisms. The annual energy capture of a staggered array of four turbines alternately using standard fixed pitch, bi-directional, passively adaptive and actively adaptive blades has been calculated. It was found that while passively active turbine blades could increase annual energy capture by around 10%, and bi-directional blades by 70%, actively adaptive blades could improve the annual energy capture of a fixed blade turbine by up to 120%. It is thought that the development of actively adaptive blades is an area of considerable scope for future consideration.

6.2 Further Work

While a design tool for the optimisation of passively adaptive composite blades has been developed, it is felt that the structural model could be further refined to take into account plywise failure of composites and thus model physical composite spars more accurately. More comprehensive structural optimisation should be included, alongside a blade cost model, in order to minimise the amount of material in the blade and hence cost.

Turbine blades experience a varying inflow depending upon their location around the rotor disk at any moment in time. The CFD analysis should be updated to reflect this fluctuation and a transient FEA used for a more accurate loading scenario. Coupling of the design tool with an optimisation code, for example a Genetic Algorithm, could prove beneficial with regards to finding the best possible blade for a certain situation whilst minimising computational expense.

Further construction and testing of passively adaptive composites should be undertaken in order to validate the numerical design tool. Research and use of different types of composite and manufacturing processes could be beneficial in order to construct the test blades more precisely. Both model and full scale blades should be built and tested.

The concept of an actively adaptive blade has been investigated and it is thought that this is an area of potential breakthrough in HATT blade design. Further consideration of the concept should be undertaken; specifically to assess appropriate materials with good properties in fatigue and low creep rates for use as the snap-through laminate skins and analysis of appropriate actuation methods and powering of such methods.

There is also potential to apply the adaptive composite technology to other fields, not least race car aerodynamics, aircraft control surfaces, surface ship and underwater vehicle control surfaces, and wind turbines.

6.3 Concluding Remarks

Tidal energy is an immature industry with great potential. Horizontal axis tidal turbines are likely to be the winner in the race for a commercially feasible device. Current blade design is functional but has significant room for optimisation. Bi-directional blade sections could be implemented for improved performance throughout the whole tidal cycle, but is relatively site specific. Passively adaptive composite blades have been proven to increase annual energy capture and decrease thrust on a device, thereby increasing efficiency and life expectancy whilst potentially minimising maintenance. A design tool has been created for the development of passively adaptive bend-twist coupled HATT blades and analysis of several example devices indicates that a significant improvement could be gained through the use of passively adaptive blades. The concept of an actively adaptive HATT blade utilising asymmetric laminates for snap-through skins has been investigated and potentially shows an improvement of up to 120% in annual energy capture when compared to a standard fixed blade design.

References

1. Kirke, B. (2005) *Developments in Ducted Water Current Turbines*. 12.
2. Charlier, R.H., *A "Sleeper" Awakes: Tidal Current Power.* Renewable and Sustainable Energy Reviews, 2003. **7**: p. 515-529.
3. Callaghan, J. and Boud, R., *Future Marine Energy*. 2006, Carbon Trust.
4. ENTEC and BWEA, *Marine Renewable Energy - State of the Industry Report*, R. UK, Editor. 2009.
5. VanZwieten, J., Driscoll, F.R., Leonessa, A., and Deane, G., *Design of a Prototype Ocean Current Turbine - Part I: Mathematical Modeling and Dynamics Simulation.* Ocean Engineering, 2006.
6. Harrison, G.P. and Wallace, A.R., *Climate Sensitivity of Marine Energy.* Journal of Renewable Energy, 2005. **30**(12): p. 1801-1817.
7. Pearce, N., *Worldwide Tidal Current Energy Developments and Opportunities for Canada's Pacific Coast.* International Journal of Green Energy, 2005. **2**: p. 365-386.
8. Nicholls-Lee, R.F. and Turnock, S.R., *Tidal Energy Extraction: Renewable, Sustainable and Predictable.* Science Progress, 2008. **91**(1): p. 81-111.
9. Burton, T., Sharpe, D., Jenkins, N., and Bossanyi, E., *Wind Energy Handbook*. 2004, Chichester: John Wiley & Sons Ltd.
10. Bungartz, H.-J. and Schafer, M.E., *Fluid-Structure Interaction*. Lecture Notes in Computational Science and Engineering. 2006: Springer. 251.
11. Karaolis, N., Mussgrove, P., and Jeronimidis, G. *Active and Passive Aeroelastic Power Control Using Asymmetric Fibre Reinforced Laminates for Wind Turbine Blades*. in *Proceedings of the 10th British Wind Energy Conference*. 1988. London, U.K.
12. Lobitz, D.W. and Veers, P.S., *Aeroelastic Behavior of Twist-Coupled HAWT Blades*, in *36th Aerospace Sciences Meeting and Exhibit and 17th ASME Wind Energy Symposium*. 1998, American Institute of Aeronautics and Astronautics: Reno, Nevada, USA.
13. Malcolm, D.J. and Laird, D.L., *Modelling of Blades as Equivalent Beams for Aeroelastic Analysis*, in *41st Aerospace Sciences Meeting and Exhibit*. 2003, American Institute of Aeronautics and Astronautics: Reno, Nevada, USA.
14. Veers, P., Bir, G., and Lobitz, D., *Aeroelastic tailoring in Wind Turbine Blade Applications*, in *Windpower '98, American Wind Energy Association Meeting and Exhibition*. 1998, Sandia National Laboratories: Bakersfield, California, USA.
15. Wilson, J.R., *Active Aeroelastic Wing: A New/Old Twist on Flight.* Aerospace America, 2002: p. 34-37.
16. Khan, A.M., Adams, D.O., Dayal, V., and Vogel, J.M., *Effects of Bend-Twist Coupling on Composite Propeller Performance.* Mechanics of Composite Materials and Structures, 2000. **7**: p. 383-401.
17. Young, Y.L., Michael, T.J., Seaver, M., and Trickey, M.T. *Numerical and Experimental Investigations of Composite Marine Propellers*. in *26th Symposium on Naval Hydrodynamics*. 2006. Rome, Itlay.

18. Liu, Z. and Young, Y., *Utilization of Bend-Twist Coupling for Performance Enchancement of Composite Marine Propellers.* Journal of Fluids and Structures, 2009. **25**: p. 1102-1116.
19. Young, Y.L., *Dynamic Hydroelastic Scaling of Self-Adaptive Composite Marine Rotors.* Composite Structures, 2010. **92**: p. 97-106.
20. Young, Y., Baker, J., and Motley, M., *Reliability-Based Design and Optimization of Adaptive Marine Structures.* Composite Structures, 2010. **92**: p. 244-253.
21. Hyer, M., *Some Observations on the Cured Shape of Thin Unsymmetric Laminates.* Journal of Composite Materials, 1981. **15**(2): p. 175-194.
22. Hyer, M., *Calculations of the Room-Temperature Shapes of Unsymmetric Laminates.* Journal of Composite Materials, 1981. **15**: p. 296-310.
23. Hyer, M., *The Room-Temperature Shapes of Four-Layer Umsymmetric Laminates.* Journal of Composite Materials, 1982. **16**: p. 319-340.
24. Schlecht, M., Schulte, K., and Hyer, M., *Advanced Calculation of the Room-Temperature Shapes of Unsymmetric Composite Laminates.* Journal of Composite Materials, 1999. **33**(16): p. 1472-1490.
25. Pugh, D., *Tides, Surges and Mean Sea-Level*. 2nd ed. 1996: John Wiley & Sons.
26. Cartwright, D., *Tides: a Scientific History*. 1999: Cambridge University Press.
27. DTI (2004) *Annual Mean Tidal Power Density*. Atlas of UK Marine Renewable Energy Resources.
28. Myers, L. and Bahaj, A.S., *Simulated Electrical Power Potential Harnessed by Marine Current Turbine Arrays in the Alderney Race.* Journal of Renewable Energy, 2005. **30**: p. 1713-1731.
29. Blunden, L.S. and Bahaj, A.S., *Initial Evaluation of Tidal Stream Energy Resources at Portland Bill, UK.* Journal of Renewable Energy, 2006. **31**: p. 121-132.
30. Batten, W.M.J., Bahaj, A.S., Molland, A.F., and Blunden, L.S., *Yawed Performance of Horizontal Axis Marine Current Turbines*, in *Conference on Renewable Energy in Island Maritime Climate*. 2006: Dublin.
31. Pontes, M.T. and Falcao, A., *Ocean Energies: Resources and Utilisation*, in *18th World Energy Conference*. 2001: Buenos Aires, Argentina.
32. Bahaj, A.S. and Myers, L., *Analytical Estimates of the Energy Yield Potential from the Alderney Race (Channel Islands) Using Marine Current Energy Converters.* Journal of Renewable Energy, 2004. **29**: p. 1931-1945.
33. Rivas, L.N. and Herreros, M.A., *Gibraltar's Strait a Marine Renewble Energy Source*, in *World Maritime Technology Conference*. 2006, IMarEST: London.
34. EC, *Non-nuclear Energy - JOULE II Project: The Exploitation of Tidal and Marine Currents*. 1996: European Commission.
35. *Phase II UK Tidal Stream Energy Resource Assessment*, C. Trust, Editor. 2005.
36. Blunden, L.S. and Bahaj, A.S., *Tidal Energy Resource Assessment for Tidal Stream Generators.* Proceedings of the Institution of Mechanical Engineers, Part A: Journal of Power and Energy, 2007. **221**(2): p. 137-146.
37. Perier, C., *The Rance Tidal Power Plant*, in *Wave and Tidal Technology Symposium*. 2007, Renewable Energy Association: Cowes, Isle of Wight, U.K.
38. Macnaughton, D., Fraenkel, P., Paish, O., Hunter, R., and Derrick, A. *Tidal Stream Turbine Development*. in *IEE Conference No. 385*. 1993. London, UK.

39. Roach, J., *Underwater Windmill Helps Power Arctic Village.* National Geographic News, 2003.
40. Hulsbergen, K., Steijn, R.C., Hassan, R., Klopman, G., and Hurdle, D., *Dynamic Tidal Power (DTP)*, in *6th European Wave and Tidal Energy Conference* 2005: Glasgow, UK.
41. Hulsbergen, K., van Banning, G., Steijn, R., and Klopman, G., *Dynamic Tidal Power A New Approach to Exploit Tides*, in *2nd International Conference on Ocean Energy (ICOE 2008)*, Ifremer, Editor. 2008: Brest, France.
42. Turnock, S.R., Muller, G., Nicholls-Lee, R.F., Denchfield, S., Hindley, S., Shelmerdine, R., and Stevens, S., *Development of a Floating Tidal Energy System Suitable for use in Shallow Water*, in *7th European Wave and Tidal Energy Conference* 2007: Porto, Portugal.
43. *The Severn Barrage*, C. Cyfeillion y Ddaear, Editor. 2007.
44. Ullman, P., *Offshore Tidal Power Generation - A New Approach to Power Conversion of the Oceans' Tides.* Marine Technology Society Journal, 2003. **36**(4): p. 16-24.
45. Kerr, D., *Marine Energy.* Philosophical Transactions of The Royal Society, A: Mathematical, Physical and Engineering Sciences, 2007. **365**: p. 971-992.
46. Betz, A., *Schraubenpropeller mit Geringstem Enegieverlust*, in *Gottinger Nachr*. 1919: Germany.
47. Thorpe, T., *The Advantages of Ducted over Unducted Turbines*, in *6th European Wave and Tidal Energy Conference*. 2005: Glasgow, UK.
48. Clarke, J.A., Connor, G., Grant, A.D., and Johnstone, C.M., *Design and Initial Testing of a Contra-Rotating Tidal Current Turbine*, in *6th European Wave and Tidal Energy Conference*. 2005: Glasgow, UK.
49. Block, E., *Tidal Power: an Update.* Renewable Energy Focus, 2008. **9**(6): p. 58-61.
50. *Stingray Tidal Stream Device - Phase 2*, DTI, Editor. 2003, The Engineering Business Ltd.
51. Fraenkel, P., *Marine Current Turbines Ltd's Tidal Turbine Developments: The Development of an Entirely New Energy Conversion System*, in *World Maritime Technology Conference*. 2006, IMarEST: London.
52. ISSC. *Ocean Wind and Wave Energy Utilization*. in *19th International Ship and Offshore Structures Congress*. 2006. Southampton, UK: University of Southampton Press.
53. Goldin, D., Venneri, S., and Noor, A., *Fresh Air, Wide-Open Space.* Mechanical Engineering, 2001. **123**(11): p. 48-55.
54. Hulsbergen, K., Steijn, R., van Banning, G., and Klopman, G., *Dynamic Tidal Power - A New Approach to Exploit Tides*, in *2nd International Conference on Ocean Energy (ICOE 2008)*. 2008, Ifremer: Brest, France.
55. Jones, J.A. and Chao, Y., *Offshore Hydrokinetic Energy Conversion for Onshore Power Generation*, in *28th International Conference on Ocean, Offshore and Arctic Engineering*. 2009: Honolulu, Hawaii.
56. Minesto. *Minesto Tidal Energy*. 2007 [cited 2011 4th February]; Available from: http://www.minesto.com/.
57. Flumill. *Flumill Power Tower - The Future of Renewable Energy*. 2008 [cited 2011 4th February]; Available from: http://www.flumill.co.uk/.

58. Tidalsails. *Tidal Sails*. 2004 [cited 2011 4th February]; Available from: http://www.tidalsails.com/.
59. Manchester, R., *The TidEL Floating Free-Stream Tidal Turbine System*, in *World Maritime Technology Conference*. 2006, IMarEST: London.
60. DTI, *Stingray Tidal Stream Energy Device - Phase 2*, DTI, Editor. 2003. p. 22.
61. Energy, B. *Blue Energy Tidal Power*. 1997 [cited 2008 16th February]; Available from: http://www.bluenergy.com.
62. Power, V. *Verdant Power*. 2009 [cited 2009 17th April]; Available from: http://verdantpower.com/.
63. Electric, T. *Tidal Electric*. 2011 [cited 2011 26th February]; Available from: http://www.tidalelectric.com/.
64. *Energy From Tidal Barrages Technology Route Map*, D.o.T.a. Industry, Editor. 2003, Department of Trade and Industry.
65. Energy, K. *Kepler Energy*. 2011 [cited 2011 5th February]; Available from: http://www.keplerenergy.co.uk.
66. Atlantis. *Atlantis Resources Corporation*. 2009 [cited 2011 5th February]; Available from: http://www.atlantisresourcescorporation.com/.
67. Orme, J.A.C. and Masters, I., *Analysis and Comparison of Support Structure Concepts for Tidal Stream Turbines*, in *World Maritime Technology Conference*. 2006, IMarEST: London.
68. *Huge Tidal Experiment Begins*. 2006 [cited 2006 14/12/2006]; News excerpt]. Available from: http://news.bbc.co.uk/nolavconsole/ukfs_news/hi/newsid_6170000/newsid_6171200/bb_wm_6171219.stm.
69. Turnock, S.R. and Nicholls-Lee, R.F., *Design of Three Bladed Tidal Turbine Blades for Bi-Directional Fixed Pitch or Azimuthing Variable Pitch Operation*, in *Economic Viability of a Simple Tidal Stream Energy Capture Device*, Log+1/Alstom/WUMTIA, Editor. 2006.
70. *New Electricity Trading Arrangements Daily Report*. 2006 Daily [cited 2006 14/12/2006]; Available from: http://www.bmreports.com/bwx_reporting.htm.
71. Fraenkel, P., *Progress with Marine Current Turbines*, in *6th European Wave and Tidal Energy Conference*. 2005: Glasgow, UK.
72. Bahaj, A.S. and Myers, L.E., *Fundamentals Applicable to the Utilisation of Marine Current Turbines for Energy Production.* Journal of Renewable Energy, 2003. **28**(14): p. 2205-2211.
73. OPSI, *The Renewables Obligation Order 2009*. 2009.
74. Akwensivie, F., *Marine Current Energy Baseload Supply Strategy for Scotland 2004*, in *Energy Systems and the Environment MSc Group Project*. 2004: Strathclyde.
75. Molland, A.F., Bahaj, A.S., Chaplin, J.R., and Batten, W.M.J., *Measurements and Predictions of Forces, Pressures and Cavitation on 2-D Sections Suitable for Marine Current Turbines.* Proceedings of the Institute of Mechanical Engineers, 2004. **218**(M): p. 127-138.
76. Molland, A.F. and Turnock, S., *Marine Rudders and Control Surfaces*. 2007: Butterworth-Heinemann. 448.
77. Ellsmore, P., *Optimisation of a Bi-Directional Section*, in *School of Engineering Sciences*. 2002, University of Southampton: Southampton.

78. Batten, W.M.J., Bahaj, A.S., Molland, A.F., and Chaplin, J.R., *Hydrodynamics of Marine Current Turbines.* Journal of Renewable Energy, 2006. **31**: p. 249 - 256.
79. Barnsley, M.J. and Wellicome, J.F., *Dynamic Models of Wind Turbines - Aerodynamic Model Development*. 1993.
80. Buckland, H.C., Masters, I., Chapman, J.C., and Orme, J.A.C., *Blade Element Mometum Theory in Modelling Tidal Stream Turbines*, in *18th UK Conference on Computational Mechanics (ACME-UK)*. 2010: Southampton, UK.
81. Hess, J., *Panel Methods in Computational Fluid Dynamics.* Annual Review of Fluid Mechanics, 1990. **22**: p. 225-274.
82. Katz, J. and Plotkin, A., *Low Speed Aerodynamics*. 2001, Cambridge University Press: Cambridge, U.K.
83. Turnock, S.R., *Palisupan User Guide*. 2000.
84. Pashias, C., *Propeller Tip Vortex Simulation Using Adaptive Grid Refinement Based on Flow Feature Identification*, in *School of Engineering Sciences*. 2005, University of Southampton: Southampton.
85. Launder, B. and Spalding, D., *The Numerical Computation of Turbulent Flows.* Computer Methods in Applied Mechanics and Engineering, 1974. **3**: p. 269-289.
86. Fan, R. and Zhou, Z., *Numerical Predictions and Experimental Verifications for the Hydrodynamic Performance of Horizontal Axis Marine Current Turbine*, in *11th Numerical Towing Tank Symposium (11th NuTTs)*, ENSIETA, Editor. 2008: Brest, France. p. 91-96.
87. Grant, A.D., Johnstone, C.M., and McCombes, T., *Unsteady Hydrodynamic Modelling of Rotor Systems used in Marine Current Turbines*, in *10th World Renewable Energy Congress*. 2008: Glasgow, U.K.
88. Barnaby, S.W., *On the Formation of Cavities in Water by a Screw Propeller at High Speed.* Insitute of Naval Architects, 1897.
89. Parsons, C., *The Application of the Compund Steam Turbine to the Purpose of Marine Propulsion.* Insitute of Naval Architects, 1897.
90. Wang, D. and Atlar, M., *Experimental Investigation on Cavitation Performance, Noise Characteristics and Slipstream Wash of an Ocean Stream Turbine*, in *World Maritime Technology Conference*. 2006, IMarEST: London.
91. Bhagat, R.B., *Cavitation Erosion of Composites.* Journal of Materials Science Letters, 1987. **6**: p. 1473-1475.
92. Hammond, D.A., Amateau, M.F., and Queeney, R.A., *Cavitation Erosion Performance of Fiber Reinforced Composites.* Journal of Composite Materials, 1993. **27**(16): p. 1522-1544.
93. Light, K.H., *Development of a Cavitation Erosion Resistant Advanced Material System*, in *Mechanical Engineering*. 2005, University of Maine: Maine. p. 66.
94. ITTC. *The Specialist Committee on Cavitation Erosion on Propellers and Appendages on High Powered/High Speed Ships*. in *24th ITTC*. 2005. Edinburgh, U.K.
95. Young, Y.L., *Fluid-Structure Interaction Analysis of Flexible Composite Marine Propellers.* Journal of Fluids and Structures, 2008. **24**: p. 799-818.
96. *Principles of Naval Architecture*, ed. J.P. Comstock. 1967, New York, USA: Society of Naval Architects and Marine Engineers.
97. Cook, R., Malkus, D., and Plesha, M., *Concepts and Applications of Finite Element Analysis*. Third Edition ed. 1989: John Wiley & Sons.

98. Batten, W.M.J., Bahaj, A.S., Molland, A.F., and Chaplin, J.R., *Experimentally Validated Numerical Method for the Hydrodynamic Design of Horizontal Axis Tidal Turbines*, in *6th European Wave and Tidal Energy Conference* 2005: Glasgow, UK.
99. Gretton, G. and Bruce, T., *Preliminary Results from Analytical and Numerical Models of a Variable-Pitch Vertical-Axis Tidal Current Turbine*, in *6th European Wave and Tidal Energy Conference*. 2005: Glasgow, UK.
100. Drela, M. and Youngren, H., *XFOIL 6.94 User Guide*. 2001.
101. Reddy, J.N., *Mechanics of Laminated Composite Plates and Shells: Theory and Analysis*. 2nd Edition ed. 2004, Boca Raton, Florida, USA: CRC Press LLC.
102. Eisler, G.R. and Veers, P.S., *Parameter Optimisation Applied to Use of Adaptive Blades on a Variable Speed Wind Turbine*. 1998, Sandia National Laboratories.
103. Fraenkel, P.L., *Power from Marine Currents.* Journal of Power and Energy, 2002. **216**(1): p. 1-14.
104. Locke, J. and Hidalgo, I.C., *The Implementation of Braided Composite Materials in the Design of a Bend-Twist Coupled Blade*, in *Sandia Report*. 2002, Sandia National Laboratories.
105. Kooijman, H., *Bending-Torsion Coupling of a Wind Turbine Rotor.* 1996.
106. Lobitz, D.W., Veers, P.S., and Migliore, P.G., *Enhanced Performance of HAWTs Using Adaptive Blades*, in *Wind Energy '96, ASME Wind Energy Symposium*. 1996: Houston, U.S.A.
107. Lobitz, D.W. and Laino, D.J., *Load Mitigation With Twist Coupled HAWT Blades*, in *37th Aerospace Sciences Meeting and Exhibit and 18th ASME Wind Energy Symposium*. 1999, American Institute of Aeronautics and Astronautics: Reno, Nevada, USA.
108. Maheri, A., *A New Approach in Simulation of Wind Turbines Utilising Bend-Twist Adaptive Blades*. 2006, University of the West of England: Bristol.
109. Greenhalgh, E.S., Pastore, C., and Garfinkle, M., *A Continuous-Fiber Composite Wing Box-Beam Exhibiting Twist-Beam Coupling.* Composite Engineering, 1993. **3**.
110. Ong, C.H. and Tsai, S.W., *Design, Manufacture and Testing of a Bend-Twist D-Spar*, S.N. Laboratories, Editor. 1999, Department of Aeronautics and Astronautics, Stanford University: Stanford, California.
111. Griffin, D.A., *Evaluation of Design Concepts for Adaptive Wind Turbine Blades*, in *Sandia Report*. 2002, Sandia National Laboratories.
112. Maheri, A., Noroozi, S., Toomer, C., and Vinney, J., *A Simple Algorithm to Modify an Ordinary Wind Turbine Blade to an Adaptive One*, in *EWEC 2006*. 2006: Athens, Greece.
113. Inc., A., *ANSYS 12.1 Help*. 2009, Canonsburg, Pennsylvania.
114. Gurit, *SE84LV - Low Temperature Cure Epoxy Prepreg System*, Gurit. p. 6pp.
115. Benham, P.P., Crawford, R.J., and Armstrong, C.G., *Mechanics of Engineering Materials*. 2nd Edition ed. 1996, Harlow, England: Addison Wesley Longman Limited.
116. Jones, R.M., *Mechanics of Composite Materials*. Second Edition ed. 1999, Abingdon: Taylor & Francis Group.
117. Judd, N.C.W. and Wright, W.W., *Voids and their Effects on the Mechanical Properties of Composites - An Appraisal.* SAMPE Journal, 1978. **14**: p. 10-14.

118. Molland, A.F. and Turnock, S.R., *The Design and Construction of Model Ship Propeller Blades in Hybrid Composite Materials.* Composites Manufacturing, 1991. **2**(1).
119. Strong, A.B., *Fundamentals of Composite Manufacturing: Materials, Methods and Applications*. 1989, Dearborn, MI: Society of Manufacturing Engineers.
120. Nicholls-Lee, R. and Turnock, S., *Enhancing Performance of a Horizontal Axis Tidal Turbine using Adaptive Blades*, in *Oceans '07*. 2007, IEEE: Aberdeen, Scotland.
121. Turnock, S.R. and Wright, A.W., *Directly Coupled Fluid Structural Model of a Ship Rudder Behind a Propeller.* Marine Structures, 2000. **13**(1): p. 53-72.
122. Casagrande, A., *Coupled Dynamic Fluid Structural Model of a Propeller at One Time Step*, in *School of Engineering Sciences*. 2000, University of Southampton: Southampton.
123. Rycroft, N. and Turnock, S., *Three Dimensional Multiblock Grid Generation: Fleximesh*. 1997, Univeristy of Southampton: Southampton.
124. Commission, I.E., *Wind Turbine Generator Systems - Part 1: Safety Requirements*. 1999, International Electrotechnical Commission: Geneva.
125. Daruvala, J., Galbraith, D., Griffiths, J., Grimshaw, I., Harrison, R., Holroyd, S., Pingree, R., Pitt, T., Sharp, J., and Sinclair, D., *Seapower SW Review - Resources, Constraints and Development Scenarios for Wave and Tidal Stream Power in the South West of England*, M. plc, Editor. 2004.
126. Nielsen, F., Argyriadis, K., Fonseca, N., Le Boulluec, M., Liu, P., Suzuki, H., Sirkar, J., Tarp-Johansen, N., Turnock, S., Waegter, J., and Zong, Z. *[Report of] Specialist Committee V.4: ocean, wind and wave energy utilization.* in *17th International Ship and Offshore Structures Congress*. 2009. Seoul National Univeristy, Korea.
127. Hardisty, J., *The Analysis of Tidal Stream Power*. 2009, Chichester, U.K.: Wiley-Blackwell.
128. McCann, G., *Tidal Current Turbine Fatigue Loading Sensitvity to Waves and Turbulence - A Parametric Study*, in *7th European Wave and Tidal Energy Conference (EWTEC 2007)*. 2007: Porto, Portugal.
129. Turnock, S.R., Phillips, A.B., Banks, J., and Nicholls-Lee, R.F., *Modelling tidal current turbine wakes using a coupled RANS-BEMT approach as a tool for analysing power capture of arrays of turbines.* Ocean Engineering (submitted), 2010.

Appendix A – Annual Energy Capture

In order to calculate the annual energy capture of a HATT the tidal cycle has been approximated by a double sinusoid; one with a period of 12.4 hours representing the diurnal cycle, and the other a period of 353 hours representing the fortnightly spring-neap period. The following equation, as shown by Fraenkel [93], provides a model for the prediction of the velocity, *V*, of a tidal current:

$$V = \left[K_0 + K_1 \cos\left(\frac{2\pi t_i}{T_1} \right) \right] \cos\left(\frac{2\pi t_i}{T_0} \right) \qquad \text{(A.1)}$$

K_O and K_1 were derived from the variation of the flow velocity over a tidal cycle.

In Equation (A.1), T_O =353 hours (1 lunar month) and T_1 =12.4 hours. The variation due to the daily tidal cycle was $\cos\left(2\pi t_i / T_1 \right)$ and that due to the lunar month tidal cycle was $\cos\left(2\pi t_i / T_0 \right)$. The maximum flow velocity for the spring tide was 2.5m/s and the ratio of maximum spring to maximum neap tide was 2.0. Since the maximum spring tide occurred at $t = 0$, an equation in terms of K_O and K_1 were derived:

$$V_{spring} = 2.5 = K_O + K_1 \qquad \text{(A.2)}$$

Plotting the sum of the two tidal variations shows that the maximum neap tide occurred at approximately $\cos\left(2\pi t_i / T_1 \right) = 1$ and $\cos\left(2\pi t_i / T_0 \right) = -1$. A second relationship was derived as:

$$V_{neap} = 1.25 = K_0 - K_1 \qquad \text{(A.3)}$$

Or

$$\frac{V_{spring}}{V_{neap}} = 2.0 = \frac{K_0 + K_1}{K_0 - K_1} \qquad \text{(A.4)}$$

The two simultaneous equations can then be solved to produce a final relationship for flow velocity variation with time of:

$$V = \left[1.88 + 0.63\cos\left(\frac{2\pi t_i}{353}\right)\right]\cos\left(\frac{2\pi t_i}{12.4}\right) \qquad \text{(A.5)}$$

The Matlab code behind the annual energy capture program is detailed below.

```
% Program to find the frequency of energy capture for the tidal stream

%Design parameters
k0=1.875;
k1=0.625;
days=365;
T0=353;
T1=12.4;

diameter=20;
A=pi*(diameter^2)*0.25;
rho=1.025;
rpm=10;
omega=2*pi*(rpm/60);

%imports the power coefficient data
inputfile='cp.txt'; cpdata=load(inputfile,'-ascii');
vflow=cpdata(:,1);
tsr=cpdata(:,2);
cp=cpdata(:,3);
fppower=cpdata(:,6);

%inputs the corresponding power data calculated in excel
inputfile='powerdat.txt'; powerdata=load(inputfile,'-ascii');
vflow2=powerdata(:,1);
fppower2=powerdata(:,2);
%plots the power against velocity
figure;
plot(vflow,fppower,'b-'); hold on;
plot(vflow2,fppower2,'ro'); hold off;
xlabel('flow velocity (m/s)'); ylabel('power (kW)'); grid;

% speed range 0 - 2.5, derivation of frequency of occurrence of velocity
speedres = 0.05;
speedarray = zeros(2.5/speedres+1, 1);
count=0;
for t=0:1:(days*24);
    count=count + 1;
    x=cos((2*pi*t)/T0);
    y=cos((2*pi*t)/T1);
    V=(k0 +(k1*x))*y;

    if V<0
        Vact=-V;
    else
        Vact=V;
    end

    index = floor((Vact/speedres)+0.5)+1;
    speedarray(index) = speedarray(index) + 1;

end
```

```
freqocc=speedarray./count;
totalfreq=sum(freqocc)
%plot of frequency of occurrence
figure;
plot([0:speedres:2.5], freqocc, 'ro'); hold on;
plot([0:speedres:2.5], freqocc, 'b-'); hold off;
grid; xlabel('Velocity (m/s)'); ylabel('frequency of occurance');
%calculation of energy capture for the fixed pitch turbine
powercapture=freqocc.*fppower2;
energycapture=powercapture.*(days*24);
annualpower=sum(powercapture);
annualenergy=annualpower*(days*24)
%plot of the energy capture of the fixed pitch turbine
figure;
plot([0:speedres:2.5], powercapture, 'ro'); hold on;
plot([0:speedres:2.5], powercapture, 'b-'); hold off;
grid; xlabel('Velocity (m/s)'); ylabel('energy capture (kWh)');
```

Appendix B - Palisupan Sensitivity Analysis

The complexity of the shape of a HATT, high aspect ratio blades and low hub pitch, requires a complex process of adjustment to deliver a suitable quality of panel distribution without requiring an enormous number of panels on the blade/hub and in the wake. Propgen [81] allows a reasonably rapid search to be made through adjustment of the parameters in a base data file, of which there are many with a high level of interdependency.

Number of Panels

The number of panels on the blade was varied until the total force and momentum differed by less than 2.5% as the number of panels was increased. This was found to require of the order of 3,000 panels on the blade with approximately 40 panels in the chordwise direction and 75 in the spanwise direction. This ratio of panels is comparable with that typically found both for low aspect foils (rudders/keels) [1] but also the much lower aspect ratio propeller blades [2]. Not withstanding that the forces/moments are still changing with numbers of panels previous experience has shown that relative changes are well predicted with this level of accuracy. A further variable which is the Kutta condition for convergence was maintained at a value of 0.01.

Validation Study

Figure B-1 presents a comparison of the performance of the BEMT code, Cwind, and the lifting surface panel code, Palisupan, alongside the original experimental data of Barnsley et al [3] for the tip pitch setting of 2 deg and with a two bladed configuration.

It should be noted that for this study the following assumptions were made:

- The BEMT section was represented by a single series of NACA 63-2xx C_l and C_d performance data. The actual sections due to changes in camber and t/c vary above and below this.
- Following the work of Barnsley et al the influence of three-dimensional behaviour is to prolong stall, and give much higher working C_L before stall is initiated. This extra increment of lift was included to some extent.
- In the Palisupan calculations the iterative boundary layer prediction method was not included. This explains the continuing rise in C_{pow} at higher tip speed ratios. In

practice an amount of performance loss would have been initiated due to the onset of stall.

A good correlation can be observed between the three sources of data.

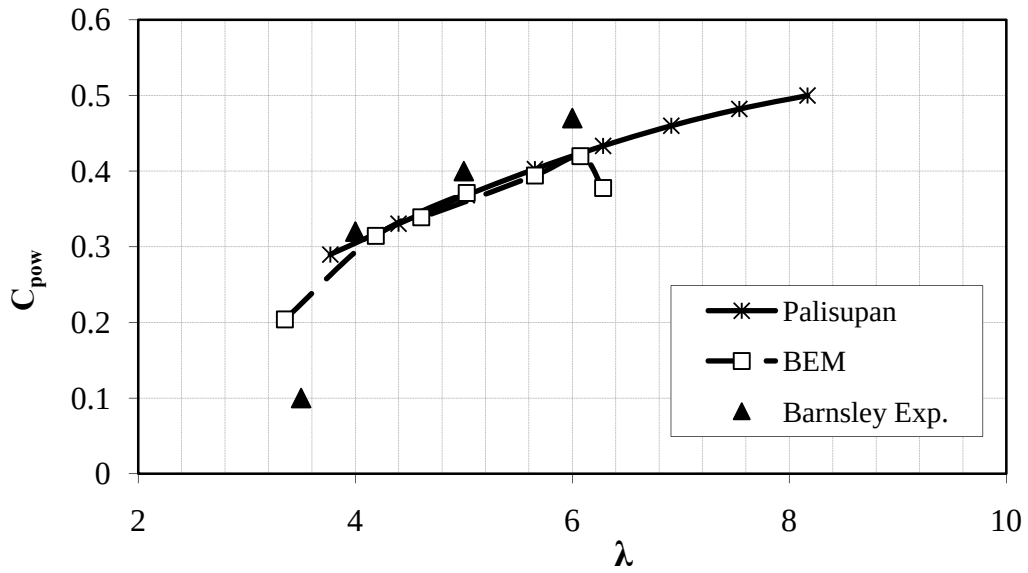

Figure B-1: Comparison of different methods for performance prediction

1. Molland, A.F. and S. Turnock, *Marine Rudders and Control Surfaces*. 2007: Butterworth-Heinemann. 448.
2. Pashias, C., *Propeller Tip Vortex Simulation Using Adaptive Grid Refinement Based on Flow Feature Identification,* in *School of Engineering Sciences*. 2005, University of Southampton: Southampton.
3. Barnsley, M.J. and J.F. Wellicome, *Dynamic Models of Wind Turbines - Aerodynamic Model Development*. 1993.

Appendix C – FEA Mesh Sensitivity Analysis

The blade of the example turbine in Section 5.2 was solved structurally in ANSYS 12.1 for ten different mesh densities, ranging from under 25000 elements to over 225000 elements. The element used was the same as the analysis in Section 4.5, SHELL 281. The sensitivity of solution for both the maximum bend and induced twist in the central spar at different mesh densities are illustrated in Figure C1 a) and b) respectively. Both solutions converged as the mesh density increased, with the optimum number of elements for both accuracy of solution and minimising computational time being 200,000. The computer used was a standard desktop PC with four intel Xeon processors and 12GB of RAM.

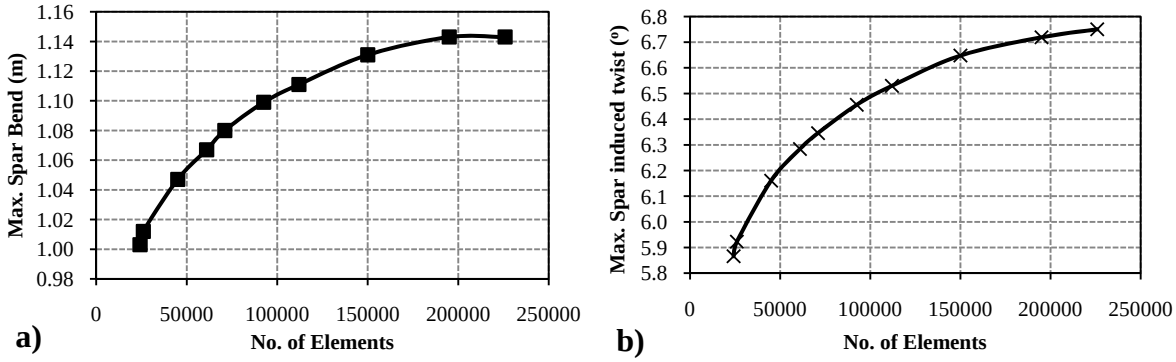

Figure C1: Solution convergence for increasing mesh density, a) bend, b) induced twist

Appendix D – Excerpts of FSI Coupling code

Propgen Input files

There are two main input files for Propgen which are generated through Matlab, *'Propeller'* and *'Propoptions'*; annotated versions of these files are presented.

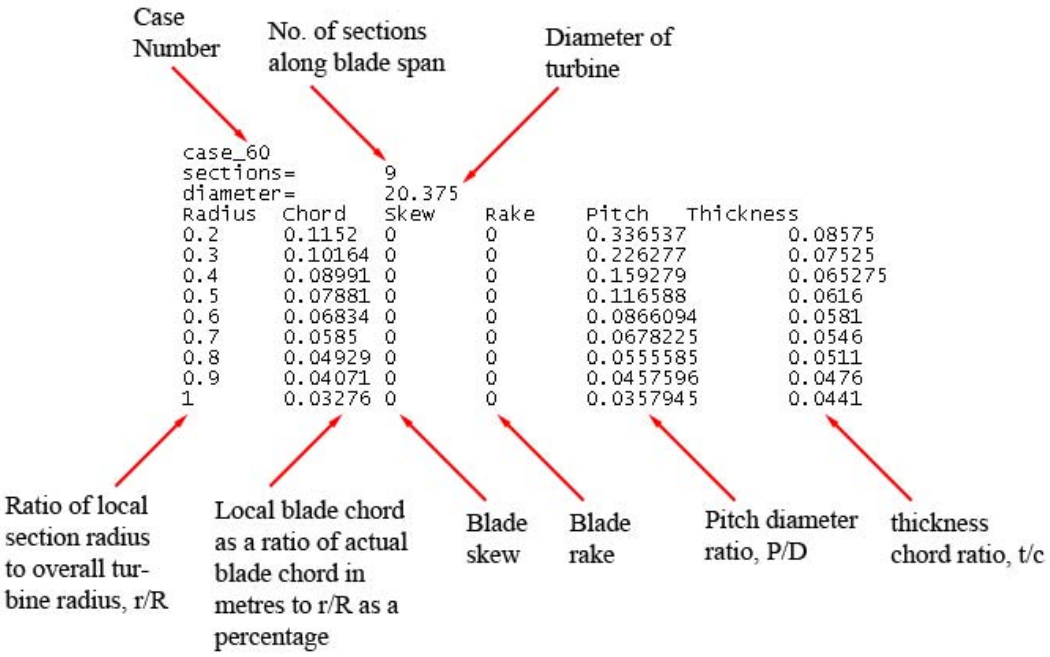

C 1 : Propeller.dat

The Matlab code reads the case number and associated date (number of blades, rps, flow velocity, diameter etc.) from a predefined table and generates the corresponding input files for Propgen. The program is then run and a *.uns* file produced for the next stage.

```
!set to one for volume mesh
volume_mesh=0

!Duct options
!use lower case
duct_length=.22
duct_thickness=.181
duct_nt=4
duct_upper_ns=22
duct_leading_lower_ns=7
duct_trailing_lower_ns=7
duct_wake_free_ns=25
duct_wake_fixed_ns=20
duct_wake_length=5
duct_wake_free_length=.33
duct_images=3
duct_P=0.4
duct_Q=2.0
```

Options for use of a duct, not used in this work

```
!Blade options
blade_number=2
blade_nt=6
blade_ns=23
blade_wake_length=0.5
blade_wake_free_length=0.3333
blade_wake_fixed_ns=160
blade_wake_free_ns=300
blade_P=0.3
blade_Q=1.0
blade_advance_speed=1.8875
blade_rps=0.1767
blade_tip_cluster=0.8
!set to 1 for full contraction and 0 for none
blade_wake_contraction=0
blade_wake_transition=0.5
blade_wake_final_pitch=0.15
```

Blade information defining number of blades, spanwise and chordwise panel distribution, clustering of panels towards the LE, TE, tip and root of blade, tidal flow velocity, turbine rps, wake panel distribution, wake contraction and wake pitch

```
!Ring options
!for no ring put ring_width =0
ring_width=0
ring_split=1
ring_ns=4
ring_nt=20
ring_strips=2
```

Inner duct ring information - not used in this work

```
!Hub options
!strips possible values 3 4 5 6 8 default 3
hub_strips=4
hub_nt = 27
hub_ns = 5
hub_length=3.2
hub_vtrailing=0.3
hub_vleading=-0.25
hub_offset_le=0
```

Hub information regarding panel distribution, number of hub sections, and where the blade sits in relation to the hub

```
!Cap options
!internal_length has to be less than cap_side_length
cap_internal_length=0.7
cap_side_length=0.8
cap_nt=13
cap_ns=13
cap_section_auto=0
```

Cap information including panel distribution and length. Cap can either be spherical or a section can be defined

C 2 : Propoptions.txt

Adaptflexi

The following is an example of the file that is generated and used to run Adaptflexi.

V8.0.9d - *defines the version of Adaptflexi to use*
0 0 -1 10 1 - *chooses to input a file*
1 1 -1 10 2 - *selects a single .uns file for input*
2 0 -1 10 6 - *manipulates the geometry*
3 1 -1 10 4 - *rotates the geometry*
4 1 -1 10 2 – *about the x axis*
5 1 0 20 90.000000 - *by 90 degrees*
6 1 -1 10 17 - *set rotational speed*
7 1 0 50 1 - *confirms change in rotational speed*
8 1 1 20 10.600000 – *to 10.6 RPM*
9 1 -1 10 18 - *chooses to use rotational images*
10 1 0 50 1 - *confirms the number of rotational images will change, in this case blades*
11 1 -1 10 2 - *defines turbine with 2 blades*
12 1 -1 10 0
13 0 -1 10 10 - *create mesh*
14 1 -1 10 1
15 1 0 50 0 - *the whole mesh, not just part of it*
16 1 -1 10 0
17 0 -1 10 2 - *output a file*
18 1 -1 10 2 - *specifically a .uns file*
19 1 0 50 0 - *files are to be placed in the default directory*
20 1 1 50 0
21 1 2 50 0 - *do not accept default command file values for this body*
22 2 -1 10 10 - *turns rotation on*
23 2 0 50 1
24 2 -1 10 12 - *pressures are recorded in output file*
25 2 0 50 1
26 2 -1 10 13 - *geometry is recorded in output file*
27 2 0 50 1
28 2 -1 10 17 - *alter fluid flow properties*
29 3 -1 10 1 - *chose fluid density*
30 4 -1 10 1 - *changes fluid density to sea water*
31 4 -1 10 0
32 3 -1 10 2 - *change flow velocity field*
33 4 -1 10 3 - *by defining a velocity at a point*
34 4 0 50 1
35 4 1 50 1
36 4 2 20 1.887500 - *to 1.8875 m/s*
37 4 -1 10 0
38 4 0 30 1.000000 0.000000 0.000000 - *in the positive x-direction*
39 4 -1 10 0
40 3 -1 10 0
41 2 -1 10 0
42 1 -1 10 1 - *run Palisupan straight away*
43 1 -1 10 0
44 0 -1 10 0
45 0 0 50 1 - *end program*

Palisupan is then run automatically and the output file generated which includes pressure and geometry data.

Palisupan to ANSYS

The Palisupan output file is then read into Matlab and manipulated to produce an ANSYS batch file.

```
clear all %clears all variables in the workspace
clc

data=fopen('case_1.txt','r');%opens adaptflexi data file
newdata=fopen('Block_1.txt','w');%opens empty txt file for data set 1 -
pressure date etc
newdata_2=fopen('Block_2.txt','w');%opens empty txt file for data set 2
- corners of panels
newdata_3=fopen('Block_3.txt','w');%opens empty txt file for data set 3
- keypoint coords
newdata_4=fopen('Fx.txt','w');%opens empty txt file for data set  -
forces and moments line

sec1_start=13;%defines the lines in the initial data file from which to
cut sections by
sec1_end=1686;

sec2_start=1688;
sec2_end=3361;

sec3_start=20765;
sec3_end=26664;

%loop to split the initial data file and write the data to the 3 files
%defined earlier for this very purpose.
i=1;
while i<(sec3_end+1) %feof(data)==0
    new_line = fgets(data);

    if i==10
        fprintf(newdata_4,new_line);
    end

     if i>sec1_start && i<sec1_end

        fprintf(newdata,new_line);
     end

     if i>sec2_start && i<sec2_end

        fprintf(newdata_2,new_line);
     end

      if i>sec3_start && i<sec3_end

        fprintf(newdata_3,new_line);
     end
```

```
    i=i+1;

end
fclose(newdata);%closes files written
fclose(newdata_2);
fclose(newdata_3);
fclose(newdata_4);

%%
clear filterindex ans filename data i new_line newdata newdata_2
newdata_3 newdata_4 sec1_end sec1_start sec2_end sec2_start sec3_end
sec3_start

Block_1 = importdata('Block_1.txt');%imports the newly cropped bits of
data from their text files
Block_2 = importdata('Block_2.txt');
Block_3 = importdata('Block_3.txt');
F = importdata('Fx.txt');
F=F{1,1};%defines F as a 1x1 cell
F2 = regexp(F,'\t','split');%splits the data in F using a tab delimiter
Fx = F2(:,1);%pulls out the data for Fx from F2
Mx = F2(:,4);%pulls out the data for Mx from F2

delete('Block_1.txt')%deletes the temporary text files used for the
initial data split
delete('Block_2.txt')
delete('Block_3.txt')
delete('Fx.txt')

panel_no = Block_1(:,1); %defines the list of panels on the body
cx = Block_1(:,2);%x coord for centre of the panel and where the
pressure loading is located
cy = Block_1(:,3);%y coord for centre of the panel
cz = Block_1(:,4);%z coord for centre of the panel
coords(:,2) = Block_1(:,2);%grouping the panel centres into one matrix
coords(:,3) = Block_1(:,3);
coords(:,4) = Block_1(:,4);
cp = Block_1(:,6);%extracting the Cp data from the file into one matrix
pnx = Block_1(:,14);%extracting the panel pressure normal data - X
pny = Block_1(:,15);% panel pressure normal - Y
pnz = Block_1(:,16);% panel pressure normal - Z
panel_area = Block_1(:,17);%extracts the panel area data to a matrix

KPN = panel_no + 1;%adds 1 to the panel numbers so that the data can be
used in ansys which doens't support zero values for area/KP definition
coords(:,1) = KPN + 5898;%extracts all of the ??

Panel_Centre_coordsT = coords'%transpose of the panel centre coords for
%writing to a batch file

NN = linspace(1,5898,5898);%Creates a one row matrix from 1 to 5898
NC(:,1) = NN';%transpose of line vector
NC(:,2) = Block_3(:,1);%defines the rest of the NC variable
NC(:,3) = Block_3(:,2);
NC(:,4) = Block_3(:,3);
NCT = NC';%takes transpose of the NC variable for writing into txt files

PCorners(:,1) = Block_2(:,1);%figures out the coordinates and numbers of
the panel corners
```

```
PCorners(:,2) = Block_2(:,2);
PCorners(:,3) = Block_2(:,3);
PCorners(:,4) = Block_2(:,4);
PCornersCorr = PCorners + 1;
PCornersCorrT = PCornersCorr';

Pressure1 = 0.5*1025*v*v;%calculates pressure from Cp, panel area, speed
and dnesity data
Pressure2 = panel_area.*cp;
Pressure = Pressure1*Pressure2;
AreasPressure(:,1) = KPN;%Lines pressures up with panel areas
AreasPressure(:,2) = Pressure;
AreasPressureT = AreasPressure';

kps = [1,2,37:78];%writes a vector for the defined keypoint in order to
constrain them in ANSYS - these are the blade root

CornersF (:,1) = Block_2(:,1);
CornersF (:,2) = Block_2(:,2);
CornersF (:,3) = Block_2(:,3);
CornersF (:,4) = Block_2(:,4);
CornersT = CornersF';

%Code to create KP coords for surface of blade only - removes wake
coords
cornersF =  [CornersF(:,1) ; CornersF(:,2) ; CornersF(:,3) ;
CornersF(:,4)]; %make corner points into one long list
CornersF =  sort(CornersF); %sort numbers into ascending order
CornersF =  unique(CornersF); %removes duplicates in array
CornersF = CornersF+1;

corners = [];

for i = 1:size(CornersF)

    corners = [corners ; NC(CornersF(i),:)];

end

cornersT2 = corners';
Nodes = cornersT2(1,:);

%writes the data into an ANSYS batch file for further analysis
batch = fopen('batch.txt','w');%opens the ANSYS batch file for writing
into
fprintf(batch,'/BATCH\n');%prints all the stuff for the beginning of the
ANSYS batch file
fprintf(batch,'! /COM,ANSYS RELEASE 12.1    UP20091102       11:05:55
05/27/2010\n');
fprintf(batch,'/input,menust,tmp,'',,,,,,,,,,,,,,1\n');
fprintf(batch,'! /GRA,POWER\n');
fprintf(batch,'! /GST,ON\n');
fprintf(batch,'! /PLO,INFO,3\n');
fprintf(batch,'! /GRO,CURL,ON\n');
fprintf(batch,'! /CPLANE,1\n');
fprintf(batch,'! /REPLOT,RESIZE\n');
fprintf(batch,'WPSTYLE,,,,,,,,0\n');
fprintf(batch,'/PREP7\n');%means you cna write commands and not just use
the GUI
fprintf(batch,'K,%d,%6.4f,%6.4f,%6.4f\n',cornersT2);%writes the panel
```

```
corner node coords into the ansys batch file as KP commands
fprintf(batch,'NKPT,,%d\n',Nodes);%maybe creates nodes at panel corner
kps
fprintf(batch,'!*\n');
fprintf(batch,'A,%d,%d,%d,%d\n',PCornersCorrT);%creates areas between
KPs in ansys
fprintf(batch,'A,62,4739,4703,53,\n');%LE areas central spar
fprintf(batch,'A,4739,4740,4704,4703,\n');
fprintf(batch,'A,4740,4741,4705,4704,\n');
fprintf(batch,'A,4741,4742,4706,4705,\n');
fprintf(batch,'A,4742,104,95,4706,\n');
fprintf(batch,'A,104,4907,4871,95,\n');
fprintf(batch,'A,4907,4908,4872,4871,\n');
fprintf(batch,'A,4908,4909,4873,4872,\n');
fprintf(batch,'A,4909,4910,4874,4873,\n');
fprintf(batch,'A,4910,146,137,4874,\n');
fprintf(batch,'A,146,5075,5039,137,\n');
fprintf(batch,'A,5075,5076,5040,5039,\n');
fprintf(batch,'A,5076,5077,5041,5040,\n');
fprintf(batch,'A,5077,5078,5042,5041,\n');
fprintf(batch,'A,5078,188,179,5042,\n');
fprintf(batch,'A,188,5243,5207,179,\n');
fprintf(batch,'A,5243,5244,5208,5207,\n');
fprintf(batch,'A,5244,5245,5209,5208,\n');
fprintf(batch,'A,5245,5246,5210,5209,\n');
fprintf(batch,'A,5246,230,221,5210,\n');
fprintf(batch,'A,230,5411,5375,221,\n');
fprintf(batch,'A,5411,5412,5376,5375,\n');
fprintf(batch,'A,5412,5413,5377,5376,\n');
fprintf(batch,'A,5413,5414,5378,5377,\n');
fprintf(batch,'A,5414,272,263,5378,\n');
fprintf(batch,'A,272,5579,5543,263,\n');
fprintf(batch,'A,5579,5580,5544,5543,\n');
fprintf(batch,'A,5580,5581,5545,5544,\n');
fprintf(batch,'A,5581,5582,5546,5545,\n');
fprintf(batch,'A,5582,314,305,5546,\n');
fprintf(batch,'A,314,5747,5711,305,\n');
fprintf(batch,'A,5747,5748,5712,5711,\n');
fprintf(batch,'A,5748,5749,5713,5712,\n');
fprintf(batch,'A,5749,5750,5714,5713,\n');
fprintf(batch,'A,5750,356,347,5714,\n');
fprintf(batch,'A,356,5865,5847,347,\n');
fprintf(batch,'A,5865,5866,5848,5847,\n');
fprintf(batch,'A,5866,398,389,5848,\n');%end LE areas
fprintf(batch,'A,70,4771,4671,45,\n');%Trailing edge areas central spar
fprintf(batch,'A,4771,4772,4672,4671,\n');
fprintf(batch,'A,4772,4773,4673,4672,\n');
fprintf(batch,'A,4773,4774,4674,4673,\n');
fprintf(batch,'A,4774,112,87,4674,\n');
fprintf(batch,'A,112,4939,4839,87,\n');
fprintf(batch,'A,4939,4940,4840,4839,\n');
fprintf(batch,'A,4940,4941,4841,4840,\n');
fprintf(batch,'A,4941,4942,4842,4841,\n');
fprintf(batch,'A,4942,154,129,4842,\n');
fprintf(batch,'A,154,5107,5007,129,\n');
fprintf(batch,'A,5107,5108,5008,5007,\n');
fprintf(batch,'A,5108,5109,5009,5008,\n');
fprintf(batch,'A,5109,5110,5010,5009,\n');
fprintf(batch,'A,5110,196,171,5010,\n');
fprintf(batch,'A,196,5275,5175,171,\n');
fprintf(batch,'A,5275,5276,5176,5175,\n');
```

```
fprintf(batch,'A,5276,5277,5177,5176,\n');
fprintf(batch,'A,5277,5278,5178,5177,\n');
fprintf(batch,'A,5278,238,213,5178,\n');
fprintf(batch,'A,238,5443,5343,213,\n');
fprintf(batch,'A,5443,5444,5344,5343,\n');
fprintf(batch,'A,5444,5445,5345,5344,\n');
fprintf(batch,'A,5445,5446,5346,5345,\n');
fprintf(batch,'A,5446,280,255,5346,\n');
fprintf(batch,'A,280,5611,5511,255,\n');
fprintf(batch,'A,5611,5612,5512,5511,\n');
fprintf(batch,'A,5612,5613,5513,5512,\n');
fprintf(batch,'A,5613,5614,5514,5513,\n');
fprintf(batch,'A,5614,322,297,5514,\n');
fprintf(batch,'A,322,5779,5679,297,\n');
fprintf(batch,'A,5779,5780,5680,5679,\n');
fprintf(batch,'A,5780,5781,5681,5680,\n');
fprintf(batch,'A,5781,5782,5682,5681,\n');
fprintf(batch,'A,5782,364,339,5682,\n');
fprintf(batch,'A,364,5881,5831,339,\n');
fprintf(batch,'A,5881,5882,5832,5831,\n');
fprintf(batch,'A,5882,406,381,5832,\n');%end TE areas
fprintf(batch,'A,53,4703,4671,45,\n');%Front areas central spar
fprintf(batch,'A,4703,4704,4672,4671,\n');
fprintf(batch,'A,4704,4705,4673,4672,\n');
fprintf(batch,'A,4705,4706,4674,4673,\n');
fprintf(batch,'A,4706,95,87,4674,\n');
fprintf(batch,'A,95,4871,4839,87,\n');
fprintf(batch,'A,4871,4872,4840,4839,\n');
fprintf(batch,'A,4872,4873,4841,4840,\n');
fprintf(batch,'A,4873,4874,4842,4841,\n');
fprintf(batch,'A,4874,137,129,4842,\n');
fprintf(batch,'A,137,5039,5007,129,\n');
fprintf(batch,'A,5039,5040,5008,5007,\n');
fprintf(batch,'A,5040,5041,5009,5008,\n');
fprintf(batch,'A,5041,5042,5010,5009,\n');
fprintf(batch,'A,5042,179,171,5010,\n');
fprintf(batch,'A,179,5207,5175,171,\n');
fprintf(batch,'A,5207,5208,5176,5175,\n');
fprintf(batch,'A,5208,5209,5177,5176,\n');
fprintf(batch,'A,5209,5210,5178,5177,\n');
fprintf(batch,'A,5210,221,213,5178,\n');
fprintf(batch,'A,221,5375,5343,213,\n');
fprintf(batch,'A,5375,5376,5344,5343,\n');
fprintf(batch,'A,5376,5377,5345,5344,\n');
fprintf(batch,'A,5377,5378,5346,5345,\n');
fprintf(batch,'A,5378,263,255,5346,\n');
fprintf(batch,'A,263,5543,5511,255,\n');
fprintf(batch,'A,5543,5544,5512,5511,\n');
fprintf(batch,'A,5544,5545,5513,5512,\n');
fprintf(batch,'A,5545,5546,5514,5513,\n');
fprintf(batch,'A,5546,305,297,5514,\n');
fprintf(batch,'A,305,5711,5679,297,\n');
fprintf(batch,'A,5711,5712,5680,5679,\n');
fprintf(batch,'A,5712,5713,5681,5680,\n');
fprintf(batch,'A,5713,5714,5682,5681,\n');
fprintf(batch,'A,5714,347,339,5682,\n');
fprintf(batch,'A,347,5847,5831,339,\n');
fprintf(batch,'A,5847,5848,5832,5831,\n');
fprintf(batch,'A,5848,389,381,5832,\n');%end front areas
fprintf(batch,'A,62,4739,4771,70,\n');%back areas central spar
fprintf(batch,'A,4739,4740,4772,4771,\n');
```

```
fprintf(batch,'A,4740,4741,4773,4772,\n');
fprintf(batch,'A,4741,4742,4774,4773,\n');
fprintf(batch,'A,4742,104,112,4774,\n');
fprintf(batch,'A,104,4907,4939,112,\n');
fprintf(batch,'A,4907,4908,4940,4939,\n');
fprintf(batch,'A,4908,4909,4941,4940,\n');
fprintf(batch,'A,4909,4910,4942,4941,\n');
fprintf(batch,'A,4910,146,154,4942,\n');
fprintf(batch,'A,146,5075,5107,154,\n');
fprintf(batch,'A,5075,5076,5108,5107,\n');
fprintf(batch,'A,5076,5077,5109,5108,\n');
fprintf(batch,'A,5077,5078,5110,5109,\n');
fprintf(batch,'A,5078,188,196,5110,\n');
fprintf(batch,'A,188,5243,5275,196,\n');
fprintf(batch,'A,5243,5244,5276,5275,\n');
fprintf(batch,'A,5244,5245,5277,5276,\n');
fprintf(batch,'A,5245,5246,5278,5277,\n');
fprintf(batch,'A,5246,230,238,5278,\n');
fprintf(batch,'A,230,5411,5443,238,\n');
fprintf(batch,'A,5411,5412,5444,5443,\n');
fprintf(batch,'A,5412,5413,5445,5444,\n');
fprintf(batch,'A,5413,5414,5446,5445,\n');
fprintf(batch,'A,5414,272,280,5446,\n');
fprintf(batch,'A,272,5579,5611,280,\n');
fprintf(batch,'A,5579,5580,5612,5611,\n');
fprintf(batch,'A,5580,5581,5613,5612,\n');
fprintf(batch,'A,5581,5582,5614,5613,\n');
fprintf(batch,'A,5582,314,322,5614,\n');
fprintf(batch,'A,314,5747,5779,322,\n');
fprintf(batch,'A,5747,5748,5780,5779,\n');
fprintf(batch,'A,5748,5749,5781,5780,\n');
fprintf(batch,'A,5749,5750,5782,5781,\n');
fprintf(batch,'A,5750,356,364,5782,\n');
fprintf(batch,'A,356,5865,5881,364,\n');
fprintf(batch,'A,5865,5866,5882,5881,\n');
fprintf(batch,'A,5866,398,406,5882,\n');%end back areas
fprintf(batch,'ET,1,SHELL281\n');%defines element type
fprintf(batch,'MPTEMP,,,,,,,\n');%defines material properties UD Carbon
SE84LV
fprintf(batch,'MPTEMP,1,0\n');
fprintf(batch,'MPDATA,EX,1,,129.2E9\n');
fprintf(batch,'MPDATA,EY,1,,8.76E9\n');
fprintf(batch,'MPDATA,EZ,1,,8.76E9\n');
fprintf(batch,'MPDATA,PRXY,1,,0.335\n');
fprintf(batch,'MPDATA,PRYZ,1,,0.0172\n');
fprintf(batch,'MPDATA,PRXZ,1,,0.0172\n');
fprintf(batch,'MPDATA,GXY,1,,5.76E9\n');
fprintf(batch,'MPDATA,GYZ,1,,5.76E9\n');
fprintf(batch,'MPDATA,GXZ,1,,5.76E9\n');%end material props
fprintf(batch,'MPDATA,EX,2,,66.4E9\n');%defines material properties
twill Carbon SE84LV
fprintf(batch,'MPDATA,EY,2,,66.4E9\n');
fprintf(batch,'MPDATA,EZ,2,,8.76E9\n');
fprintf(batch,'MPDATA,PRXY,2,,0.05\n');
fprintf(batch,'MPDATA,PRYZ,2,,0.05\n');
fprintf(batch,'MPDATA,PRXZ,2,,0.05\n');
fprintf(batch,'MPDATA,GXY,2,,5.76E9\n');
fprintf(batch,'MPDATA,GYZ,2,,5.76E9\n');
fprintf(batch,'MPDATA,GXZ,2,,5.76E9\n');%end material props
fprintf(batch,'sect,1,shell,,\n');%defines layup data for bend twist
beam
```

```
fprintf(batch,'secdata, 0.00843,1,45,3\n');
fprintf(batch,'secdata, 0.00562,1,20,3\n');
fprintf(batch,'secdata, 0.001405,1,60,3\n');
fprintf(batch,'secoffset,BOT\n');
fprintf(batch,'seccontrol,,,, , , ,\n');%end sec data
fprintf(batch,'sect,2,shell,,\n');%defines layup data for blade skin
fprintf(batch,'secdata, 0.00398,2,0,3\n');
fprintf(batch,'secoffset,BOT\n');
fprintf(batch,'seccontrol,,,, , , ,\n');%end sec data
fprintf(batch,'CSKP,11,0,45,53,4671,1,1\n');%defines local coord systems
for meshing bend twist beam
fprintf(batch,'CSKP,12,0,53,62,4703,1,1\n');
fprintf(batch,'CSKP,13,0,62,70,4739,1,1\n');
fprintf(batch,'CSKP,14,0,70,45,4771,1,1\n');
fprintf(batch,'CM,_Y,AREA\n');%defines element attributes on beam LE
fprintf(batch,'ASEL,,,,1673,1710,1,\n');%selects LE areas
fprintf(batch,'CM,_Y1,AREA\n');
fprintf(batch,'CMSEL,S,_Y\n');
fprintf(batch,'CMSEL,S,_Y1\n');
fprintf(batch,'AATT,1,,1,12,1\n');%uses coord sys 12, mat 1, sec data 1
fprintf(batch,'CMSEL,S,_Y\n');
fprintf(batch,'CMDELE,_Y\n');
fprintf(batch,'CMDELE,_Y1\n');
fprintf(batch,'CM,_Y,AREA\n');%defines element attributes on beam TE
fprintf(batch,'ASEL,,,,1711,1748,1,\n');%selects TE areas
fprintf(batch,'CM,_Y1,AREA\n');
fprintf(batch,'CMSEL,S,_Y\n');
fprintf(batch,'CMSEL,S,_Y1\n');
fprintf(batch,'AATT,1,,1,14,1\n');%uses coord sys 14, mat 1, sec data 1
fprintf(batch,'CMSEL,S,_Y\n');
fprintf(batch,'CMDELE,_Y\n');
fprintf(batch,'CMDELE,_Y1\n');
fprintf(batch,'CM,_Y,AREA\n');%defines element attributes on beam back
fprintf(batch,'ASEL,,,,1749,1786,1,\n');%selects back areas
fprintf(batch,'CM,_Y1,AREA\n');
fprintf(batch,'CMSEL,S,_Y\n');
fprintf(batch,'CMSEL,S,_Y1\n');
fprintf(batch,'AATT,1,,1,11,1\n');%uses coord sys 11, mat 1, sec data 1
fprintf(batch,'CMSEL,S,_Y\n');
fprintf(batch,'CMDELE,_Y\n');
fprintf(batch,'CMDELE,_Y1\n');
fprintf(batch,'CM,_Y,AREA\n');%defines element attributes on beam front
fprintf(batch,'ASEL,,,,1787,1824,1,\n');%selects front areas
fprintf(batch,'CM,_Y1,AREA\n');
fprintf(batch,'CMSEL,S,_Y\n');
fprintf(batch,'CMSEL,S,_Y1\n');
fprintf(batch,'AATT,1,,1,13,1\n');%uses coord sys 13, mat 1, sec data 1
fprintf(batch,'CMSEL,S,_Y\n');
fprintf(batch,'CMDELE,_Y\n');
fprintf(batch,'CMDELE,_Y1\n');
fprintf(batch,'CM,_Y,AREA\n');%defines element attributes on blade
surface
fprintf(batch,'ASEL,,,,1,1672,1,\n');%selects surface areas
fprintf(batch,'CM,_Y1,AREA\n');
fprintf(batch,'CMSEL,S,_Y\n');
fprintf(batch,'CMSEL,S,_Y1\n');
fprintf(batch,'AATT,2,,1,0,2\n');%uses global coord sys, mat 2, sec data
2
fprintf(batch,'CMSEL,S,_Y\n');
fprintf(batch,'CMDELE,_Y\n');
fprintf(batch,'CMDELE,_Y1\n');
```

```
fprintf(batch,'SMRT,5\n');%smart sizes the mesh to a coarse mesh (fine
is 1)
fprintf(batch,'MSHAPE,0,2D\n');%mesh shape
fprintf(batch,'MSHKEY,0\n');%mesh free or mapped - in this case free
fprintf(batch,'FLST,5,1200,5,ORDE,2\n');
fprintf(batch,'FITEM,5,1\n');
fprintf(batch,'FITEM,5,-1200\n');
fprintf(batch,'CM,_Y,AREA\n');
fprintf(batch,'ASEL,ALL\n');%selects all areas
fprintf(batch,'CM,_Y1,AREA\n');
fprintf(batch,'CMSEL,S,_Y\n');
fprintf(batch,'AMESH,_Y1\n');%and meshes them
fprintf(batch,'CMDELE,_Y\n');
fprintf(batch,'CMDELE,_Y1\n');
fprintf(batch,'CMDELE,_Y2\n');
fprintf(batch,'SFA,%d,1,PRES,%6.6f\n',AreasPressureT);%applies pressures
to each area
fprintf(batch,'DK,45,,0,,0,ALL,,,,,,\n',kps);%constrains the root of the
cetral spar
fprintf(batch,'DK,53,,0,,0,ALL,,,,,,\n',kps);
fprintf(batch,'DK,62,,0,,0,ALL,,,,,,\n',kps);
fprintf(batch,'DK,70,,0,,0,ALL,,,,,,\n',kps);
fprintf(batch,'!*\n');
fprintf(batch,'FINISH\n');
fprintf(batch,'/SOL\n');
fprintf(batch,'/STATUS,SOLU\n');
fprintf(batch,'NLGEOM,ON\n');%makes the analysis a non-linear one to
account for large displacements
fprintf(batch,'SOLVE\n');%Solves current LS
fprintf(batch,'FINISH\n');
fprintf(batch,'/POST1\n');
fprintf(batch,'/HEADER,OFF,OFF,OFF,OFF,OFF,OFF\n');%turns off headers in
results file
fprintf(batch,'/PAGE,,,450000,\n');%makes results file really long
fprintf(batch,'/FORMAT,7,G,15,4,,\n');%formats results file
fprintf(batch,'/OUTPUT,c:\ANSYS\results\case_60,dat,,\n');%defines
results file location
fprintf(batch,'PRNSOL, U,COMP\n');%writes displaced node positions
fprintf(batch,'PRNSOL, S,COMP\n');%writes stresses
fclose(batch);%closes the ansys batch file

system ('"C:\Program Files\Ansys Inc\V110\ANSYS\bin\intel\ansys110" -p
aa_r -b -i H:\PhD\Research\FSI\Matlab\batch.txt -o
C:\ANSYS\Results\case_60_results.txt'); % runs ANSYS in batch mode and
writes results to file
```

ANSYS to Palisupan

The ANSYS results file is then read into Matlab, the maximum stress checked to fall in line with the operating constraints of the materials and situation defined.

```
clear all
NLIST = importdata('NLIST.lis');%imports initial node data

NLISTlook (:,1) = NLIST(:,2);
NLISTlook (:,2) = NLIST(:,3);
```

```
NLISTlook (:,3) = NLIST(:,4);
NLISTlook (:,4) = NLIST(:,1);

%Loop to find the nodes that match the original KPs
for i = 1:1716
    for j = 1:387775
        if corners(i,2) == NLISTlook(j,1)&& corners(i,3) ==
NLISTlook(j,2)&& corners(i,4) == NLISTlook(j,3)

            NodeNum(i) = NLISTlook(j,4);
        end
    end
end

Results = importdata('case_60.lis');%imports nodal results data
Maximums = max(Results,[],1); %determines the maximum values in each
column of the results file
if Maximums (:,5)<== sigma_yield/2 %if the max stress is less than half
the yield stress
        ANSYStoPAN.m %run code to calc bend and ind twist and regenerate
mesh for CFD and start next iteration loop
    else
        No_Layers = No_Layers + 5 %if not, add 5 ;layers to the main
bend-twist coupling beam mid layers
        PANtoANSYS.m %rerun ansys analysis for thicker material
end
```

In the even the maximum stress in the blade meets the failure criteria the bend and induced twist are calculated.

```
%generates a matrix with the KP numbers, coordinates and Node numbers
KPxyzN (:,1) = corners (:,1);
KPxyzN (:,2) = corners (:,2);
KPxyzN (:,3) = corners (:,3);
KPxyzN (:,4) = corners (:,4);
KPxyzN (:,1) = NLISTlook (:,4);

%creates a matrix from the results of the x,y,and z displacements of the
%nodes
dxdydz (:,1) = Results (:,2);
dxdydz (:,2) = Results (:,3);
dxdydz (:,3) = Results (:,4);
dxdydz (:,4) = NLISTlook (:,4);

%calculates the new vector position of the nodes/KPs
DispxyzN(:,1) = KPxyzN(:,2)+dxdydz(:,1);
DispxyzN(:,2) = KPxyzN(:,3)+dxdydz(:,2);
DispxyzN(:,3) = KPxyzN(:,4)+dxdydz(:,3);
DispxyzKP(:,4) = KPxyzN(:,1);

Original (:,1) = KPxyzN(:,2);
Original (:,2) = KPxyzN(:,3);
Original (:,3) = KPxyzN(:,4);

Displaced (:,1) = DispxyzN(:,1);
```

```
Displaced (:,2) = DispxyzN(:,2);
Displaced (:,3) = DispxyzN(:,3);

%uses the cos rule to calcualate induced twist at each point
AdotBst = Original.*Displaced;
AdotB = AdotBst(:,1)+AdotBst(:,2)+AdotBst(:,3);
Osquaresst = Original.*Original;
Osquares = Osquaresst(:,1)+Osquaresst(:,2)+Osquaresst(:,3);
Dsquaresst = Displaced.*Displaced;
Dsquares = Dsquaresst(:,1)+Dsquaresst(:,2)+Dsquaresst(:,3);
LOriginal = sqrt(Osquares);
LDisplaced = sqrt(Dsquares);
mdOmdD = LOriginal.*LDisplaced;
cosAng = AdotB./mdOmdD;
AngRad = acos(cosAng);
AngDeg = (AngRad/pi)*180;
AngDegR = real(AngDeg);

SpTw (:,1) = -KPxyzN(:,3);
SpTw (:,2) = AngDegR;

%writes matrix containing spanwise location, induced twist, bend and KP
%number
SpTwBKp (:,1) = SpTw (:,1);
SpTwBKp (:,2) = SpTw (:,2);
SpTwBKp (:,3) = dxdydz(:,1);
SpTwBKp (:,4) = KPxyzN(:,1);

UNS = fopen('case_60.uns','r');%opens adaptflexi input file file
UNSnew_1=fopen('UNS_1.txt','w');%opens empty txt file for data set 1 -
Panel location data
UNSnew_2=fopen('UNS_2.txt','w');%opens empty txt file for data set 2 -
Keypoint coords

UNS1_start=17;
UNS1_end=57244;

UNS2_start=57243;
UNS2_end=76824;

%loop to get data from UNS file and put it into blocks for editing
i=1;
while i<(UNS2_end+1)
    new_line = fgets(data);

     if i>UNS1_start && i<UNS1_end

        fprintf(UNS_1,new_line);
     end

     if i>UNS2_start && i<UNS2_end

        fprintf(UNS_2,new_line);
     end

    i=i+1;

end
fclose(UNS_1);%closes files written
fclose(UNS_2);
```

```
%%
% clear all
clear filterindex ans filename data i new_line newdata newdata_2
newdata_3 newdata_4 sec1_end sec1_start sec2_end sec2_start sec3_end
sec3_start

panel_assoc = importdata('UNS_1.txt');%imports the newly cropped bits of
data from their text files
KP_coords = importdata('UNS_2.txt');

%loop to displace the blade KPs in the UNS file to the new locations
k=1;
while k<1717
    Disp_KP_coords (k,:)= KP_coords (k,:) + dxdydz (k,:);

    k=k+1;
end

%loop to look for associated wake panel numbers attached to the trailing
edge
%blade panels and adjust them by the amount that the corresponding TE
panel
%moved by and do forth back through the wake

%splits the file into te panels, 1st wake panels, fixed wake panels and
%free wake panels
p = 1;
q = 2;
while p < 1673
    if panel_assoc (p,2) = -1
        wake_t (p) = panel_assoc (q);
        if panel_assoc (p,2) = 2
            wake_1 (p) = panel_assoc (q);
            if panel_assoc (p,2) = 3
                wake_fixed (p) = panel_assoc (q);
                if panel_assoc (p,2) = 4
                    wake_free (p) = panel_assoc (q);
                end
            end
        end
    end

    p=p+2;
    q+q+2;
end

%deletes the multiple TE panels that do not relate properly in the UNS
file
%to the 1st wake panels
r=1;
if wake_1 (:,2) = wake_t (:,1) && wake_1 (:,3) = wake_t (:,4)
    wake_T (r) = wake_t(r);

    r=r+1;
end

%finds out which KPS are connected to which on the TE ofthe body and
%displaces them by the same amount as the conrrespondig KP on the TE.
x=1
```

```
if wake_1 (x,2) = wake_T(:,1)
    lKP = wake_1(x,1);
    sKP = wake_T(:,1);
    new_KP_coords (lKP,:) = KP_coords (lKP,:) + dxdydz (sKP,:);

     if wake_1 (x,3) = wake_T(:,4)
         lKP = wake_1(x,4);
         sKP = wake_T(:,4);
         new_KP_coords (lKP,:) = KP_coords (lKP,:) + dxdydz (sKP,:);

% these "if" statements carry on for a while until the whole wake has
been displaced - Palisupan is then rerun and subsequently ANSYS until
the bend between iterations is less than 10mm different.
```

The key points relating to the wake panels are then sorted, and the relevant displacements added throughout the wake to reflect the deflection of the trailing edge of the blade.

Final Performance Data – BEMT

Once the blade has been designed through the FSI, the turbine is then run through the BEMT code to ascertain final turbine performance data which is compared to that obtained through the CFD analysis. The following is an example input file for the BEMT code, this is used alongside section 2D lift and drag data to gain C_{pow}, C_T, and absorbed power data for the device.

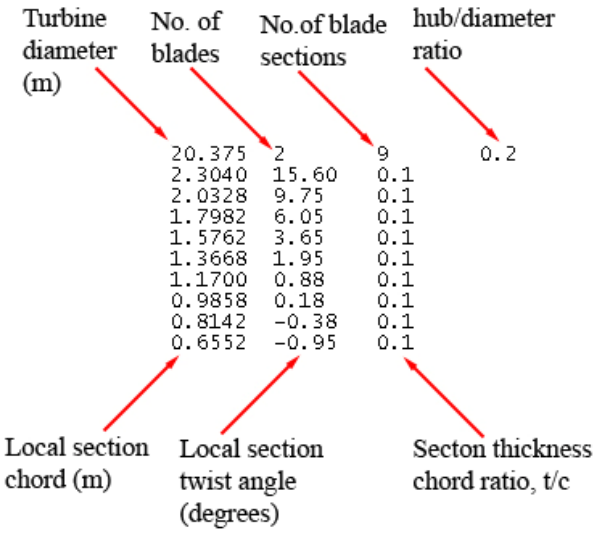

Appendix E - Actively Adaptive Blades

Through the combination of fibre-reinforced composites and actuators, it is possible to design structures that have the ability to change shape. Structures that can change shape are often termed morphing structures. In recent years the National Aeronautics and Space Administration (NASA) has shown significant interest in morphing structures; much of this interest has been directed towards morphing wings of future aircraft [1, 2]. In addition, the Air Force [3] and the Defence Advanced Research Projects Agency (DARPA) [4] are conducting research to examine adaptive structures on aircraft.

Mechanical actuation technologies vary widely in their intrinsic displacement, force, speed and efficiency, as exemplified by the range of active materials that have been developed to meet diverse needs. Many are currently used in applications ranging from ultrasonic motors to micropositioners, adaptive optics and medical stents. There exists an unmet need for materials that could enable generalised, large scale, structural actuation. Existing ferroic materials, such as piezoelectrics, electrostrictors and magnetostrictors, require high operating voltages or magnetic fields and often have more bandwidth than necessary. They only generate low strain and force capability when compared to, for example, conventional hydraulics. Shape memory metals are amongst the highest energy density active materials and can deliver several percent strain with high actuation force, but, being dependent upon thermal phase transitions, are intrinsically slower and require temperature regulation for their operation.

Examples of ferroic based actuators include RAINBOW (Reduced And Internally Biased Oxide Wafer) actuators [5], SMA (Shape Memory Alloy) actuators [6], MFC (Macro Fiber Composite) actuators [7], and THUNDER (THin layer UNimorph ferroelectric Driver and sensor) actuators [8]. Such actuators are useful for the applications listed above, although they have very low strain and force capabilities, and also require a constant supply of electricity for operation – as such they are not useful for the active adaptation of turbine blades. Quackenbush et al [9, 10] described a ducted propeller with a deformable shroud that produces a steering force. The deformation was provided by electrically-actuated Shape Memory Alloy (SMA) cables. Potential advantages of this technology for naval applications were claimed, including enhanced low-speed manoeuvring for submarines, reduction or elimination of conventional steering surfaces, and elimination of hydraulic actuators in favour of all-electric components.

Experiments in a water tunnel produced significant side force with relatively small change in the angle of duct trailing edge. Measurements and computational results were in good agreement. Major issues with this concept for full scale applications are the difficulties associated with the mechanical complexity and the power required for SMA deflection. Braided pneumatic actuators [11] have higher strain and force capabilities and could therefore be useful in the field of adaptive structures, though are complex and costly and when attempting to optimise availability, reliability and maintainability, would not be suitable.

High strain, high force mechanical actuation technologies are desirable for numerous applications ranging from microelectromechanical systems (MEMS) to large scale "smart structures" that are able to change shape to optimise performance. Koyama et al [12] considered simultaneous electrochemical expansion of the $LiCoO_2$/Graphite cathode/anode couple for use in larger adaptive structures and claim that actuation under stresses of up to ~20MPa is achievable. Again, however, such technology requires a continuous source of electricity.

It is apparent that actively adaptive devices often require a continuous supply of current in order for the morphing structure to stay deformed. Considering the application of active adaptation to free stream tidal energy, the requirement of a continuous supply of current is somewhat contradictory to the aim of generating as much electricity as possible whilst utilising renewable energy resources. Thus it would be desirable to have some method of holding a shape change without having to apply continuous current to a device. It is thought that composites that have two stable equilibrium shapes at room temperature and can be "snapped" from one to the other by a temporary force or moment could be beneficial in the realm of shape changing blades.

Snap-Through Composites

Composites with an unsymmetric layup are generally characterised by warpage phenomena due to residual stresses caused in the manufacturing process or during operation conditions. For certain cases of unsymmetric fibre reinforced, and textile reinforced, composites more than one stable deformation state occurs due to the residual stresses caused by thermal effects, moisture absorption, and chemical shrinkage. In certain cases the thermally induced stresses which develop during processing can cause out-of-plane curvature as the laminate cools from the processing temperature to room

temperature. Depending on stacking sequence and geometry, these processing stresses may cause the laminate to have more than one stable configuration with out-of-plane curvature at room temperature. In the case of the existence of two stable equilibrium states, a snap through from one stable deformation state to the second state is possible which can be initiated by forces and moments generated by adapted actuators.

After snap through, the panel will remain in the new configuration until alternative forces are applied. The curvature of these multiple configurations can be significantly different, resulting in different structural forms, Figure 0-1. An advantage of using this characteristic to develop morphing structures is the ability to have multiple shapes without continually supplying power; that is, power is required only to transform the structure from one shape to another, and not to hold it in the transformed shape with continuous application of force.

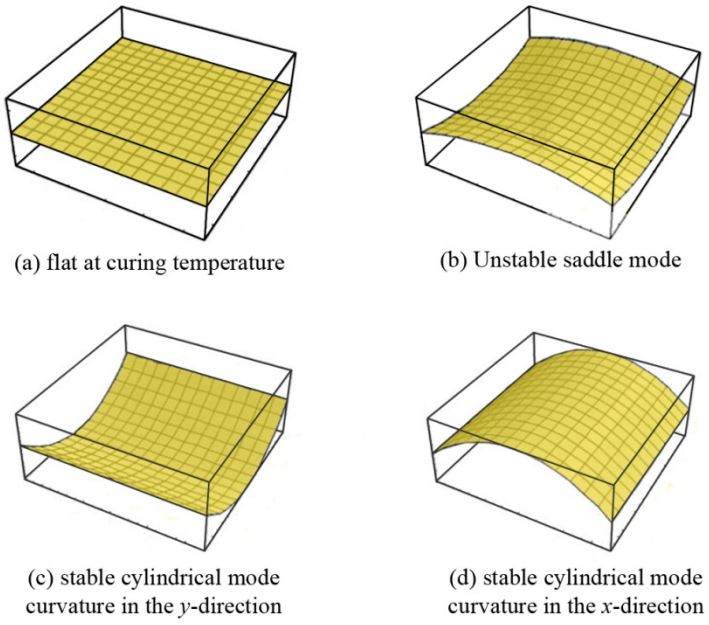

Figure 0-1: The four possible mode shapes of snap-through laminates

The phenomenon of unsymmetric laminates having multiple stable configurations at room temperature was first considered in 1981 [13], previous to this it had been assumed that the cured shape of an unsymmetric laminate was that of a saddle, Figure 0-1b). Subsequently Hyer [14, 15] successfully modelled the room-temperature shapes of unsymmetric cross ply graphite-epoxy laminates using the Rayleigh-Ritz technique and classical lamination theory (CLT) with the addition of nonlinear terms in the strain-displacement relations. It was found that, for certain geometric conditions, there were three room-temperature equilibrium shapes: an unstable saddle shape, Figure 0-1b), which

is predicted by geometrically linear CLT, and two stable cylindrical shapes, Figure 0-1c) and Figure 0-1d), which cannot be found without the geometrically non-linear terms. For other geometric conditions, there was only the saddle shape, which in these cases was stable.

Hamomoto and Hyer [16] continued the work with unsymmetric cross-ply laminates by examining the effects on the laminate slope of raising and lowering the temperature concluding that agreement between experiments and the theory was good. To this point, the laminates under consideration were all cross-ply laminates – i.e. those with layers at 0^o and 90^o only. Jun and Hong [17] began to expand the previous theory for unsymmetric laminates with arbitrary layup angles. Dano and Hyer [18-20], Ren et al [21], and Potter and Weaver [22] continued to explore the mechanics of unsymmetric laminates by expanding the Rayleigh-Ritz formulation to more general angle-ply laminates. The predictions were compared with physical experiments measuring the response of the laminates to simple applied forces. The correlation between predicted results, experimental measurements, and FEA was found to be quite good, in both terms of movement levels and in strain response. A phenomenon was noticed by Potter et al [23] regarding the snap-through process of unsymmetric laminates increasing the understanding of the mechanics of the action still further. The snap-through process was seen to take place not as a single bifurcation but as two closely coupled bifurcations, as first one side snaps through and then the other.

Schlecht et al [24] developed simple active deformable composite structures based on unsymmetric laminates and incorporated shape memory alloy (SMA) wires. The theory was tweaked to incorporate those effects from the SMA wires, and compared to Finite Element Analysis (FEA) results with good agreement. Hufenbach et al [25] began to introduce a level of automation into the actuation method by integrating NiTi (smart alloy) wires in the composite layup. There was good correlation between experimental and predicted results. Schultz's [26] research combined several mathematical modelling techniques, using elasticity-type solutions and the finite element method to predict shapes of unsymmetric laminates with piezoelectric layers attached. Experiments were used to confirm that the proposed models accurately predicted the response of unsymmetric laminates to the effects of activating the piezoelectric layers. The use of piezoelectric actuators was further examined by Bowen et al [27] for different combinations of actuators and externally applied load suggesting that a combination of the two offers a

practical solution to the control and morphing of unsymmetrical composite structures. Hufenbach et al [28] extended the already comprehensive theory still further to predict the shapes of the laminates with integrated Macro Fibre Composite actors.

While the possibility of using snap-through composites in morphing structures has essentially been the motivation for the majority of the previous work it is only very recently that conceptual ideas have been proposed. Mattioni et al [29] investigated an alternative design for variable sweep wings. It consists of a two-spar carbon fibre reinforced wing, with truss like ribs. The spar uses snap-through composites to increase the moment of inertia to withstand bending stresses and, under certain loading conditions, to behave like an elastic hinge to allow the sweep angle of the wing to change. Schultz [30, 31] has considered a system consisting of two curved shells that are joined at the longitudinal edges to form an airfoil-like structure with two stable configurations. These configurations were shown to have a difference in axial twist. Several composite and one steel model were considered as proof of concept designs, with FEA used to study how changes in the geometric input values affected the shape and operational characteristics of the structures.

Concept Design

Consideration of the use of actuators, and snap through laminates, in adaptive blade design has resulted in the “back of the envelope” idea illustrated in Figure 0-2.

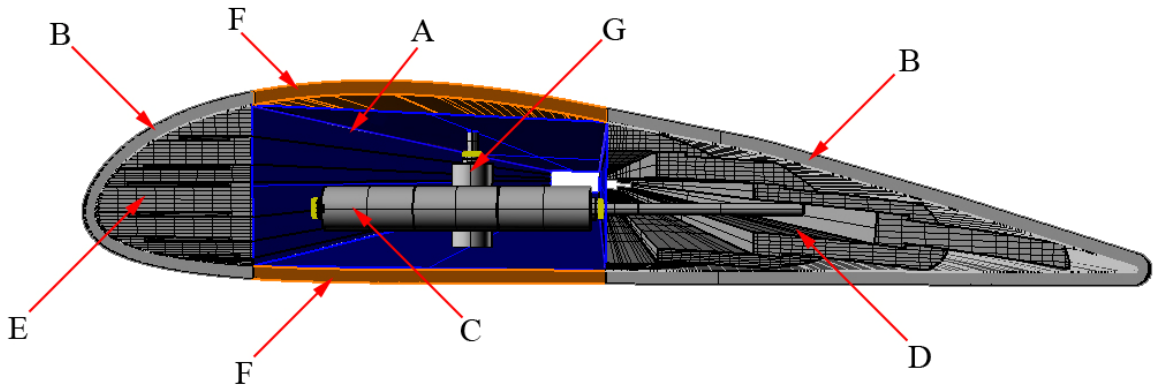

Figure 0-2: Conceptual adaptive foil sketch

The central spar of the blade is a bend twist coupled beam, A, shown previously to optimise performance of HATT blades in fluctuating inflows. The nose and tail cone sections are constructed of a thick flexible rubber sheet, B, which is stretched over a telescopic arrangement at either end. Upon sending a current through the transverse

solenoid, C, one telescopic mechanism extends, stretching the rubber sheet out to create the trailing edge, D; whilst the other contracts and the rubber sheet snaps back over the supports to form a smooth, rounded leading edge, E. The main foil body is constructed of "snap through" carbon skins, F, with the vertical solenoid controlling the actuation of these surfaces, G. This vertical solenoid is mounted on the bend-twist coupled central spar. As the leading and trailing edges reverse so does the mid body creating an asymmetric foil but in the opposite direction. Hence a totally bi-directional, efficient, asymmetric, sealed foil unit is developed. The use of two other vertical solenoids at the leading and trailing edges to control the deflection of the aft region of the section once it is in use has also been considered but deemed unnecessary with the bend-twist coupled central spar in operation. The blade is both passively (bend-twist coupled) and actively (snap-through composites and telescopic sections) adaptive.

In order to develop any design using relatively untried and untested technology it is imperative to generate a design methodology in order to make the process repeatable and compare for various designs. In the case of an actively adaptive tidal turbine blade where snap-through composites are utilised for part of the hydrofoil construction it is essential to be able to predict the shape of the laminate after cooling from cure temperature in order to develop and manufacture the chosen airfoil section for the blade correctly. Other considerations consist of fatigue analysis of the blade (required to operate efficiently through a 20 year lifespan), the fluid structural dynamics of the blade, and interaction with the turbine support system. The internal structure of the blade is likely to be complex and requires careful deliberation.

Design Methodology

All of the analysis methods discussed so far can be brought together towards the goal of a design methodology for the concept actively adaptive blade. An overview of this design methodology is illustrated in Figure 0-3. Each section is an iterative procedure. For example, in the fluids section, 2D analysis of several airfoil sections is carried out, whilst a pitch angle for the blade and a twist distribution of the sections along the span of the blade are decided. This information is then used in a BEMT analysis to assess the performance of the initial device. The process is repeated until a suitably performing blade has been created, at which point a three dimensional CFD analysis is carried out and the design is ready to move to the first stage of the structures section.

Here, basic beam theory is used to perform a simple analysis on a designated stock, and a number of fixed webs are chosen for the basic blade structure. The stock and webs are then modelled in an FE analysis, using the surface pressure loading information created in the CFD analysis. If the system performs inadequately, and a reasonable margin of safety is met, then alternative stocks and web arrangements may be considered until the blade is deemed sufficiently sound.

Detailed design of the internal and external structure of the blade can then be developed. This includes design, development and thorough testing of sensitive areas such as the telescopic leading and trailing edge mechanisms, and unsymmetric laminate snap-through mechanisms. Components of the structure are then tested in order to determine the level of fatigue imposed on them by a prospective 20 year life cycle. If these test results are found to be inadequate, the design is modified and the procedure carried out again.

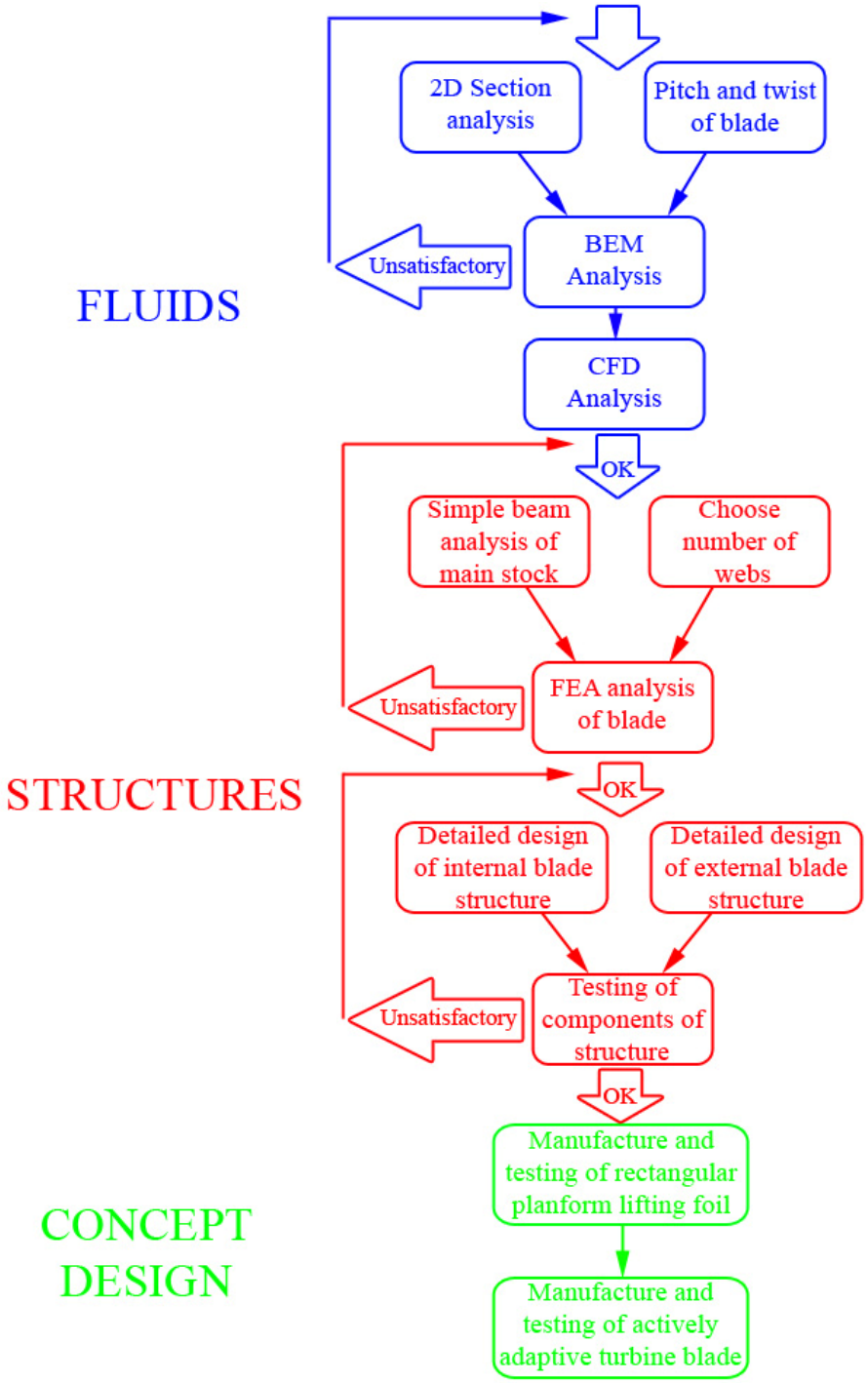

Figure 0-3: Design methodology flow chart

Once the detailed design of the internal and external structure is deemed to perform efficiently and effectively, a model rectangular lifting surface is constructed utilising combining the parts designed thus far. This lifting surface is then tested in a wind tunnel to assess the performance and highlight any problems. Once these are resolved, a fully operational model of the actively adaptive blade can be constructed and tested. Several

areas of the design methodology have already been started, and the following sections detail the results of the research thus far.

Modified Classical Lamination Theory

The composite laminates throughout this study consist of thin layers, or lamina, that are made of either glass or carbon fibres in several different matrix materials, and are manufactured on a flat aluminium plate. The possibility exists for an arbitrary number of layers to be stacked together with arbitrary ply orientation angles. In order to consolidate and cure these composite laminates, they are heated under pressure. In the case of symmetric laminates, a panel that is cured on a flat form tends to remain flat after cure and cooling to the operating temperature. A laminate is symmetric if the material, angle, and the thickness of the plies are the same above and below the midplane [32], as illustrated in Figure 0-4a). As has been discussed the thermally induced stresses developed in unsymmetric laminates cause curvature to develop as the panel cools. The laminates of interest are thin unsymmetric laminates with more than one stable equilibrium state at room temperature.

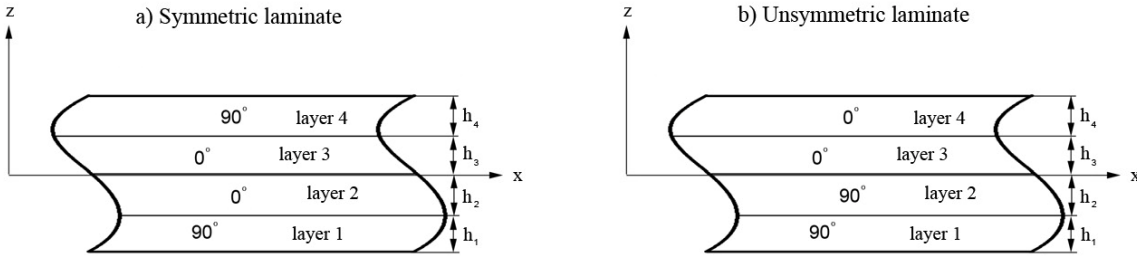

Figure 0-4: Schematic of a) a symmetric laminate and b) an unsymmetric laminate

Cross ply laminates, laminates with only 0^o and 90^o fibre orientations, are examined because they have the simplest laminate stiffness matrices, and modelling the behaviour of cross-ply laminates is more straightforward. Unsymmetric cross-ply laminates also have greater room temperature curvature, and lower bending stiffness, than other unsymmetric laminates. The increased curvature will make it more difficult for an actuator to snap the laminate; however, the lower bending stiffness of cross-ply laminates should mitigate this effect. Figure 0-4b) is a schematic of a typical laminate construction under investigation.

As has been shown extensively in previous research, CLT with geometric nonlinear extensions can be successfully used to model the room temperature shapes of

unsymmetric laminates [14-22]. The coordinate system implemented is that used in conventional CLT, i.e. a structural, or global, coordinate system in *x*, *y*, and *z*, with the *z* direction as the thickness direction; and a material coordinate system in 1, 2, and 3, with fibres in the 1 direction, and thickness in the 3 direction. CLT is a plate theory for laminated composite materials, in which properties are smeared through the thickness and defined at a reference surface. In-plane loads are defined in terms of force and moment resultants acting on the reference surface. In CLT, a number of simplifying assumptions are made [32]:

- each laminate is orthotropic;
- each lamina is homogeneous;
- a line straight and perpendicular to the middle surface remains straight and perpendicular to the middle surface during deformation;
- a straight line in the *z*-direction remains of constant length;
- the laminate is loaded only in its plane;
- displacements are continuous and small throughout the laminate;
- each lamina is elastic;
- no slip occurs between the lamina interfaces.

CLT is an extension of classic linear elastic Kirchhoff theory for homogenous plates, to laminated composite plates. The previous work focused on predicting which shape, or shapes, the laminate will deform into as it cools from the elevated cure temperature to room temperature, in a quasi-static manner. The linear theory predicts that only the saddle of Figure 0-1b) can exist; and Hyer [14, 15] and Hamamoto and Hyer [16] have shown that CLT cannot always accurately predict the room-temperature shapes of unsymmetric laminates. If geometric nonlinearities are included in the theory by using nonlinear strain-displacement equations, the shapes can be much more accurately predicted. A summary of the equations developed in previous research that are considered applicable to the current research is given in this section.

The behaviour of a laminate is studied by examining its total potential energy. At a given temperature below cure, the shape (or shapes) which minimise the total potential energy will be the ones to occur. Since the problem is non-linear, the total potential energy is examined within the context of Ritz approximations to the displacement field.

With the Rayleigh-Ritz technique, approximate displacement fields are assumed in terms of undetermined parameters and the total potential energy is made stationary with respect to the undetermined parameters in the displacement fields.

The total potential energy of the laminate, *W*, including the effects of thermal expansion is given by:

$$W = \int_{Vol} \left(\frac{1}{2} C_{ijkl} \varepsilon_{ij} \varepsilon_{kl} - \beta_{ij} \varepsilon_{ij} \Delta T \right) dVol \tag{0.1}$$

Where standard summation convention on the indices *i, j, k,* and *l* is implied and the indices each have values 1, 2, and 3. The C_{ijkl} terms are the elastic constants and the β_{ij} terms are constants related to the elastic and thermal expansion properties of the material. The ε_{ij} terms are the strains in the material, and ΔT is the temperature change of the material relative to stress-free temperature, i.e. the change in temperature from the cure temperature to room temperature. A positive ΔT corresponds to a temperature increase. For simplicity the C_{ijkl} and β_{ij} terms are assumed to be independent of temperature. Hooke's law then takes the form:

$$\sigma_{ij} = C_{ijkl} \left(\varepsilon_{kl} - \alpha_{kl} \Delta T \right) \tag{0.2}$$

where α_{kl} are the linear coefficients of thermal expansion. The volume integral is over the undeformed volume of the material. The undeformed laminate has dimensions $L_x \times L_y \times h$. With the origin of the *x, y, z*-coordinates system at the geometric centre of the undeformed volume, the limits on the volume integral are:

$$W = \int_{x=-L_x/2}^{L_x/2} \int_{y=-L_y/2}^{L_y/2} \int_{z=-h/2}^{h/2} \left(\frac{1}{2} C_{ijkl} \varepsilon_{ij} \varepsilon_{kl} - \beta_{ij} \varepsilon_{ij} \Delta T \right) dxdydz \tag{0.3}$$

Since there are no mechanical loads acting on the laminate, there can be no contribution to the total potential energy from external loads. If each lamina can be assumed to be in a state of plane stress, then the total potential energy expression simplifies to:

$$W = \frac{1}{2} \int_{x=-L_x/2}^{L_x/2} \int_{y=-L_y/2}^{L_y/2} \int_{z=-h/2}^{h/2} \left\{ \left(\sigma_x - \sigma_x^T \right) \varepsilon_x + \left(\sigma_y - \sigma_y^T \right) \varepsilon_y + \left(\tau_{xy} - \tau_{xy}^T \right) \gamma_{xy} \right\} dxdydz \tag{0.4}$$

Where σ_x^T, σ_y^T, τ_{xy}^T are the equivalent thermal stresses. Hooke's law for a single layer can be described by the reduced stiffness matrix:

$$\begin{Bmatrix}\sigma_x\\ \sigma_y\\ \tau_{xy}\end{Bmatrix}=\begin{bmatrix}\overline{Q}_{11} & \overline{Q}_{12} & \overline{Q}_{16}\\ \overline{Q}_{12} & \overline{Q}_{22} & \overline{Q}_{26}\\ \overline{Q}_{16} & \overline{Q}_{26} & \overline{Q}_{66}\end{bmatrix}\begin{Bmatrix}\varepsilon_x-\varepsilon_x^T\\ \varepsilon_y-\varepsilon_y^T\\ \gamma_{xy}-\gamma_{xy}^T\end{Bmatrix} \tag{0.5}$$

Where:

$$\begin{Bmatrix}\sigma_x^T\\ \sigma_y^T\\ \tau_{xy}^T\end{Bmatrix}=\begin{bmatrix}\overline{Q}_{11} & \overline{Q}_{12} & \overline{Q}_{16}\\ \overline{Q}_{12} & \overline{Q}_{22} & \overline{Q}_{26}\\ \overline{Q}_{16} & \overline{Q}_{26} & \overline{Q}_{66}\end{bmatrix}\begin{Bmatrix}\varepsilon_x^T\\ \varepsilon_y^T\\ \gamma_{xy}^T\end{Bmatrix} \tag{0.6}$$

Using the assumption that the Kirchhoff hypothesis is valid for the laminate as a whole, the strain-displacement relations take the form:

$$\begin{aligned}\varepsilon_x&=\varepsilon_x^o+z\kappa_x^o\\ \varepsilon_y&=\varepsilon_y^o+z\kappa_y^o\\ \gamma_{xy}&=\gamma_{xy}^o+z\kappa_{xy}^o\end{aligned} \tag{0.7}$$

The ε_x^T, ε_y^T, γ_{xy}^T are the equivalent thermal strains and are given by:

$$\begin{Bmatrix}\varepsilon_x^T\\ \varepsilon_y^T\\ \gamma_{xy}^T\end{Bmatrix}=\begin{Bmatrix}\alpha_x\\ \alpha_y\\ \alpha_{xy}\end{Bmatrix}\Delta T \tag{0.8}$$

Where α_x, α_y, α_{xy} are the thermal expansion coefficients. The quantities ε_x^0, ε_y^0, γ_{xy}^o are the midplane strains and the κ_x^o, κ_y^o, κ_{xy}^o terms are the midplane curvatures and the form given for them in equations (0.9) reflects inclusion of non-linear effects:

$$\begin{aligned}\varepsilon_x^0&=\frac{\partial u^0}{\partial x}+\frac{1}{2}\left(\frac{\partial w^0}{\partial x}\right)^2\\ \varepsilon_y^0&=\frac{\partial v^0}{\partial y}+\frac{1}{2}\left(\frac{\partial w^0}{\partial y}\right)^2\\ \gamma_{xy}^0&=\frac{1}{2}\left(\frac{\partial u^0}{\partial y}+\frac{\partial v^0}{\partial x}+\frac{\partial w^0}{\partial x}\frac{\partial w^0}{\partial y}\right)\end{aligned} \tag{0.9}$$

$$\begin{aligned}\kappa_x^0&=-\frac{\partial^2 w^0}{\partial x^2}\\ \kappa_y^0&=-\frac{\partial^2 w^0}{\partial y^2}\\ \kappa_{xy}^0&=-2\frac{\partial^2 w^0}{\partial x\partial y}\end{aligned} \tag{0.10}$$

The quantities u^0, v^0, and w are the displacements of the laminate midplane in the *x*-, *y*-, and *z*-directions, respectively. They are functions of *x* and *y* only.

In order for the Rayleigh-Ritz technique to be effective, displacement fields that accurately represent the displacements are needed. It has been shown that, for rectangular unsymmetric cross-ply laminates, the displacements of the room temperature shapes can be accurately represented by the following functional forms [15, 16]:

$$\begin{aligned} u^0(x,y) &= cx - \frac{a^2x^3}{6} - \frac{abxy^2}{4} \\ v^0(x,y) &= dy - \frac{b^2y^3}{6} - \frac{abx^2y}{4} \\ w^0(x,y) &= \frac{1}{2}\left(ax^2 + by^2\right) \end{aligned} \qquad (0.11)$$

Where the coordinates x and y are measured from the geometric centre of the initially flat laminate. In the above a, b, c, and d are constants which are determined as part of the minimisation process. The parameters a and b represent the negative curvatures in the x and y directions, respectively. The parameters c and d represent the portion of the strains in the x and y directions that are independent of spatial location within the laminate, respectively – i.e. the in-plane strains. These strains are associated with the laminate coefficients of thermal expansion. These four parameters define completely the shape of the laminate. A discussion of these approximate displacements is given by Hyer [15].

Back substituting the assumed displacements, equations (0.11), into the definitions of the mid-plane strain and curvatures, equations (0.9) and (0.10), and these in turn into the total strains, equations (0.7), and so forth back into the definition of total potential energy, equation (0.4); then the utilisation of the definitions of the **A**, **B** and **D** matrices enables the spatial integrations in equation (0.4) to be carried out. The final result is an algebraic expression for the total potential energy of the laminate of the form:

$$W = W\left(a,b,c,d,\Delta T\right) \qquad (0.12)$$

W is also a function of the laminate material properties and geometry (elements of the **A**, **B** and **D** matrices, L_x and L_y), but here interest centres on the deformations and temperature change which are key to the modelling of an unsymmetric laminate.

To study the deformation of the laminate as it is cooled from the cure temperature, $\Delta T<0$, the variation of the total potential energy is used. Equating the first variation to zero results in equilibrium equations for the laminate. The first variation is of the form:

$$\begin{aligned}\partial W = &\left\{ f_a\left(a,b,c,d,\Delta T\right)\right\}\partial a + \left\{ f_b\left(a,b,c,d,\Delta T\right)\right\}\partial b \\ &+ \left\{ f_c\left(a,b,c,d,\Delta T\right)\right\}\partial c + \left\{ f_d\left(a,b,c,d,\Delta T\right)\right\}\partial d\end{aligned} \tag{0.13}$$

And equating it to zero results in the four non-linear equations:

$$\begin{aligned} f_a &= \left(a,b,c,d,\Delta T\right) = 0 \\ f_b &= \left(a,b,c,d,\Delta T\right) = 0 \\ f_c &= \left(a,b,c,d,\Delta T\right) = 0 \\ f_d &= \left(a,b,c,d,\Delta T\right) = 0 \end{aligned} \tag{0.14}$$

This reduces to solving a series of simultaneous algebraic equation for the undetermined coefficients, specifically, setting the partial derivatives of *W* with respect to *a, b, c,* and *d* equal to zero, and solving for the four coefficients from:

$$\frac{\partial W}{\partial a} = 0 \qquad \frac{\partial W}{\partial b} = 0 \qquad \frac{\partial W}{\partial c} = 0 \qquad \frac{\partial W}{\partial d} = 0 \tag{0.15}$$

These solutions correspond to the equilibrium shapes of the laminate. The stability for the configurations can be assessed by examining the higher-order variations of the total potential energy, i.e. $\delta^2 W$, etc. The second variation can be expressed in quadratic form as:

$$\begin{aligned}\delta^2 W &= \tfrac{1}{2}\begin{bmatrix}\delta a & \delta b & \delta c & \delta d\end{bmatrix}\begin{bmatrix} k_{11} & k_{12} & k_{13} & k_{14} \\ k_{12} & k_{22} & k_{23} & k_{24} \\ k_{13} & k_{23} & k_{33} & k_{34} \\ k_{14} & k_{24} & k_{34} & k_{44}\end{bmatrix}\begin{bmatrix}\delta a \\ \delta b \\ \delta c \\ \delta d\end{bmatrix} \\ &= \tfrac{1}{2}\begin{bmatrix}\delta a & \delta b & \delta c & \delta d\end{bmatrix}\left[K\right]\begin{bmatrix}\delta a \\ \delta b \\ \delta c \\ \delta d\end{bmatrix}\end{aligned} \tag{0.16}$$

If the second variation is not zero, stability of the equilibrium is associated with the matrix **K** being positive definite. The relevant substitution and calculus has been carried out and the full derivation of the coefficients *a, b, c,* and *d* is shown in Appendix D.

Numerical Example

In order to use the equations derived in the previous section the material properties of the laminates under investigation are required; specifically the Young's modulus, Poisson's ratio, and coefficients of thermal expansion in both the transverse and longitudinal directions, and the shear modulus in the *xy* direction.

If the Young's modulus and volume fraction of both the fibres and the resin matrix is known then the Young's modulus in both the longitudinal and transverse directions can be determined using the Rule of Mixtures.

$$E_1 = E_f V_f + E_m V_m$$
$$E_2 = \frac{E_f E_m}{E_f V_m + E_m V_f} \tag{0.17}$$

Where the subscripts *f* and *m* denote *fibres* and *matrix* respectively and:

$$V_f = \frac{A_f}{A_f + A_m}$$
$$V_m = \frac{A_m}{A_f + A_m} \tag{0.18}$$

The major and minor Poisson's ratios, υ_{12} and υ_{21}, and the shear modulus, G_{12}, may be estimated by the following equations:

$$\upsilon_{12} = \upsilon_f V_f + \upsilon_m V_m$$
$$\upsilon_{21} = \upsilon_{12} \frac{E_2}{E_1} \tag{0.19}$$
$$G_{12} = \frac{G_f G_m}{G_f V_m + G_m V_f}$$

These equations, however, are only an approximation of the material properties of a laminate as they do not take into account the interaction between the fibres and the matrix in each laminate direction. In order to determine more accurate material properties, experiments must be carried out on samples of the materials used.

Using the geometry shown in Figure 0-4b) an example problem is examined. This problem consists of a four layer square laminate with carbon/epoxy layers each 0.122mm thick and side lengths of 0.25m. The laminate is flat at curing temperature and is then cooled to room temperature without any constraints ensuring it can form whichever mode is most stable. The material properties for the layers are given in Table 0-1. It is assumed that the laminate is cooled 150^{o}C from curing to the operating temperature - room temperature.

Table 0-1: Layer properties used in the initial model, obtained from literature.

Property	Carbon/epoxy layers
E_1 (GPa)	171.0

E_2 (GPa)	8.76
G_{12} (GPa)	5.76
v_{12}	0.335
v_{21}	0.0172
α_1 (/^{o}C)	0.5094 x 10^{-6}
α_2 (/^{o}C)	27.6 x 10^{-6}

The mode shapes may also be represented by the curvatures κ_x^o and κ_y^o (recall that $a = -\kappa_x^o$ and $b = -\kappa_y^o$). At point A (cure temperature), both *a* and *b* are zero since the laminate is flat. Observing Figure 0-5, *a* and *b* take on non-zero values as the temperature reduces. Specifically *a* is positive, and *b* is equal in magnitude to *a* but negative.

This corresponds to a shallow saddle shape, Figure 0-1b). As the temperature decreases further, to point B, the temperature-curvature relationship bifurcates. With a further reduction in temperature this relationship follows either path BC, path BD or path BE. With path BC, the curvature in the *x*-direction increases, whilst curvature in the *y*-direction decreases. At room temperature the curvature in the *y*-direction virtually disappears and the laminate takes the form of Figure 0-1c). With path BE the curvature in the *y*-direction increases whilst that in the *x*-direction decreases. At room temperature the curvature in the *x*-direction is negligible and the laminate takes the form of Figure 0-1d). Lastly, with path BD the curvatures in both directions increase and stay relatively equal in magnitude but opposite in sign. This corresponds to the saddle shape, Figure 0-1b). A stability analysis shows that paths BC and BE are stable, but path BD is not. At room temperature, application of force causes the laminate to snap through from the configuration represented by point C to that represented by point E, or vice versa.

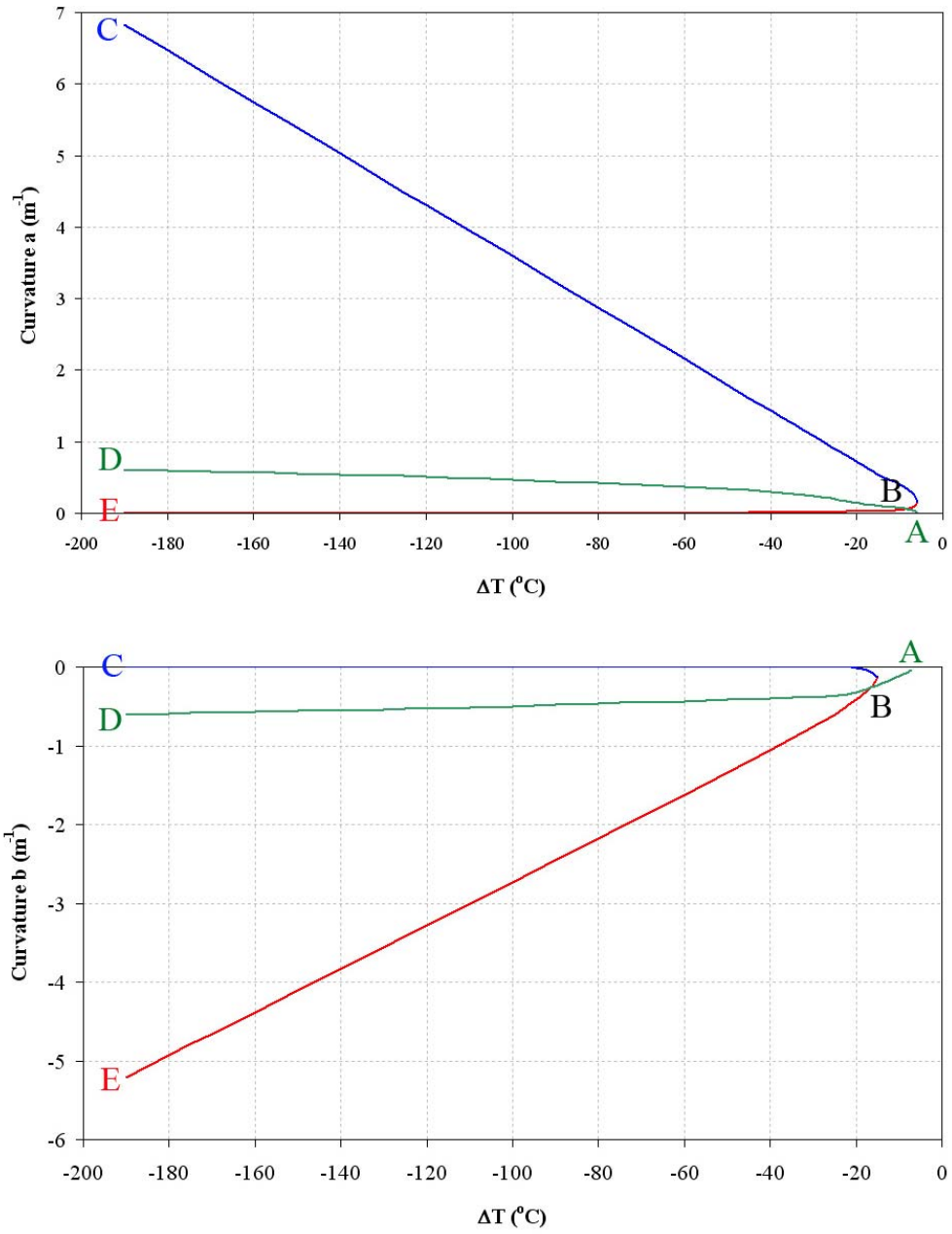

Figure 0-5: Temperature-curvature relationship of a square [0_2/90_2] carbon-epoxy laminate

The advantages of using snap-through composites in tidal turbine blade design are as follows:

- the requirement for an expensive and hard to maintain variable pitch mechanism would be negated;
- the numbers of areas in which the turbine could operate effectively without new blades being designed for each one could be increased;
- the device could capture energy with high efficiency during both the flood and ebb of the tide;

- the blade efficiency overall could be improved, and ultimately the annual energy capture of a device would be increased.

In the literature explored the majority of the snap-through composites manufactured and analysed have been carbon fibres in an epoxy matrix. This combination produces the greatest amount of room temperature curvature of the more common fibre/matrix combinations. This is because the difference between the coefficient of thermal expansion of carbon is an order of magnitude smaller than that of glass, aramid, epoxy and polyester. Carbon, however, is expensive and becoming difficult to obtain due to large increase in its application in both the US and European aeronautical industries; and for use as the central section of a hydrofoil the large radii of curvature achieved when working with carbon are unnecessary – therefore glass fibre reinforcements are largely considered in this work, which are considerably less expensive and more readily available than carbon.

Another factor to consider in the previous work is the epoxy matrix, while proven to produce good snap-through composites in a laboratory environment it is prone to problems caused by moisture absorption which is inevitable in a subsea environment. It is also relatively brittle, and recognising that a tidal turbine will be required to have a life cycle of anywhere between 10 and 20 years, this would impose somewhere between 15000-30000 snap cycles for a single blade – it is unlikely that the epoxy matrix would survive this number of snaps without becoming more brittle, cracking and failing. The decommissioning and recyclability of carbon-epoxy blades is also limited and difficult [33], and with global awareness becoming ever prevalent this is an important factor to consider.

In order to eliminate some of these problems use of a thermoplastic matrix reinforced with glass fibres has been considered. There are a number of thermoplastics that are comparatively inexpensive, wholly recyclable, tough yet not brittle, water resistant, relatively easy to work with, resistant to marine growth and readily available; thus making them a serious contender for use as the matrix of snap-through composites.

Thermoplastics

Thermoplastics are a class of polymeric materials that soften when heated (and eventually liquefy) and harden when cooled – processes that are totally reversible and may be repeated, and as such these polymers are wholly recyclable. These materials are

normally fabricated by the simultaneous application of heat and pressure. On a molecular level, as the temperature is raised, secondary bonding forces are diminished (by increased molecular motion) so that relative movement of adjacent chains is facilitated when a stress is applied. Irreversible degradation results when the temperature of a molten thermoplastic polymer is raised to the point at which molecular vibrations become violent enough to break primary covalent bonds.

At the outset, glass reinforced polypropylene (PP) was chosen for the manufacture of the snap-through panels for the body of the aerofoil section of the turbine blade. The formula for PP is illustrated in Figure 0-6.

$$(\text{-CHCH}_3\text{-CH}_2\text{-})_n$$

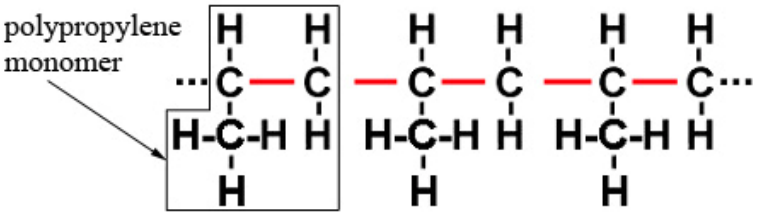

Figure 0-6: Molecular formula of polypropylene

PP has many properties in its favour. It is easily processed (a temperature of 190^{o}C and a vacuum are required for consolidation which is relatively low when compared to other thermoplastics), inexpensive, readily available and wholly recyclable. It is also relatively robust and resists marine growth, and thus may not require an anti-foul coating.

Initial [0/90] test panels were made by stripping fibres from a woven cloth consisting of co-mingled polypropylene and glass fibres to create a coarse unidirectional cloth, Twintex produced by O.C.V. The panels seemed relatively successful, insofar as the snap-through phenomena was observed to occur to a small degree, although consolidation was poor. As a result a source of unidirectional polypropylene fibre reinforced tape was found, Celstran produced by Ticona. A comprehensive range of fibre reinforcements, thermoplastic matrices and custom tape widths are available. A second set of panels made from Celstran was manufactured, one [0/90] and one [0_2/90_2]. The panels were laid up on a flat aluminium plate coated with Freekote so that the samples did not stick to the surface, sealed in a vacuum bag, and cured at 190^{o}C for fifteen minutes,

Figure 0-7. Once the cure cycle was complete, the oven was switched off, the door opened, and the vacuum bag cut away in order remove any external loading on the panel allowing it to deform solely due to the thermal strains imposed on it during cooling.

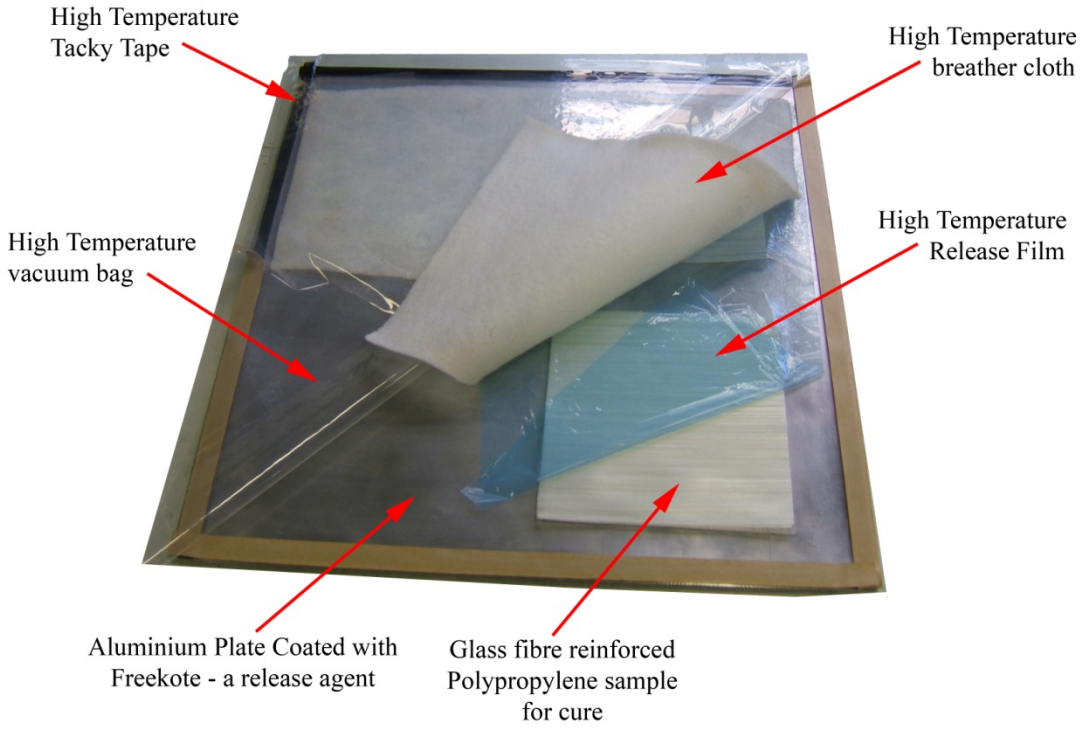

Figure 0-7: Layup of a polypropylene sample

When the cooled panels were first removed from the mould the [0/90] exhibited a large amount of curvature, although it only had one stable equilibrium shape and could not be snapped to a second. The $[0_2/90_2]$ panel seemed to be more successful, and clearly had two distinct stable states and could be snapped through from one to the other. After one hour the four ply panel had relaxed into a slight saddle shape, although it did still snap through to a cylindrical second stable shape. After a couple of hours it had relaxed such that it could not sustain the second equilibrium configuration and therefore no longer snapped through. Both the two ply and the four ply panels had also reduced in curvature considerably over time. It is thought that this shape change was due to a combination of stress relaxation and creep under the pre-stressed state that the asymmetric lay-up, and the curing cycle, imposed on the panel.

It is important to realise that viscoelastic behaviour was also observed to occur with the carbon-epoxy snap-through panels investigated by Schultz [26]. Over the course of approximately four months, the curvature of the manufactured panels was believed to have lessened. The two major curvatures in the x and y directions decreased by around

65% of the original values. This was deemed to occur due to moisture absorption of the laminate. The laminate was then heated in one stable configuration at 50^{o}C for 24 hours, the plate was then snapped through and heated for a further 24 hours at the same temperature in an effort to drive the moisture out of the laminate. Once the laminate had cooled the radii of curvature had increased to approximately 77% of the original values, indicating that moisture absorption had been part of the cause of the relaxation. The prolonged heating, however, also recreated a proportion of the originally induced thermal strains that occur due to the difference in thermal expansivity of the fibres and matrix, and it is unknown as to what proportion this took.

It seems unlikely that the relaxation observed in the polypropylene panels was due to moisture absorption as, although PP is prone to moisture absorption, such a phenomenon is unlikely to occur rapidly enough (i.e. in the span of a few hours) to cause the slump. Therefore it has been assumed that the cause of the loss of curvature was down to a mixture of both creep and stress relaxation.

Amorphous polymers may behave like glass at low temperatures, a rubbery solid at intermediate temperatures (above glass transition temperature), and a viscous liquid as the temperature is increased further. For relatively small deformations, the mechanical behaviour at low temperatures may be elastic; that is in conformity to Hooke's Law, $\sigma=E\varepsilon$. At the highest temperatures, however, viscous behaviour prevails. Most polymers are viscoelastic – they exhibit both elastic and viscous behaviour – and therefore will deform under load with both an immediate response (elastic) and a slower response (viscous) and thus exhibit the combined mechanical characteristics of these two extremes.

The viscoelastic behaviour of polymeric materials is dependent on both time and temperature. Stress relaxation is one method of quantifying this behaviour – a decrease in stress in a material subjected to prolonged constant strain at a constant temperature as the molecular relaxation process takes place within the polymer.

Creep can be defined as deformation that occurs over a period of time when a material is subjected to constant stress at constant temperature. Creep at room temperature is more common in plastic materials and is called cold flow or deformation under load. The creep of a material can be divided into three stages. First stage, or primary creep, starts at a rapid rate and slows with time. Second stage (secondary) creep has a relatively

uniform rate. Third stage (tertiary) creep has an accelerating creep rate and terminates by failure of material at the time of rupture; this is illustrated in Figure 0-8.

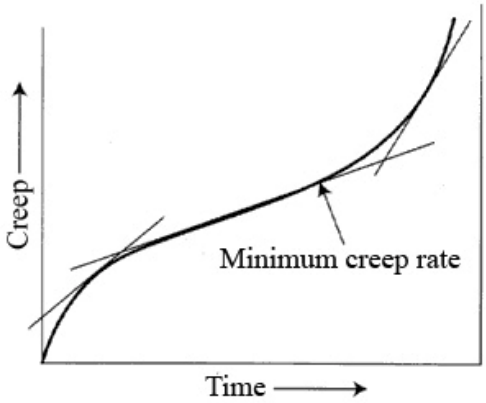

Figure 0-8: Graphical representation of creep in a thermoplastic

In polymers, creep is the stretching – or rather lengthening – of the C-C bonds in the chain illustrated in red in Figure 0-6. The CH_3 groups do help prevent creep as they "collide" and prevent further movement than would be possible in a more pure polymer, such as Nylon which has no side groups and stretches considerably with relatively little effort. This is known as steric hindrance which acts between adjacent groups and restricts torsional bond angles.

Many early publications on stress relaxation dealt with the amorphous materials, and the behaviour of these single phase materials is fairly well understood. The viscoelastic response of semi-crystalline materials, such as PP, is more complex [34, 35]. A number of fundamental studies on the mechanical relaxations in PP have been published [35-37], dealing with molecular mechanisms and kinetics. More recent studies on stress relaxation in PP have focused on time-temperature superposition [38-40], nonlinear effects [41, 42], viscoelastic constitutive equations [43], effects of strain rate and cyclic preloading [44-46], blends, and the interaction between viscoelastic and structural relaxation. One type of structural relaxation that has received much attention is physical ageing.

Creep measurements have been used in many of these studies on PP [47-49], but stress relaxation tests have been applied as well [50]. Internal stresses have also been considered in relation to the viscoelasticity of PP [51], as have morphological effects [52]. Although the aspect of creep in fibre reinforced PP has been touched on [49] little is to be found on the subject of stress relaxation of continuous fibre reinforced PP.

In order to try and quantify the rate of relaxation of the four ply glass-PP cross-ply unsymmetric laminates some basic creep tests were carried out. A 20cm × 20cm $[0_2/90_2]$ laminate was manufactured and cured at 190°C for 15 minutes. The specimen was then left unconstrained to cool to room temperature. It was then placed on a smooth, flat aluminium plate with a displacement pot clamped perpendicular to the midpoint of the axis of curvature, a heavy steel bracket next to one straight edge, and an extensometer resting against the other edge. A flat horizontal metal strip was bolted on to the bottom of the displacement pot in order to gain an accurate measurement of the midpoint of the laminate as it relaxes and moves sideways. Figure 0-9 illustrates the experimental set up.

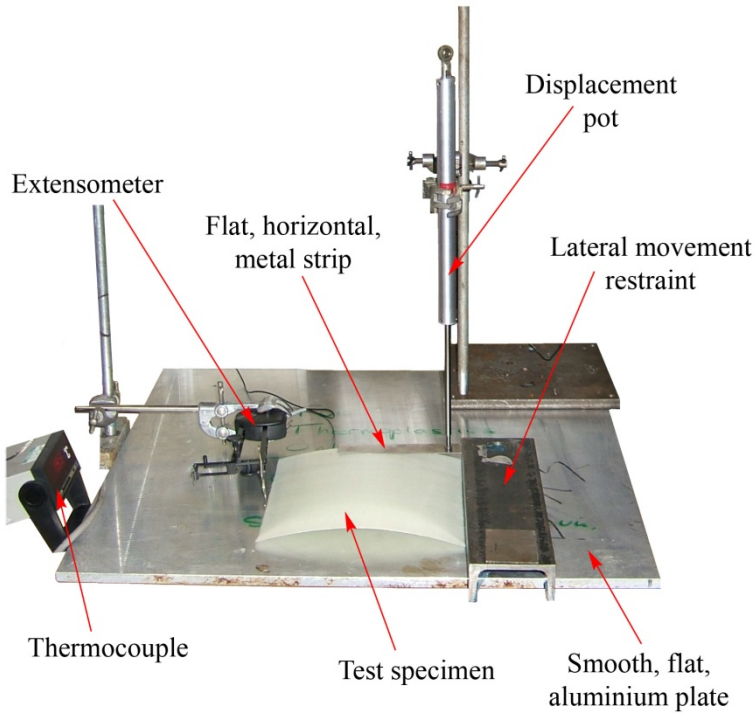

Figure 0-9: Creep/stress relaxation experimental set up

Unfortunately, at the time of these preliminary experiments connection of the thermocouple to the data acquisition software was not available and therefore a track of temperature overnight was not recorded. With temperatures outside the laboratory at this time of year (February 2008) dropping to below zero then it can be assumed that the room temperature would also substantially decrease. This assumption can be observed to be correct by regarding the plot of sample radius of curvature against time in Figure 0-10. The temperature of the atmosphere surrounding the sample was 19°C for the first 2.75 hours of the experiment. During this time the radius of curvature of the specimen was seen to decrease linearly. After 2.75 hours had passed the temperature decreased overnight and the radius of curvature began to increase slowly. Relaxation occurred once

again the following morning corresponding to the time that the heating in the building was switched on.

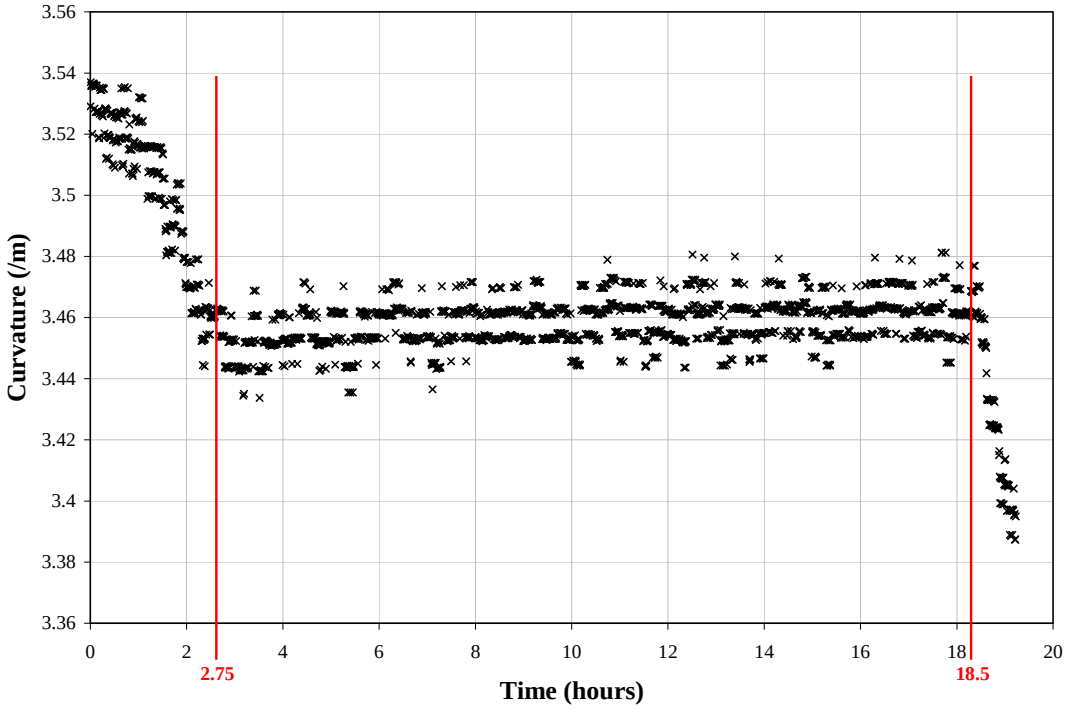

Figure 0-10: Laminate curvature against time

After over 19 hours the sample had relaxed, albeit not enough to prevent snap-through, and still had two stable configurations at room temperature. However, after being left in a room at 20°C for the rest of the day the sample had crept enough such that it was unable to hold the second, previously stable, shape and was beginning to curl up significantly at the corners. This suggests that in an equilibrium state it would revert to the saddle predicted by CLT, Figure 0-1b).

In practise a tidal turbine will be operating tens of metres below the surface of the sea in a swift tidal stream. This region is still considered to be in the surface layer of the ocean which is well mixed from top to bottom and sea temperature has a global average of about 17°C. Although at higher latitudes the polar seas can be as cold as -2°C, and the Persian Gulf as warm as 36°C. Therefore the amount of creep of a PP blade would vary with location. Even if the turbine were to be situated in cooler than average waters, however, it should be recalled that the manufacturing and installation processes of the blades would require long periods to be spent at temperatures ranging from 0°C to 30°C. This is dependent on the season and operating environment but would cause the snap-

through component of the device to relax and therefore cease to operate even when installed in the cooler subsea environment.

Further creep tests were carried out on another sample with the same experimental set up, however these were done in a climate controlled area where the temperature was fixed at 20°C for the period of 2.8 days, (68 hours). At the end of the experiment the laminate no longer had two stable room temperature shapes, i.e. snap-through did not occur indicating that the internal strains resulting from the curing process at elevated temperature caused relaxation of the laminate. Observation of Figure 0-11 clearly shows a reduction in the curvature of the sample over time, this relates to an increase in radius of curvature or rather creep and relaxation of the test specimen. The rate of relaxation of the sample decreased with time until the specimen reached a state at which relative equilibrium was achieved (after 53 hours or 2.2 days) and the curvature does not decrease further.

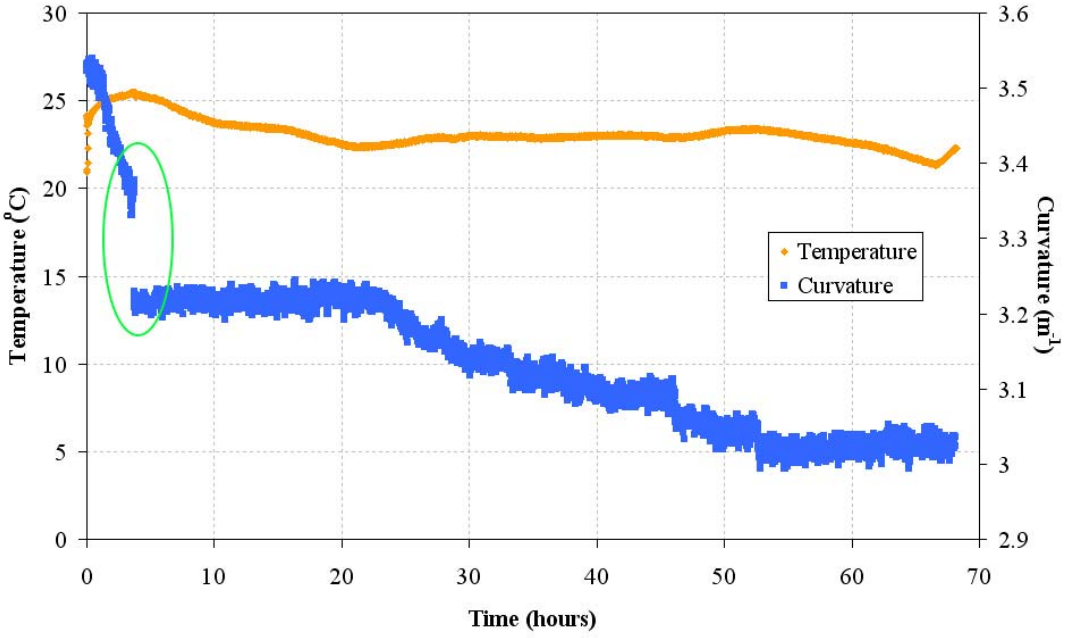

Figure 0-11: Sample curvature and temperature against time

While the temperature of the sample stayed relatively constant throughout the duration of the experiment, there is a considerable jump in curvature a few hours into the experiment. This can be better explained by referring to Figure 0-12.

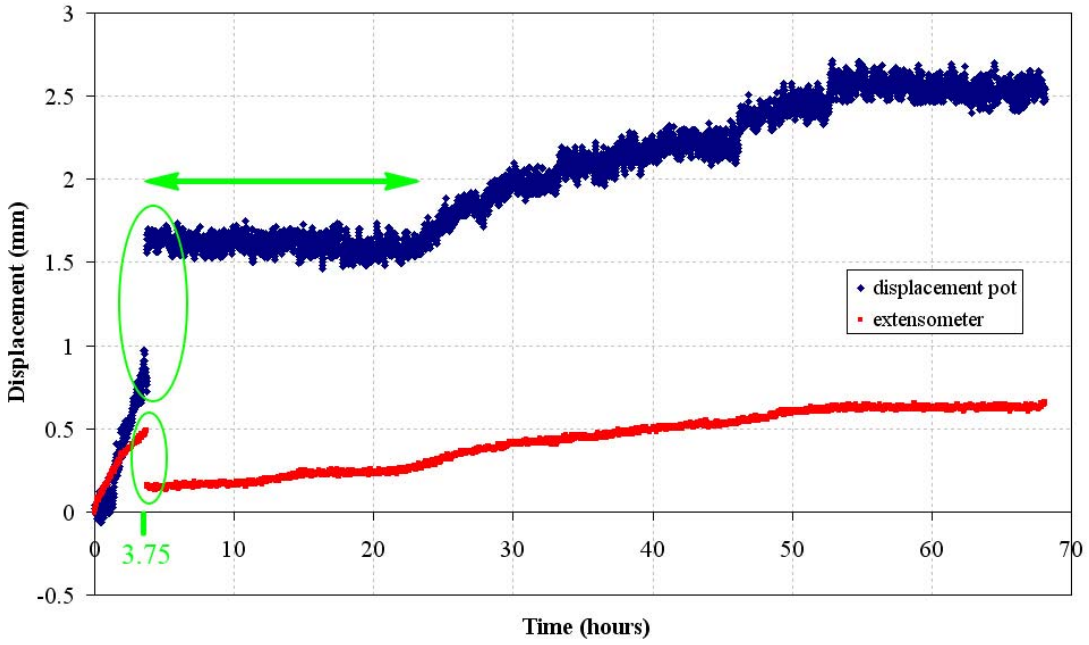

Figure 0-12: Direct displacement measurements of laminate against time

The jump can be seen to occur after 3.75 hours of running time, circled in green. This corresponds to the door to the oven being opened and shut, the shock of which caused the measurement equipment and the laminate to be disturbed.

The displacement pot measured the change in height of the laminate. At the time of the disturbance the laminate appears to have slumped over half a millimetre, represented by an increase in the displacement measured at this time. After this slump, it took a further 19.5 hours for creep/relaxation to begin again. The sudden drop in displacement measured by the extensometer, however, indicates that it was not just laminate slump that occurred. If this had been the case the extensometer curve would have stepped up, not down, as the laminate collapsed. It is thought that this decrease in displacement may have been caused by the laminate slipping under the tip of the extensometer to a new point of contact from which relaxation continued. Despite the disturbance creating a jump in the results, the fact that the laminate no longer snapped through after the duration of the test indicates that the polypropylene matrix is not feasible for use in manufacturing snap-through laminates.

While polypropylene exhibits many of the qualities required for the use as part of the turbine blade – durable, resistance to marine growth, recyclable, readily available, inexpensive – it is clear that it is unable to withstand the internal stresses created when manufactured into an unsymmetric laminate and still hold its initial curvature. Therefore

another plastic matrix must be considered. Concerns for the durability of epoxy, and its tendency to absorb moisture, and the fact that it is not recyclable make it unlikely that this is the solution to the problem. Initial thoughts are that either PEEK (Polyetheretherketone) or ABS (Acrylonitrile butadiene styrene) may be more suitable.

PEEK, Figure 0-13, is a semicrystalline thermoplastic that is highly resistant to thermal degradation, organic and aqueous environments; and is commonly used in bearings, piston parts, pumps, and in the medical industry. It is one of the few plastics compatible with ultra-high vacuum applications. In a carbon fibre reinforced form, PEEK has come under consideration as an aerospace structural material due to its high strength-to-weight ratio. Although PEEK requires high processing temperatures, it can be processed using standard equipment. It exhibits good chemical resistance, although is still considerably easier to bond than PP due to the presence of the ketone group. The main disadvantage of PEEK is that, as it is still a relatively newly developed thermoplastic, initial manufacturing costs are high – although these are likely to decrease with time and as more applications are found.

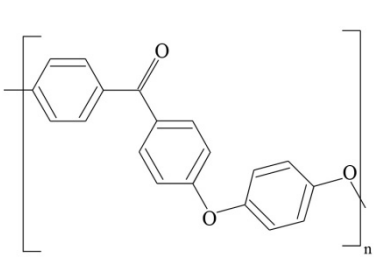

$[C_{19}H_{12}O_3]_n$

PEEK

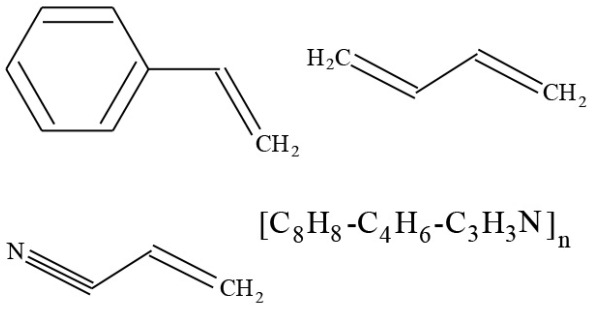

$[C_8H_8\text{-}C_4H_6\text{-}C_3H_3N]_n$

ABS

Figure 0-13: Chemical formula for Polyetheretherketone, PEEK, and Acrylonitrile Butadiene Styrene, ABS

The ABS three monomer system, Figure 0-13, can be tailored to yield a good balance of properties: styrene contributes ease of processing characteristics, acrylonitrile imparts chemical resistance and increased surface hardness, and the butadiene contributes impact strength and overall toughness. Stability under load is also good when under limited loads and it should be noted that the impact resistance of the thermoplastic does not fall off rapidly at lower temperatures. Glass-reinforced ABS has improved properties

over the non-reinforced resin. This advantage opens a wide range of high performance opportunities, particularly in applications requiring high strengths, rigidity and dimensional stability. ABS, however, is severely attacked by some solvents. Prolonged exposure to aromatic solvents, ketones and esters should be avoided. This poor resistance to solvents does allow solvent bonding as a means of assembly, which would make manufacture of the concept blade considerably easier.

As both PEEK and ABS have a more complex molecular geometry, the effect of steric hindrance will be much greater in these thermoplastics than in PP. Therefore it is much less likely that creep will occur to the degree that it does in PP and either of these polymers could be suitable for the manufacture of snap-through composites and hence horizontal axis tidal turbine blade construction. It is intended that further negotiations are undertaken with Ticona in order to obtain some unidirectional fibre reinforced PEEK and ABS, although careful consideration will be required as to where to manufacture the laminates due to the high cure temperature required.

Further research is required into the field of thermoplastics, as it is felt that the fact that they are all recyclable is a considerable bonus, and as such those that are both resistant to moisture absorption and creep, and are good under load should be considered.

Manufactured Panels

Three different sets of $[0_2/90_2]$ snap-through panels have been manufactured to date; a glass fibre/epoxy, carbon fibre/epoxy and glass fibre/polypropylene panel. In order to compare the effect of different fibre reinforcements and resin matrices on the curvature of the samples, measurements were taken from each sample of the chord length and the chord height of the specimen and the radius of curvature calculated using equation (0.20).

$$R = \frac{\sin\left(\arctan\left(\frac{d_c}{h_c}\right)\right)\sqrt{{d_c}^2 + {h_c}^2}}{\sin\left(\pi - 2\arctan\left(\frac{d_c}{h_c}\right)\right)} \qquad (0.20)$$

$$\kappa^o = \frac{1}{R}$$

Where R is the radius of curvature, κ^o is the same as the curvature determined from the modified CLT and the terms d_c and h_c are as shown in Figure 0-14.

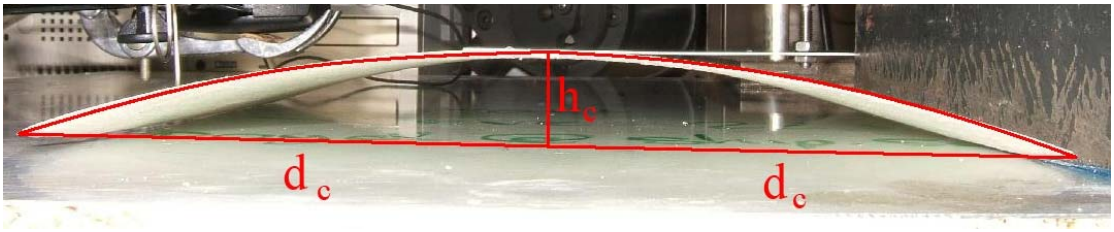

Figure 0-14: Calculating radius of curvature of a manufactured laminate

Table 0-2 gives both the *a* and *b* curvature of the three specimens and the radius of curvature in each configuration. Also shown are typical coefficients of thermal expansion (CTE) for each fibre type and matrix. It is clear that the two specimens that had glass fibre reinforcements resulted in similar levels of curvature at room temperature. Of the three specimens the glass fibre/epoxy laminate has the greatest *a* and *b* curvature. This is unexpected as in previous work carbon fibre/epoxy laminates exhibit a large degree of curvature, up to $12.8m^{-1}$ (0.078m radius) [26] due to the large difference between the coefficient of thermal expansion (CTE) of carbon and that of epoxy. In this case it is thought that the smaller curvature of the carbon fibre/epoxy specimen was caused by a high fibre volume fraction thus resulting in too little resin for the difference in CTE to cause a large curvature.

Table 0-2: Experimental curvature data for the three samples

Type of Laminate (CTE ($x10^{-5}$ /^oC))	*a* curvature (m^{-1})	*b* curvature (m^{-1})	Radius of curvature *a* (m)	Radius of curvature *b* (m)
Glass Fibre (2.2) /epoxy (5.4)	3.91	2.87	0.256	0.348
Carbon fibre (0.2) /epoxy (5.4)	2.02	1.69	0.495	0.592
Glass fibre (2.2) /Polypropylene (8.6)	3.53	2.17	0.283	0.460

While it is relatively simple to manufacture plain panels with two curvature configurations, these curvatures are not opposites of each other. Rather they are opposite but rotated through 90^o, Figure 0-1c) and Figure 0-1d). Thus if two panels are placed in the positions indicated in Figure 0-2, activating both panels at once would not have the desired effect of snapping the camber line of the airfoil, effectively reflecting the camber line in the horizontal. Using the technology suggested by Mattioni et al [29] with an unsymmetric laminate adjoining a flat panel, Figure 0-15a), or using the transverse reinforcement strips the laminate can be encouraged to snap from a cylindrical configuration to essentially a flat plate, Figure 0-15b); thus representing the two sides of an asymmetric airfoil section more effectively.

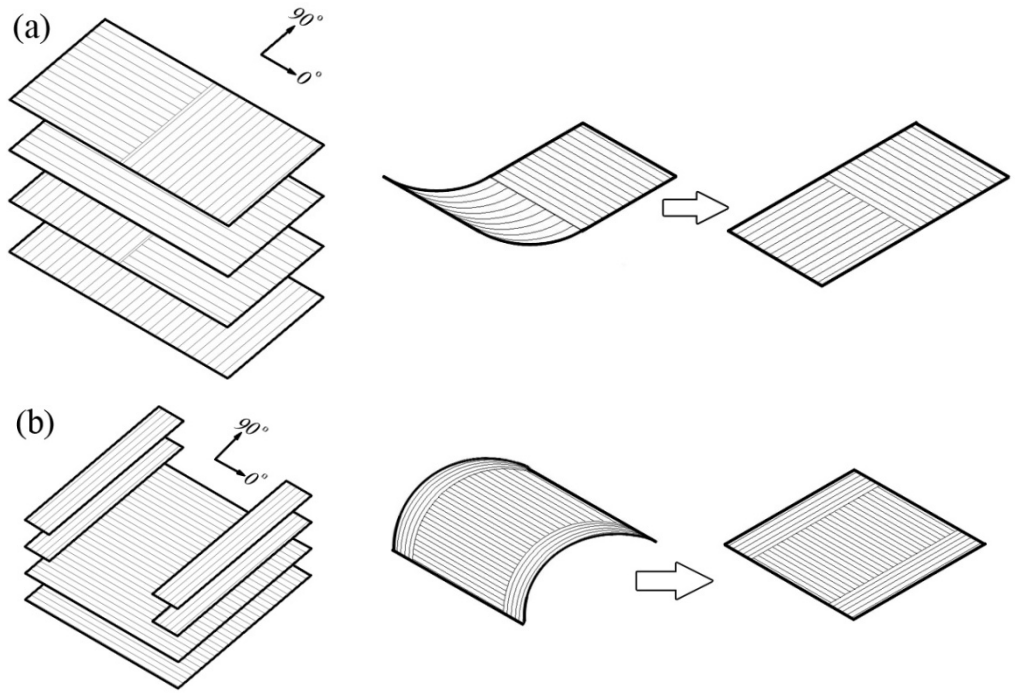

Figure 0-15: Alternative Snap-through laminate layups and stable room temperature configurations

A free stream device with actively adaptive blades in a semi-diurnal tidal location will need to perform in the order of 30,000 snap cycles for a 20 year life span. With such a range of fibre reinforcements and thermoset and thermoplastic matrices, fatigue testing of several snap-through panels in order to assess the durability of the matrix over many thousands of cycles, and also the stability of the two snap through geometries is essential.

It is intended that specimens of both types of laminate illustrated in Figure 0-15 will be constructed and incorporated into a simple, rectangular planform, airfoil on which experiments can be carried out as to the suitability of adhesives between the laminates and nose and tail sections, and wind tunnel tests to determine which technique is preferable – or whether a hybrid technique maybe developed which is more suited to the purpose of an adaptive lifting surface.

Structural Considerations

With any such novel concept design as that shown in Figure 0-2, there are many aspects of the assembly that require careful consideration. The external skin of the adaptive blade is highly important, being the first surface in contact with the harsh subsea environment and any inquisitive sea life. It needs to be resistant to marine growth, waterproof, durable, and easy to construct and maintain. With such a range of different materials amalgamated into one blade, difficulties are likely to be experienced bonding the areas of the blade together. While several of the more appropriate thermoplastics for use

as a matrix in a snap-through composite are commonly renowned for their durability, and resistance to chemical attack, it is these very properties that cause the material to be difficult to bond. Few adhesives will bond such a material to another easily, and the resulting bond is often weak. Whilst both PEEK and ABS can be bonded relatively easily, when compared to PP, neither has been proven to be the best material for the snap through part of the concept blade. Therefore this is still an area that will necessitate much research, with trial and error experiments of a range of bonding agents and loaded seams, and resistance welding. As yet, a flexible and also durable material has not been found for the morphing leading and trailing edges of the foil, though it is clear that research will need to be carried out in this area.

Another area of concern within the design is that of the internal structure. To begin simply, a structure undergoing the cyclic loading that will be imposed on a tidal turbine blade requires a substantial spanwise support. In conjunction with this the snap-through areas of the blade will require the relevant space to complete the snap-through cycle and assume the new shape. The method of fixing the actuators inside the blade for the nose and tail sections, and the bi-stable composites needs to be considered carefully. Fatigue and wear of the telescopic nose and tail sections is a serious concern, and will require careful design and extended fatigue testing to ensure that these delicate areas will not be a source of problems for blades in use.

It is proposed that the blade be a sealed unit, making maintenance simpler as a blade can simply be removed and replaced with a new one, and the faulty one taken to the shore for repair. As such the internal mechanisms do not need to be water resistant. It is also likely that, at the depth of operation (approximately 20 metres below the seas surface), the ambient temperature of the sea will be enough to cool the systems and prevent overheating.

Summary

Previously passively adaptive blades have been shown to offer potential improvements in HATT efficiency and design. The addition of active adaptation to the passively adaptive blades in the manner of snap-through blade skins has been suggested as a method to optimise the efficiency of a device throughout the entire tidal cycle without the need for complex variable pitch or vaning mechanisms. Different materials have been considered for use as the snap-though skins and a combination of creep and stress

relaxation identified as a governing factor on the choice of these materials. It is thought that the development of actively adaptive blades is an area of considerable scope for future consideration.

1. Goldin, D., S. Venneri, and A. Noor, *Fresh Air, Wide-Open Space.* Mechanical Engineering, 2001. **123**(11): p. 48-55.
2. Sietzen, F., *New Blueprint for NASA Aeromautics.* Aerospace America, 2002: p. 24-28.
3. Agnes, G., *Adaptive Structures.* Aerospace America, 2001: p. 78.
4. Wilson, J., *Active Aeroelastic Wing: A New/Old Twist on Flight.* Aerospace America, 2002: p. 34-37.
5. Hyer, M. and A. Jilani, *Deformation Characteristics of Circular RAINBOW Actuators.* Smart Materials and Structures, 2002. **11**: p. 175-195.
6. Dano, M. and M. Hyer, *SMA-induced Snap Through of Unsymmetric Fibre-reinforced Composite Laminates.* International Journal of Solids and Structures, 2003. **40**: p. 5949-5972.
7. Williams, R.B., et al., *Nonlinear Tensile and Shear Behaviour of Macro Fiber Composite Actuators.* Journal of Composite Materials, 2004. **38**(10): p. 855-869.
8. Aimmanee, S. and M. Hyer, *Analysis of the Manufactured Shape of Rectangular THUNDER-type Actuators.* Smart Materials and Structures, 2004. **13**: p. 1389-1406.
9. Quackenbush, T., W. Usab, and B. Carpenter, *Ducted Propulsors with Steerable Outflow Using Smart Materials Technology*, in *Advanced Marine Materials Conference*. 2004, RINA: London, UK.
10. Quackenbush, T., B. Carpenter, and S. Gowing, *Design and Testing of a Variable Geometry Ducted Propulsor Using Shape Memory Alloy Actuation*, in *AIAA 43rd Aerospace Sciences Meeting*. 2005, AIAA: Reno, Nevada, USA.
11. Davis, S., et al., *Enhnaced Modelling and Performance in Braided Pneumatic Muscle Actuators.* The International Journal of Robotics Research, 2003. **22**: p. 213-227.
12. Koyama, Y., et al., *Harnessing the Actuation Potential of Solid-state Intercalation Compounds.* Advanced Functional Materials, 2006. **16**: p. 492-498.
13. Hyer, M., *Some Observations on the Cured Shape of Thin Unsymmetric Laminates.* Journal of Composite Materials, 1981. **15**(2): p. 175-194.
14. Hyer, M., *Calculations of the Room-Temperature Shapes of Unsymmetric Laminates.* Journal of Composite Materials, 1981. **15**: p. 296-310.
15. Hyer, M., *The Room-Temperature Shapes of Four-Layer Umsymmetric Laminates.* Journal of Composite Materials, 1982. **16**: p. 319-340.
16. Hamamoto, A. and M. Hyer, *Non-Linear Temperature-Curvature Relationships for Unsymmetric Graphite-Epoxy Laminates.* International Journal of Solids and Structures, 1987. **23**(7): p. 919-935.
17. Jun, W. and C. Hong, *Cured Shape of Unsymmetric Laminates with Arbitrary Lay-Up Angles.* Journal of Reinforced Plastics and Composites, 1992. **11**(12): p. 1352-1366.

18. Dano, M. and M. Hyer, *The Response of Unsymmetric Laminates to Simple Applied Forces.* Mechanics of Composite Materials and Structures, 1996. **3**(1): p. 65-80.
19. Dano, M. and M. Hyer, *Thermally-Induced Deformation Behaviour of Unsymmetric Laminates.* International Journal of Solids and Structures, 1998. **35**(17): p. 2101-2120.
20. Dano, M. and M. Hyer, *Snap-Through of Unsymmetric Fiber-Reinforced Composite Laminates.* International Journal of Solids and Structures, 2002. **39**: p. 175-198.
21. Ren, L., A. Parvizi-Majidi, and Z. Li, *Cured Shape of Cross-Ply Composite Thin Shells.* Journal of Composite Materials, 2003. **37**(20): p. 1801-1820.
22. Potter, K. and P. Weaver, *A Concept for the Generation of Out-Of-Plane Distortion from Tailored FRP Laminates.* Composites Part A: Applied Science and Manufacturing, 2004. **35**(12): p. 1353-1361.
23. Potter, K., et al., *Phenomena in the Bifurcation of Unsymmetric Composite Plates.* Composites Part A: Applied Science and Manufacturing, 2007. **38**(1): p. 100-106.
24. Schlecht, M., K. Schulte, and M. Hyer, *Advanced Calculation of the Room-Temperature Shapes of Unsymmetric Composite Laminates.* Journal of Composite Materials, 1999. **33**(16): p. 1472-1490.
25. Hufenbach, W., M. Gude, and L. Kroll, *Design of Multistable Composites for Application in Adaptive Structures.* Composites Science and Technology, 2002. **62**(16): p. 2201-2207.
26. Schultz, M., *Use of Piezoelectric Actuators to Effect Snap-Through Behaviour of Unsymmetric Composite Laminates*, in *Engineering Mechanics*. 2003, Virginia Polytechnic Institute: Virginia.
27. Bowen, C., et al., *Morphing and Shape Control using Unsymmetrical Composites.* Journal of Intelligent Material Systems and Structures, 2007. **18**(1): p. 89-98.
28. Hufenbach, W., M. Gude, and C. Czulak, *Actor-initiated Snap-Through of Unsymmetric Composites with Multiple Deformation States.* Journal of Materials Processing Technology, 2006. **175**(1-3): p. 225-230.
29. Mattioni, F., et al., *The Application of Residual Stress Tailoring of Snap-Through Composites for Variable Sweep Wings*, in *47th AIAA/ASME/ASCE/ARS/ASC Structures, Structural Dynamics, and Materials Conference*. 2006, AIAA: Newport, Rhode Island, USA.
30. Schultz, M. *A New Concept for Active Bistable Twisting Structures*. in *Smart Structures and Materials 2005: Smart Structures and Integrated Systems*. 2005. Bellingham, WA.
31. Schultz, M., *A Concept for Airfoil-like Active Bistable Twisting Structures.* Journal of Intelligent Material Systems and Structures, 2008. **19**(2): p. 157-169.
32. Kaw, A., *Mechanics of Composite Materials*. 1997, Florida: CRC Press LLC.
33. Pickering, S., *Recycling Technologies for Thermoset COmposite Materials - Current Status.* Composites Part A: Applied Science and Manufacturing, 2006. **37**(8): p. 1206-1215.
34. Boyd, R., *Relaxation Processes in Crystalline Polymers: Experimental Behaviour - A Review.* Polymer, 1985. **26**(3): p. 323-347.
35. Boyd, R., *Relaxation Processes in Crystalline Polymers: Molecular Interpretation - A Review.* Polymer, 1985. **26**(8): p. 1123-1133.
36. McCrum, N., *The Kinetics of the Alpha and Beta Relaxations in Isotactic Polypropylene.* Polymer, 1984. **25**(3): p. 299-308.

37. Read, B., *Mechanical Relaxation in Isotactic Polypropylene.* Polymer, 1989. **30**(8): p. 1439-1445.
38. Wortmann, F.-J. and K. Schulz, *Stress Relaxation and Time/Temperature Superposition of Polypropylene Fibres.* Polymer, 1995. **26**(2): p. 315-321.
39. Wortmann, F.-J. and K. Schulz, *Investigations on the Thermorheological Simplicity of Polypropylene Fibres in the Alpha-Transition Range.* Polymer, 1995. **36**(8): p. 1611-1615.
40. Wortmann, F.-J. and K. Schulz, *Thermomechanics of Isotactic Polypropylene Between -67 and +140 C: Investigation of the Relaxation Behaviour based on Literature Data.* Polymer, 1996. **37**(5): p. 819-824.
41. Wortmann, F.-J. and K. Schulz, *Non-linear Viscoelastic Performance of Nomes, Kevlar and Polypropylene Fibres in a Single-Step Stress Relaxation Test: 1. Experimental Data and Principles of Analysis.* Polymer, 1994. **35**(10): p. 2108-2116.
42. Wortmann, F.-J. and K. Schulz, *Non-Linear Viscoelastic Performance of Nomex, Kevlar and Polypropylene Fibres in a Single-Step Stress Relaxation Test: 2. Moduli, Viscosities and Isochronal Stress/Strain Curves.* Polymer, 1995. **36**(12): p. 2363-2369.
43. Dutta, N. and G. Edward, *Generic Relaxation Spectra of Solid Polymers. 1. Developement of Spectral Distribution Model and its Application to Stress Relaxation of Polypropylene.* Applied Polymer Science, 1997. **66**(6): p. 1101-1115.
44. Ariyama, T., *Stress Relaxation Behaviour After Cyclic Preloading in Polypropylene.* Polymer Engineering and Science, 1993. **33**(22): p. 1494-1501.
45. Ariyama, T., *Effect of Mean Strain on the Cyclic Deformation and Stress Relaxation in Polypropylene.* Polymer Engineering and Science, 1995. **35**(18): p. 1455-1460.
46. Ariyama, T., Y. Mori, and K. Kaneko, *Tensile Properties and Stress Relaxation of Polypropylene at Elevated Temperatures.* Polymer Engineering and Science, 1997. **37**(1): p. 81-90.
47. Tomlins, P. and B. Read, *Creep and Physical Ageing of Polypropylene: A Comparison of Models.* Polymer, 1998. **39**(2): p. 355-367.
48. Read, B. and P. Tomlins, *Time-Dependent Deformation of Polypropylene in Response to Different Stress Histories.* Polymer, 1997. **38**(18): p. 4617-4628.
49. Read, B. and P. Tomlins, *Creep and Physical Ageing of Injection Molded Fiber Reinforced Polypropylene.* Polymer Engineering and Science, 1997. **37**(9): p. 1572-1581.
50. Buckley, C. and M. Habibullah, *Physical Ageing of Drawn Polypropylene Fibres.* Journal of Applied Polymer Science, 1981. **26**(8): p. 2613-2623.
51. Teoh, S., A. Poo, and G. Ong, *Effective and Recovery Stresses in Deformation Studies of Polyvinyl Chloride and Polypropylene Using the Modified Strain Transient Dip Test.* Journal of Materials Science, 1994. **29**(18): p. 4918-4926.
52. Andreassen, E., *Stress Relaxation of Polypropylene Fibres with Various Morphologies.* Polymer, 1999. **40**(14): p. 3909-3918.